FOG

Freiberg Online Geoscience

FOG is an electronic journal registered under **ISSN 1434-7512**

2015, Volume 39

Broder Merkel & Mandy Hoyer

FOG special volume: Regional Hydrogeology in Asia and the Middle East

130 pages, 6 contributions

List of contents

Classification of karst springs based on discharge and water chemistry in Makook karst system, Kurdistan Region, Iraq

Mustafa, Omed — Institute of Geology, Technische Universität Bergakademie Freiberg, Gustav-Zeuner Str.12, 09599 Freiberg, Germany. Email: omedgeology@gmail.com

Merkel, Broder — Institute of Geology, Technische Universität Bergakademie Freiberg, Gustav-Zeuner Str.12, 09599 Freiberg, Germany. Email: merkel@geo.tu-freiberg.de

Abstract: The characterization and classification of karst springs is difficult due to non-homogeneity in the hydrodynamic properties and the fact that hydrochemical processes are governing karstification. This work characterizes the karst springs (Makook karst system, Kurdistan Region, Iraq) by combining the hydrodynamic and hydrogeochemical properties of karst waters. The ratio of minimum to maximum discharges was correlated to the hydrogeochemical parameters of karst waters. Based on this correlation a karst index (*KI*) is calculated and a classification proposed. According to this *KI*, karst springs of the area are categorized into four classes, with the lowest value of *KI* referring to the lowest degree of karstification, and the highest value for the most developed karst. The proposed *KI* may help for better classification of karst systems as well as contribute to modeling and assessment of water resources management.

Keywords: Karst springs, Kurdistan Region, Makook karst system, karst index, hydrodynamics, hydrochemistry

1 Introduction

Karstification in carbonate rocks is accompanied by changes in hydrogeochemical parameters which can be used as tracers (Glynn and Plummer 2005; Karimi et al. 2005; Aquilina et al. 2005). A number of different authors have studied the relationship between the hydrochemical and hydrodynamic properties of karst waters and systems by means of hydrographs and chemographs (Jakucs 1959; Shuster and White 1971; Ternan 1972; Scanlon and Thrailkill 1987; Rovey 1994; Raeisi and Karami 1997; Martin and Dean 2001; Grasso and Jeannin 2002; Perrin et al. 2003; Aquilina et al. 2005). Jakucs (1959) combined both hydrographs and chemographs of karst springs, recognizing that their response to precipitation depends on the nature of the recharge. A number of different authors have agreed that flow regimes in karst systems can be classified as either conduit or diffuse (White 1969; Shuster and White 1971; Atkinson 1977; Smart and Hobbs 1986; Martin and Dean 2001; White 2006; Liñán Baena et al. 2009). Smart and Hobbs (1986) attempted to categorize karst aquifers on a conceptualized basis into those exhibiting concentrated and dispersed recharge, saturated and unsaturated storage. Birk et al. (2004) characterize the local recharge and conduit flow in karst aquifers by linking the hydraulic and physico-chemical responses of springs to recharge events. Perrin et al. (2003) investigates the share of karst storage from the infiltrated recharges by means of hydro-iso graphs. Aquilina et al. (2005) used the hydro-chemograph of karst springs to interpret the recharge and storage mechanisms during rainfall events. Moral et al. (2008) classify the karst springs depending on magnesium content and temperature of karst water. Milanović (1981) connected the degree of karstification to aquifer

depth, assuming that shallow depths are associated with a greater degree of karstification. Rashed (2012) proposed a new method to assess the degree of karstification (D_k) taking the whole hydrograph component into consideration.
The present work introduces a new approach to the classification of karst springs based on the correlation between hydrograph components and the corresponding hydrogeochemical parameters. A karst index (*KI*) describes karst springs using both quantitative and qualitative approaches. Thus the characteristics of a karst system can also be predicted. The *KI* can help researchers in better classify karst systems via the use of discharge and chemical data.

2 Materials and methods

2.1 Study area

The area of interest is located in the Kurdistan region in the northeast of Iraq, mainly in Sulaimani governorate, Ranya district (Fig.1). The area is situated within latitudes 36°10'– 36°35' north and longitudes 44°30'– 44°50' east in the elevation range of 500 to >2000 meter (m) above sea level. Makook Anticline Mountain lies in a northwest–southeast direction and is surrounded by Shawre valley in the northeast and Balisan valley in the southwest. The area of interest comprises about 400 km^2 and is part of the Dokan lake catchment. The studied area is characterized by humid to moist climate. Rainy season starts from October and mainly ends in May with minor showers in June, July, and September. The highest precipitation rate, highest relative humidity, and lowest temperature are observed in February. The mean annual precipitation for the area of interest is 570.5 mm and the average annual temperature is 20 °C. The mean annual evaporation (pan) is about 2000 mm and the mean relative humidity is about 47% (Mustafa et al. 2015).
Rocks of Mesozoic and Cenozoic age can be found in the region of interest (Fig.1). Two units of Jurassic rocks are cropping out representing older rocks: i) Sarki and Sehkaniyan formation, which are composed mainly of limestone, dark dolomite, and shale (Jassim and Goff 2006), and ii) Sargelu formation (Bajocian–Bathonian), Naokelekan formation (Late Oxfordian–Early Kimmeridgian), Barsarin formation (Kimmeridgian–Early Tithonian), and Chia Gara formation (Late Tithonoan), which include bedded to massive dolomite, limestone, bituminous limestone, and marl. The Cretaceous unit comprises Balambo and Sarmord formation (marly and bedded limestone, bedded dolomite, and marl), Qamchuqa formation (mainly massive limestone and dolomite), Bekhme formation and locally Kometan formation (well bedded to massive limestone), Shiranish formation (well bedded limestone and marl), and Tanjero formation (sandstone, claystone, and conglomerate) (Bellen et al. 2005). Kometan formation doesn't appear in the geological map (Fig.1), while it is a regional map and the existence of Kometan formation was during the time of mapping still uncertain. Near Sarwchawa town, Kometan formation changes laterally to Bekhme formation through a transitional zone (Karim et al. 2012), and both formations are possibly overlain by Shiranish formation. Jurassic and Cretaceous rocks are occasionally overlain by Quaternary fan deposits (boulders, gravel, and fine clastics) and a thin layer of soil (mainly in the valleys, because of soil erosion in that mountainous area).
Makook Anticline represents a double plunging anticline (NW–SE) within in the parallel trend of Zagros folded structures between Ranya and Palawan anticlines and Sahwre and Balisan synclines (in between) in the NE and SW respectively (Fig.1). The area is characterized by tectonic distortion, especially in the northwest part of Makook Anticline.
Generally, all springs are within the Makook Anticline Mountain except Chewa spring, which is located in the NW plunge of the Palawan anticline. Makook karst system is composed of three karst aquifers: Bekhme, Kometan and Shiranish aquifers (Mustafa et al. 2015). Bekhme karst aquifer supplies major springs along Makook anticline including Zewa, Qala Saida and Gullan springs (Fig.1). Bekhme aquifer is a well karstified, thick, semi-confined aquifer underlain by Sarmord formation (aquiclude). The effective recharge for Bekhme aquifer was estimated to be >50% of the total precipitation (Stevanovic and Markovic 2004). The Kometan aquifer is represents the source of Sarwchawa, Betwata, Chewa and Bla springs (Mustafa et al. 2015). Kometan formation is a well karstified, highly fissured aquifer with confined to semi-confined conditions and overlain by Shiranish formation (Stevanovic and Markovic 2004). The aquifer is composed of carbonate rocks and contains a large amount of

groundwater, varying in space and time. One of the springs (Shkarta) drains poorly developed karst (with small fissures). This spring is located in the Shiranish formation (marl and marly limestone), which was inconsistently recognized as a fissured aquitard (locally in the marly limestone part) by Al Manmi (2008).The general groundwater flow direction is from the NW to the SE of the studied area (Al Manmi 2008). Strong karstification cycles took place in the aquifer system during the Paleocene–Miocene period (Stevanovic et al., 2009), and are ongoing process, even recently.

Concerning the karst features, depressions and sinkholes are rarely recognized, but remote sensing investigations revealed that cores of some of the major anticlines are pitted due to karstification (Stevanovic and Markovic 2004).

Betka cave near Sarwchawa town was described by Stevanovic et al. (2009). At the entrance of Betka cave a hall with 20 m length, 7 m width and 10 m height was found. The existence of the Qamchuqa formation aquifer in the region of interest is possible, as mentioned by Al Manmi (2008), but no field evidence has been reported so far.

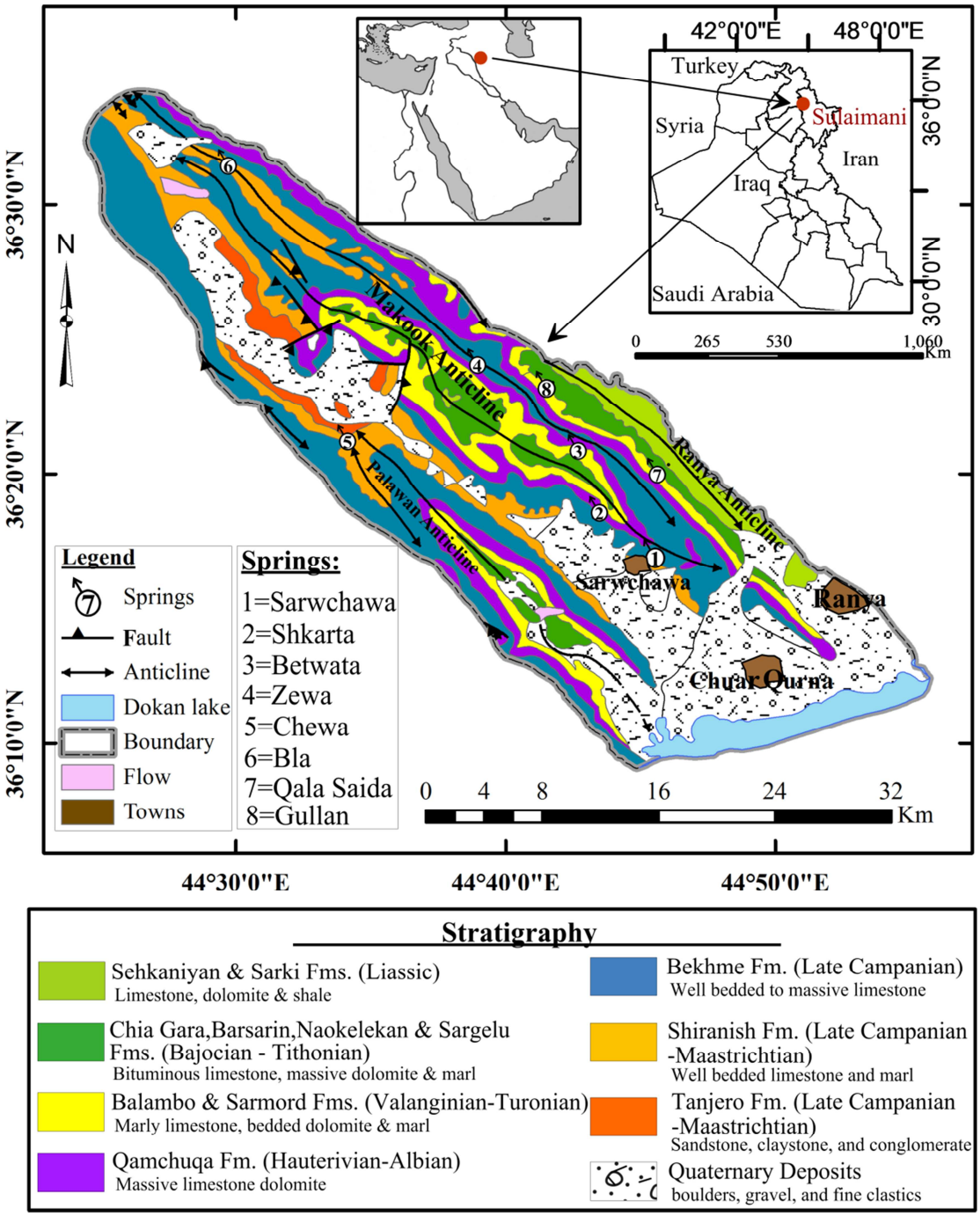

Fig.1: Geology and location of the study area in Kurdistan Region, Iraq (modified after Sisakian 1998)

2.2 Methodology

Because no continuous discharge measurements of the springs were available, different methods (current meter and volumetric readings) were employed to record the discharge of the springs during the monitoring period from September 2011 to November 2012. Due to time restrictions flow measurements and field parameters were measured only six times (Sep.2011, Dec.2011, Apr.2012, Jun.2012, Sep.2012 and Nov. 2012) accompanying the sampling processes.

The sampling and measurements of field parameters were conducted at the spring's outlet. Redox potential (Eh) was measured via a WinLab redox meter and WTW SenTix-ORP electrode and checked by standard redox buffer (pH=7 and 220 millivolts at 25 °C). The parameters pH, specific conductance (SpC), dissolved oxygen (DO), and water temperature (T) were measured on-site using a multi-parameter WTW model 3430, WTW pH electrode SenTix-940, WTW TetraCon-925 conductivity electrode and WTW FDO-925 optical dissolved oxygen sensor. A three-point calibration was carried out for the pH electrode via technical WTW buffers (pH=4.01, pH=7 and pH=10). The EC electrode was checked with WTW standard control solution; settings were chosen so that the output of the electrode was converted to a water temperature of 25 °C. A certified mercury-thermometer was employed for air temperature measurement. Alkalinity was determined immediately after sampling by means titration and converted to hydrogen-carbonate (HCO_3^-) according to APHA (1998).

Eight karst springs (Sarwchawa, Shkarta, Betwata, Zewa, Chewa, Bla, Qala Saida, and Gullan) were sampled six times between September 2011 and November 2012. Thus a total of 48 samples were taken. The temporal sampling from each spring was planned to be representative for the dry and wet periods (Appendix 1). The measurement of major cations, anions, trace elements and stable isotopes of δD was conducted in the laboratories of the Hydrogeology Department, Technische Universität Bergakademie Freiberg, Germany. Major cations (Ca^{2+}, Mg^{2+}, Na^+ and K^+) content were determined via ion chromatography (IC) using an 850 Professional IC Metrohm with Metrosep C4-150 column and 2 mM dipicolinic acid eluent. The SO_4^{2-}, Cl^- and F^- anion levels were determined with a Metrohm Compact IC Pro 881 and Metrosep A sup 15-150 column was used with 3 mM $NaHCO_3$ and 3.5 mM Na_2CO_3 as eluent. The determination of Li, P, Si and Sr (and other elements, not reported here) were done with an ICP-MS XSeries-2 (Thermo Scientific) either in direct mode or using the collision mode. The reproducibility of IC and ICP-MS determinations was around 2% and 5% respectively. Stable isotopes of δD were measured by means of an LGR liquid–water isotope analyzer (DLT-100), with a precision of < 0.3‰.

The ion balance, partial pressure of CO_2 (P_{CO2}) and saturation index of calcite ($SI_{Calcite}$), dolomite ($SI_{Dolomite}$), gypsum (SI_{Gypsum}), fluorite ($SI_{Fluorite}$), halite (SI_{Halite}) and SI in other minerals were calculated by means of PHREEQC (Parkhurst and Appelo 2013) using the WATEQ4F database. The data used in this work were subjected to different quality assurance procedures and statistical tests using SPSS software package (Landau and Everitt 2003). Non-parametric two-tailed correlation analysis (Kendall and Spearman correlations) was performed for the hydrogeochemical and field parameters in addition to basic statistical treatment. The climate of the area was characterized by means of meteorological data of Dokan lake station (not shown in Fig.1) obtained from Directorate of Meteorology and Seismology, Kurdistan Regional Government, Ministry of Transportation and Communication (MTC).

3 Results and disscussion

The summery of the statistical analysis for the hydrogeochemistry, physico-chemical parameters and hydrogeochemical modeling of the springs are shown in Tab. 1, Tab. 2 and Tab. 3. The detailed data set is included in appendices 1, 2 and 3.

3.1 Hydro-chemograph characteristics

The hydrographs patterns for the studied springs are shown in Fig. 2. The hydrograph of Sarwchawa spring presents a rapid increasing of discharge as response to precipitation events, which corresponds to decrease in water temperature, SpC and pH (Fig. 2a and Tab. 1). The rapid response of Q, T, and SpC of karst springs indicates a short transit time and an effective conduit system (Birk et al. 2004; Liñán Baena et al. 2009). In contrast, the response of Shkarta spring discharge to precipitation events is gradual and on a smaller scale compared to that of the majority of the springs. The fact that low discharge levels commonly observed in marly rocks result in increased residence times (Pearson and Scholtis, 1995) means that low flow rates in micro-fractures of Shiranish marly limestone are likely the reason for the recorded long residence time and gradual variation in discharge in the Shkarta spring. The hydrograph of the Betwata spring shows two amplitudes in response to the Oct - Dec 2011 and Apr – Jun 2012 precipitation events. The same pattern is visible in the graph for the Chewa spring albeit with a lesser response to the earlier event. A gentle rise in the Zewa spring hydrograph was recorded, which together with the steep slope of discharge decreasing until recovery likely reflects the low storage capacity of the associated karst system. The Bla spring hydrograph is characterized by an interesting decrease in Dec 2011 matching the rhythm of temperature and SpC variation in response to the Oct 2011 - May 2012 precipitation events.

Tab. 1: Statistics of the physico-chemical, flow and isotopic characteristics of the karst springs

Spring & Code	*East Longitude*	*North Latitude*	*Elevation (m)*	*Statistics*	*pH*	*Eh (mV)*	*SpC (µS/cm)*	*Water T (°C)*	*Air T (°C)*	*DO (mg/l)*	*Flow (l/s)*	*δD (‰)*
Sarwchawa (1)	36°16'32.9"	44°45'19.4"	584	***St.D***	0.2	32.3	65.5	3	8.9	0.02	762.3	1.6
				Min	7.1	343	482	11	10	6.45	2370	-43.39
				Max	7.6	434	664	18.7	30.5	6.49	4630	-39.18
				Mean	7.3	388	551	15.1	19.4	6.48	3233	-40.3
Shkarta (2)	36°18'21.7"	44°43'15.7"	578	***St.D***	0.2	31.1	65.5	6.1	6.5	0.57	0.4	1.3
				Min	7.1	335	406	6	16	7.03	0.1	-35.57
				Max	7.8	431	583	23.4	32.5	7.36	1.1	-31.9
				Mean	7.4	383	453.8	17.4	23.8	6.37	0.5	-32.9
Betwata (3)	36°20'39.5"	44°42'30.7"	1063	***St.D***	0.3	33.4	177.4	4	7.8	0.74	14.8	1.3
				Min	7.2	337	380	9	14	8.03	18.8	-43.87
				Max	7.9	433	831	19	32	8.46	59.3	-40.39
				Mean	7.6	383	470	13.4	23.5	7.17	30.2	-41.2
Zewa (4)	36°24'10"	44° 34' 25"	943	***St.D***	0.4	34.1	21.7	3.1	7.3	0.9	45.9	1.1
				Min	7.3	324	296	8	11	7.8	48	-45.93
				Max	8.4	416	350	15.2	31	8.34	165.8	-42.79
				Mean	7.8	367	320.3	11.6	18.8	6.7	109	-43.8
Chewa (5)	36°20'50.4"	44°34'20.2"	838	***St.D***	0.2	29.3	254.7	4.5	6	0.09	86.3	1.5
				Min	7.2	358	444	8	19	5.95	101	-43.75
				Max	7.8	442	1117	19	35	6.05	332.5	-39.57
				Mean	7.4	392	602.5	14.2	26.8	5.9	160.2	-41.1

Bla (6)	36°31'23.9"	44°29'46.3"	945	***St.D***	0.2	46.9	69.1	3.2	7.8	0.7	265	1.5
				Min	7.2	351	396	8	10	7.25	126	-44.71
				Max	7.8	478	599	15.5	28	7.64	875	-40.2
				Mean	7.4	397	488.8	11.4	20	6.47	450.1	-42
Qala Saida (7)	36°20'19.9"	44°46'02.1"	953	***St.D***	0.2	33.7	122.7	2.9	11.2	1	2	1.3
				Min	7.3	357	383	9	5	7.58	1.5	-41.62
				Max	7.8	446	722	17	34	8.15	6.8	-37.9
				Mean	7.5	381	488.8	14.2	21.5	6.43	3	-39.7
Gullan (8)	36°23'23.7"	44°41'44.8"	1309	***St.D***	0.4	35.7	33	2.4	8	1.4	21.6	1.4
				Min	7.3	323	265	8	3.5	7.71	27.4	-45.02
				Max	8.2	432	360	14.1	26	8.5	87.6	-41.1
				Mean	7.7	373	310.5	9.5	15.1	6.13	50.6	-42.3

Eh = oxidation reduction potential; ***SpC*** = Electrical conductivity; ***T*** = temperature; ***DO*** = dissolved oxygen; ***Flow*** = discharge of the springs; ***St.D*** = standard deviation; ***Min*** = minimum; ***Max*** = maximum; The statistical tests are based on 6 measurements (***n***) for each springs, except ***DO*** that measured only 3 times

Regarding specific conductance, the Sarwchawa spring exhibits a unique concave pattern compared to that of the other springs with an abnormal increase observed during the rainy period of Oct – Nov 2012. The SpC pattern at Betwata spring (Fig. 2c) is close to that observed at Shkarta, with a delay in increase from Apr – Jun 2012. The complexity and roughness of the Qala Saida and Gullan spring SpC patterns (Fig. 2g and Fig. 2h) is indicative for the heterogeneity of the karst system associated with the Bekhme aquifer.

The calcium chemographs of spring water mainly show decreasing calcium concentration during recharge periods, except Zewa spring (Fig. 2d and Tab. 2) which shows the reverse (increasing Ca^{2+} concentration with increasing recharge). Similar decreasing of Ca^{2+} through dilution by low mineralized recharge water was reported by Vesper and White (2004) for karst springs in Kentucky, USA. A zigzag-like pattern in Ca^{2+} chemographs of Chewa and Bla springs was observed and indicates the similarity in recharges and flow systems for both springs. A time lag was enhanced by the most noticeable changes in hydrogeochemistry after the recharge events. This time lag suggests the presence of piston phenomena (recharge water flush the storage water in the karst aquifer before discharging at the spring outlet) (Vesper and White 2004).

Sulfate concentrations show the same variation as Ca^{2+} corresponding to the dilution with recharge water, except in Zewa and Gullan springs showing opposite patterns (Fig. 2d and Fig. 2h). The sulfate concentration is higher in Sarwchawa spring. Oxidation of pyrite concretions (Al Manmi 2002; Mustafa 2007), and gypsum impurities along the flowpath of Kometan aquifer is possibly leads to formation of this sulfate rich water. Sulfate concentrations are low during high discharge periods but generally increase as discharge decreases, and thus can be used as a tracer for quantifying mixing ratios (Lee and Krothe 2003). Dilution of karst water by recharged water was obvious at Sarwchawa during the period of peak discharge (Apr.2012). Low temporal variation in SO_4^{2-} in karst waters implies the effective mixing of recharged water with groundwater before discharge from the spring (Martin and Gordon, 2000) a process likely occurring in some majority of the studied springs.

A general trend of increasing P_{CO2} with increasing discharge was observed in the karst springs. This reflects the decrease of diffuse atmospheric CO_2 and increase of CO_2 in soil (Gillon et al. 2009; Delbart et al. 2014). The patterns of P_{CO2} in karst springs were consistence with sulfate patterns rather than the Ca^{2+} ones (Fig. 2). Increasing of P_{CO2} *is* accompanied by increasing of Ca^{2+}, sulfate, SpC, T and Eh. Although, the water temperature pattern for the Shkarta spring is similar to that of the Sarwchawa spring, the former exhibited the highest values among the studied springs (Fig. 2a and Fig. 2b). A lateral groundwater influx from one aquifer to another, together with the presence of clay and marl layers in the vicinity of the springs, leads to mixing and causes a decrease in water temperature (Bundschuh 1993).

According to the local stratigraphic superposition, a lateral influx of water from the Kometan aquifer to the Shiranish aquitard is assumed to be the reason for the Oct – Nov 2012 temperature decrease in the Shkarta spring thermograph. The water temperature pattern at Betwata is more or less the same as

that of the two aforementioned springs with the exception of a near two month delay in recovery. A delay in the temperature recovery of a karst spring is the result of a short transit time, less developed karstification, and a diffuse flow pattern (Liñán Baena et al. 2009). Depending on the temporal variation of temperature and δD, two main categories were recognized. The first, includes Sarwchawa, Shkarta and Betwata springs. The temporal variation in these springs follows the same trend: temperature and δD decreased and increased with respect to precipitation events (Fig. 2a, b and c). Such similar behavior is related to depth, reservoir extent, hydraulic conductivity and kinetics of recharged precipitation and groundwater inside the karst system. The difference in water temperature at Shkarta is the highest of all studied springs (Tab. 1) and indicated shallow depth of the aquifer. The second category comprises Zewa, Chewa, Bla, Qala Saida and Gullan springs. This group is mainly characterized by depletion of δD patterns corresponding to precipitation events and decreasing of the temperature (Fig. 2d, e, f, g and h), which makes it different from the first group. The significant changes of isotopic signature corresponds to the recharge events indicating a direct influence of the karst aquifer by infiltrated water (Perrin et al. 2003). Temporal variation of δD in springs discharging from limestone aquifer (Sarwchawa, Betwata, Chewa and Bla springs) and Shiranish aquitard (Shkarta spring) are consistent with SpC changes. This might indicate a correlation between karstification of carbonates and isotope evolution.

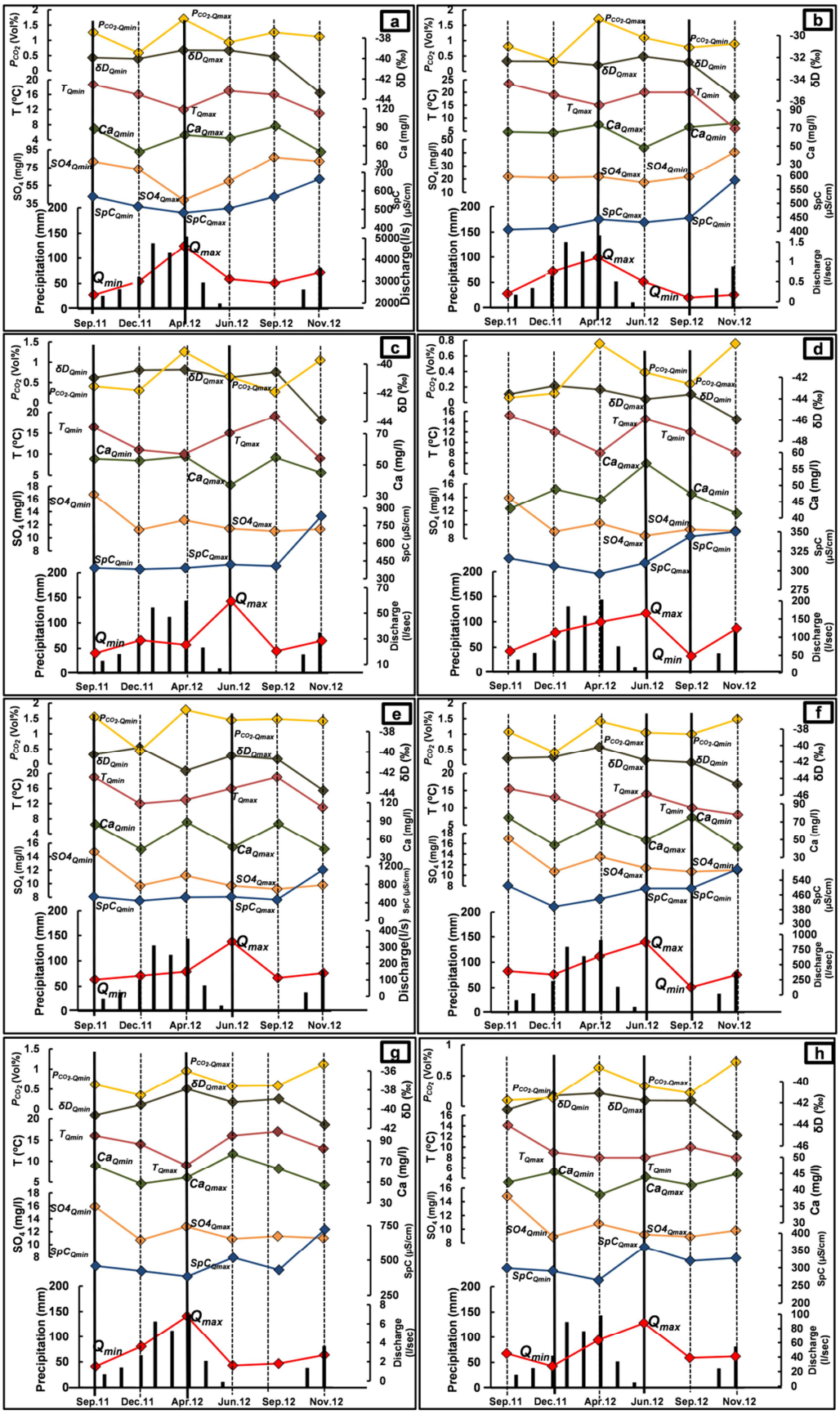

Fig. 2: **Hydro-chemograph of the studied springs. (a) Sarwchawa (b) Shkarta (c) Betwata (d) Zewa (e) Chewa (f) Bla (g) Qala Saida (h) Gullan; Q_{max} = maximum discharge of spring (l/s); Q_{min} = minimum discharge of spring (l/s); the solid vertical lines indicates Q_{max} and Q_{min} and there corresponds values.**

Tab. 2: Statistics of the hydrogeochemical characteristics of the karst springs

Spring & Code	*Statistics*	Na^+	K^+	Ca^{2+}	Mg^{2+}	Cl^-	SO_4^{2-}	HCO_3^-	F^-	*Si*	*Sr*	*P*	*Li*	*E%*
		Concentrations in mg/L												
Sarwchawa(1)	***St.D***	0.09	0.06	14.7	2.5	0.6	18.1	12	0.05	0.2	0.17	0.005	0.0004	NA
	Min	2.32	0.7	49.9	17	2	39	265.7	0.07	4.3	0.44	0.007	0.0025	-1
	Max	2.53	0.85	91.7	23.9	3.5	86.6	298.9	0.19	4.9	0.88	0.019	0.0036	1
	Mean	2.41	0.77	76.1	21.5	2.6	70.4	279.3	0.13	4.7	0.75	0.013	0.0031	-0.3
Shkarta(2)	***St.D***	0.82	0.25	9.9	1.5	4	8.2	15	0.03	0.4	0.06	0.012	0.0003	NA
	Min	3.59	1.48	48.2	9.6	4.8	17.4	213.7	0.06	8.5	0.29	0.011	0.0009	-4
	Max	5.89	2.27	75.3	13.7	15.5	40.4	253.9	0.14	9.4	0.44	0.04	0.0017	0
	Mean	4.36	1.84	66.5	10.7	8.3	24	231.5	0.09	8.9	0.33	0.023	0.0013	-1
Betwata(3)	***St.D***	0.03	0.05	7.2	0.8	0.5	2.2	9.1	0.01	0.2	0.01	0.003	0.0001	NA
	Min	1.23	0.38	37.2	18	1.3	11	235.1	0.04	3.9	0.12	0.005	0.0007	-1
	Max	1.3	0.5	55.4	20.4	2.6	16.7	260	0.07	4.3	0.14	0.012	0.001	1
	Mean	1.28	0.44	49.8	18.8	1.8	12.4	243.9	0.06	4.1	0.12	0.008	0.0009	-0.3
Zewa(4)	***St.D***	0.06	0.2	5.4	0.9	0.5	2	4.3	0.01	0.1	0.01	0.005	0.0001	NA
	Min	0.79	0.41	41.4	12.9	0.9	8.4	180	0.04	2.7	0.1	0.003	0.0005	-1
	Max	0.94	0.94	56.6	15.5	2.1	13.9	192	0.07	3.2	0.13	0.015	0.0007	3
	Mean	0.88	0.55	47.1	14.2	1.4	10	186.1	0.05	2.9	0.11	0.009	0.0006	0.7
Chewa(5)	***St.D***	0.08	0.07	22.7	0.7	0.5	2.1	7.6	0.02	0.3	0.01	0.004	0.0002	NA
	Min	1.77	0.46	43.3	18.5	1.8	9.2	332.3	0.06	5.3	0.17	0.008	0.0013	0
	Max	2.03	0.66	88.1	20.5	3	14.7	350	0.11	6	0.21	0.017	0.0018	1
	Mean	1.91	0.54	65.3	19.2	2.4	10.7	340.4	0.08	5.6	0.18	0.011	0.0017	0.5
Bla(6)	***St.D***	0.08	0.11	15.8	2	0.5	2.5	10.9	0.02	0.3	0.02	0.005	0.0001	NA
	Min	1.37	0.52	41.4	17.1	1.6	10.7	289.3	0.04	3.5	0.11	0.006	0.0008	0
	Max	1.62	0.81	75.1	22.6	3	16.9	318.5	0.11	4.3	0.18	0.016	0.0011	1
	Mean	1.52	0.65	58.9	21	2.1	12.4	305.3	0.06	3.8	0.14	0.01	0.001	0.3
Qala Saida(7)	***St.D***	0.08	0.04	11.6	0.8	0.5	2	14.6	0.02	0.2	0.01	0.005	0.0002	NA
	Min	1.24	0.35	47.2	20.4	1.5	10.7	242.1	0.03	3	0.07	0.004	0.0005	-2
	Max	1.47	0.48	77.3	22.5	2.8	15.9	286.2	0.08	3.5	0.09	0.016	0.001	1
	Mean	1.32	0.42	59.4	21.6	1.9	12.1	267.6	0.05	3.3	0.08	0.009	0.0008	-0.5
Gullan(8)	***St.D***	0.53	0.05	2.6	1	0.7	2.3	9.4	0.01	0.1	0	0.004	0.0001	NA
	Min	0.72	0.27	38.5	11.4	0.9	8.9	159.4	0.02	2.1	0.06	0.003	0.0004	-1
	Max	2.09	0.39	45.5	14.4	2.8	14.8	185.1	0.05	2.4	0.07	0.013	0.0007	1
	Mean	1.02	0.31	42.7	12.8	1.4	10.4	172.2	0.04	2.2	0.06	0.008	0.0006	-0.5

E% = Anion cation balance calculated by PHREEQC; NA = Not available; Na^+, K^+, Ca^{2+}, Mg^{2+}, F^-, Cl^- and SO_4^{2-} were measured by Ion Chromatography (IC); HCO_3^- measured by Titration; ***Si, P, Li*** and ***Sr*** measured by Inductively Coupled plasma – Mass Spectrophotometer (ICP-MS); ***St.D*** = standard deviation; ***Min*** = minimum; ***Max*** = maximum; The statistical tests are based on 6 measurements (***n***) for each spring; Spring codes can be used to trace the locations of the springs in ***Fig.1***

3.2 Hydrogeochemical processes and correlations

3.2.1 Saturation indices of minerals

Calculated saturation indices (Tab. 3 and Appendix 3) indicate that Zewa, Chewa and Qala Saida springs are oversaturated (SI ≥ 0.05) with calcite while Sarwchawa, Shkarta, Betwata and Bla springs are in equilibrium (-0.05 ≤ SI ≤ 0.05). Dedolomitization processes are in progress in waters in equilibrium with calcite and undersaturated with dolomite (Pavlovskiy and Selle 2014). Only Gullan spring is undersaturated (SI ≤ -0.05) with respect to calcite, which suggests shorter flowpath and shorter residence time in the aquifer compared to the other springs (Fig. 3c and Fig. 4). Regarding the SIDolomite, only Qala saida spring is in equilibrium, and the rest is undersaturated with respect to dolomite. All springs are undersaturated with respect to gypsum, fluorite, and halite. Obviously, incongruent dissolution of dolomite occurs in waters of Sarwchawa, Shkarta, Betwata and Bla springs.

3.2.2 Factors controlling the hydrogeochemical processes in karst springs

In order to investigate the factors that control the hydrogeochemistry in karst waters, two types of correlation analysis were applied (two tailed, ≤ 0.05 Pearson correlations). 1) Correlation analysis between mean values of water components in all springs (Fig. 3a, c, and f). 2) Correlation analysis between the values of water components in a single spring (temporal variation of one spring).

P_{CO2} correlates inversely with pH (r = -0.95, n = 8, p <0.001; mean values of the springs), controlling the increasing of Ca^{2+} (Fig. 3a), and consistently increasing SpC (r = -0.9, n = 8, p <0.001; mean values of the springs). In contrast, Mg^{2+} doesn't correlate to P_{CO2} (r = -0.1, n = 8, p = 0.3) and pH (r = -0.2, n = 8, p = 0.1). Therefore, other factors rather than P_{CO2} and pH control the Mg^{2+} concentration in karst waters. Oxidation-reduction processes in karst waters of the region of interest is correlated with P_{CO2} (r = -0.9, n = 8, p = 0.001; mean values of the springs). On a temporal scale, the water temperature controls the dissolution of dolomite in Zewa, Qala Saida and Gullan springs (discharged from dolomitic rocks of Bekhme aquifer), and oxidation - reduction processes in Shkarta, Chewa and Bla springs (r = 0.7 - 0.8; n = 6, p = 0.01 for each of the springs). Regarding the water – air temperature correlation, only Betwata spring shows a significant correlation (r = 0.8, n = 6, p = 0.01; temporal values), which reflects various depth for the aquifers and different recharge processes.

The temporal variations of many parameters are controlled by the flow of the springs. In Betwata spring increasing of flow is accompanied by decrease in Ca^{2+} concentration (r = 0.8, n = 6, p = 0.01) (Fig. 3d). This can be interpreted by less time for water to react with aquifer rocks in high flow periods compared to the low flow periods. Li concentration increases with increasing of SI_{Gypsum} which indicates the presence of Li in $CaSO_4$ minerals in karst carbonates according to Chiarenzelli et al. (2007) and O'Connor et al. (2010) who concluded that the dissolution of evaporitic minerals could be the source of Li and Sr in groundwater. Interesting is the depletion and enrichment of δD with increasing of silica and decreasing of SpC. Based on mean values of the springs, δD depletes with increasing of Si (Fig. 3f), which might be related to traces of silicate minerals in karst rocks. On the other hand enrichment of δD correlated significantly (r = 0.7-0.9, n = 6 p = 0.01 - 0.001; temporal values for each spring) to the increasing of SpC in karst springs discharged from the limestone aquifer (Sarwchawa, Betwata, Chewa and Bla), but this is not the case in springs discharging from the dolomitic aquifers (Zewa, Qala Saida and Gullan). The variation of silica and SpC with the evolution of δD in the studied springs indicates a certain physico - chemical process during the dissolution of the karst carbonates.

3.3 Classification of springs by means of a karst index (*KI*)

In order to classify the studied karst spring, hydrodynamic (flow) and hydrogeochemistry were linked to each other. The ratio of the maximum discharge to the minimum discharge represents a useful tool for describing the flashiness of an aquifer (White 2006). Therefore the ratio of minimum to the maximum discharge of the springs was investigated (Tab. 4). Different discharge ratios provide an impression of heterogeneity in the studied karst system. This difference in flow rates was used to classify the springs. A correlation test was performed between each of the minimum and maximum discharges and the previously discussed hydrogeochemical parameters (sections: 3.1 and 3.2). This correlation was used as indicator for different karst aquifers.

Tab. 3: Saturation indices of selected mineral and CO_2 in the karst springs

Spring & Code	*Statistics*	P_{CO2}	$SI_{Calcite}$	$SI_{Dolomite}$	SI_{Gypsum}	$SI_{Fluorite}$	SI_{Halite}
Sarwchawa(1)	***Min***	0.59	-0.25	-1	-1.9	-3.2	-9.8
	Max	1.70	0.31	0.3	-1.6	-2.3	-9.6
	Mean	1.09	0.02	-0.3	-1.7	-2.7	-9.8
Shkarta(2)	***Min***	0.32	-0.23	-1.1	-2.4	-3.4	-9.3
	Max	1.70	0.43	0.3	-1.9	-2.5	-8.6
	Mean	0.83	0.006	-0.6	-2.2	-3	-9
Betwata(3)	***Min***	0.27	-0.33	-1	-2.7	-3.8	-10.3
	Max	1.26	0.48	0.8	-2.4	-3.3	-10
	Mean	0.55	0.03	-0.2	-2.6	-3.5	-10.2
Zewa(4)	***Min***	0.06	-0.47	-1.3	-2.7	-3.8	-10.6
	Max	0.76	0.71	1.2	-2.6	-3.2	-10.2
	Mean	0.27	0.06	-0.2	-2.7	-3.6	-10.5
Chewa(5)	***Min***	0.44	-0.17	-0.6	-2.7	-3.5	-10
	Max	1.78	0.32	0.4	-2.4	-2.9	-9.8
	Mean	1.24	0.08	-0.1	-2.6	-3.2	-9.9
Bla(6)	***Min***	0.40	-0.41	-1	-2.7	-3.8	-10.1
	Max	1.48	0.29	0.5	-2.3	-2.9	-9.9
	Mean	0.99	-0.02	-0.3	-2.5	-3.4	-10.1
Qala Saida(7)	***Min***	0.35	-0.26	-0.8	-2.7	-4	-10.3
	Max	1.12	0.32	0.4	-2.4	-3.2	-10
	Mean	0.65	0.11	0.002	-2.5	-3.5	-10.1
Gullan(8)	***Min***	0.10	-0.58	-1.6	-2.7	-4.3	-10.7
	Max	0.72	0.49	0.7	-2.5	-3.5	-9.8
	Mean	0.28	-0.09	-0.6	-2.7	-3.8	-10.4

P_{CO2} = Partial pressure of CO_2 (Vol.%); ***SI*** = Saturation index of minerals; ***SI*** = Saturation index < 0.1; ***SI*** = Saturation index <- 0.1; ***Min*** = minimum; ***Max*** = maximum; The statistical tests are based on 6 measurements (***n***) for each spring; The data was calculated with PHREEQC; Spring codes can be used to trace the locations of the springs in ***Fig.1***

Minimum and maximum discharge rates of the spring and their corresponding hydrogeochemical concentrations (Tab. 4) are used to calculate an arithmetic index. The proposed karst index (*KI*) is a dimensionless number calculated as follows:

$$\text{Karst Index } (KI) = M \times 100 \quad (1)$$

$$M = \frac{\sum_{i=1}^{n} ki}{n} \quad (2)$$

$$ki = \frac{Q_{min} \times i_{Qmin}}{Q_{max} \times i_{Qmax}} \quad (3)$$

where:

M = Arithmetic mean

ki = Ratio of minimum to maximum flow multiplied by their corresponding values for a specific parameter (i)

Q_{min} = Minimum discharge of spring (l/s, or equivalent)

Q_{max}= Maximum discharge of spring (l/s, or equivalent)

i_{Qmin} = Value of specific water parameter corresponding to the minimum discharge rate (unit)

i_{Qmax} = Value of specific water parameter corresponding to the maximum discharge rate (unit)

n = number of hydrogeochemical parameters

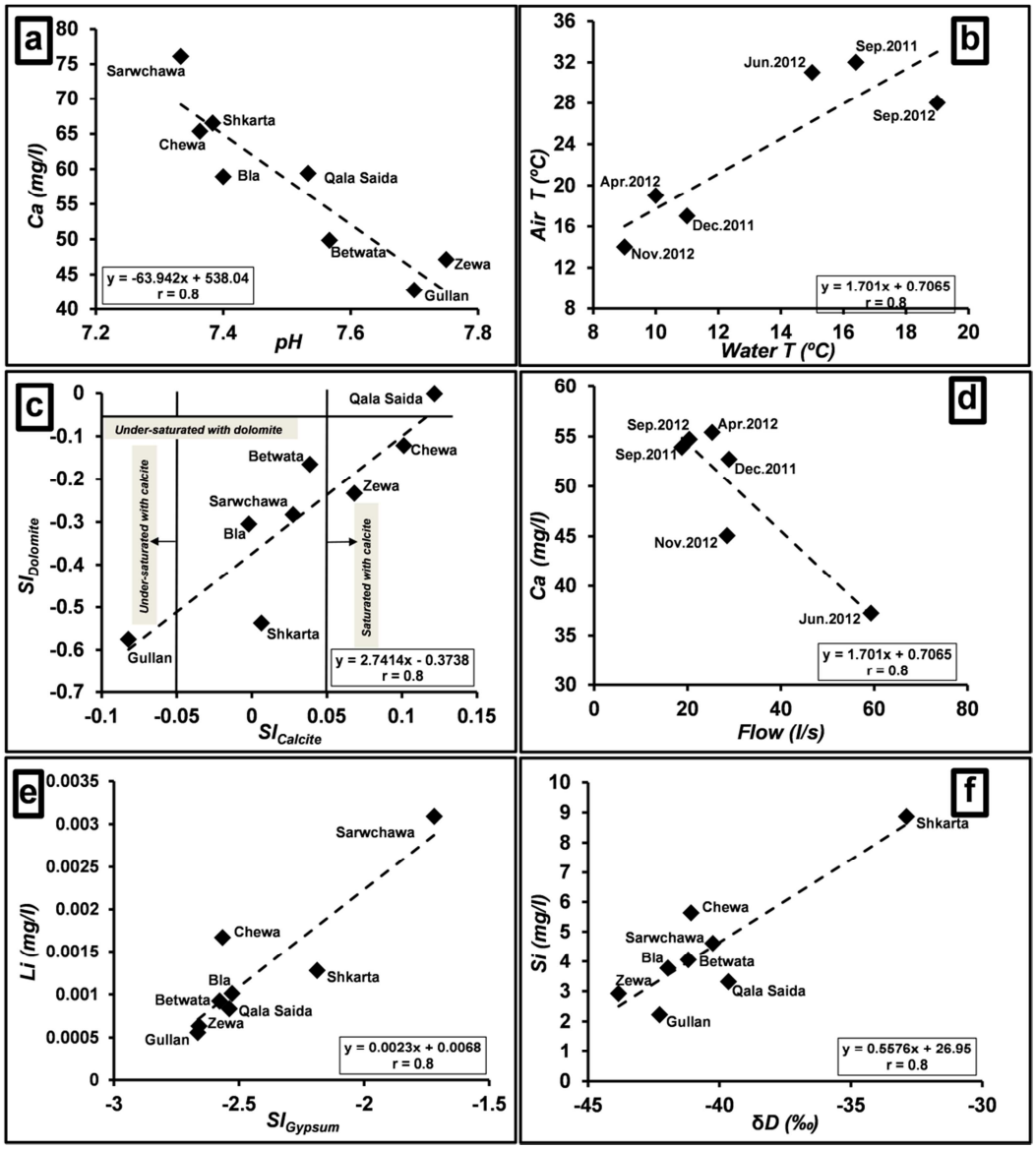

Fig. 3: Correlations of hydrogeochemical parameters in karst springs. Correlations in (b) and (d) are based on temporal values (n=6) in Betwata spring. Values of the correlated parameters in (a), (c), (e) and (f) represents mean value of 6 periods during Sept.2011-Nov.2012.

The i_{Qmin} and i_{Qmax} values do not necessarily represent minimum and maximum concentrations of the hydrogeochemical parameters rather being selected according to their corresponding minimum and maximum flow rates (Tab. 4 and Fig. 2). In addition to the discharge the values of pH, Eh, SpC, HCO_3^- and δD were involved in calculation of the *KI* (Tab. 4). Even with increasing or decreasing the number of hydrogeochemical parameters springs stay in the same *KI* class. For example, in case of using only pH, SpC and HCO_3^- the calculated *KI* is more or less the same as the former case (including all parameters). Vice versa if we increase the number of parameters and include Na^+, Ca^{2+}, SO_4^{2-}, Si, Li, P_{CO2}, SI_{Gypsum}, $SI_{Fluorite}$ and SI_{Halite} (Appendix 4), the *KI* value is more or less the same. The obtained values also exhibit different levels of sensitivity for the parameter suggesting that a range of different factors affects the studied springs (relating to the nature of their respective donor aquifers). The proposed *KI* classifies the studied springs into four types. The range of *KI* values calculated using different hydrogeochemical parameters probably supports the idea of a qualitative (i.e., hydrogeochemical) rather than quantitative (i.e., flow rate) effect on karstification processes. The value of *KI* varies between 8.8 (Shkarta) and 55.8 (Sarwchawa) in the region of interest generally reflecting the effects of minimum and maximum spring flow rates on the index (Tab. 4). However, this is not the case for the Bla and Qala Saida springs, which exhibits the reverse situation (higher *KI* in Qala Saida, which has a

lower discharge compared to Bla). The *KI* values for these two springs indicate that the hydrogeochemical characteristics of water at these locations have a greater influence than the flow rate on the karst index. Thus, *KI* reveals sensitive classification of karst springs depending on quantity (flow rate) and hydrogeochemical parameters.

Tab. 4: Parameters used for the karst springs classification

Spring &Code	*Sarwchawa(1)*	*Shkarta(2)*	*Betwata(3)*	*Zewa(4)*	*Chewa(5)*	*Bla(6)*	*Qala Saida(7)*	*Gullan(8)*
Qmin/Qmax	0.51	0.09	0.32	0.29	0.3	0.14	0.22	0.31
$\mathbf{pH_{Qmin}/pH_{Qmax}}$	1.03	1.04	1.03	1.03	1	1	1.04	1.05
$\mathbf{ki_{pH}}$	0.53	0.09	0.33	0.30	0.3	0.14	0.23	0.33
$\mathbf{Eh_{Qmin}/Eh_{Qmax}}$	1.13	0.99	1.07	1.09	1.08	0.88	1.15	0.97
$\mathbf{ki_{EH}}$	0.58	0.09	0.34	0.32	0.33	0.13	0.25	0.3
$\mathbf{SpC_{Qmin}/SpC_{Qmax}}$	1.18	1.01	0.93	1.11	1.01	1	1.2	0.81
$\mathbf{ki_{SpC}}$	0.61	0.09	0.3	0.32	0.31	0.14	0.26	0.25
$\mathbf{\delta D_{Qmin}/\delta D_{Qmax}}$	1.02	0.99	1	0.99	1	1.01	1.07	0.99
$\mathbf{ki_{\delta D}}$	0.52	0.09	0.32	0.29	0.3	0.14	0.24	0.31
$\mathbf{HCO3_{Qmin}/HCO3_{Qmax}}$	1.08	0.85	0.99	0.99	0.98	1.01	1.18	1.05
$\mathbf{ki_{HCO3}}$	0.55	0.08	0.31	0.29	0.3	0.15	0.26	0.33
ΔMg	6.9	4.1	2.4	2.6	2	5.5	2.1	3
ΔSO_4	47.6	23	5.7	5.5	5.5	6.2	5.2	5.9
ΔSr	0.44	0.15	0.02	0.03	0.04	0.07	0.02	0.01
ΔDO	0.04	0.099	1.29	1.64	0.15	1.17	1.72	2.37
KI	***55.8***	***8.8***	***32***	***30.4***	***30.8***	***14***	***24.8***	***30.4***

Qmin/Qmax = ratio between minimum and maximum discharge of the spring; $\boldsymbol{i_{Qmin}}$ = Value of specific water parameter corresponding to the minimum discharge rate; $\boldsymbol{i_{Qmax}}$ = Value of specific water parameter corresponding to the maximum discharge rate; **ki** = Ratio of minimum to maximum flow multiplied by their corresponding values for a specific parameter (*i*); $\boldsymbol{\Delta}$ = maximum – minimum value of the parameter in mg/l; ***KI*** = Karst index (%)

The implementation of *KI* on the karst springs of the Makook system produced a range of values and thus different karst classes. The variation in *KI* from 8.8 to 55.8 can be assumed to represent an adequate range for a classification. Four classes were recognized, and the description of each class is summarized in Tab. 5.

Rocks of several springs have been exposed to different processes in addition to carbonate dissolution. For example, tectonics also play a role in the maturity of karstification in Sarwchawa spring (class-IV), thus these types of springs are more frequent in the plunges of highly-folded rocks. But the openings in Shkarta spring (class-1) are micro-fractures or fissures formed by tectonic stress.

Residence time and depth of the aquifers do alter as well as the hydrogeochemical composition. The microbial utilization of oxygen during longer flowpaths results in less dissolved oxygen and indicates a longer residence time and a deeper karst aquifer (Gordon 1998). On contrary, the degree of karstification is generally assumed to decrease with depth (Milanović 2004; Goldscheider and Drew 2007). However, this is not always the case in folded rocks (Goldscheider and Drew 2007) and never in geothermal karst (Goldscheider et al. 2010) and karst based on sulfuric acid (Hose 2013). But, the region of interest is a karst system based on biogenic CO_2 from the soil zone. The higher dissolved oxygen concentration (Tab. 1) and variation thereof observed in Gullan spring (lower *KI*, class-III) is referring to a shallow karst aquifer and short flow path (Fig. 4), while the lower concentration and variation in Sarwchawa water (higher *KI*, class-IV) refers to a deeper pathway (circulation) and a longer residence time. In karst aquifers magnesium is dissolved more slowly than calcium; the former can be used as a tracer for residence time (Batiot et al. 2003; Goldscheider and Drew 2007). In homogeneous aquifers (concerning lithology and structure), higher Mg^{2+} levels are indicators for a longer residence

time and more hydrogeochemical evolution (Moral et al. 2008). The highest change in Mg^{2+} concentration (ΔMg = 6.9 mg/l) was recorded at the Sarwchawa spring, indicating a longer residence time (long flowpath) here than elsewhere in the study area (Tab. 4 and Fig. 4).

Regarding the flow regime, the conduit flow is predominate in Sarwchawa spring (higher *KI* class), which characterized by the direct response of Q, SpC, T and pH to recharge, and it exhibits higher Ca and SO_4^{2-} content and variations. In contrast, diffuse flow predominates in lower magnitude *KI* classes (I, II and III), whose springs are characterized by a delayed response to recharge in terms of temperature and they exhibits lower Ca^{2+} and SO_4^{2-} concentrations (Fig. 4).

Karst systems can be recharged via concentrated or diffuse (dispersed) recharge (Gunn 1983; Smart and Hobbs 1986). These processes in turn may exhibit either recharge through outcropping karst or through non-karstified rocks (Field, 2002; Taylor and Green, 2008). The distinction between these types of recharge is important because their relative proportions significantly affect spring discharge and hydrochemistry (Ford and Williams, 2007). The type of recharge, groundwater flowpath, stratigraphic relationships and openings of each of the studied karst aquifers are illustrated in Fig. 4. In the case of the Shkarta spring (class-I), the source of water seems to be diffuse recharge from the marly limestone of the Shiranish aquitard (Fig. 4). This assumption is based on the spring's distinctive Q, temperature, Mg^{2+}, SO_4^{2-} and isotopic signatures compared with those of the other studied springs. The recharged water in class-III springs flows through well - connected bedding and fault fissures and moderately mature conduits. In case of Sarwchawa spring (class-IV), the recharged water takes a longer path compared to the other springs.

Tab. 5: Classification of Karst springs depending on *KI*

KI	***Class***	***Level of Karstification***	***Spring***	***[1]Hydrochemistry***	***[2]Flow Type***	***[3]Depth of Karst***	***[4]Maturity of karst***
≤10	I	Poorly karstified spring	Shkarta	Medium ΔMg, ***ΔSO$_4$*** and ***ΔSr***	Diffuse flow	Shallow	Non-karst
11-20	II	Slightly karstified spring	Bla	Low ***ΔMg***, ***ΔSO$_4$*** and ***ΔSr***	Diffuse flow	Moderate	Young karst
21-50	III	Moderately karstified spring	Betwata, Zewa, Chewa, Qala Saida & Gullan	Low ***ΔMg***, ***ΔSO$_4$*** and ***ΔSr***	Mixed diffuse and conduit flow	Moderate	Young to mature karst
51-70	IV	Well karstified spring	Sarwchawa	High ***ΔMg***, ***ΔSO$_4$*** and ***ΔSr***	Developed conduit flow	Deep karst	Mature karst

KI = karst index (%); Units of hydrochemical criteria are in mg/l; ***Δ*** = maximum-minimum value in mg/l; **1** = from the studied springs; **2**= from the interpretation of hydrochemical data of the studied springs; **3** = from dissolved oxygen concentration and variation (***ΔDO***); **4** = Modified from Klimchouk classification (2004) and field observations, geology and the interpretation of hydrochemical data of the studied springs

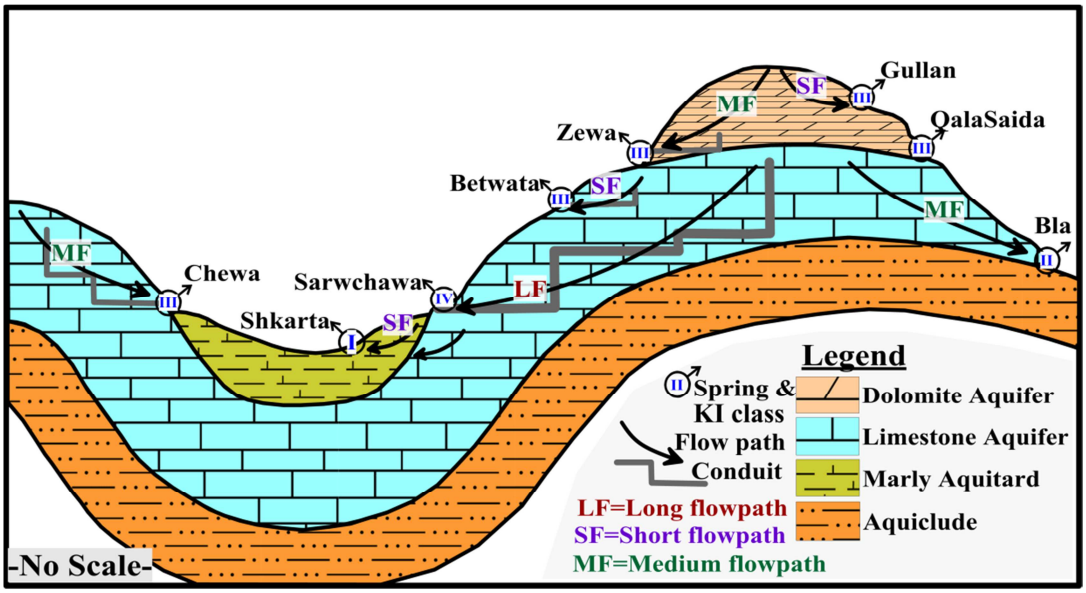

Fig. 4: Idealized conceptual karst model based on KI classification

3.3.1 Validation of *KI*

In order to validate the *KI* classification, well-known karst springs over the world were selected for the purpose of comparison with the present studied springs (

Tab. **6**). The springs are (from low to high degree of karstification) Marbella spring (Spain), Gallusquelle spring (Germany), Berghan spring (Iran), Beaver spring (USA) and Cheddar spring (England). The required values for *KI* validation cases were extracted from the corresponding values of Q_{max} and Q_{min} in hydro-chemographs of the springs. In addition to geographic distribution, different criteria were used for choosing the springs, like: karst morphology and geology, hydro-chemograph pattern and type of flow. The *KI* of Marbella spring (8.2) refers to a poorly karstified spring (class-I), which is consistence with the findings of López-Chicano et al. (2001) for the spring (low karstification degree). The karstification in Gallusquelle spring (Germany) and Berghan spring (Iran) is described as moderate by Heinz et al. (2009) and Raeisi and Karami (1997), respectively. The calculated *KI* for Gallusquelle and Berghan springs (28.3 and 32) refers to moderately karstified karst (class-III), which is in agreement with the conclusions of the previous authors based on different techniques. In case of Beaver (Vesper and White 2003) and Cheddar springs (Atkinson 1977), they assumed to be well karstified karst, which is more or less the same, as *KI* class-IV (well karstified). From the previous justification it can be concluded that the *KI* classification is valid for assessment of karstification. This classification was adapted for the studied springs and springs used for the validation, but it could be not valid for other springs. Because any classification has it is limitation and could not be generalized to include all springs and karst aquifers, especially when we deal with the case of karstification, which is sensitive and controlled by different factors.

4 Conclusions

The results of this study demonstrate that hydrogeochemical behavior of karst springs characterizes its karst system along with flow and hydrodynamic behavior. Brief conclusions on the most finding of the present work are as follow:

- A classification of karst springs can be performed by linking the hydrodynamic and hydrogeochemical data of springs.
- The ratio of minimum to maximum discharge of springs correlate with corresponding hydrogeochemical data and can be used to calculate a karst index (*KI*).

Tab. 6: Validation of *KI* using springs world-wide

Spring	*Location*	*Karst description*	*Parameters used for KI calculation*	*KI*	*KI class*
[1]Marbella	Spain	Low karstification, carbonate	Q_{max}= 230, Q_{min} = 15, SpC_{Qmax}= 550, SpC_{Qmin} = 700, $SO4_{Qmax}$= 61, $SO4_{Qmin}$ = 76	8.2	Poorly karstified
[2]Gallusquelle	Germany	Moderately karstification, carbonate	Q_{max} = 1150, Q_{min} = 250, SpC_{Qmax} = 515, SpC_{Qmin} = 550, Na_{Qmax}= 6.5, Na_{Qmin} = 10	28.3	Moderatly karstified
[3]Berghan	Iran	Moderately karstification, carbonate	Q_{max} = 1.4, Q_{min} = 0.4, SpC_{Qmax} = 250, SpC_{Qmin} = 255, $HCO3_{Qmax}$= 137, $HCO3_{Qmin}$ = 171	32	Moderatly karstified
[4]Beaver	USA	Flashy, karstified	$*Q_{max}$ = 120, $*Q_{min}$ = 43, SpC_{Qmax} = 340, SpC_{Qmin} = 460,Ca_{Qmax} = 47, Ca_{Qmin} = 72	51.7	well karstified
[5]Cheddar	England	Flashy, karstified	Q_{max} = 4100, Q_{min} = 1900, $**H_{Qmax}$= 223, $** H_{Qmin}$ = 247	51.3	well karstified

1= López-Chicano et al. (2001); **2**= Heinz et al. 2009; **3**= Raeisi and Karami (1997); **4**= Vesper and White (2003); **5**= Atkinson (1977); Q_{max} = maximum discharge in l/s; Q_{min} = minimum discharge in l/s; SpC_{Qmax} = specific conductance at maximum discharge in µS/cm; SpC_{Qmin} = specific conductance at minimum discharge in µS/cm; $SO4_{Qmax}$ = sulfate at maximum discharge; $SO4_{Qmin}$ = sulfate at minimum discharge; Na_{Qmax}= sodium at maximum discharge; Na_{Qmin} = sodium at minimum discharge; $HCO3_{Qmax}$ = hydrogen carbonate at maximum discharge; $HCO3_{Qmin}$ = hydrogen carbonate at minimum discharge; Ca_{Qmax} = calcium at maximum discharge; Ca_{Qmin} calcium at maximum discharge; $*Q_{max}$ and $*Q_{min}$ = are represented by stage elevation in meter in Beaver spring; $**H$= Hardness; H_{Qmax}= Hardness at maximum discharge; H_{Qmin} = Hardness at minimum discharge; concentrations are in mg/l

- For some springs, however, hydrogeochemical characteristics have a greater influence on the *KI* values than their discharge.
- In case of application of *KI* classification for other springs, it is not necessary to use the same hydrogeochemical parameters used in this study. According to our tests the *KI* can be calculated from two or three of the available hydrogeochemical parameters.
- The chemograph patterns of the springs represent a descriptive tool for *KI* classification.
- Classification of karst springs with *KI* facilitates the characterization of aquifers with respect to residence times, aquifer depths, flow regimes and recharge.

5 Acknowledgements

The present study was carried out as a part of a HCDP scholarship offered by Ministry of Higher Education and Scientific Research / Kurdistan Regional Government / Iraq. The first author is grateful to Nokhsha Aziz for her great support during the entire study. He thanks Sanger Ahmed for his continuous support during the work. He is grateful to staff of the water-chemistry laboratory at the Hydrogeology Department, TU Bergakademie Freiberg for their support.

6 List of references

Al Manmi DA (2002) Chemical and Environmental Study of Groundwater in Sulaimaniyah city and its Outskirts. Unpublished M.Sc. Thesis, University of Baghdad

Al Manmi DA (2008) Water resources management in Rania area, Sulaimaniyah NE-Iraq. Unpublished PhD Dissertation, University of Baghdad, Iraq

APHA (1998) Standard methods for the examination of water and wastewater, 20th ed. American Public Health Association, Washington

Aquilina L, Ladouche B, Dörfliger N (2005) Recharge processes in karstic systems investigated through the correlation of chemical and isotopic composition of rain and spring-waters. Applied Geochemistry 20: 2189 – 2206

Atkinson TC (1977) Diffuse flow and conduit flow in limestone terrain in the Mendip Hills, Somerset (Great Britain). Journal of Hydrology 35(1-2): 93–110

Batiot C, Emblanch C, Blavoux B (2003) Carbone organique total (COT) et magnésium (Mg^{2+}). Deux traceurs complémentaires du temps de séjour dans l'aquifère karstique. Comptes Rendus Geoscience 335(2): 205–214

Bellen RC, Dunnington HV, Wetzel R, Morton DM, Dubertret L (2005) Stratigraphic lexicon of Iraq. Gulf PetroLink, Manama, Bahrain

Birk S, Liedl R, Sauter M (2004) Identification of localised recharge and conduit flow by combined analysis of hydraulic and physico-chemical spring responses (Urenbrunnen, SW-Germany). Journal of Hydrology 286: 179–193

Bundschuh J (1993) Modeling annual variations of spring and groundwater temperatures associated with shallow aquifer systems. Journal of Hydrology 142(1-4): 427–444

Chiarenzelli J, Shrady C, Cady C, General K, Snyder J, Benedict-Debo A, David T (2007) Multi-Element analyses of private wells on the St. Regis Mohawk Nation (Akwesasne). Northeastern Geology and Environmental Sciences 29: 167-175

Delbart C, Barbecot F, Valdes D, Tognelli A, Fourre E, Purtschert R, Couchoux L, Jean-Baptiste P (2014) Investigation of young water inflow in karst aquifers using SF_6–CFC–^{3}H/He–^{85}Kr–^{39}Ar and stable isotope components. Applied Geochemistry 50: 164–176

Field MS (2002) A lexicon of cave and karst terminology with special reference to environmental karst hydrology. National Center for Environmental Assessment, Washington Office, Office of Research and Development, U.S. Environmental Protection Agency, Washington

Ford, D, Williams PD (2007) Karst hydrogeology and geomorphology. Revised ed. John Wiley & Sons, Chichester, England

Gillon M, Barbecot F, Gibert E, Corcho Alvarado J, Marlin C, Massault M (2009) Open to closed system transition traced through the TDIC isotopic signature at the aquifer recharge stage, implications for groundwater ^{14}C dating. Geochimica et Cosmochimica Acta 73: 6488–6501

Glynn PD, Plummer LN (2005) Geochemistry and the understanding of ground - water systems. Hydrogeology Journal 13(1): 263–287

Goldscheider N, Drew D (2007) Methods in karst hydrogeology. 1. ed. Taylor & Francis, Leiden

Goldscheider N, Mádl-Szőnyi J, Erőss A, Schill E (2010) Thermal water resources in carbonate rock aquifers. Hydrogeology Journal 18(6):1303–1318

Gordon SL (1998) Surface and Ground Water Mixing in an Unconfined Karst Aquifer, Ichetucknee River Ground Water Basin, FL. University of Florida, Gainesville

Grasso DA, Jeannin, P.–Y (2002) A Global Experimental System Approach of Karst Springs1 Hydrographs and Chemographs. Ground Water 40(6): 608–618

Gunn J (1983) Point-recharge of limestone aquifers — A model from New Zealand karst. Journal of Hydrology 61(1-3): 19–29

Heinz B, Birk S, Liedl R, Geyer T, Straub, KL, Andresen J, Bester K, Kappler A (2009) Water quality deterioration at a karst spring (Gallusquelle, Germany) due to combined sewer overflow: evidence of bacterial and micro-pollutant contamination. Environmental Geology (4): 797–808

Hose LD (2013) Karst geomorphology: sulfur karst processes. In: Treatise on Geomorphology, Shroder JF, Frumkin A eds. Academic Press, San Diego. Volume 6, Karst Geomorphology, pp. 29–37

Jakucs L (1959) Neue Methoden der Hohlenforschung in Ungarn und ihre Ergebnisse. Hohle 10(4): 88–98

Jassim SZ, Goff JC (2006) Geology of Iraq. 1. ed. Dolin, Prague and Moravian Museum, Czech Republic

Karim KH, Al Hamadani RK, Ahmad SH (2012) Relations between Deep and Shallow Stratigraphic Units of Northern Iraq during Cretaceous. Iranian Journal of Earth Sciences 4(2): 495–103

Karimi H, Raeisi E, Bakalowicz M (2005) Characterising the main karst aquifers of the Alvand basin, northwest of Zagros, Iran, by a hydrogeochemical approach. Hydrogeology Journal 13(5–6): 787–799

Klimchouk A. (2004) Towards defining, delimiting and classifying epikarst: its origin, processes and variants of geomorphic evolution. Speleogenesis and evolution of karst aquifers. Virtual Science Journal (2): 1–13

Landau S, Everitt B (2004) A handbook of statistical analyses using SPSS. Chapman & Hall/CRC, Boca Raton.

Lee ES, Krothe NC (2003) Delineating the karst flow system in the upper Lost River drainage basin, south central Indiana: using sulphate and $\delta^{34}SSO_4$ as tracers. Applied Geochemistry 18(1): 145–153

Liñán Baena C, Andreo B, Mudry J, Carrasco CF (2009) Groundwater temperature and electrical conductivity as tools to characterize flow patterns in carbonate aquifers: The Sierra de las Nieves karst aquifer, southern Spain. Hydrogeology Journal 17(4): 843–853

López-Chicano M, Bouamama M, Vallejos A, Pulido-Bosch A (2001) Factors which determine the hydrogeochemical behaviour of karstic springs. A case study from the Betic Cordilleras, Spain. Applied Geochemistry 16(9-10): 1179–1192

Martin JB, Gordon S (2000) Surface and ground water mixing, flow paths and temporal variations in chemical compositions of karst springs, In: Groundwater Flow and Contaminant Transport in Carbonate Aquifers, Sasowsky ID, Wicks CM eds. Balkema, Rotterdam, pp. 65–92

Martin JB, Dean RW (2001) Exchange of water between conduits and matrix in the Floridan aquifer. Chemical Geology 179(1-4): 145–165

Milanović P (1981) Karst Hydrogeology. 1. ed. Water Resources Publication, Colorado

Milanović P (2004) Water resources engineering in Karst. 1. ed. CRC Press, Boca Raton

Moral F., Cruz-Sanjulián JJ, Olías M (2008) Geochemical evolution of groundwater in the carbonate aquifers of Sierra de Segura (Betic Cordillera, southern Spain). Journal of Hydrology 360: 281–296

Mustafa OM (2007) Impact of Sewage Wastewater on the Environment of Tanjero River and its Basin within Sulaimaniyah city, NE Iraq. Unpublished M.Sc. Thesis, University of Baghdad

Mustafa O, Merkel B, Weise SM (2015) Assessment of Hydrogeochemistry and Environmental Isotopes in Karst Springs of Makook Anticline, Kurdistan Region, Iraq. Hydrology 2: 48–68

O'Connor M, Zabik M, Cady C, Cousens B, Chiarenzelli J (2010) Multi-Element Analysis and Geochemical Spatial Trends of Groundwater in Rural Northern New York. Water 2(2), 217–238

Parkhurst DL, Appelo CA (2013) Description of Input and Examples for PHREEQC (Version 3)-A Computer Program for Speciation, Batch-Reaction, One-Dimensional Transport, and Inverse Geochemical Calculations. Chapter 43 of section A, Groundwater Books, Modeling Techniques. http://pubs.usgs.gov/tm/06/a43. Accessed: 09 March 2015

Pavlovskiy I, Selle B (2014) Integrating hydrogeochemical, hydrogeological, and environmental tracer data to understand groundwater flow for a karstified aquifer system. Groundwater. DOI: 10.1111/gwat.12262

Pearson F, Scholtis A (1995) Controls on the Chemistry of Pore Water in a Marl of Very Low Permeability. In: Water-rock interaction, Kharaka YK, Chudaev OV eds. Proceedings of the 8th International Symposium on Water-Rock Interaction, WRI-8, Vladivostok, Russia. Rotterdam, Netherlands, Brookfield, Balkemapp. 35-38.

Perrin J, Jeannin P.-Y, Zwahlen F (2003) Epikarst storage in a karst aquifer: a conceptual model based on isotopic data, Milandre test site, Switzerland. Journal of Hydrology 279: 106–124

Raeisi E, Karami G (1997) Hydrochemographs of Berghan karst spring as indicators of aquifer characteristics. Journal of Cave and Karst Studies 59(3): 112–118

Rashed KA (2012) Assessing degree of karstification: A new method of classifying karst aquifers. Sixteenth International Water Technology Conference, IWTC, Istanbul, Turkey. http://iwtc.info/wp-content/uploads/2012/06/G87-WT39-GS05.pdf. Accessed: 09 March 2015

Rovey CW (1994) Assessing flow systems in carbonate aquifers using scale effects in hydraulic conductivity. Environmental Geology 24(4): 244–253

Scanlon BR, Thrailkill J (1987) Chemical similarities among physically distinct spring types in a karst terrain. Journal of Hydrology 89(3-4): 259–279

Shuster ET, White WB (1971) Seasonal fluctuations in the chemistry of limestone springs: A possible means for characterizing carbonate aquifers. Journal of Hydrology 14(2): 93-128

Sisakian V (1998) The Geology of Erbil and Mahabad Quadrangle Sheet NJ-38-14 and NJ-38-15, Scale 1:250 000. Iraq Geological Survey, Baghdad, Iraq

Smart PL, Hobbs SL (1986) Characterization of carbonate aquifers: a conceptual base. In: Environmental problems in karst terranes and their solutions conference, 1. ed. Bowling Green, Kentucky. National Water Well Association, Dublin, Ohio, pp. 1–14

Stevanovic Z, Iurkiewicz A, Maran A (2009) New insights into karst and caves of Northwestern Zagros (Northern Iraq). Acta Carsologica 38: 83–96

Stevanovic Z, Marcovic M (2004) Hydrogeology of Northern Iraq. General Hydrogeology and Aquifer System, vol 2, 1. ed. FAO, Rome, Italy

Taylor CJ, Green EA (2008) Hydrogeologic Characterization and Methods Used in the Investigation of Karst Hydrology". In: Field Techniques for Estimating Water fluxes Between Surface Water and Ground Water. Rosenberry DO, LaBaugh JW eds. pp. 75-111

Ternan JL (1972) Comments on the use of a calcium hardness variability index in the study of carbonate aquifers: With reference to the central pennines, England. Journal of Hydrology 16(4): 317–321

Vesper DJ, White WB (2003) Metal transport to karst springs during storm flow: an example from Fort Campbell, Kentucky/Tennessee, USA. Journal of Hydrology 276: 20–36.

Vesper DJ, White WB (2004) Storm pulse chemographs of saturation index and carbon dioxide pressure: implications for shifting recharge sources during storm events in the karst aquifer at Fort Campbell, Kentucky/Tennessee, USA. Hydrogeology Journal 12(2): 135- 143

White WB (1969) Conceptual Models for Carbonate Aquifers. Groundwater 7(3): 15–21.

White WB (2006) Groundwater flow in karstic aquifers. In: The Handbook of Groundwater Engineering, 2. ed. Delleur JW ed. Boca Raton, FL, CRC Press, pp. 21-1–21-47

Appendix 1: The physio-chemical, flow and isotopic characteristics of the karst springs

Springs & Code	*Date*	*pH*	*Eh (mV)*	*SpC (µS/cm)*	*DO (mg/l)*	*Water T (°C)*	*Air T (°C)*	*Flow (l/s)*	*δD (‰)*
Sarwchawa (1)	15.09.2011	7.3	434.4	570	6.49	18.7	30.5	2370	-39.91
	06.12.2011	7.6	414.4	516	NA	16	10	2990	-40.02
	26.04.2012	7.1	384.1	482	6.45	12	14	4630	-39.18
	04.06.2012	7.4	372.3	506	NA	17	28	3100	-39.2
	05.09.2012	7.3	381.8	568	6.49	16	23	2910	-39.81
	11.11.2012	7.3	342.6	664	NA	11	11	3400	-43.39
Shkarta (2)	15.09.2011	7.4	430.6	406	7.36	23.4	32.5	0.2	-32.33
	06.12.2011	7.8	396.3	411	NA	19	21	0.75	-32.35
	26.04.2012	7.1	378	443	6.37	16	16	1.1	-32.7
	04.06.2012	7.3	384.1	432	NA	20	29	0.5	-31.9
	05.09.2012	7.4	375.3	448	7.36	20	26	0.1	-32.43
	11.11.2012	7.3	335	583	NA	6	18	0.17	-35.57
Betwata (3)	15.09.2011	7.7	432.6	391	8.46	16.4	32	18.8	-40.95
	06.12.2011	7.8	383.8	380	NA	11	17	28.9	-40.42
	26.04.2012	7.2	378.5	391	7.17	10	19	25.3	-40.39
	04.06.2012	7.5	403.8	420	NA	15	31	59.3	-40.92
	05.09.2012	7.9	359.7	407	8.46	19	28	20.4	-40.56
	11.11.2012	7.3	336.9	831	NA	9	14	28.5	-43.87
Zewa (4)	15.09.2011	8.4	415.5	316	8.34	15.2	20	61.4	-43.57
	06.12.2011	8.1	388.1	306	NA	12	11	112.8	-42.79
	26.04.2012	7.3	375.8	296	6.7	8	16	142.1	-43.14
	04.06.2012	7.6	334.2	310	NA	14.5	31	165.8	-44.03
	05.09.2012	7.8	365.8	344	8.34	12	22	48	-43.59
	11.11.2012	7.3	323.8	350	NA	8	13	124	-45.93
Chewa (5)	15.09.2011	7.28	442	535	5.9	19	32	101	-40.26
	06.12.2011	7.8	378	444	NA	12	22	125	-39.57
	26.04.2012	7.2	384.7	522	6.05	8	27	149.9	-41.84
	04.06.2012	7.3	408.1	530	NA	16	35	332.5	-40.38
	05.09.2012	7.3	379.4	467	5.9	19	26	112	-40.7
	11.11.2012	7.3	358.4	1117	NA	11	19	141	-43.75
Bla (6)	15.09.2011	7.4	478.4	510	7.64	15.5	28	393.3	-41.57
	06.12.2011	7.8	368	396	NA	13	10	336.2	-41.42
	26.04.2012	7.2	388.9	438	6.47	8	18	638	-40.2
	04.06.2012	7.4	424.6	495	NA	14	25	875	-41.79
	05.09.2012	7.4	373.5	495	7.64	10	27	126	-42.08
	11.11.2012	7.2	350.6	599	NA	8	12	331.8	-44.71
Qala Saida (7)	15.09.2011	7.6	445.7	458	8.15	16	34	1.5	-40.64
	06.12.2011	7.8	359.9	422	NA	14	5	3.6	-39.55
	26.04.2012	7.3	386.8	383	6.43	9	19	6.8	-37.9
	04.06.2012	7.6	357.1	518	NA	16	31	1.6	-39.28
	05.09.2012	7.6	374.9	430	8.15	17	27	1.8	-38.95
	11.11.2012	7.3	360.8	722	NA	13	13	2.7	-41.62
Gullan (8)	15.09.2011	8.2	432.4	299	8.5	14.1	26	45	-42.64
	06.12.2011	8	359.9	291	NA	9	3.5	27.4	-41.32
	26.04.2012	7.3	384.6	265	6.13	8	12	63.5	-41.1
	04.06.2012	7.6	371	360	NA	8	17	87.6	-41.79
	05.09.2012	7.8	365	320	8.5	10	21	39	-41.81
	11.11.2012	7.3	323.2	328	NA	8	11	41	-45.02

Eh = oxidation reduction potential; ***SpC*** = Electrical conductivity; ***T*** = temperature; ***DO*** = dissolved oxygen; ***Flow*** = discharge of the springs; NA = not available; The ***DO*** is measured only 3 times; The field parameters were measured onsite and isotopes in Lab by means of LGR liquid–water isotope analyzer; Spring codes can be used to trace the locations of the springs in ***Fig.1***

Appendix 2: The hydrogeochemical characteristics of the karst springs

Springs & Code	*Date*	Na^+	K^+	Ca^{2+}	Mg^{2+}	Cl^-	SO_4^{2-}	HCO_3^-	F^-	*Si*	*Sr*	*P*	*Li*	*E%*
		Concentrations in mg/L												
Sarwchawa(1)	**15.09.2011**	2.39	0.85	87.5	23.9	3.5	81.8	286.2	0.17	4.9	0.85	0.015	0.0025	-1
	06.12.2011	2.39	0.80	78.0	22	2.4	73.2	275	0.07	4.7	0.88	0.017	0.0030	1
	26.04.2012	2.32	0.71	77.3	17	3.4	39	265.7	0.13	4.9	0.44	0.019	0.0028	0
	04.06.2012	2.51	0.78	72.2	20.9	2.1	59.7	270	0.09	4.6	0.67	0.008	0.0034	0
	05.09.2012	2.32	0.70	91.7	21.8	2.4	86.6	298.9	0.19	4.3	0.82	0.010	0.0033	-1
	11.11.2012	2.53	0.78	49.9	23.4	2	82.2	280	0.11	4.5	0.85	0.007	0.0036	-1
Shkarta(2)	**15.09.2011**	3.59	1.75	65.8	10.3	4.8	21.9	213.7	0.10	9.4	0.34	0.032	0.0009	-1
	06.12.2011	4.57	1.84	64.8	10.4	9.2	21	230	0.06	8.9	0.31	0.014	0.0013	0
	26.04.2012	4.24	2.27	73.8	10.3	8.7	21.8	253.9	0.14	9.1	0.30	0.040	0.0013	-4
	04.06.2012	3.96	1.82	48.2	9.8	4.9	17.4	240	0.07	8.5	0.29	0.011	0.0012	-1
	05.09.2012	3.92	1.48	71.1	9.6	6.6	21.8	216.6	0.10	8.5	0.30	0.030	0.0012	0
	11.11.2012	5.89	1.88	75.3	13.7	15.5	40.4	235	0.08	8.8	0.44	0.013	0.0017	0
Betwata(3)	**15.09.2011**	1.23	0.47	53.9	20.4	2.6	16.7	235.1	0.04	4.3	0.14	0.010	0.0007	1
	06.12.2011	1.29	0.50	52.7	18.5	1.4	11.2	242	0.06	3.9	0.12	0.006	0.0010	0
	26.04.2012	1.26	0.45	55.4	18.6	2	12.7	248	0.06	4.3	0.13	0.012	0.0010	-1
	04.06.2012	1.30	0.38	37.2	18.6	1.3	11.4	237	0.05	4.0	0.12	0.005	0.0010	-1
	05.09.2012	1.30	0.43	54.7	18.0	2	11	241	0.06	3.9	0.12	0.009	0.0009	-1
	11.11.2012	1.30	0.39	45.1	18.4	1.3	11.3	260	0.07	3.9	0.12	0.005	0.0009	0
Zewa(4)	**15.09.2011**	0.93	0.47	42.9	15.5	2.1	13.9	187.6	0.04	2.9	0.13	0.007	0.0005	0
	06.12.2011	0.84	0.58	48.8	14.1	1.1	9	180	0.04	2.7	0.10	0.003	0.0007	1
	26.04.2012	0.79	0.45	45.6	12.9	1.5	10.2	189	0.04	3	0.10	0.015	0.0006	0
	04.06.2012	0.89	0.47	56.6	14.7	0.9	8.4	185	0.06	3.2	0.11	0.013	0.0007	1
	05.09.2012	0.94	0.94	47.3	13.6	1.6	9.3	183	0.05	2.8	0.11	0.010	0.0007	3
	11.11.2012	0.87	0.41	41.4	14.5	0.9	9.1	192	0.07	2.9	0.10	0.005	0.0007	-1
Chewa(5)	**15.09.2011**	1.77	0.57	84.4	20.5	3	14.7	332.3	0.07	6	0.21	0.017	0.0013	1
	06.12.2011	1.92	0.55	43.3	18.8	1.8	9.7	341	0.06	5.4	0.17	0.008	0.0017	0
	26.04.2012	1.88	0.46	88.1	18.8	2.8	11.2	348.4	0.08	6	0.18	0.015	0.0017	0
	04.06.2012	2.03	0.66	46.9	19.5	1.9	9.7	338	0.06	5.7	0.18	0.008	0.0018	0
	05.09.2012	1.92	0.48	85.5	18.5	2.8	9.2	332.5	0.08	5.3	0.18	0.009	0.0017	1
	11.11.2012	1.94	0.52	43.7	19	1.8	9.8	350	0.11	5.5	0.17	0.008	0.0018	1
Bla(6)	**15.09.2011**	1.53	0.74	74.6	22.6	3	16.9	318.5	0.05	4.3	0.18	0.016	0.0009	0
	06.12.2011	1.56	0.81	43.8	21.6	1.7	10.7	302	0.05	3.6	0.13	0.006	0.0011	0
	26.04.2012	1.37	0.52	69.5	17.1	2.3	13.5	289.3	0.05	3.5	0.11	0.014	0.0008	0
	04.06.2012	1.55	0.59	49.2	21.3	1.6	11.4	310	0.04	3.7	0.13	0.006	0.0011	1
	05.09.2012	1.51	0.56	75.1	21.8	2.1	10.7	314.2	0.06	3.7	0.15	0.012	0.0011	1
	11.11.2012	1.62	0.70	41.4	21.8	1.7	11.0	298	0.11	3.7	0.13	0.007	0.0011	0
Qala Saida(7)	**15.09.2011**	1.33	0.43	66	22.2	2.8	15.9	286.2	0.04	3.5	0.09	0.007	0.0005	0
	06.12.2011	1.27	0.48	48.4	21.9	1.5	10.7	264	0.03	3.3	0.07	0.004	0.0008	-1
	26.04.2012	1.24	0.39	54.5	20.4	2.3	12.8	242.1	0.05	3.5	0.08	0.016	0.0009	-2
	04.06.2012	1.31	0.43	77.3	22.5	1.5	10.9	270	0.06	3.4	0.08	0.015	0.0010	-1
	05.09.2012	1.29	0.42	63	20.9	2.0	11.3	274.5	0.05	3.0	0.07	0.005	0.0009	0
	11.11.2012	1.47	0.35	47.2	21.6	1.6	11.0	269	0.08	3.2	0.07	0.006	0.0009	1
Gullan(8)	**15.09.2011**	2.09	0.39	42.3	14.4	2.8	14.8	185.1	0.03	2.4	0.07	0.013	0.0004	-1
	06.12.2011	0.78	0.35	45.5	13.4	1	8.9	173	0.04	2.3	0.06	0.005	0.0006	-1
	26.04.2012	0.78	0.27	38.5	11.4	1.5	10.8	159.4	0.04	2.2	0.06	0.012	0.0006	0
	04.06.2012	0.72	0.27	43.9	12.4	0.9	9.2	165	0.02	2.1	0.06	0.003	0.0005	-1
	05.09.2012	0.88	0.27	41.4	12.5	1.4	8.9	170.8	0.05	2.1	0.06	0.012	0.0007	1
	11.11.2012	0.87	0.33	44.9	12.9	1	9.8	180	0.05	2.2	0.06	0.006	0.0006	-1

E% = Anion cation balance calculated by PHREEQC; Na^+, K^+, Ca^{2+}, Mg^{2+}, F^-, Cl^- and SO_4^{2-} were measured by Ion Chromatography (IC); HCO_3^- measured by Titration; ***Si, P, Li*** and ***Sr*** measured by Inductively Coupled plasma – Mass Spectrophotometer (ICP-MS) ; Spring codes can be used to trace the locations of the springs in ***Fig.1***

Appendix 3: Saturation indices of selected mineral in the karst springs

Springs & Code	*Date*	P_{CO2}	$SI_{Calcite}$	$SI_{Dolomite}$	SI_{Gypsum}	$SI_{Fluorite}$	SI_{Halite}
Sarwchawa(1)	**15.09.2011**	1.26	0.11	-0.09	-1.63	-2.42	-9.65
	06.12.2011	0.59	0.31	0.29	-1.70	-3.18	-9.80
	26.04.2012	1.70	-0.25	-1	-1.94	-2.56	-9.65
	04.06.2012	0.93	0.09	-0.12	-1.81	-3	-9.84
	05.09.2012	1.26	0.10	-0.19	-1.58	-2.26	-9.82
	11.11.2012	1.12	-0.24	-0.68	-1.80	-2.90	-9.84
Shkarta(2)	**15.09.2011**	0.81	0.08	-0.32	-2.24	-2.99	-9.33
	06.12.2011	0.32	0.43	0.34	-2.26	-3.38	-8.93
	26.04.2012	1.70	-0.23	-1.10	-2.19	-2.54	-8.98
	04.06.2012	1.10	-0.15	-0.70	-2.44	-3.37	-9.26
	05.09.2012	0.78	0.06	-0.46	-2.21	-2.91	-9.15
	11.11.2012	0.89	-0.20	-1.11	-1.90	-2.89	-8.57
Betwata(3)	**15.09.2011**	0.41	0.23	0.26	-2.43	-3.79	-10.04
	06.12.2011	0.31	0.25	0.19	-2.59	-3.36	-10.27
	26.04.2012	1.26	-0.33	-1.01	-2.52	-3.32	-10.14
	04.06.2012	0.65	-0.13	-0.36	-2.72	-3.71	-10.30
	05.09.2012	0.27	0.48	0.75	-2.61	-3.46	-10.14
	11.11.2012	1.05	-0.31	-0.90	-2.64	-3.25	-10.30
Zewa(4)	**15.09.2011**	0.06	0.71	1.19	-2.57	-3.85	-10.24
	06.12.2011	0.12	0.42	0.46	-2.69	-3.73	-10.56
	26.04.2012	0.76	-0.44	-1.35	-2.65	-3.69	-10.46
	04.06.2012	0.39	0.03	-0.32	-2.68	-3.36	-10.63
	05.09.2012	0.24	0.12	-0.15	-2.69	-3.55	-10.34
	11.11.2012	0.76	-0.47	-1.32	-2.74	-3.25	-10.62
Chewa(5)	**15.09.2011**	1.55	0.16	-0.01	-2.36	-3.18	-9.84
	06.12.2011	0.44	0.32	0.44	-2.75	-3.47	-10.00
	26.04.2012	1.78	0.04	-0.42	-2.44	-2.95	-9.83
	04.06.2012	1.45	-0.08	-0.32	-2.73	-3.49	-9.96
	05.09.2012	1.48	0.19	-0.01	-2.55	-3.05	-9.84
	11.11.2012	1.41	-0.17	-0.57	-2.73	-2.92	-9.99
Bla(6)	**15.09.2011**	1.07	0.17	0.03	-2.33	-3.47	-9.90
	06.12.2011	0.40	0.29	0.45	-2.70	-3.64	-10.11
	26.04.2012	1.41	-0.21	-0.94	-2.41	-3.36	-10.03
	04.06.2012	1.05	-0.03	-0.23	-2.64	-3.80	-10.15
	05.09.2012	1.00	0.08	-0.25	-2.50	-3.22	-10.03
	11.11.2012	1.48	-0.41	-1.01	-2.69	-2.89	-10.09
Qala Saida(7)	**15.09.2011**	0.62	0.28	0.31	-2.40	-3.71	-9.99
	06.12.2011	0.35	0.29	0.44	-2.66	-4.05	-10.26
	26.04.2012	0.95	-0.26	-0.85	-2.52	-3.47	-10.08
	04.06.2012	0.58	0.32	0.33	-2.50	-3.30	-10.25
	05.09.2012	0.59	0.26	0.29	-2.56	-3.55	-10.13
	11.11.2012	1.12	-0.22	-0.60	-2.66	-3.19	-10.17
Gullan(8)	**15.09.2011**	0.10	0.49	0.72	-2.54	-4.08	-9.77
	06.12.2011	0.14	0.23	0.04	-2.71	-3.71	-10.61
	26.04.2012	0.63	-0.58	-1.60	-2.67	-3.75	-10.44
	04.06.2012	0.33	-0.21	-0.89	-2.70	-4.30	-10.70
	05.09.2012	0.22	0.01	-0.38	-2.74	-3.66	-10.42
	11.11.2012	0.72	-0.47	-1.39	-2.67	-3.50	-10.57

P_{CO2} = Partial pressure of CO_2 (Vol%); ***SI*** = Saturation index of minerals; The data was calculated with PHREEQC; Spring codes can be used to trace the locations of the springs in ***Fig.1***

Appendix 4: Extra parameters used for the karst springs classification

Spring &Code	*Sarwchawa(1)*	*Shkarta(2)*	*Betwata(3)*	*Zewa(4)*	*Chewa(5)*	*Bla(6)*	*Qala Saida(7)*	*Gullan(8)*
Qmin/Qmax	0.51	0.09	0.32	0.29	0.3	0.14	0.22	0.31
Na_{Qmin}/Na_{Qmax}	1.03	0.92	0.95	1.06	0.87	0.97	1.07	1.09
ki_{Na}	0.53	0.08	0.3	0.31	0.27	0.14	0.24	0.34
Ca_{Qmin}/Ca_{Qmax}	1.13	0.96	1.45	0.84	1.8	1.53	1.21	1.04
ki_{Ca}	0.58	0.09	0.46	0.24	0.55	0.22	0.27	0.32
Mg_{Qmin}/Mg_{Qmax}	1.41	0.93	1.1	0.93	1.05	1.02	1.09	1.08
ki_{Mg}	0.72	0.08	0.35	0.27	0.32	0.15	0.24	0.34
$SO4_{Qmin}/SO4_{Qmax}$	2.1	1	1.46	1.1	1.51	0.94	1.24	0.97
ki_{SO4}	1.07	0.09	0.46	0.32	0.46	0.13	0.27	0.3
Si_{Qmin}/Si_{Qmax}	1	0.94	1.06	0.89	1.05	0.99	0.99	1.07
ki_{SI}	0.51	0.09	0.34	0.26	0.32	0.14	0.22	0.33
Sr_{Qmin}/Sr_{Qmax}	1.93	1	1.2	1.02	1.16	1.12	1.13	1.1
ki_{Sr}	0.99	0.09	0.38	0.29	0.35	0.16	0.25	0.34
Li_{Qmin}/Li_{Qmax}	0.89	0.92	0.71	0.96	0.71	0.95	0.56	1.26
ki_{Li}	0.46	0.08	0.22	0.28	0.22	0.14	0.12	0.39
$PCO2_{Qmin}/PCO2_{Qmax}$	1.08	1.19	1.09	1.09	0.99	1.01	1.1	1.15
$ki_{logPCO2}$	0.55	0.11	0.35	0.32	0.3	0.15	0.24	0.36
$SIgyp._{Qmin}/SIgyp._{Qmax}$	0.84	1.01	0.89	1	0.86	0.95	0.95	1
$ki_{SIgyp.}$	0.43	0.09	0.28	0.29	0.26	0.14	0.21	0.31
$SIfluo._{Qmin}/SIfluo._{Qmax}$	0.94	1.15	1.02	1.06	0.91	0.85	1.07	0.86
$ki_{SIfluo.}$	0.48	0.1	0.32	0.31	0.28	0.12	0.24	0.27
$SIhal._{Qmin}/SIhal._{Qmax}$	1	1.02	0.97	0.97	0.99	0.99	0.99	0.99
$ki_{SIhal.}$	0.51	0.09	0.31	0.28	0.3	0.14	0.22	0.31
KI	***62***	***9***	***34.3***	***28.8***	***33***	***14.8***	***23***	***32.8***

Qmin/Qmax = ratio between minimum and maximum discharge of the spring; i_{Qmin} = Value of specific water parameter corresponding to the minimum discharge rate; i_{Qmax} = Value of specific water parameter corresponding to the maximum discharge rate; **ki** = Ratio of minimum to maximum flow multiplied by their corresponding values for a specific parameter (*i*); P_{CO2} = Partial pressure of CO_2; ***SI*** = Saturation index of minerals; ***KI*** = Karst index (%); Spring codes can be used to trace the locations of the springs in ***Fig.1***

Enhancing SRTM digital elevation data using ANUDEM algorithm for delineation of drainage pattern in flat terrain: case study Al Qweek River, Aleppo, Syria

Abo, Rudy — Institute of Geology, Technische Universität Bergakademie Freiberg, Gustav-Zeuner Str.12, 09599 Freiberg, Germany. Email: rudy.abo@hotmail.de

Merkel, Broder — Institute of Geology, Technische Universität Bergakademie Freiberg, Gustav-Zeuner Str.12, 09599 Freiberg, Germany. Email: merkel@geo.tu-freiberg.de

Abstract: The objective of this study is to enhance the quality of the 3 arc-second SRTM v2 elevation model by integrating Ground Control Points (GCPs), Lidar data of the Geoscience Laser Altimeter System (GLAS), and regional spatial information using the drainage enforcement algorithm (ANUDEM). The algorithm is also used to promote the tracing efficiency of hydrological drainage network in Al Qweek valley. Despite the effect of vegetation and urbanization, Digital Elevation Models (DEMs) render detailed three-dimensional replication of the earth surface derived by topographic survey or satellite observations. These models are being used in many applications of geology, geomorphological sciences, hydrogeology, hydrology and natural water resource management in the last decades. Nowadays and after the accelerating technological revolution, ground elevation data at different resolutions are provided for free or by paying Government institutions, research centers, and enterprises. Delineation of hydrological drainage pattern is one of DEMs applications, and it is the key challenge facing researchers in the field of the geographic information system (GIS) and hydrology, particularly in flat terrains. Therefore, high resolution DEMs are usually required to indicate small changes on the terrain surface. Therefore, DEM enhancement is carried out in the study region in the southern part of Aleppo basin, which is characterized by a flat topography and a semi-arid environment. The validity of the enhanced DEM is statistically investigated using different approaches, including histogram and regression analyses, dataset variation, and profile lines statistics considering SRTM90, DLR SRTM30, commercial NEXTmap World30 and the GeoEye-1 high-resolution elevation data. The results show a good convergence between the enhanced DEM and World30 datasets in flat areas of Al Qweek valley, with elevation difference ranges from 1–2 m and an average standard deviation SD= 1.68 m. The calculated residual mean squared error (RMSE) in the enhanced data varies from 0.67 to 2.10 m with respect to topographic and CLAS GCPs, respectively, while RMSE = 1.44 m between the enhanced DEM and the GeoEye-1 elevation model. The results also show significant improvement in tracing performance of the drainage network in the region and reveal the lowest horizontal displacement (0.5–25 m) from the actual drainage lines in comparison with other DEMs.

Keywords DEM, flat topography, drainage pattern, ANUDEM, GCP, ICEsat GLAS, DEM enhancement

1 Introduction

Topography is a very important factor that controls water flow and surface hydrological processes within watersheds, such as infiltration, surface runoff, erosion and drainage network formation. Watershed delineation provides spatial and geometric information about drainage, channel length, and subcatchments (Garbrecht and Martz 2000). Within the last three decades, methods have been developed to automatically derive this information from digital elevation data, using different GIS and commercial software. Thus, digital elevation models (DEMs) have been widely used in hydrological modeling and surface analysis, including watershed processing in flat regions (Al-Muqdadi and Merkel 2011), soil and landslide hazard (Claessens et al. 2005; Chaubey et al. 2005).

Hydrological processing using digital elevation models (DEMs) is a challenging issue in areas of flat terrain (Garbrecht and Martz 1997; Martz and Garbrecht 1998; Gallant and Dowling 2003). Various methods are available today to process DEM data automatically for drainage pattern extraction as well as watersheds delineation and topographic parameterization. These methods simulate surface flow and drainage direction to define different hydrological parameters of a basin, which is relatively difficult in depressions and flat landscapes (Martz and Garbrecht 1998). Hence, methods and algorithms have been established to process DEMs, and enhance elevation data for better and more precise representation of the earth's geomorphology and drainage networks, particularly in flat topography. One method to improve the hydrologic correctness is known as DEM reconditioning, using linear feature correction (i.e. known stream line), which warps the raw DEM and adjusts the generated drainage network to be consistent with stream position (Callow et al. 2007). The Sink/depression filling technique of digital elevation data is another often used procedure in flat regions, where uncorrected DEMs can contain gaps in the horizontal resolution, or anomalies in the elevation cells in the original raster data owing to errors in interpolation and limitation of the DEM resolution (Maidment 2002). Therefore, inadequate vertical resolution is one of the sources for errors in the delineation of hydrological features in flat regions (Garbrecht and Martz 1997). Since flow direction and flow accumulation are the most important concepts in hydrological processing, many algorithms have been also developed to gather hydrographic information from DEMs. The most common method to extract flow direction from a digital elevation model is the D8, or as known as the single-flow direction method (SFD), which tracks flow direction towards from each pixel to the steepest one of eight neighboring pixels (Jenson and Domingue 1988). A more sophisticated robust method tracing the flow is known as D- ∞ algorithms proposed by Tarboton (1997). Flow direction in D-∞ is defined as the steepest downward slope on eight triangular facets centered at each grid point, where the flow direction angle is determined as the angle in radians counter-clockwise from east, as a continuous quantity between 0 and 2π (Tarboton 2002). This method is also called multiple-flow direction (MDF), and allows continuous flow angles and flow portioning between one or two neighboring pixels (Rivix 2004). New promising approaches that can be used in flat terrain are the I/O-efficient Soille's algorithm (Soille et al. 2003) and the Priority First Search (PFS) method integrated into the TerraHidro program (Rosim et al. 2013).

DEM data are commonly available in a raster format at different resolutions, and vary from one source to another. As mentioned above, the accuracy of elevation data enables a better simulation of a real hydrological model, and has significant effects on the precise determination of watershed spatial components (Wu et al. 2008; Callow et al. 2007). A variety of methods have been developed to enhance digital elevation models by integrating high- resolution satellite imagery (GeoEye-1 and Quickbird imagery) for the purpose of geomorphological mapping of karst landforms (Siart et al. 2009), residual relief separation (Hiller and Smith 2008), and/ or satellite radar data (SAR, Geosat and ERS-1) in topographical modeling (Ekholm 1996; Moreira et al. 2004). Unfortunately, these methods are relatively expensive (commercial input data) and require longtime of subsequent processing and interpretation. On the other hand, finished interpolated high accuracy DEMs are usually for commercial use and could be so expensive, particularly for large extended areas. In this study, the drainage enforcement algorithm (ANUDEM) was used to enhance the horizontal and vertical resolution of the SRTM 90 digital elevation model in the southern parts of the Al Qweek Valley, by integrating several types of spatial data (ground control points GCPs, contour maps and GLAS data) to derive a more realistic surface drainage pattern than that provided by other available DEMs at same grid resolution.

2 Study area

The new method was applied in a case study area lying in the northern part of Syria, forming the southern part of Aleppo basin (Fig.1). The region of interest has an area of 711.2 km2, and characterized by an arid and semi-arid climate with mean annual precipitation ranging from 240 mm, near Aleppo in the north, to 350 mm in Tel Hadya in the southwest. The aridity index according to UNEP (1997) is 0.25. The study area is also characterized by a flat topography, particularly in the southern parts close to the Al Qweek River outlet (Al Seha marsh), which covers a wide area of Al Matah depression to the south.

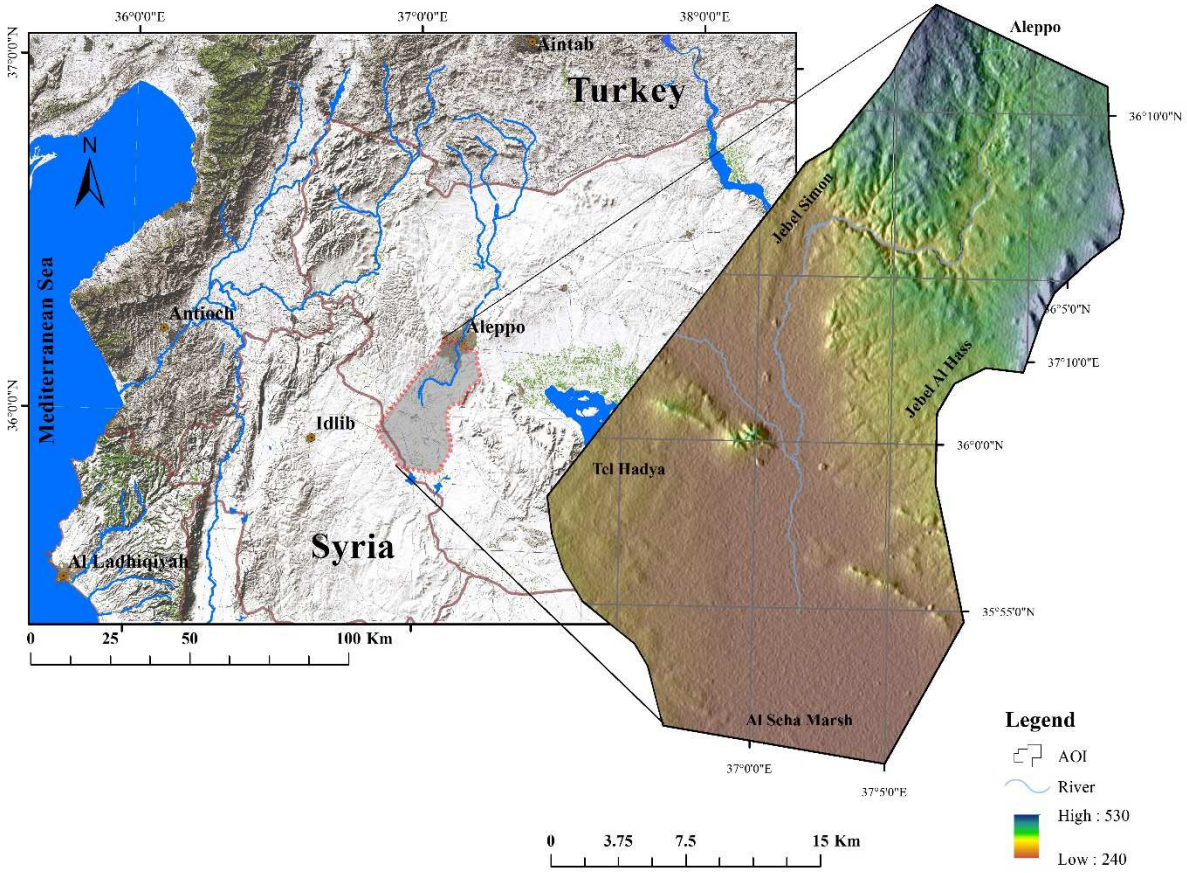

Fig. 1: Location of the case study area shows the natural terrain, land cover and main rivers of the northern parts of Syria provided by ESRI maps server (left), and 3 arc-seconds digital elevation model USGS SRTM v2

The calculated slope ranges from 0.1–2° in the Al Qweek valley, and 3–10° in the elevated terrain in the northern and eastern parts of the area (Jebel Simon and Jebel Al Hass; Fig.2). Soils are generally dominated by chromic luvisols, according to the Food and Agriculture Organization FAO classification (FAO 1974). The average soil thickness ranges from 1m in the north to more than 1.5 m in the south (Jenson and Domingue 1988; Aguilar et al. 2013; Abo and Merkel 2014). Neogene limestone is the most prominent rock formation in the region, and crops out on moderately sloped terrain (Jebel Simon and Tel Hadya). Basalt flows dominate in the east (Jebel Al Hass), while quaternary deposits (loam, pebbles and conglomerates sediments) fill the internal parts, Al Qweek terraces, and Al Matah depression. The Al Bredeh fault crosses the southern part of study area in a SE-NW direction. This region is intensively cultivated, which is accompanied by an increased irrigated area from distributed arterial canals and the Al Qweek River. Wheat, barley, and legumes are the dominant crops in the region. The increased population in the region in the last two decades, water scarcity as well as the

industrial and agricultural activity led to significant decrease in the groundwater level (Luijendijk and Bruggeman 2008). This raises many questions about water resources sustainability in the future.

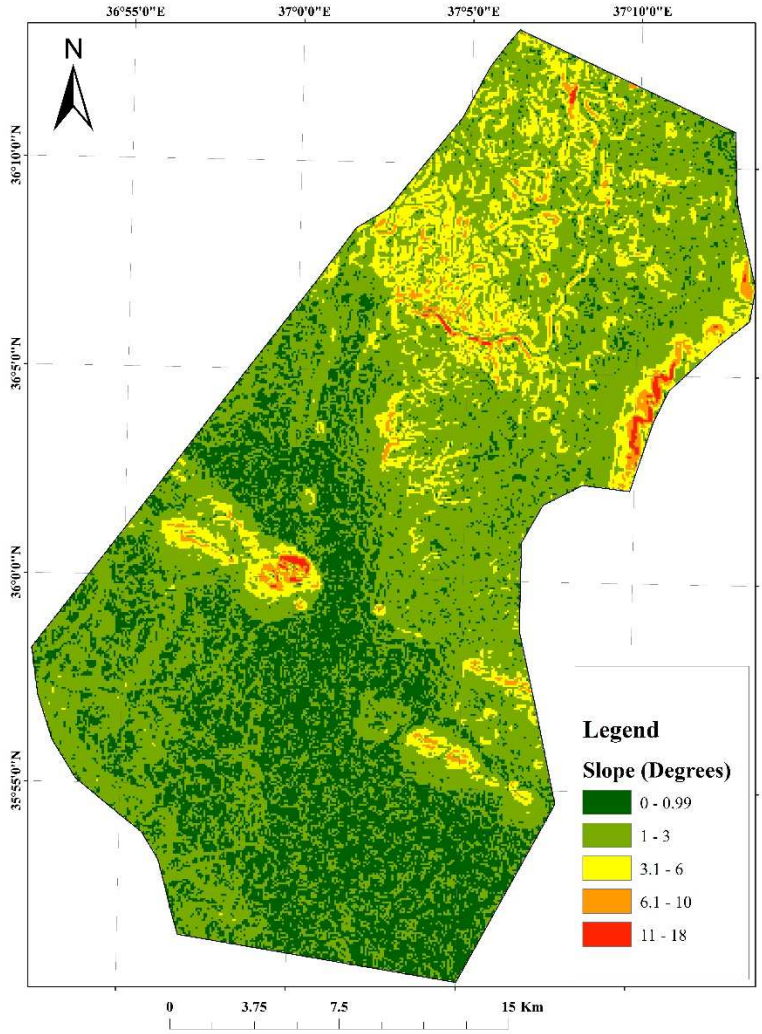

Fig. 2: Slope map of the study area based on SRTM 90 m digital elevation model

3 Materials and methods

3.1 Datasets

3.1.1 GeoEye-1 imagery

GeoEye -1 is commercial very high-resolution satellite image (DigitalGlobe, Inc.), launched in 6th September, 2008. Today, GeoEye-1 imagery has the highest geometric resolution at its nadir with 0.41 m and 1.65 m for panchromatic (PAN) and multispectral images (MSI), respectively. In this study, two GeoEye-1 Geo class images provided by DigitalGlobe were used. The images deliver 100% overlap and cover a small portion of the southern parts of the study area (31.8 Km2). GeoEye-1 Geo products are map-projected and rectified to a specific datum and area projection system (GeoEye 2009). The data was shipped with rational polynomial coefficient files (RPCs) of the sensor camera model and metadata files. The characteristics of the used GeoEye-1 imagery are shown in the Table 1. DEM extraction of GeoEye-1 images was carried out using OrthoEngine package of PC Geomatica v10.2

software. The model computed using 13 ground control points (GCPs) distributed within projected area (Fig.3). The geo-coded digital surface model (DSM) generated at 2 x 2m grid resolution. The final DSM was converted into digital terrain model (DTM) using the DSM2DTM algorithm with adjusted horizontal tile size to 100m. The horizontal and vertical error of the generated DEM were calculated based on the difference in the three-dimensional object space positions (X, Y, Z) between the ground control points (GCPs) and their intersections with the DEM grid. For that, all datasets were resampled to a 2 x 2m cell dimension, in order to replicate the GeoEye-1 DEM grid resolution. Moreover, the elevation data of the GeoEye-1 based DEM were converted into elevation points that represent the average elevation value of each pixel-center of the generated DEM. After that, 500 points were selected randomly and compared with other used elevation datasets.

Tab. 1: Characteristics of panchromatic and multispectral images from GeoEye-1 Geo production line

ID /Product line	***001/ GeoEye-1 Geo***	***002/ GeoEye-1 Geo***
Aquisition date-Time	23/07/2010 - 08:07 GMT	20/08/2010 - 08:27 GMT
Processing level	Std geometrically corrected	Std geometrically corrected
Seneor Name	GeoEye-1	GeoEye-1
Image Type	PAN/MSI	PAN/MSI
Projection	UTM zone 37	UTM zone 37
Datum	WGS84	WGS84
Pixel size	0.5m	0.5m
Cloud cover	0	0
Scan direction	reverse	reverse
Sun azimuth	123.548	143.517
Sun elevation	64.865	62.176
Nominal collection azimuth	102.48°	254.93°
Nominal collection Elevation	67.08°	72.06°
Acquired Nominal GSD (PAN-corss scan)	0.45m	0.43m
Acquired Nominal GSD (PAN-along scan)	0.47m	0.44m
Acquired Nominal GSD (MSI-cross scan)	1.8m	1.72m
Acquired Nominal GSD (MSI-cross scan)	1.91m	1.77m

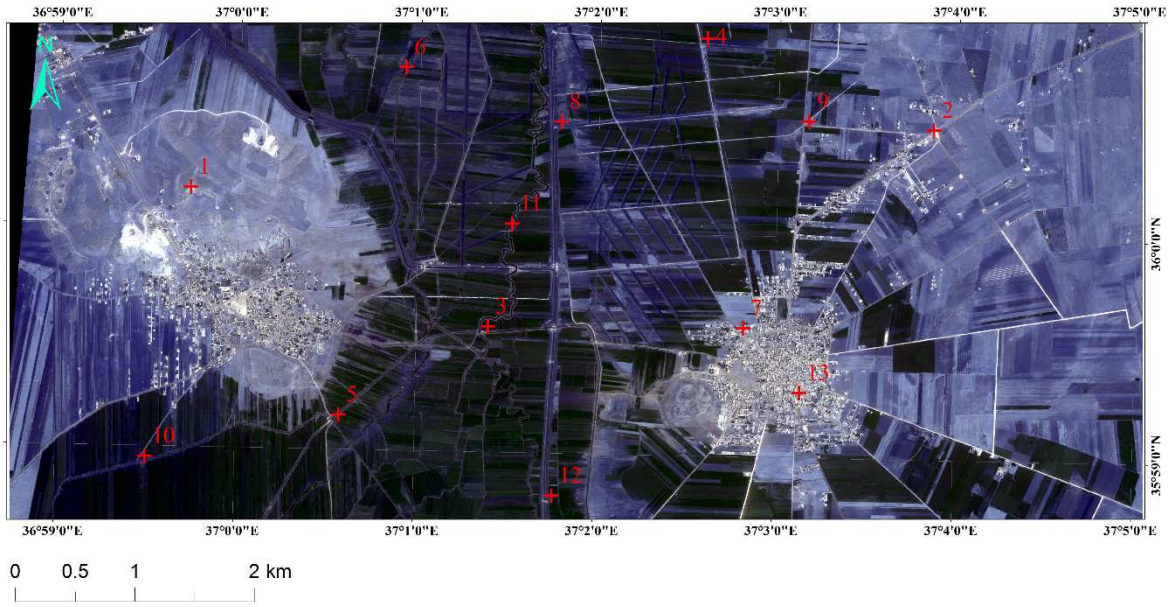

Fig. 3: GeoEye-1 overlap area shows the location of ground control points GCPs

3.1.2 Digital elevation data

The Shuttle Radar Topography Mission (SRTM v2) elevation dataset of 3-arcsecond resolution (90 m x 90 m) was used as block elevation data of the enhancement approach. The dataset was provided by the USGS ftp server (http://dds.cr.usgs.gov/srtm/). The Shuttle radar SRTM data is generally derived from C-band radar (Hensley et al. 2000). A C-band system of synthetic aperture radars (5.6 cm; C-RADAR) was used to generate contiguous mapping coverage of the earth's surface (Farr et al. 2007). However, SRTM data coverage is on a near-global scale from 56°S to 60°N. These data were validated on continental scales through comparison with nearly 9.4 million collected kinematic GPS/GCP ground control points worldwide. The average vertical absolute error over Eurasia was reported by 6.6 m with 90% confidence, which meets the mission objectives (Rodriguez et al. 2005). In addition to the C-band SRTM, X-SAR/ SRTM and NEXTmap World 30 digital elevation models were used in this study as reference elevation data in the validation model. X-SAR/ SRTM data is derived primarily using X-band (3.1 cm) single polarization (vertical send and receive), supplied by the German Aerospace Center (DLR) and the Italian Space Agency (ASI) in the shuttle radar mission. The dataset covers approximately 80% of the land surface between 56°S and 60°N, with an estimated horizontal absolute accuracy of <15m and <10 for the vertical absolute accuracy (Keydel et al. 2000). X-SAR/ SRTM has 1 arc-second raster resolution (30 m x 30 m) provided by the DLR EOWEB server (http://eoweb.dlr.de:8080/index.html), and was used in comparison after applying Earth Gravitational Geoid Model EGM96 correction, in order to convert X-band elevation values from WGS84 ellipsoid heights to heights above the WGS84 (EGM96) geoid, by means of offset information of DLR metadata (Walker et al. 2007). Furthermore, the NEXTmap World 30 commercial digital elevation data was used. They comprise a merged data model, using corrected public input data. The data were provided by the InterMap Technologies server (http://www.intermap.com/en-us/databases/world30.aspx). The World 30 elevation model also provides unified, best available surface elevation data with a 30 m x 30 m resolution, which was proposed as one of the most accurate global terrain products, covering the whole of the earth's surface area. In fact, it is a result of a combination of different input DEM (SRTM 90 v2.1, ASTER 30 v2.0, ICESat LiDAR points and GTOPO30 DSM). The vertical accuracy of these data was improved by using sophisticated vertical correction, filling all voids and removing all non-ground anomalies. The reported vertical adjustments ranges from -5 to +10 m, with an estimated mean error of 4 m (Intermap 2013). However, the final vertical accuracy over the Middle East ranges between 2.5 and 4.9 m, as shown in the map derived from over 87 million global GCPs. NEXTmap World 30 data were validated though automated elevation comparison, using ICESat LiDAR ground

control points, which provided a vertical accuracy of 25 centimeters residual mean squared error (RMSE).

3.1.3 Spatial and ground observation data

Generally, ground control points (GCPs) are defined as points on the ground surface that have known coordinates and elevation (Schowengerdt 2006). These can be derived from topographic surveys, high-accuracy differential GPS workstations, and aero-triangulation. An alternative source of GCPs is the topographic maps. Yet, collecting ground control points from topographic maps can be problematic, owing to errors resulting from the geometric transformation, and depends, in particular, on the map's scale (Smhh and Atkinson 2001; Foody 2002). In this study, vertical and horizontal correction of DEM was carried out using two groups of ground control points GCPs (Fig. 4): 18 ground control points were digitized from the 1:50,000 topographic maps, and 215 control points were derived from the Geoscience Laser Altimeter System GLAS06 L1B and GLAS14 v33 global elevation data on board ICEsat (Ice, Cloud and land Elevation Satellite), which is the only source of public satellite LIDAR data available at present (Schutz et al. 2005; Ferreira et al. 2011). GLAS integrates a laser system to measure distance, and a global position system (GPS) and altitude determination unit provides ~70 m spot diameter and ~170 m measurements interval along the earth's surface (Pirotti 2010). Owing to mission objectives and repartitioning of the discrete observation transect, GLAS provides incomplete data coverage (Fig.5). The estimated horizontal error in ICESat data using integrated residual analysis error of ocean returns, was 2.4 ± 7.3 m, and vertical error of 0.04 ± 0.13 m standard deviation per degree of incidence angle (Carabajal and Harding 2005; GeoEye 2009). Fortunately, the data provided by ICEsat partially intersect with the north and northeastern parts of the study area. In addition to the ground controlling points, a precise digitized drainage line of the Al Qweek River was integrated into the DEM processing. The digitization was performed using high-resolution satellite imagery with the help of the professional version of Google Earth, and GeoEye-1 high-resolution imagery (0.5 m panchromatic).

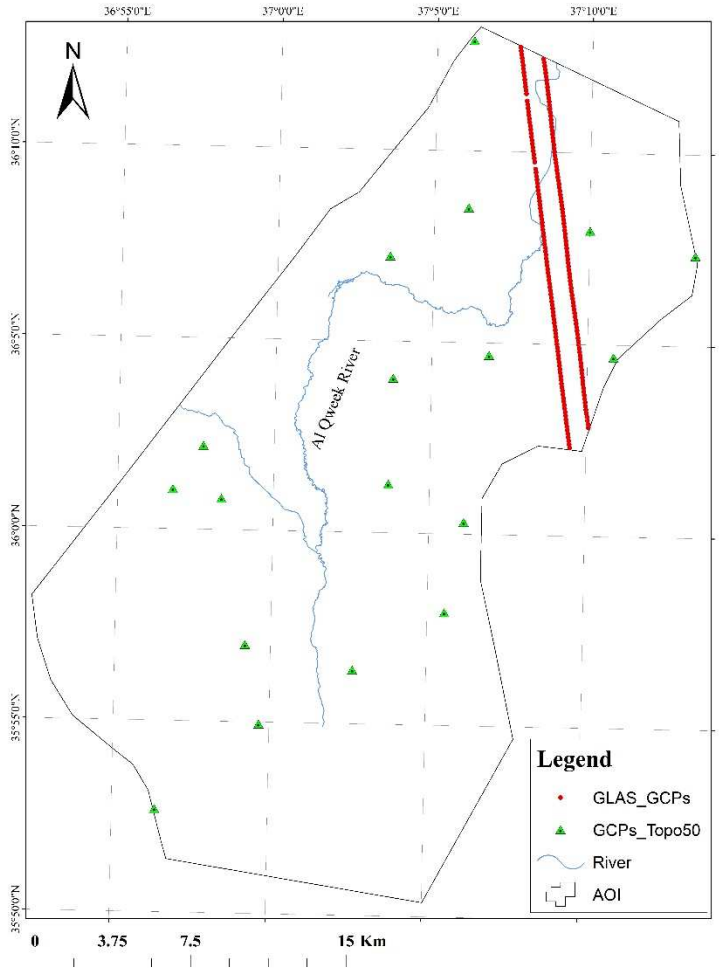

Fig. 4: **The location of ground control points (GCPs; green triangles) within study area. The two red lines represent the GLAS06 control point tracks**

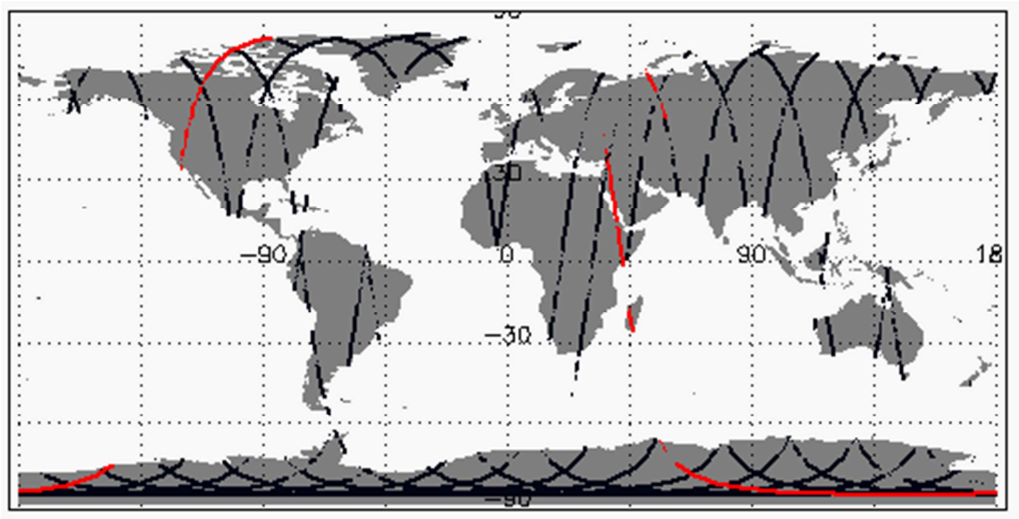

Fig. 5: **The coverage of GLAS14 land elevation data displayed using IDL visualizer developed by ICESAT/GLAS Science Computing Facility & NASA/Goddard Space Flight Center. Res lines represent the data transects where only one of them crossing the study area.**

3.2 Enhancement approach and extraction of hydrological pattern

After collecting the required data, post-possessing of raw DEM was performed, by integrating the elevation dataset of the raw raster SRTM90, topographic ground control points, GLAS LiDAR data, digitized river and the boundary area, using ArcGIS v10 topo-to-raster processing tools (Table 2). The topo-to-raster interpolation method is based on the ANUDEM algorithm developed by Michael Hutchinson (Hutchinson 1988).

Tab. 2: Input datasets used in the enhancement approach

Raw Data	*Type*	*Feature Class*	*Source*
SRTM90 v2	Digital elevation model	Points, contour lines	USGS
GLAS GCPs	Ground control points	Points	ICEsat GLAS06, 14
Topo GCPs	Ground control points	Points	1:50000 topographic map
Stream	River	Line	Digitization
AOI	Boundary area	Polygon	Digitization

ANUDEM is a specifically designed program for the creation of hydrologically correct digital elevation models, that ensures a connected drainage structure and correct representation of ridges and streams from input contour data. The interpolation algorithm of ANUDEM is described by Hutchinson (Hutchinson 1989, 2000; Tarboton 1997). Figure 6, presents a flowchart of the major steps of DEM correction, using the ANUDEM algorithm (Rivix 2004). First, the SRTM90 dataset was converted into vector points, representing the absolute elevation value of each raster pixel. Moreover, 10m contours (isolines) were generated by using a surface-contouring tool included in the spatial analysis package of ArcGIS, based on the SRTM90. As mentioned above, the contour lines are used for the correct representation of surface topography (steep areas, ridges and valleys), as well as the drainage pattern. Minimum and maximum elevations for the raster interpolation were adjusted, based on topographic maps and the information provided by raw SRTM elevation data, while the output cell size of interpolated raster was adjusted to 30m using the offered option in the ANUDEM. Finally, the enhanced DEM of 30 m x 30 m resolution was generated by integrating all those data and interpolating them into the new digital elevation model (Fig.7). In order to check the results quality and validity of enhanced DEM, different statistical approaches were applied, including histogram analysis, regression analysis, dataset variation and profile line statistics. The analysis also included estimation of the resulting error among the generated elevation model and SRTM90, SRTM30, commercial World30 and GeoEye based DTM data. This was achieved by using an elevation comparison of the intersected 1,000 randomly selected points from the enhanced data with other datasets, by using *Hawth's tools'* extension (Beyer 2004). All data were compared to GeoEye 2m resolution DEM within the overlap area. The vertical absolute error between the ground control points (topographic and GLAS GCPs) and different used DEMs was calculated using the following equation:

$$Error = Abs([GRIDCODE\ DEM] - [GRIDCODE\ DEM_{ref}]) \quad (1)$$

where GRIDCODE DEM represents the elevation of each raster cell in the enhanced DEM, while GRIDCODE DEM_{ref} is the corresponding elevation value in the reference DEM. On the other hand, the flow direction and drainage network for various used DEMs was extracted using the commonly used D8 algorithm integrated into ArcHydro Tools v10.2 (Maidment 2002). This algorithm with automatically filling depressions and fixed stream threshold of 1500 cells was suggested as a standard method for tracing drainage networks of the enhanced data and compares them with other datasets (SRTM90, World30 and GeoEye-1).

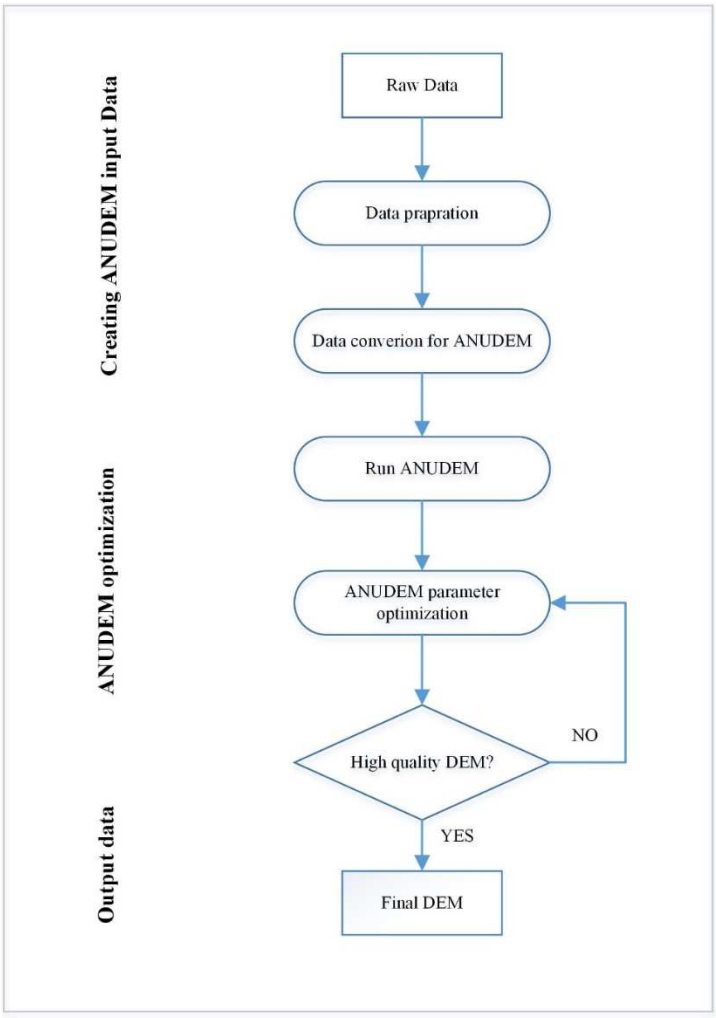

Fig. 6: Major steps used in ANUDEM algorithm in the DEM interpolation (Yang et al. 2005)

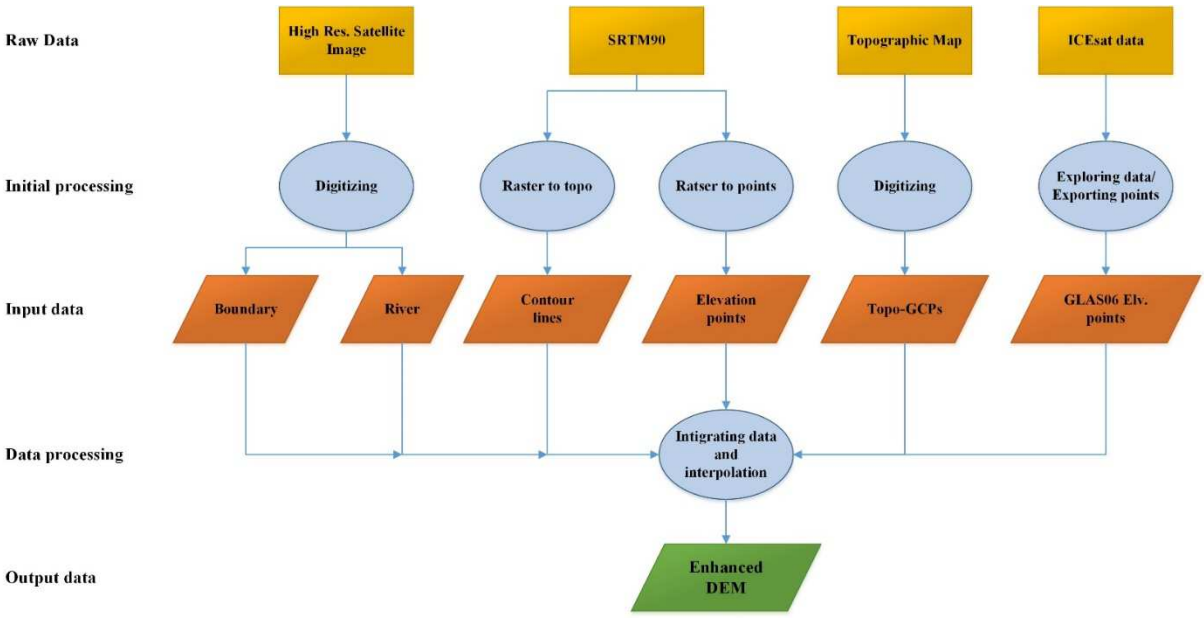

Fig. 7: Flowchart representing the main performed steps in the DEM enhancement approaches

4 Results and discussion

4.1 Error estimation

Results show an obvious convergence between the enhanced DEM and World30 dataset, particularly in the region of flat topography (Al Qweek Valley), while the SRTM 30 in contrast shows relatively higher abnormal elevations and noise values over the whole study area. The average residual between the enhanced DEM and the SRTM30 ranges from 5–10 m in the flat areas and up to 30 m in the north (hilly lands). This can be explained by ellipsoid/ geoid conversion under different terrain conditions (Walker et al. 2007), as shown in the topographic profiles of enhanced data in comparison with SRTM30, SRTM90 and World30 datasets (Fig.8).

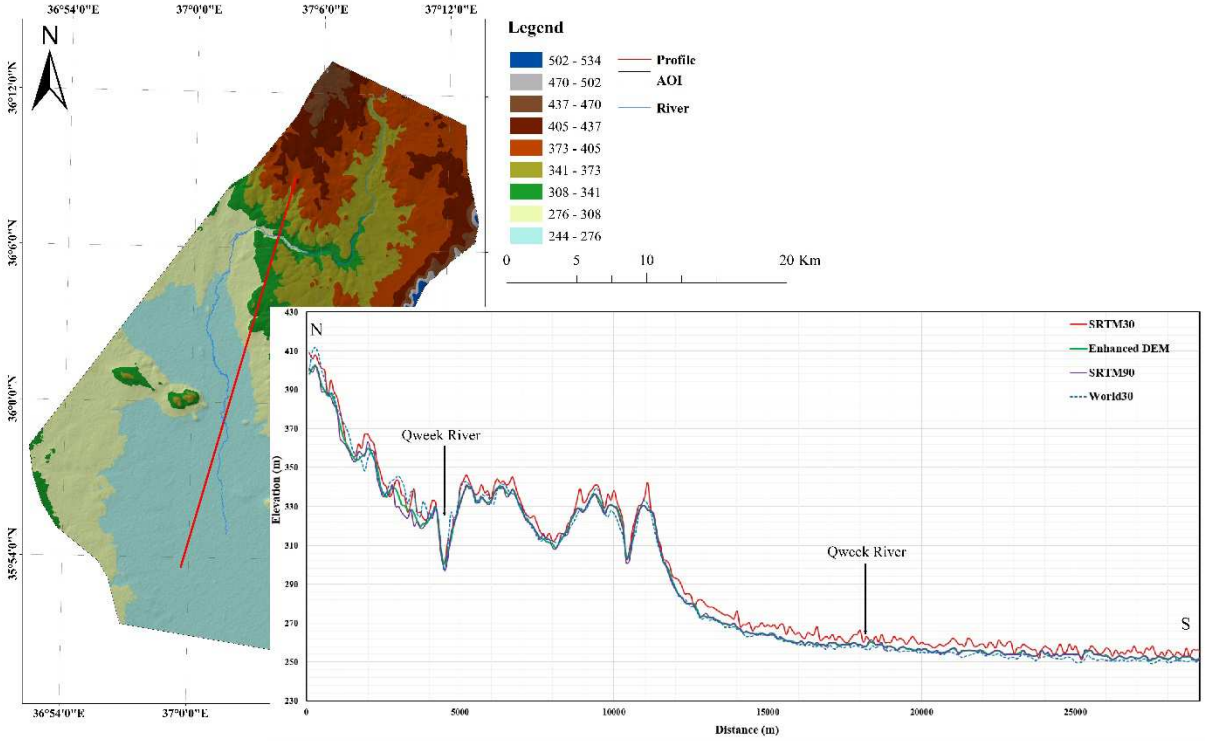

Fig. 8: A comparison between the reference DEM dataset and the enhanced DEM along the N-S elevation profile

The results also show lower noise in the DEM after enhancement in comparison to X-band SRTM30 and other used data over flat terrains in the region (Al Matah depression in the south). Table 3 presents the main statistical information along created profiles. However, the histograms of error frequency also show a vertical difference in elevation ranges from 2.5–4 m between the enhanced DEM and raw SRTM30, and about 1–2 m for the World30 data, with an average standard deviation of σ= 1.68 m (Fig.9). The higher differences in elevation seems to be more pronounced in the low elevated lands, while less significant difference are observed in the areas with averaged elevation above 390 m. On the other hand, the enhanced data show more accurate replication of the topographic surface and GCPs' intersection points in comparison with other DEMs. The vertical RMSE of the enhanced data is estimated to be 2.10 m and 0.67 m at the 95% confidence level in comparison to topographic and GLAS GCPs, respectively, while it between 0.58 m and 4.03 m for the SRTM30, and between 6.02 and 2.67 for the World30 data. Figure 10 compares the elevation frequency of ground control points (topographic and GLAS GCPs) with SRTM30, World30 and enhanced DEM data. It shows significant similarity in distribution between the enhanced DEM and both types of ground control points.

Tab. 3: Statistical data of elevation profiles

Dataset	*2D length*	*3D length*	*Max Elv.*	*Min Elv.*	*Length uphill*	*Length Downhill*	*Avg. Slope uphill*	*Avg. Slope downhill*	*Max Slope up-hill*	*Max Slope downhill*
SRTM30	29032.55	29057.63	408.98	251.03	12009.30	16848.32	1.72	1.72	8.53	10.20
SRTM90	29032.55	29049.35	402.00	251.00	8838.06	13211.29	1.50	1.63	7.41	10.20
World30	29032.55	29048.77	411.59	248.97	12206.68	16742.09	1.09	1.29	9.37	10.08
En. DEM	29032.55	29043.84	402.29	250.92	11336.06	17707.78	0.91	1.04	5.44	8.32

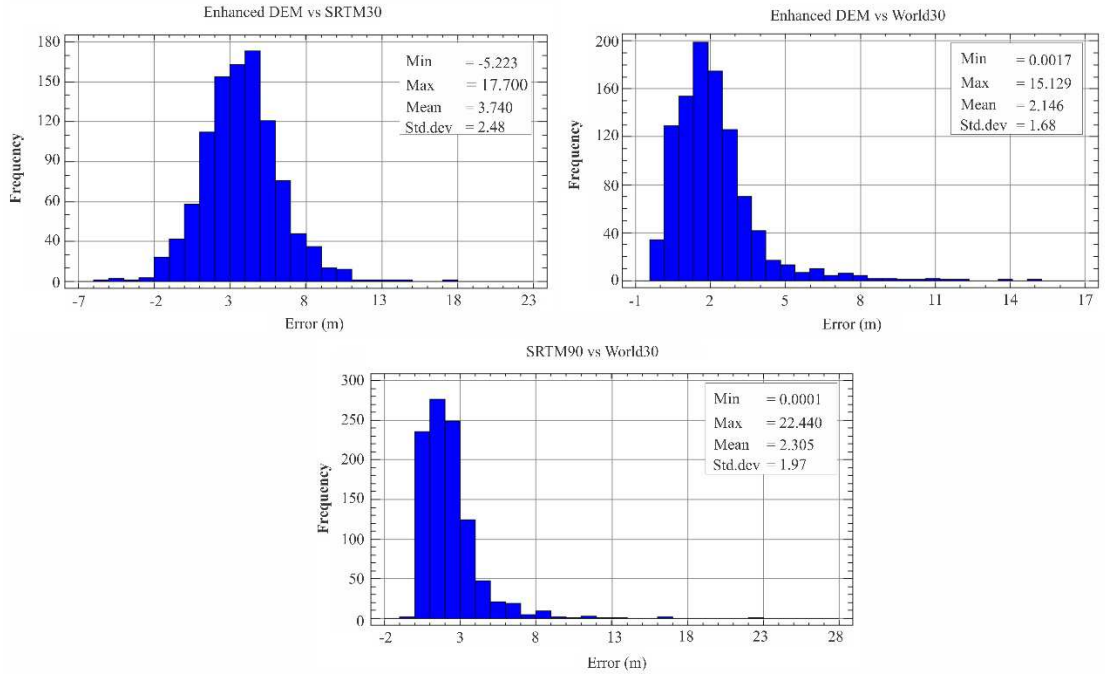

Fig. 9: The histograms of error frequency distribution shows relatively low error values between the enhanced DEM and World30 commercial data in comparison to the raw SRTM90 and X-band SRTM30

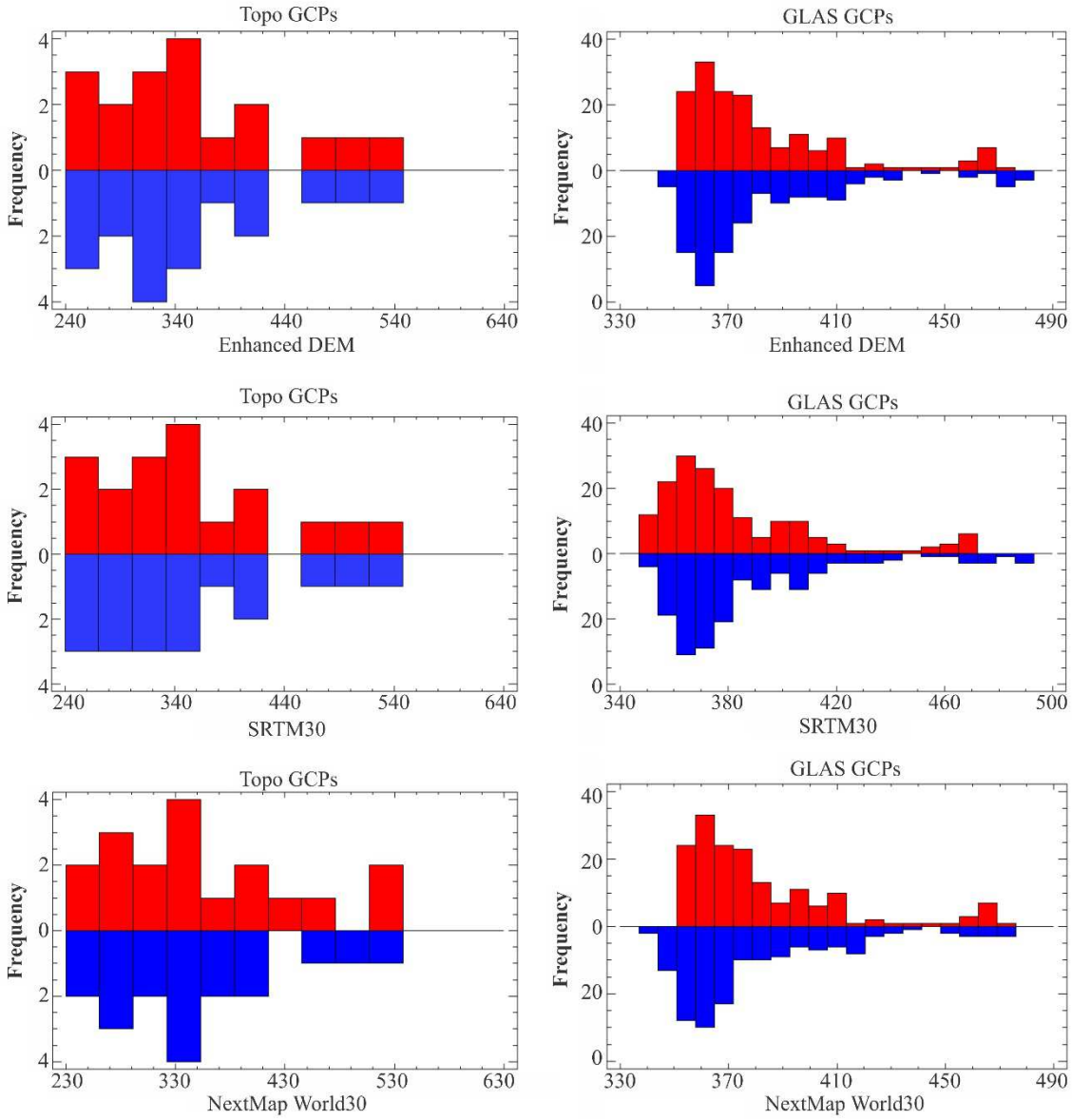

Fig. 10: Comparison between topographic/GLAS GCPs and enhanced/used DEMs

The standardized skewness values are within the range +2 to -2, which indicates normally distributed data and vice versa of GLAS GCPs (Table 4). The results of the error frequency also indicate that the enhanced DEM and World30 are relatively more homogeneous to the extracted DEM from GeoEye-1 imagery, with an RMSE of 1.44 and 3.05m, respectively. On the other hand the SRTM90 data provide more accurate elevation data (RMSE = 3.86 m) in comparison to the DLR SRTM30 dataset in the region with RMSE of 4.80 m (Fig.11).

4.2 Regression analysis

Regression analysis was performed between the different elevation datasets. The output shows the results of fitting a linear model, and describes the relationship between GLAS/ Topo GCPs and enhanced DEM, as well as raw and reference DEMs (Fig.12). The R^2 statistic indicates that the model as fitted explains 96.855% of the variability in GLAS GCPs for the enhanced DEM with a mean absolute error (MAE) of 3.77 m, and correlation coefficient equals 0.984.

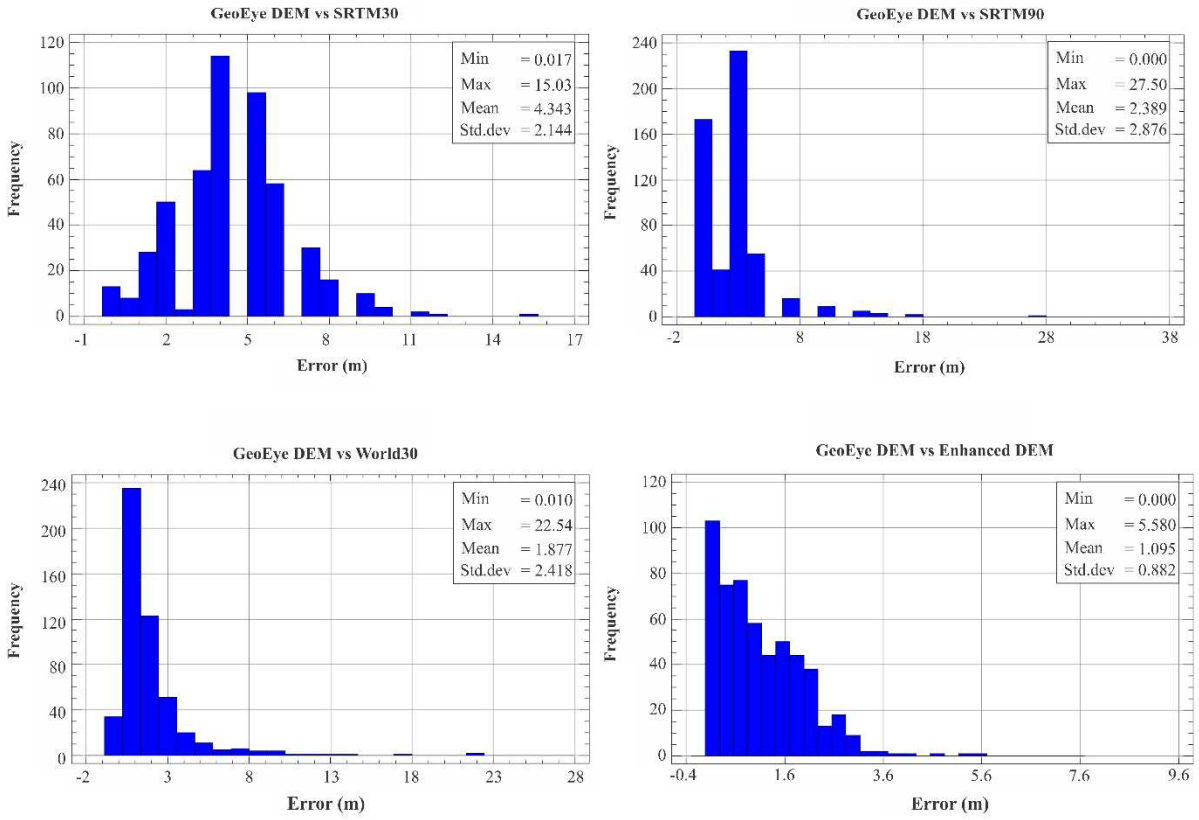

Fig. 11: Error frequency histogram for GeoEye-1 DEM in comparison to the different elevation dataset

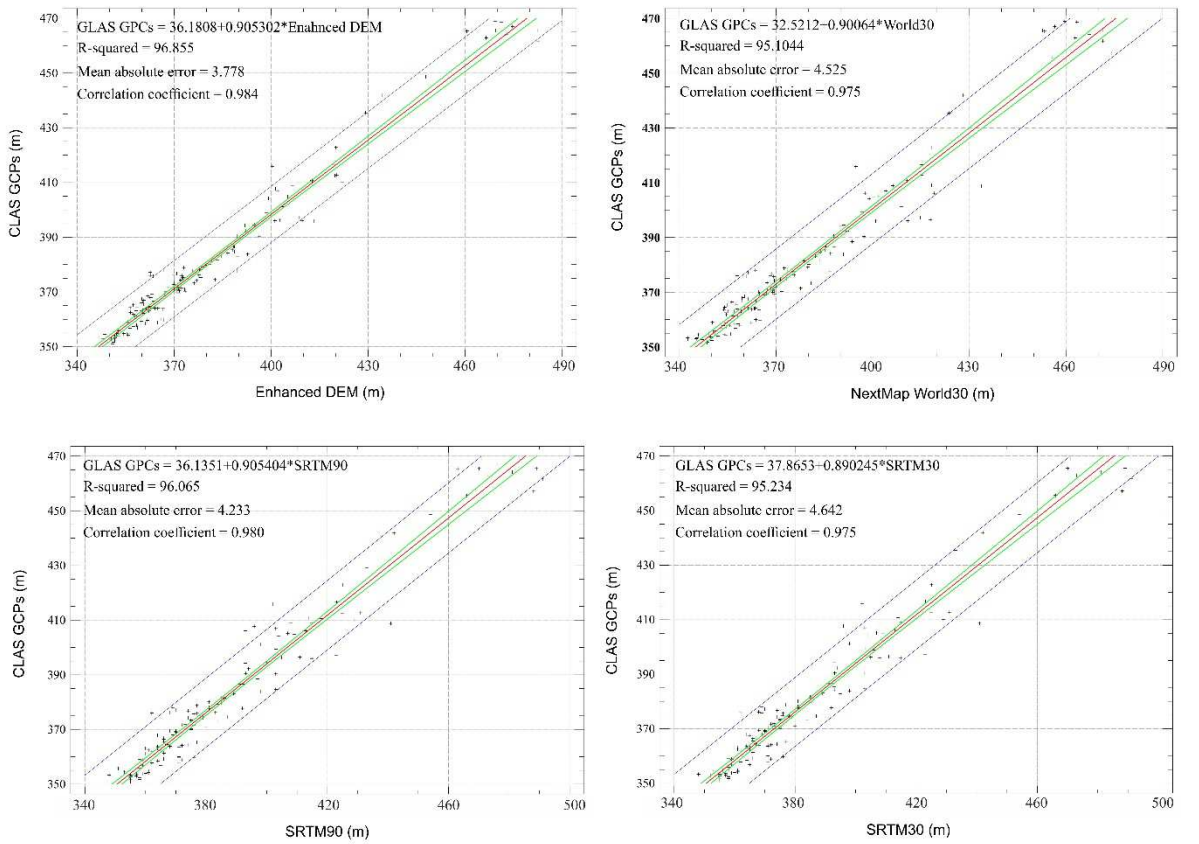

Fig. 12: Linear regression between GLAS GCPs and DEM data

The results also show an R^2 of 99.770 % between enhanced data and the topographic derived GCPs, with mean absolute error of 2.70 m. Since the P-value in the ANOVA table is less than 0.05 for all used data, a statistically significant relationship exists between both types GCPs and DEMs at the 95.0% confidence level. Table 4 shows the results derived from the regression analysis. The interpolated elevation model (enhanced DEM) seems to be the more accurate model that can reveal commercial data of the same resolution. Furthermore, the visual comparison shows better morphological representation of the topographic surface, reflected by better quality data of the enhanced elevation data in comparison to the SRTM90, as shown in Figure 13. Simple regression analysis between all elevation datasets and the high resolution DEM (2m GeoEye-1 DEM) shows average residuals of 0.772 m, and standard deviation of 0.93 m for the enhanced DEM, and 1.797 m with standard deviation of 3.03 m for the NextMap World 30 dataset at the 95.0% confidence level. Moreover, the standard deviation of the residual ranges from 1.44 to 2.37 m for the SRTM90 and SRTM30 datasets, respectively.

Tab. 4: Statistical comparison approach between the ground control points and DEM data

Summary statistics	***Topo GCPs***	***Enhanced DEM***	***DLR SRTM30***	***InterMap World30***
Avg	355.444	352.996	254.859	349.423
Std. dev	83.363	83.581	84.735	84.158
Coeff. of variation (%)	23.453	23.677	23.878	24.084
Min	257	256.42	256.02	251.2
Max	531	529.61	533.07	525.77
Std. Skewness	1.438	1.523	1.467	1.438
Interval of mean (conf. 95%)	355.44 ±41.4	352.99 ±41.5	354.85 ±42.1	349.42 ±41.8
Medians	336.5	334.6	336	329.94
Summary statistics	***GLAS GCPs***	***Enhanced DEM***	***DLR SRTM30***	***InterMap World30***
Avg	382.445	381.916	386.483	379.766
Std. Dev	29.206	31.718	31.983	30.926
Coeff. of variation (%)	7.636	8.305	8.275	8.143
Min	350.95	346.68	348.01	342.59
Max	470.38	482.66	491.08	474.25
Std. skewness	8.206	8.294	8.535	7.185
Interval of mean (conf. 95%)	382.44 ±4.4	381.91 ±4.8	386.48 ±4.8	379.76 ±4.6
Medians	373.3	370.9	375.04	368.79

4.3 Hydrological pattern

Hydrological processing of drainage network indicates considerable variation in the automatically tracked flow direction, particularly for the SRTM90 and SRTM30 datasets, while better results were achieved by using the World30 DEM, which provides relatively closer results to those, obtained using the enhanced DEM (Fig.14). It is quite clear that the enhancement of the SRTM90 dataset, using the ANUDEM algorithm, improved the performance of the tracing flow network significantly over flat terrain. It is quite clear that the enhancement of the SRTM90 dataset, using the ANUDEM algorithm, improved the performance of the tracing flow network significantly over flat terrain. This is shown in the reasonably replication of the digitized flow line of the Al Qweek River. The results also show a

horizontal shift in the traced drainage pattern for SRTM30 and World30 datasets, ranging from 5–50 m in the highland (Aleppo hill) and up to 50 m in the flat region (Al Matah depression).

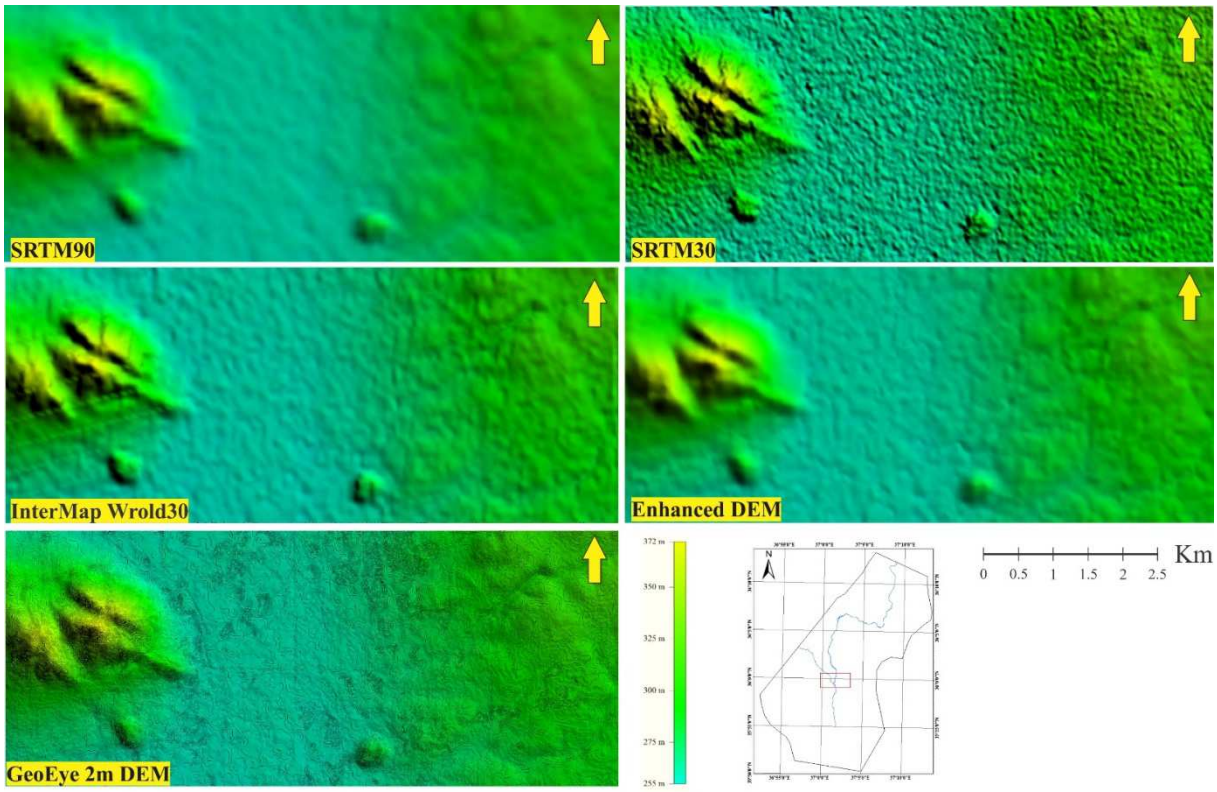

Fig. 13: Visual comparison between the five types of DEM in the flat area, in the southern part of region

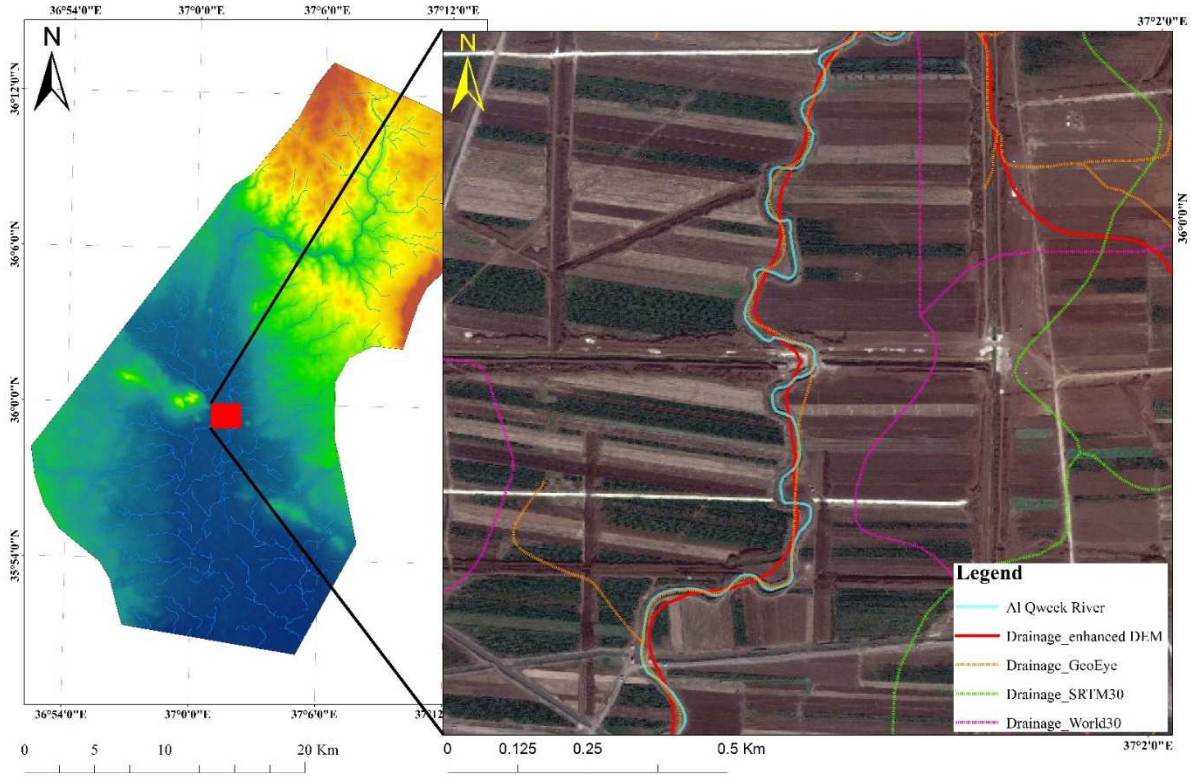

Fig. 14: Sample comparison of the delineated drainage network within the area of interest at a threshold of 1500 cells shows the trace for the Al Qweek River after data enhancement (red line)

In contrast, the delineated drainage lines extracted from enhanced DEM provide a better representation of the actual drainage line of the Al Qweek River, with horizontal displacement of 0.5 to 25 m in both flat and highland topography. The results also indicate that both the high-resolution GeoEye-1 DEM (2 x 2 m DEM) and the enhanced digital elevation data can be used with confidence for the application of hydrological processing in the regions of flat terrain, providing more accurate replication of the topographic surface, as well as more realistic drainage networks, even by using traditional D8 flow-direction algorithms. Figure 15 illustrates a horizontal cross-section through the Al Qweek River and shows the actual and calculated drainage location. A slight displacement from the actual drainage line of the Al Qweek River has been achieved using the 2 m high resolution DEM (GeoEye-1), which ranges from 0.5 to 5 m, while a higher shift value was indicated for the enhanced DEM at the same profile location, with a 15 m deviation from the actual drainage line of the Al Qweek River. No drainage lines were detected in the buffer range of the 60 m profile width for the other datasets.

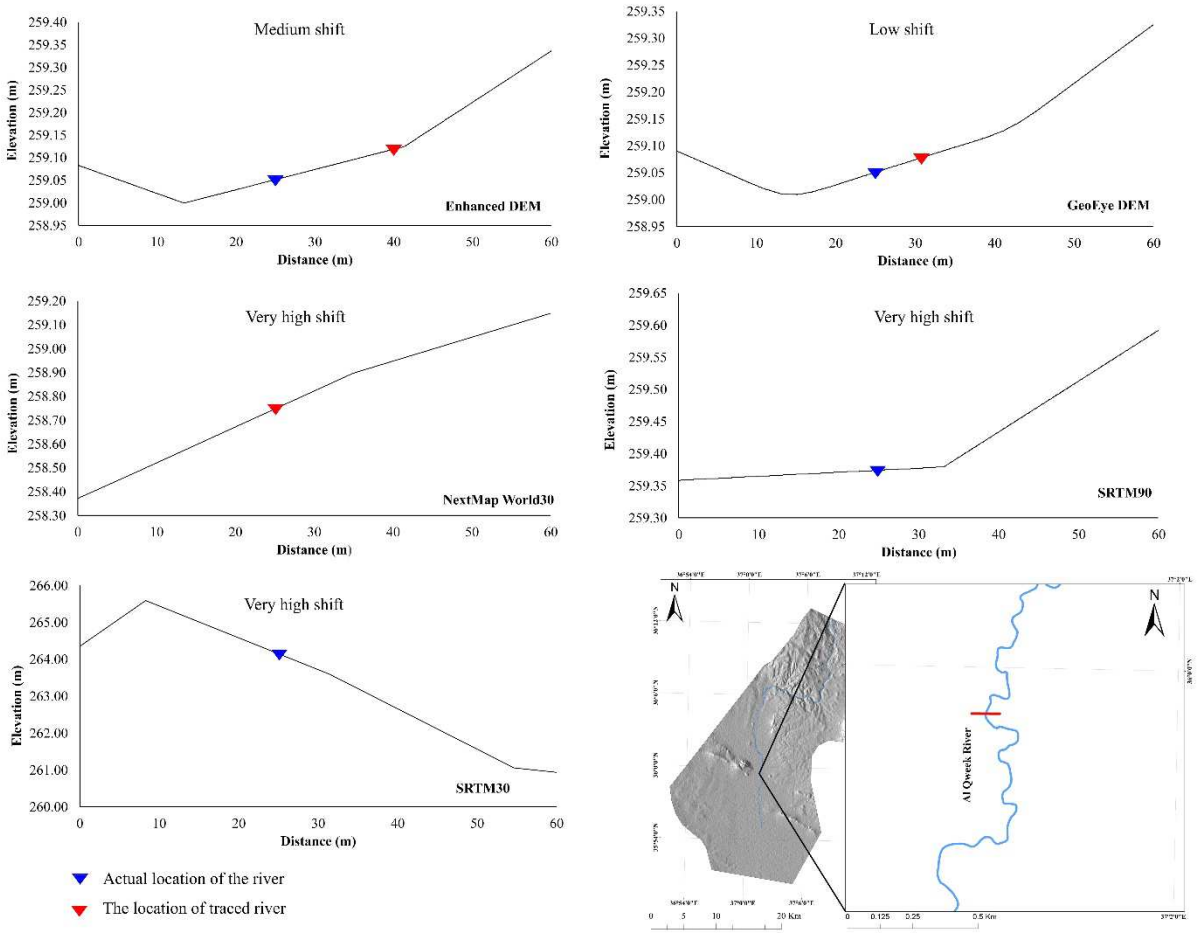

Fig. 14: Comparison cross-section of Al Qweek River for used and created DEMs, shows the location of actual (blue triangle) and extracted drainage of the river (red triangle)

5 Conclusions

The interpolation and assessment of a low-resolution digital elevation model, by integrating ground and satellite observation data, is essential to eliminate multiple sources of error that can potentially affect the accuracy of extracted spatial data, particularly in flat regions. DEM enhancement, using the ANUDEM approach, is a promising method to improve the quality of raw DEMs, which is expressed in more precise representation of flat topography and accurate spatial output. This study also shows that automatic tracing of the drainage network, by using available algorithms, is not an easy task in flat terrain, and is unfortunately, insufficient and can show a high shift value from the actual drainage path.

6 Acknowledgements

This work was supported by TU Bergakademie Freiberg and the Syrian Ministry of Higher Education. Special thanks and appreciation are given to the DigitalGlobe Foundation for providing us with high-resolution satellite images. Thanks also to the InterMap company and all our colleagues at the TU Bergakademie Freiberg for supporting this work.

7 References

Abo RK, Merkel BJ (2014) Comparative estimation of the potential groundwater recharge in Al Zerba catchment of Aleppo basin, Syria. Arabian Journal of Geosciences:1-22

Aguilar MA, Saldaña MdM, Aguilar FJ (2013) Assessing geometric accuracy of the orthorectification process from GeoEye-1 and WorldView-2 panchromatic images. International Journal of Applied Earth Observation and Geoinformation 21 (0):427-435. doi:http://dx.doi.org/10.1016/j.jag.2012.06.004

Al-Muqdadi SW, Merkel BJ (2011) Automated Watershed Evaluation of Flat Terrain. Journal of Water Resource and Protection 3 (12)

Beyer HL (2004) Hawth's analysis tools for ArcGIS. http://www.spatialecology.com/htools/.

Callow JN, Van Niel KP, Boggs GS (2007) How does modifying a DEM to reflect known hydrology affect subsequent terrain analysis? Journal of Hydrology 332 (1):30-39

Carabajal CC, Harding DJ (2005) ICESat validation of SRTM C-band digital elevation models. Geophysical Research Letters 32 (22):L22S01. doi:10.1029/2005GL023957

Chaubey I, Cotter A, Costello T, Soerens T (2005) Effect of DEM data resolution on SWAT output uncertainty. Hydrological Processes 19 (3):621-628

Claessens L, Heuvelink G, Schoorl J, Veldkamp A (2005) DEM resolution effects on shallow landslide hazard and soil redistribution modelling. Earth Surface Processes and Landforms 30 (4):461-477

Ekholm S (1996) A full coverage, high-resolution, topographic model of Greenland computed from a variety of digital elevation data. Journal of Geophysical Research: Solid Earth 101 (B10):21961-21972. doi:10.1029/96JB01912

FAO (1974) Lgend of the Soil Map of the World. Food and Agriculture Organization FAO, Rome, Italy

Farr TG, Rosen PA, Caro E, Crippen R, Duren R, Hensley S, Kobrick M, Paller M, Rodriguez E, Roth L (2007) The shuttle radar topography mission. Reviews of geophysics 45: RG2004. doi:10.1029/2005RG000183

Ferreira LG, Urban TJ, Neuenschawander A, de Araújo FM (2011) Use of Orbital LIDAR in the Brazilian Cerrado Biome: Potential Applications and Data Availability. Remote Sensing 3 (10):2187-2206

Foody GM (2002) The role of soft classification techniques in the refinement of estimates of ground control point location. Photogrammetric Engineering and Remote Sensing 68 (9):897-904

Gallant JC, Dowling TI (2003) A multiresolution index of valley bottom flatness for mapping depositional areas. Water Resources Research 39 (12):1347. doi:10.1029/2002WR001426

Garbrecht J, Martz LW (1997) The assignment of drainage direction over flat surfaces in raster digital elevation models. Journal of hydrology 193 (1-4):204-213

Garbrecht J, Martz LW (2000) Digital elevation model issues in water resources modeling. Hydrologic and hydraulic modeling support with geographic information systems:1-28

GeoEye (2009) GeoEye Product Guide. GeoEye, Inc. . http://www.geoeye.com/CorpSite/assets/docs/brochures/GeoEye_Product_Guide.pdf.

Hensley S, Rosen P, Gurrola E The SRTM topographic mapping processor. In: Geoscience and Remote Sensing Symposium, 2000. Proceedings. IGARSS 2000. IEEE 2000 International, 2000. IEEE, pp 1168-1170

Hiller JK, Smith M (2008) Residual relief separation: digital elevation model enhancement for geomorphological mapping. Earth Surface Processes and Landforms 33 (14):2266-2276. doi:10.1002/esp.1659

Hutchinson M (1989) A new procedure for gridding elevation and stream line data with automatic removal of spurious pits. journal of Hydrology 106 (3):211-232

Hutchinson M (2000) Optimising the degree of data smoothing for locally adaptive finite element bivariate smoothing splines. ANZIAM Journal 42:C774--C796

Hutchinson M (1988) Calculation of hydrologically sound digital elevation models. vol 133. Proceedings of the Third International Symposium on Spatial Data Handling, Sydney

Intermap (2013) Technical Review NEXTMap World 30 Digital Surface Model. Intermap Technologies, Inc., Englewood, CO 80112

Jenson S, Domingue J (1988) Extracting topographic structure from digital elevation data for geographic information system analysis. Photogrammetric engineering and remote sensing 54 (11):1593-1600

Keydel W, Hounam D, Pac R, Werner M (2000) X-SAR/SRTM- Part of a Global Earth Mapping Mission. RTO Meeting Proc. 61, Space-based Observation Technology, RTO MP-61, 32ff.

Maidment DR (2002) Arc Hydro: GIS for water resources, vol 1. ESRI, Redlands

Martz LW, Garbrecht J (1998) The treatment of flat areas and depressions in automated drainage analysis of raster digital elevation models. Hydrological Processes 12 (6):843-855. doi:10.1002/(SICI)1099-1085(199805)12:6<843::AID-HYP658>3.0.CO;2-R

Moreira A, Krieger G, Hajnsek I, Hounam D, Werner M, Riegger S, Settelmeyer E TanDEM-X: a TerraSAR-X add-on satellite for single-pass SAR interferometry. In: Geoscience and Remote Sensing Symposium, 2004. IGARSS '04. Proceedings. 2004 IEEE International, 20-24 Sept. 2004 2004. pp 1000-1003 vol.1002. doi:10.1109/IGARSS.2004.1368578

Pirotti F (2010) IceSAT/GLAS Waveform Signal Processing for Ground Cover Classification: State of the Art. Italian Journal of Remote Sensing 42 (2):13-26

Rivix L (2004) RiverTools, Topographic and River Network Analysis. User's Guide, RiverTools Version 3

Rodriguez E, Morris C, Belz J, Chapin E, Martin J, Daffer W, Hensley S (2005) An assessment of the SRTM topographic products, Technical Report JPL D-31639, Jet Propulsion Laboratory, Pasadena, California, p. 143

Rosim S, de Freitas Oliveira JR, Copertino Jardim A, Namikawa LM, Rennó CD TerraHidro: A Distributed Hydrology Modelling System With High Quality Drainage Extraction. In: GEOProcessing 2013, The Fifth International Conference on Advanced Geographic Information Systems, Applications, and Services, 2013. pp 161-167

Schowengerdt RA (2006) Remote sensing: models and methods for image processing. 2 edn. Academic press, San Diego, California

Schutz B, Zwally H, Shuman C, Hancock D, DiMarzio J (2005) Overview of the ICESat mission. Geophysical Research Letters 32 (21):L21S01

Siart C, Bubenzer O, Eitel B (2009) Combining digital elevation data (SRTM/ASTER), high resolution satellite imagery (Quickbird) and GIS for geomorphological mapping: A multi-component case study on Mediterranean karst in Central Crete. Geomorphology 112 (1–2):106-121. doi:http://dx.doi.org/10.1016/j.geomorph.2009.05.010

Smhh DP, Atkinson SF (2001) Accuracy of rectification using topographic map versus GPS ground control points. Photogrammetric Engineering & Remote Sensing 67 (5):565-570

Soille P, Vogt J, Colombo R (2003) Carving and adaptive drainage enforcement of grid digital elevation models. Water Resources Research 39 (12)

Tarboton DG (2002) Terrain analysis using Digital ElevationModels (TauDEM). Utah State University.

Tarboton DG (1997) A new method for the determination of flow directions and upslope areas in grid digital elevation models. Water resources research 33 (2):309-319

UNEP (1997) World Atlas of Desertification. 2nd edn. N. Middleton and D. Thomas (eds), London, Arnold

Walker WS, Kellndorfer JM, Pierce LE (2007) Quality assessment of SRTM C- and X-band interferometric data: Implications for the retrieval of vegetation canopy height. Remote Sensing of Environment 106 (4):428-448. doi:http://dx.doi.org/10.1016/j.rse.2006.09.007

Wu S, Li J, Huang G (2008) A study on DEM-derived primary topographic attributes for hydrologic applications: sensitivity to elevation data resolution. Applied Geography 28 (3):210-223

Yang Q, Van Niel TG, McVicar TR, Hutchinson MF, Li L (2005) Developing a digital elevation model using ANUDEM for the Coarse Sandy Hilly Catchments of the Loess Plateau, China. CSIRO Land and Water Technical Report 7 (05):1-74

Groundwater Modeling of Harrir plain and Mirawa valley in Shaqlawa-Harrir basins, Kurdistan Region, Iraq

Seeyan, Shwan — Institute of Geology, Technische Universität Bergakademie Freiberg, Gustav-Zeuner Str.12, 09599 Freiberg, Germany. Email: shwanom2003@yahoo.com

Merkel, Broder — Institute of Geology, Technische Universität Bergakademie Freiberg, Gustav-Zeuner Str.12, 09599 Freiberg, Germany. Email: merkel@geo.tu-freiberg.de

Abstract: With the increase in population and establishment of agricultural and industrial projects, the utilization of groundwater became more important for Kurdistan region. The increased demand for water in Kurdistan for different purposes has led to an increased consumption of groundwater from the aquifers. A three-dimensional finite-difference groundwater flow model using Visual MODFLOW was developed to investigate the change in hydrogeological conditions and to simulate the properties of the flow system under different stress scenarios for the unconfined aquifer of Harrir plain in Harrir basin and the semi-confined aquifer of Mirawa valley in Shaqlawa basin.

The plain of Harrir contains two sedimentary formations of Pleistocene and Pliocene age. The aquifer is underlain by massive beds of claystone and sandstone of Miocene age. Mirawa valley consists of Pliocene and Miocene formations which were used as upper layer and Eocene formation as lower layer for modeling. The two-layer model was calibrated under steady state conditions using hydraulic parameters obtained from observation and pumping wells. The calibrated model succeeds in producing groundwater head distribution in steady state and good accordance to observed data. The standard error was estimated as 1.06 m and 2.24 m, and the normalized root mean square error (NRMSE) are 2.6 % and 2.46% for Harrir and Mirawa respectively. By increasing the pumping rate to 200% and 400% for the pumping wells, the head decreased about 6 m and 18 m in Harrir plain, and about 1 m and 2 m in Mirawa valley respectively.

Keywords: groundwater model, Visual MODFLOW, steady state, Kurdistan Region

1 Introduction

Numerical modeling is an important method for managing groundwater resources and predicting future responses for different aquifer systems and various formations. The modular finite-difference groundwater flow model (MODFLOW) is a program used for simulating groundwater flow systems (McDonald and Harbaugh 1988; Harbaugh and McDonald 1996). Direct approach of designing MODFLOW finite difference model is less intuitive, specifically for complex boundary conditions. Therefore, a MODFLOW model can be developed either using a grid or conceptual model approach (Sohrabi et al. 2013). A groundwater model is a mathematical representation of ground water systems and comprises suppositions and facilitation made for various specific purposes. It is developed for the analysis of hydrogeological processes of flow, transport, and transformation, and has many specific applications (Kumar 2013).

Groundwater models can be used to test different conceptual models and estimate hydraulic parameters. They can be used as well for water resource management and to predict how the aquifer might respond to changes in pumping, hydraulic properties and climate change (Yaouti et al. 2008).

Groundwater in Shaqlawa-Harrir Basin represents a significant main water resource and an important source of fresh water; therefore it is important to study the groundwater systems in order to maintain this vital source and to get necessary information for studying flow system and hydraulic parameters of this area. The main objective of this article is to study the groundwater processes of the hydrogeological system of Harrir unconfined aquifer (porous aquifer) and Mirawa semi-confined aquifer (karst-fractured aquifer); two of the most important groundwater resources for domestic and agricultural sectors in Kurdistan Region. The model can be used to predict future groundwater flow conditions, estimate the hydraulic response of an aquifer, and to predict the pumping rate needed to monitor the well discharge; therefore it can be used to predict water availability and sustainability in the area.

2 Materials and methods

2.1 Description of the modeled area

Shaqlawa-Harrir basin located in northeast of Erbil City, covers an area of about 1150 km^2. Harrir plain located in center of Harrir basin lies between longitude (44^0 8' 2.4"; 44^0 26' 20.4") and latitude (36^0 36' 7.2"; 36^0 26' 31.2") bounded by Greater Zab River in north, Harrir anticline in east, and Khatibian mountain in southwest. Mirawa valley located in southeastern part of Shaqlawa basin lies between longitude (44^0 12' 28.8; 44^0 30' 18") and latitude (36^0 30' 25.2"; 36^0 17' 45.6") surrounded by Safin anticline in southwest, Shakrok anticline in west, Khatibian mountain in northwest (Fig. 1). The modeled area covers 181 km^2 of Harrir basin and 92 km^2 of Shaqlawa basin.

2.2 Geological and hydrogeological setting

The groundwater reservoir of Harrir plain consists of an unconfined aquifer characterized by the presence of Quaternary deposits (10 m thickness), the permeable Pliocene Bai Hassan and Muqdadeya formations (including thick sandstone, siltstone and conglomerate) and an impervious substratum of Fatha Formation of Miocene age which represent aquiclude (including sandstone, claystone, limestone and rare evaporite). Mirawa valley consists of semi-confined aquifer characterized by three layers; first layer comprises of Quaternary deposits and Muqdadeya formation, second layer consists of Injana and Fatha formations and third layer represent PilaSpi formation of Middle-Late Eocene age (including dolomitic limestone overlain by recrystallized and chalky limestone) which characterizes a fractured aquifer with a substratum of Gercus formation (including red mudstone, sandstone, shale and few conglomerate) of Eocene age (Fig. 2).

2.3 Data collection

The geological and hydrogeological input data for groundwater aquifers' modeling include information on surface and subsurface geology water table, precipitation, evapotranspiration, pumped abstraction, stream flows, boundary condition, and hydraulic properties. Hydrogeological properties include geological formations, lithological descriptions and a topographic map with observation wells and boreholes location. Physical parameters include the aquifer thickness, hydraulic conductivity, recharge, specific yield, and pumping rates of wells. Thirteen observation wells with three pumping wells were used for Harrir plain modeling, and nine observation wells with five pumping wells were used for Mirawa valley modeling (Tabs. 1 & 2).

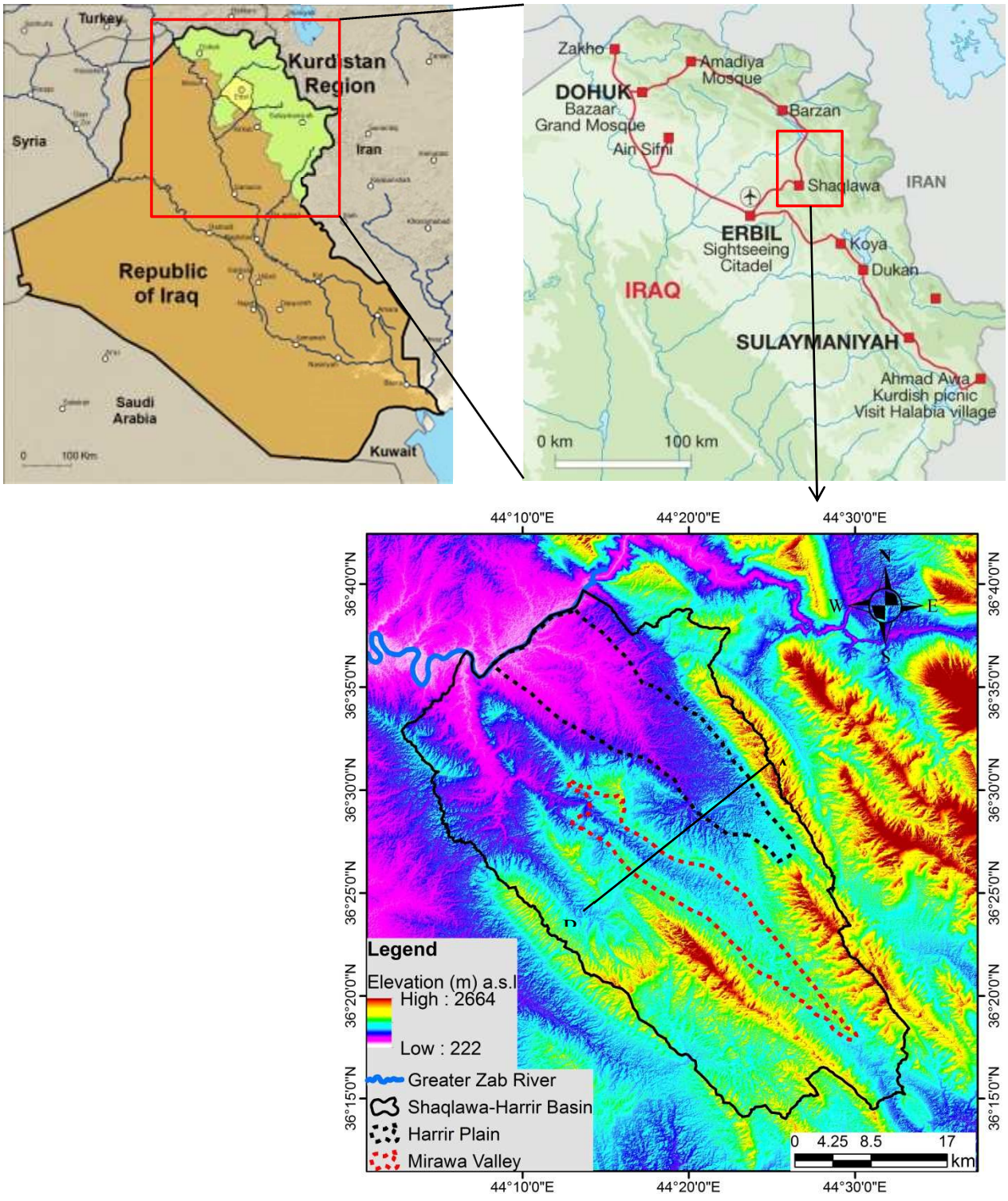

Fig. 1: Location map of Kurdistan Region, Shaqlawa-Harrir Basin, Harrir Plain and Mirawa Valley with digital terrain model showing the elevation of the study area, A-B for cross section.

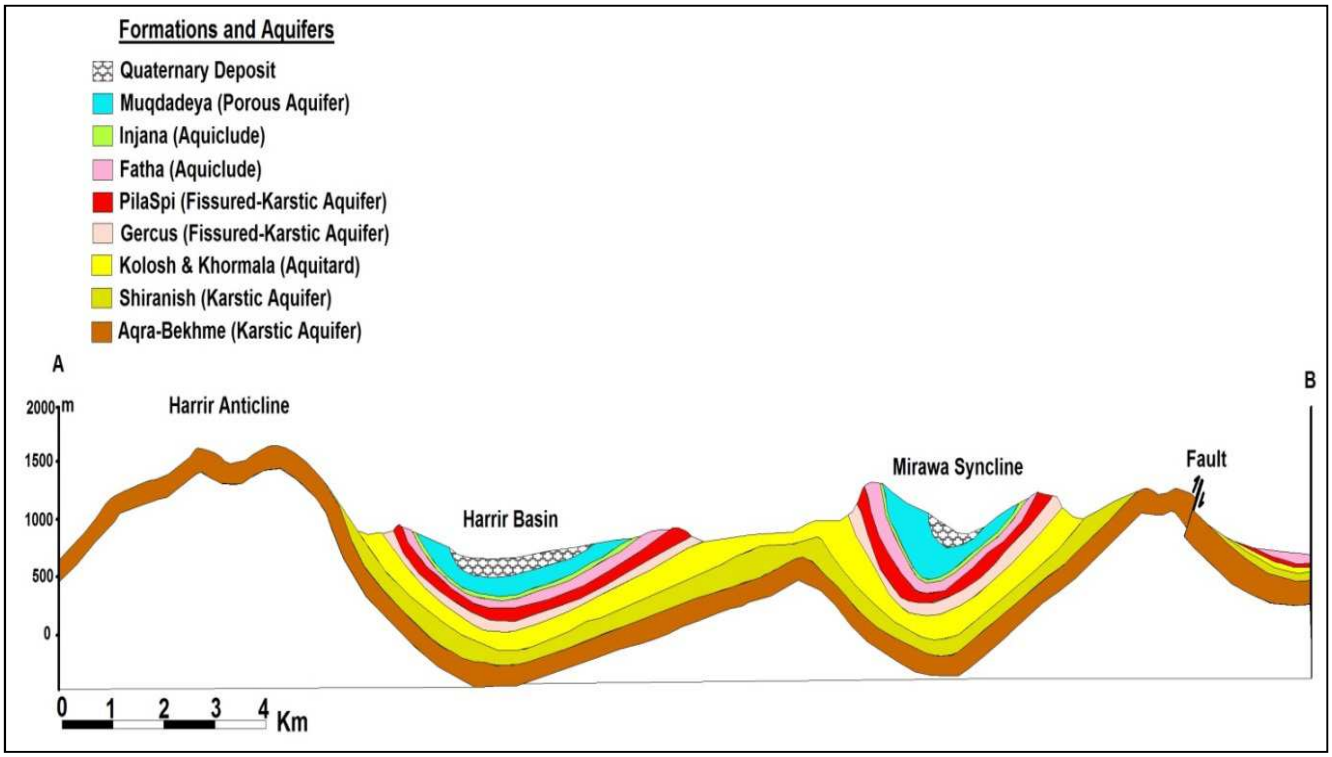

Fig. 2: Geological crosssection (A-B) of Shaqlawa-Harrir basin showing the formations and corresponding aquifers (adopted from Seeyan and Merkel 2014).

Tab. 1: Observation wells used for modeling in Mirawa Valley, UTM (WGS-84) coordination system

Well No.	Well Name	Easting	Northing	Elevation (m) a.s.l	Water table (m) a.s.l
W-1	Bawyan	444936	4041578	651	466
W-2	Barbian	429517	4053458	472	378
W-3	Qandil	426356	4053458	360	335
W-4	Qura Bag	423239	4051304	350	315
W-5	Harash	426842	4049420	435	389
W-6	Kani Khazal	428404	4048388	440	403
W-7	Basermay Kon	443207	4038657	645	470
W-8	Harir Extinguish	441106	4046032	600	450
W-9	Badel-1	434237	4047114	445	410
W-10	Baren-2	437737	4041614	514	435
W-11	Kuba	429116	4046402	455	416
W-12	Kebur	430723	4046385	450	418
W-13	Chamasur	433337	4044484	520	424

Tab. 2: Observation wells used for modeling in Mirawa Valley, UTM (WGS-84) coordination system

Well No.	Well Name	Easting	Northing	Elevation (m) a.s.l	Water table (m) a.s.l
W-1	Sarkand Khaylani	432636	4037449	725	670
W-2	Mawarani Kon	435948	4035378	796	718
W-3	Mawaran	450222	4020810	1005	959
W-4	Haji Bayz	439755	4030445	897	820
W-5	Qarata Sor	441274	4029473	892	845
W-6	Mirawa	442360	4032279	888	828
W-7	Rasan Project	452088	4020409	1019	960
W-8	Aqubani Khwaru-2	448617	4023034	981	948
W-9	Aqubani khwaru-1	445167	4025534	985	925

2.4 Hydraulic properties of the aquifers

Physical properties of the aquifer can be estimated from single well test (Kruseman and de Ridder 1994; Dellur 1999; Schaaf 2004). Hydraulic properties of the two modeled areas were obtained from the data of pumping test for three wells in Harrir plain and five wells in Mirawa valley by using the software Aquifer Test. The parameters obtained comprise transmissivity (T), hydraulic conductivity (K), specific yield (Sy) and storage coefficient (S). Theis and Numan methods were used to determine hydraulic conductivity, transmissivity, and Storage coefficient (Tab. 3).

Water recharge and discharge from an aquifer represents a change in the storage volume in a confined aquifer by changing the pressure head. For unconfined aquifers the storage coefficient is simply expressed by the product of the volume of aquifer lying between the water table at the beginning and at the end of period of time and the average specific yield of the formation (Todd 2005).

2.5 Specific yield

The quantity of water that a unit volume of the aquifer will yield when drained by gravity is called its specific yield. The part of the water that is retained in the aquifer mass is held against water that a unit volume of aquifer retains when subjected to gravity drainage is called its fractions or percentages. The sum of the specific yield and specific retention equals the porosity of the aquifer. Specific yield is calculated by:

$$Sy = \frac{\mathrm{Wy}}{\mathrm{V}} \tag{1}$$

Where: Sy is specific yield, Wy is water spent size (m^3), and V is the total volume (m^3)

The specific yield was calculated in the study area according to (Johnson 1955):

$$Sy = \frac{\text{Saturated thickness (b)}}{1000} \tag{2}$$

Saturated thickness (m) determined by the geological profile of the wells (Figs. 3 a, b).

Tab. 3: Hydraulic parameters estimated from pumping test results according to Theis and Numan using the Aquifer Test program and specific yield according to Johnson for Harrir Plain and Mirawa Valley.

Pumping Well No.	Methods						
	Theis			Numan			Johnson
	Hydraulic conductivity (K) m/d	Transmissivity (T) m^2/d	Storage coefficient (S)	Hydraulic conductivity (K) m/d	Transmissivity (T) m^2/d	Storage coefficient (S)	Specific Yield (Sy) %
Harir P.W-1	0.0136	65.7	0.0021	0.0149	65.2	0.0025	0.08
Harir P.W-2	0.0254	76.83	0.0049	0.0298	76.8	0.0081	0.085
Harir P.W-3	0.0521	84.2	0.018	0.063	83.89	0.027	0.14
Mirawa P.W-1	0.0134	13.4	0.00108	0.0156	13.4	0.00126	0.085
Mirawa P.W-2	0.0245	307	0.00569	0.0301	312	0.00875	0.079
Mirawa P.W-3	0.0842	1.19	0.02	0.089	1.19	0.031	0.069
Mirawa P.W-4	0.2946	3.27	0.107	0.317	3.8	0.115	0.11
Mirawa P.W-5	0.6402	99.5	0.5	0.7321	149	0.53	0.098

2.6 Specific capacity

Specific capacity is a measure of the productivity of a well and the value of discharge available for a unit drawdown. The specific capacity values are not constant for wells in unconfined aquifers, because an increase in drawdown at the same time decreases the water saturated thickness of the aquifer. (Fetter 1994) defined the specific capacity as the discharge of the well over drawdown:

$$Sc = \frac{\mathrm{Q}}{\mathrm{S}} \tag{3}$$

where Sc is specific capacity in m^2/day, Q is rate of discharge (m^3/day), and S is drawdown (m).

According to (Al-Sawaf 1977) the specific capacity can be calculated using the formula:

$$Sc = \frac{\mathrm{HQ}}{(\mathrm{TD} - \mathrm{SWL})\mathrm{S}} \tag{4}$$

where Sc is the specific capacity in m^2/day, Q is rate of discharge (m^3/day), H is saturated thickness (m), TD is total depth (m), SWL is static water level (m), and S is drawdown (m).

The difference between the two methods is using saturated thickness in second method, which is less than the total depth penetrated by the well (Tab. 4).

Tab. 4: Specific capacity of the pumping wells in Harri and Mirawa according to Fetter and Al-Sawaf

Well No.	H (m)	SWL (m)	Q (m^3/day)	S (m)	TD (m)	Sc (Fetter) m^2/day	Sc (Al-Sawaf) m^2/day
Harir P.W-1	81	16.78	648	16	153	40.5	24.1
Harir P.W-2	100	15	479.5	7	171	68.5	43.9
Harir P.W-3	158	34	207.4	6	253	34.6	24.9
Mirawa P.W-1	70	29	304.2	10	123	30.4	22.7
Mirawa P.W-2	66	77	518.5	20	121	25.9	38. 9
Mirawa P.W-3	42	10.5	298.1	70	145	4.3	1.3
Mirawa P.W-4	110	110	207.4	45	216	4.6	4.8
Mirawa P.W-5	98	52	583.3	7	107	83.3	148.5

2.7 Recharge

Recharge in the study area was calculated by three methods: water balance, water table fluctuation (WTF), and chloride mass balance (CMB). The average groundwater recharge value produced based on these three methods is 50.9, 114.5, and 87.4 mm/year respectively (Seeyan and Merkel 2015). The average recharge estimation of the three methods for the two modeled areas is 94.3 mm/year.

2.8 Conceptual modeling

The first step in groundwater modeling is to establish the modeling purpose and to formulate the conceptual view of the groundwater system. The adequacy of the groundwater system conceptual view dictates the resulting groundwater models' performances. A conceptual model is a simplified representation of reality with a focus on the geological and hydrogeological conditions. Construction of a conceptual model includes the definition of the basin boundaries, aquifers recharge, and discharge sources (Anderson and Woessner 1992).

In Harrir plain, groundwater system is conceptualized as a single unconfined (porous) aquifer consisting of two areas having different hydrogeological properties: the alluvial deposits and Tertiary formations (Bai Hassan and Muqdadeya Formation).

Mirawa Valley is conceptualized as two hydrogeological layers of semi-confined (karst-fractured) aquifer: the upper layer is represented by quaternary (Alluvial deposits) and Tertiary (Bai Hassn, Muqdadeya, and Fatha) Formations, and the lower layer is represented by Eocene (PilaSpi) Formation.

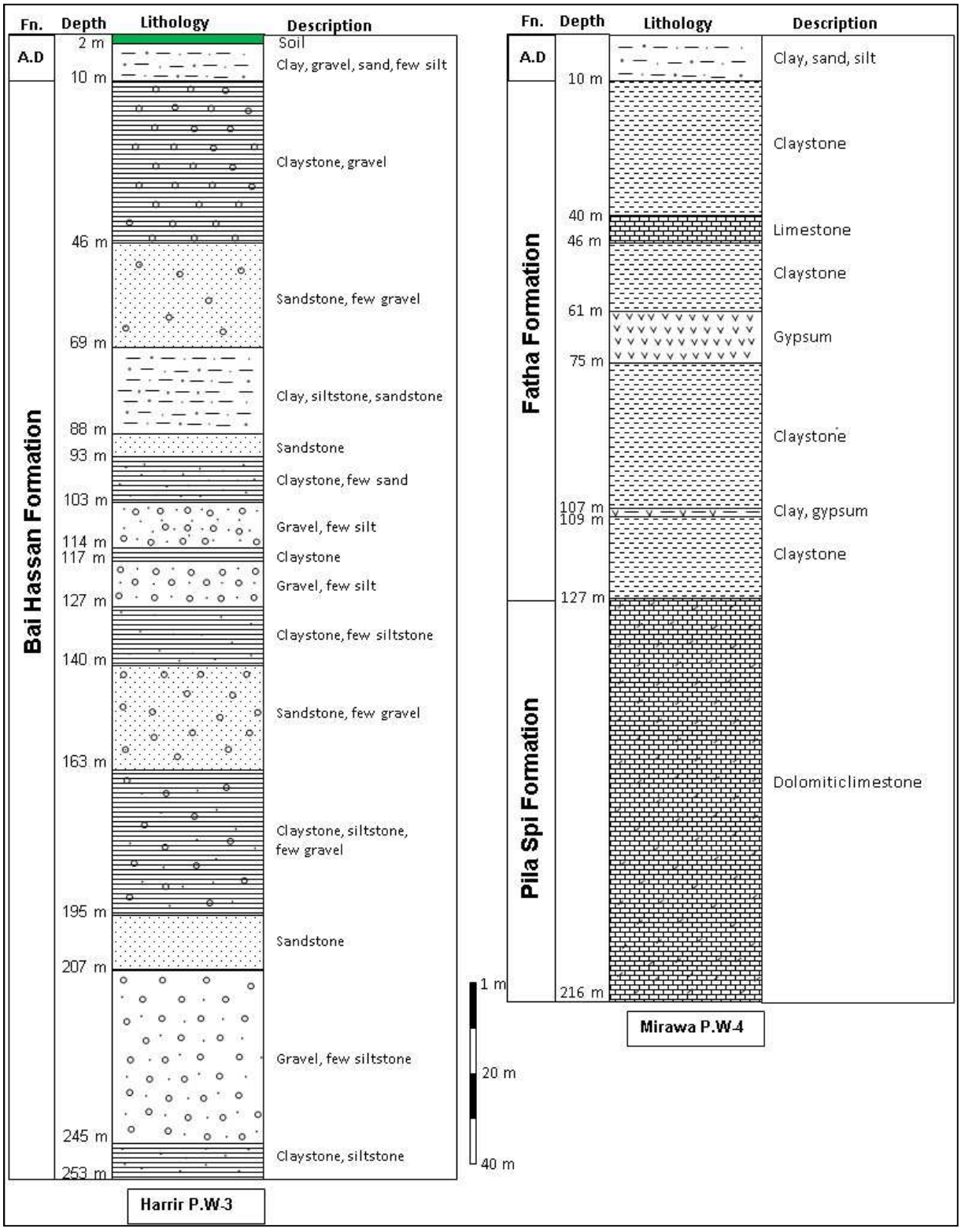

Fig. 3a: Lithological profile of two pumping wells; Harrir P.W-3 and Mirawa P.W-4 (Fn.: Formation, A.D: Alluvial Deposits, P.W: Pumping well)

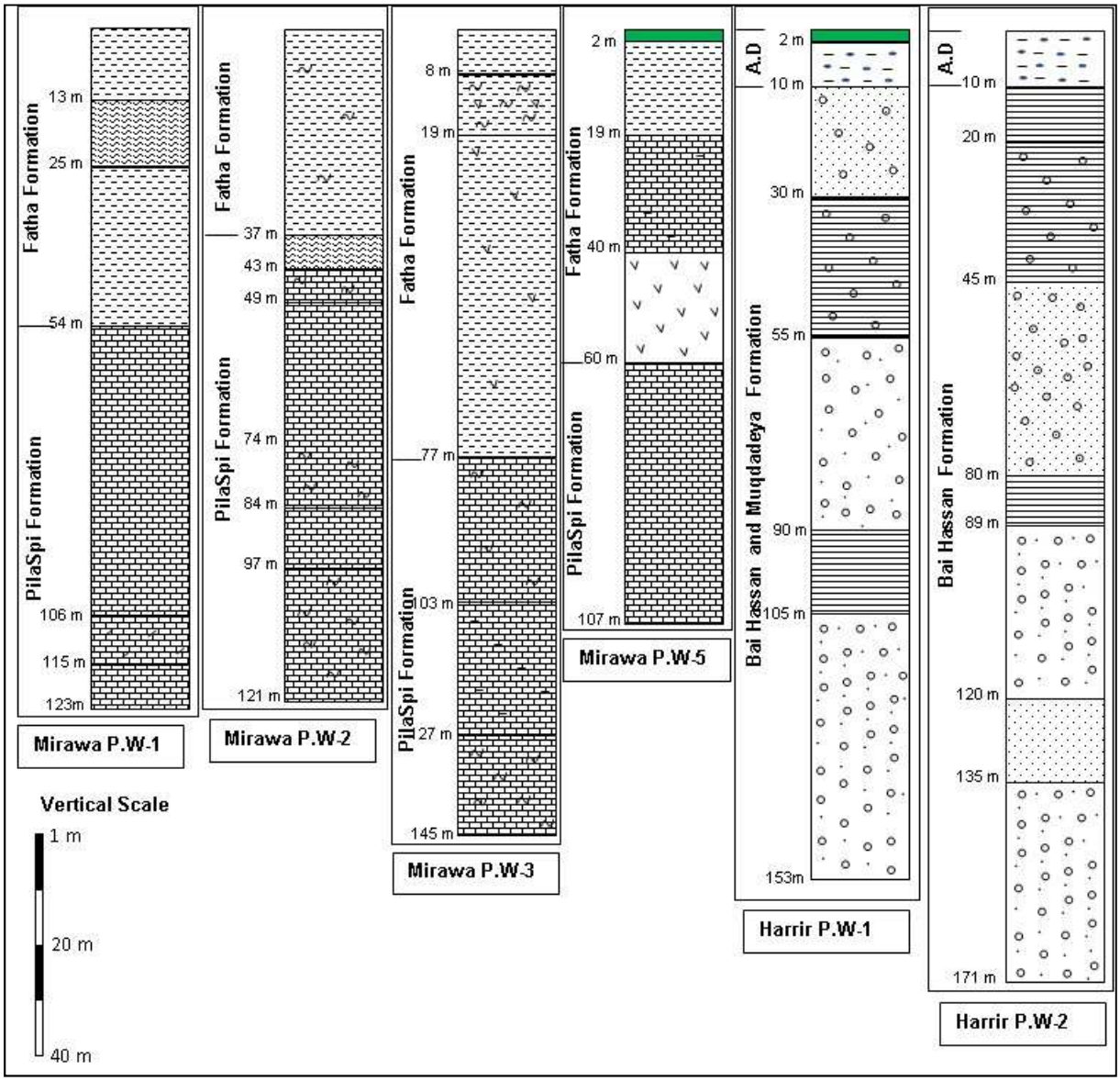

Fig. 3b: Lithological profile of the pumping wells in Harrir plain and Mirawa valley (Fn.: Formation, A.D: Alluvial Deposits, P.W: Pumping well)

2.9 Numerical Model

The finite-difference was designed with 100 x 100 m for each cell and 95 rows and 94 columns for Harrir plain and 90 rows and 84 columns for Mirawa valley.

2.9.1 Boundary conditions

Definition of proper boundary conditions is the most important step for constructing a groundwater model. Three types of boundary conditions (BC) were used for both models:

First: no flow BC

Second: River boundary conditions representing Greater Zab River, Harash River, and Mawaran River. The rivers setting are shown in Tab. 5.

The conductivity of the riverbed was assumed as 1.0E-6 m/s for Greater Zab and Harash Rivers, and 1.0E-5 m/s for Mawaran River; this riverbed conductivity was assumed to be valid for the entire river.

Third: at Harrir plain a first order (pressure head) boundary condition was set to 480 m in southeastern part, and for Mirawa valley set to 940 m in southeastern part of the model area.

Groundwater recharge for the uppermost shallow aquifer was defined as flow BC with 94.3 mm/year for the whole model area (Figs. 4 and 5).

Tab. 5: Rivers' boundary conditions for both model areas

Rivers	Model area	Water Table (m) a.s.l	River bed (m) a.s.l	River bed thickness (m)	Width of River (m)
Greater Zab	Start point in E part	350	345	4	10
	End point in W part	310	305	4	10
Harash	Start point in NW part	356	350	0.3	4
	End point in SE part	500	496	0.2	2
Mawaran	Start point in NW part	645.2	644.4	0.4	6
	End point in SE part	1060.5	1060	0.1	2

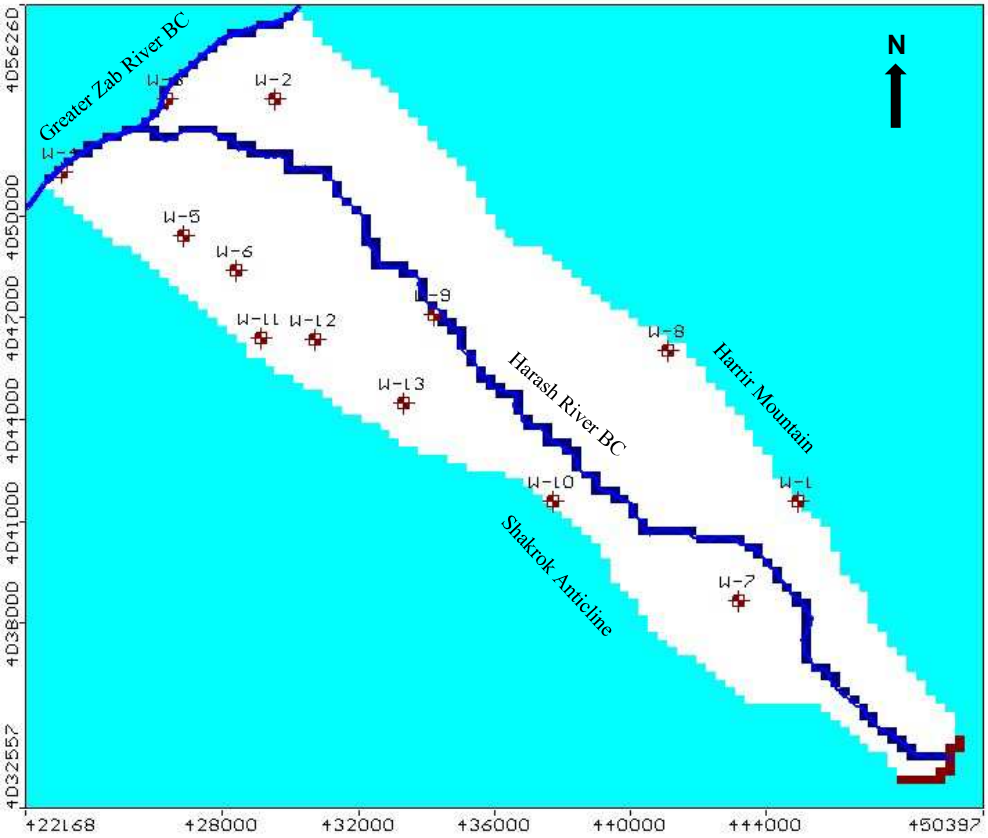

Fig. 4: Harrir plain area, observation wells (brown-white point) with boundary conditions; rivers BC (blue line), first order (pressure head) BC (red line), and no flow BC (light green area)

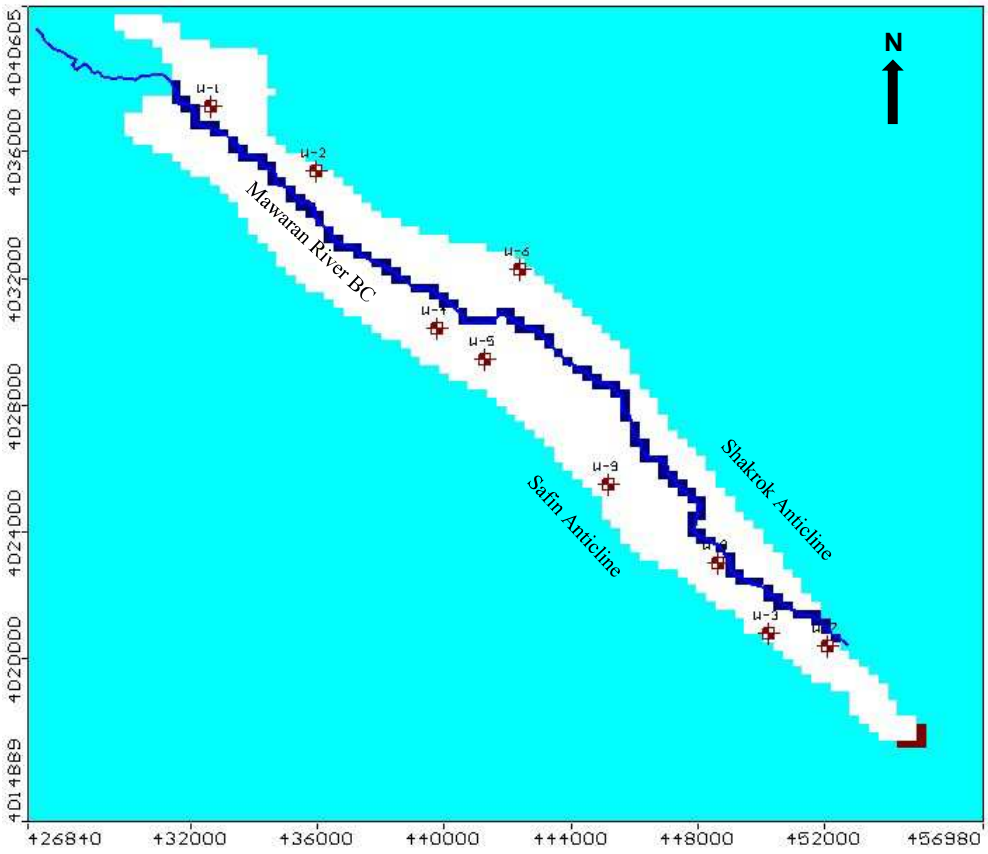

Fig. 5: Mirawa valley area, observation wells (brown-white point) with boundary conditions; rivers BC (blue line), first order (pressure head) BC (red line), and no flow BC (light green area)

2.9.2 Hydrodynamic characterization

Estimation of the hydraulic conductivity and specific storage of the unconfined aquifer system of Harrir plain and semi-confined aquifer system of Mirawa valley were obtained from the analysis of pumping tests that were carried out in the boreholes in Harrir plain and Mirawa valley. The Neuman and Theis methods were applied to obtain the values of hydraulic conductivity, coefficient storage, and the ratio of horizontal and vertical hydraulic conductivity. The measured hydraulic conductivity values (Kv) in Harrir plain range from $1.57*10^{-7}$ to $6.03*10^{-7}$ m/s (with an average of $3.5*10^{-6}$ for Kx,y and $3.5*10^{-7}$ for Kz), and for Mirawa valley ranges from $1.55*10^{-7}$ to $7.41*10^{-6}$ m/s (with an average value of $4.7*10^{-5}$ for Kx,y and $4.7*10^{-6}$ for Kz). The other parameters like total porosity, effective porosity, specific storage, and the specific yield were used as default parameters.

3 Results and discussion

3.1 Model calibration

The average groundwater head observations in thirteen observation wells in Harrir plain and nine observation wells in Mirawa valley were compared to the simulated groundwater heads.

The calibrations were performed manually by changing hydraulic conductivity with running the model several times using different hydraulic conductivities. The final hydraulic conductivity were used for calibration is $3.5*10^{-7}$ for Harrir plain model, and $4.7*10^{-6}$ for Mirawa valley model. Standard error for the model, normalized root mean square (NRMS), and correlation coefficient for both model was estimated (Tab. 6 and Fig. 6).

Table 6: Statistics of calibration under steady state flow condition for both modeled area

Parameters	Harrir Plain	Mirawa Valley
Standard error of the estimate (m)	1.06	2.24
Root mean square (m)	4.03	7.13
Normalized RMS (%)	2.6	2.46
Correlation coefficient	0.99	0.99
Maximum residual (m)	8.3 at Well no. 4	-12.26 at Well no. 9
Minimum Residual (m)	-0.004 at Well no. 5	-1.62 at Well no. 1
Residual mean (m)	1.68	-3.27
Abs. residual mean (m)	3.02	6.48

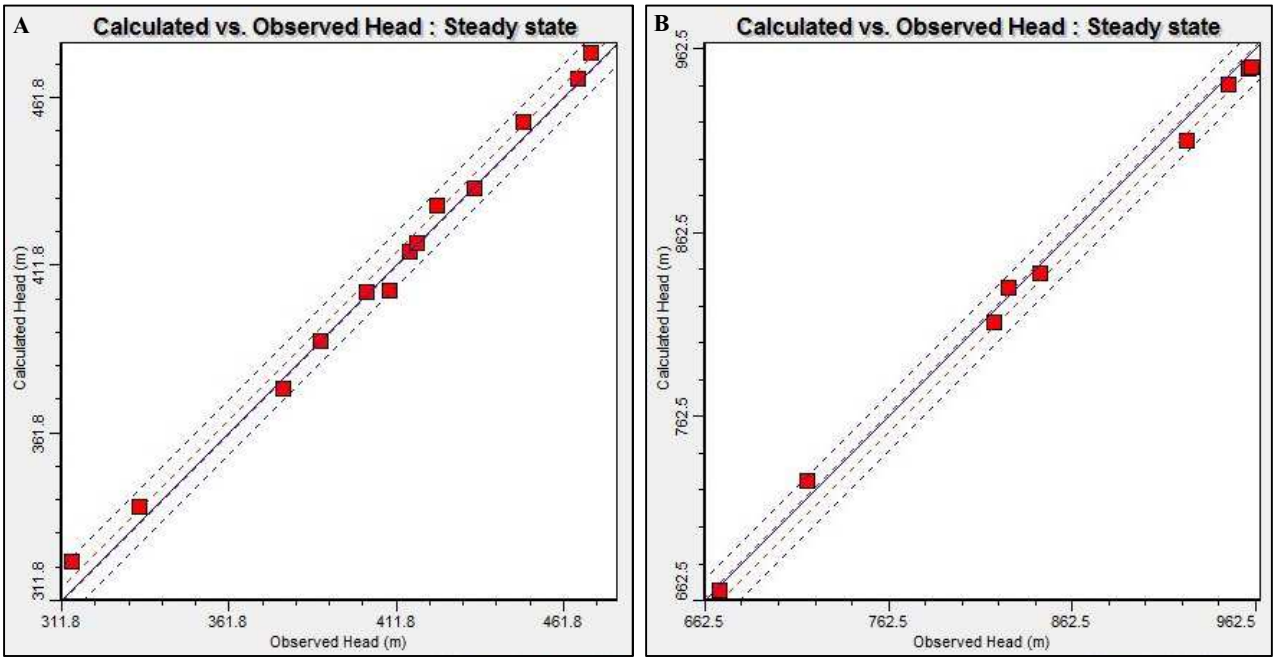

Fig. 6: Comparison of measured and simulated groundwater heads (m a.s.l) under steady-state calibration flow; A- for Harrir plain and B- for Mirawa valley.

3.2 Model results

Groundwater head simulation of Harrir plain shows that the equipotential head started from the highest level in the southeastern part at about 480 m a.s.l and decreasing to the center of the plain at about 60 m a.s.l and then decreases to the Greater Zab river direction in northwest to an elevation of 80 m a.s.l. According to the shape and patterns of groundwater potentials, an important source of the groundwater input to the aquifer is from Harrir Mountain in the southeastern and Shakrok anticline in the southwestern part of the plain (Fig. 7).

The contour lines clearly show that the Greater Zab River drains the shallow groundwater. In Mirawa valley, groundwater head starts from the southeastern part of the valley and decreases towards the northwest of the valley from 940 m to 640 m a.s.l. The most important groundwater input source to aquifer in Mirawa valley is Safin anticline and Pirmam Mountain in southwest, and Shakrok anticline in southeast (Fig. 8). On contrary to the Harrir plain aquifer for the Mirawa valley aquifer only a minor relationship between groundwater and the corresponding river can be seen, this could be either due to drainage system or because of groundwater pumping. The flow direction is from southeastern part to the Greater Zab River in northeastern part.

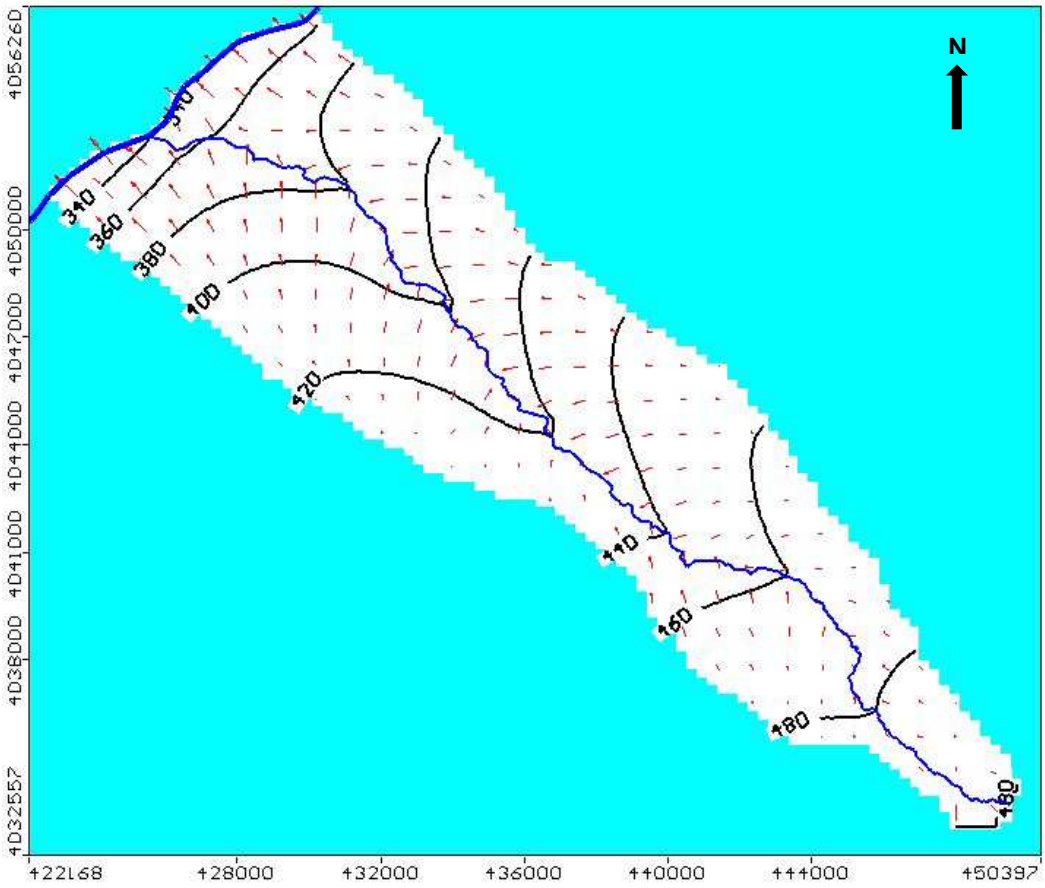

Fig. 7: Groundwater head equipotential (black line) and flow directions (red arrows) in Harrir plain, contour interval is 20 m, UTM WGS-84 coordination system.

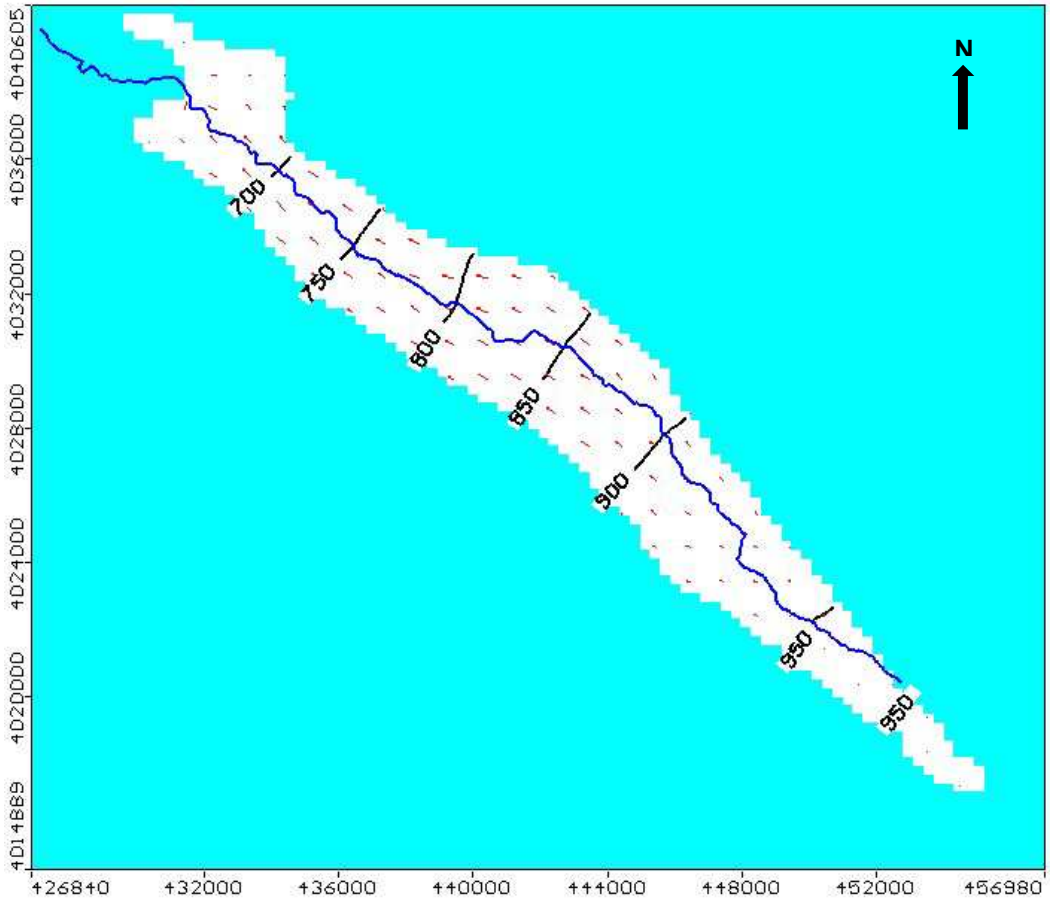

Fig. 8: Groundwater head equipotential (black line) and flow directions (red arrows) in Mirawa valley, contour interval is 40 m, UTM WGS-84 coordination system

3.3 Model prediction

The drawdown was calculated for the wells during increasing recharge rate from 94.3 mm/year to 200% and 400% for both modeled areas under steady state flow condition; which shows that the drawdown increases toward the rivers and decreases towards the mountain (Figs. 9a and 9b). The head of pumping well was calculated by increasing pumping rate in the pumping wells to 200% and 400% for both modeled areas, which shows that the head decreases by increasing the pumping rate (Tab. 7 and Fig. 10a and Fig. 10b).

The decreasing of well head by increasing pumping rate is higher in Harrir plain due to the shallower water table in porous aquifer and because the wells penetrates quaternary and tertiary deposits while the wells in Mirawa valley penetrates PilaSpi formation in karst-fractured aquifer.

4 Conclusions

The present study provides the first interpretation of the regional-scale hydrogeological modeling of regional groundwater flow in the Shaqlawa-Harrir basin, Kurdistan region under steady conditions. Both calibrated models succeed in producing groundwater head distribution in steady state and the model show good agreement between observed and calculated water levels.

Table 7: Head change in the pumping wells during increasing pumping rate to 200% and 400%

Pumping Wells	Discharge or Pumping rate (m^3/d)	Well head (m) a.s.l	Increasing pumping rate		Well head in m after increasing pumping rate	
			200%	400%	200%	400%
Harrir P.W-1	518.4	367.3	1036.8	2073.6	362.2	351.5
Harrir P.W-2	670	416.3	1340	2680	409.3	394.6
Harrir P.W-3	846.7	464.5	1693.4	3386.8	458.7	446.7
Mirawa P.W-1	345.6	669.7	691.2	1382.4	669.5	669.3
Mirawa P.W-2	648	725	1296	2592	724.7	724.1
Mirawa P.W-3	518.4	832.2	1036.8	2073.6	831.8	831.5
Mirawa P.W-4	950.4	946.7	1900.8	3801.6	945.6	943.5
Mirawa P.W-5	578.9	953.6	1157.8	2315.6	952.5	950.5

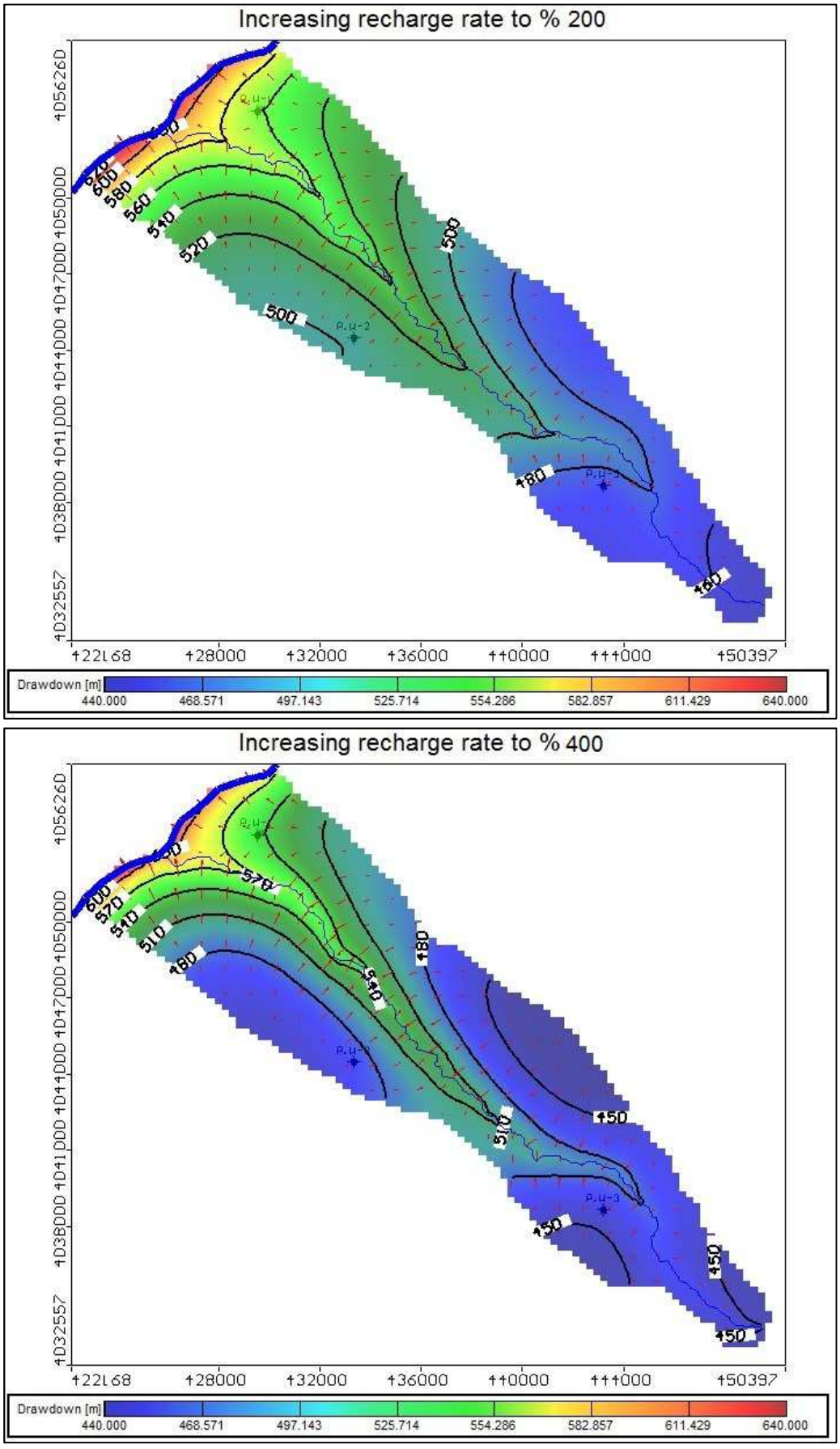

Fig. 10a: Drawdown differences by increasing recharge rate for Harrir plain, contour interval is 20 m for 200% increased recharge and 30 m for 400% increased recharge.

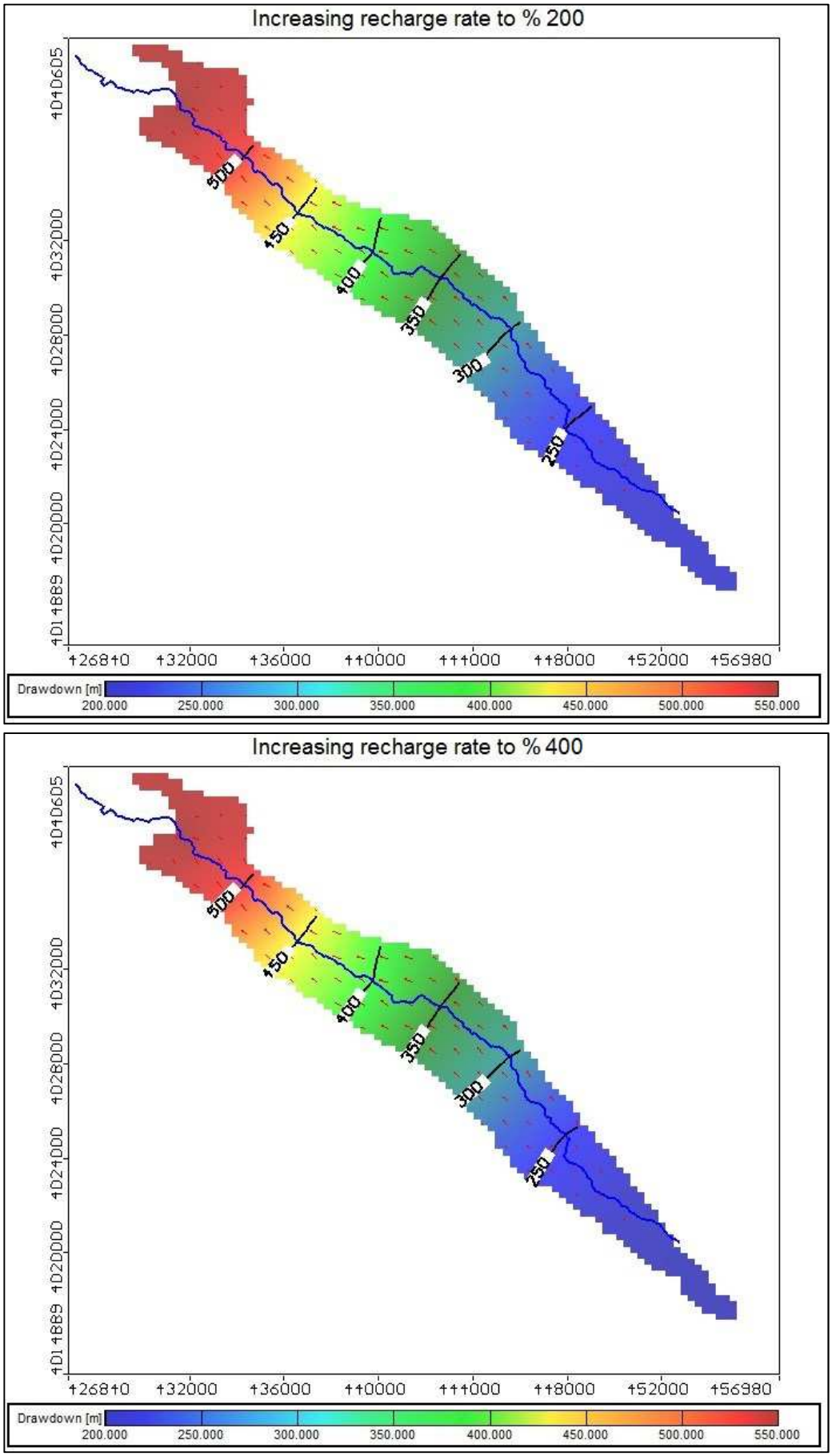

Fig. 10b: Drawdown differences by increasing recharge rate for Mirawa valley, contour interval is 50 m

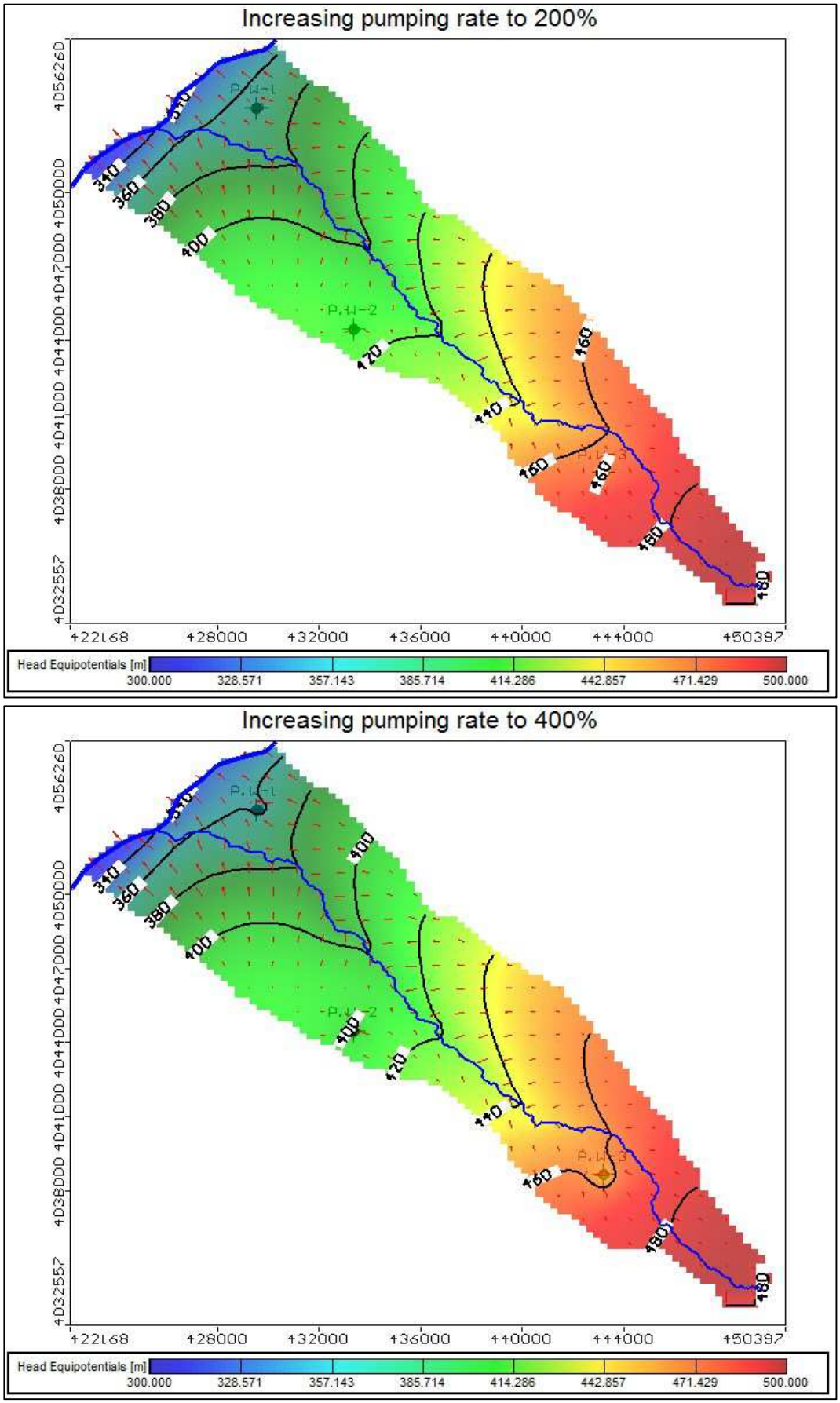

Fig. 11a: Head equipotential differences by increasing pumping rate in the pumping wells for Harrir plain, contour interval is 20 m

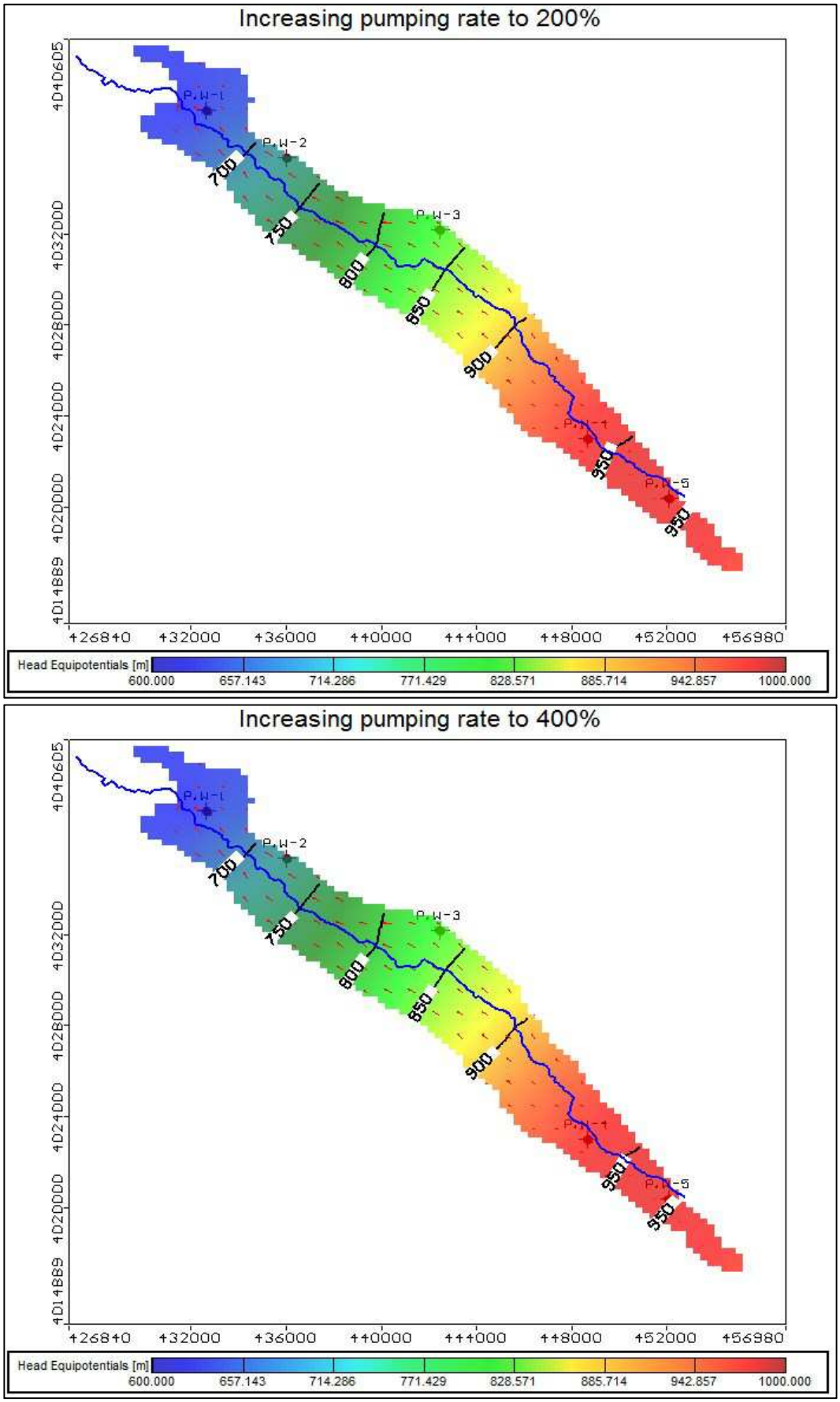

Fig. 11b: Head equipotential differences by increasing pumping rate in the pumping wells for Mirawa valley, contour interval is 50 m

5 References

Al-Sawaf FD (1977) Hydrogeology of South Sinjar Plain, Northwest Iraq. University of London.

Anderson M and Woessner W (1992) Applied groundwater modelling: Simulation of flow and advective transport. San Diego Academic Press.

Dellur JW (1999) The Hand Book of Ground Water Engineering, Purdue University, West Lafaytte, Indian.

Fetter CW (1994) Applied Hydrogeology, Prentice-Hall, Inc., A Simon & Schuster Company, Upper Saddle River, New Jersey.

Harbaugh AW and McDonald MG (1996) User's Documentation for MODFLOW-96, an update to the U.S. Geological Survey Modular Finite-Difference Ground-Water Flow Model.

Holzbecher E (1996) Modellierung dynamischer Prozesse in der Hydrologie. Grundwasser und ungesättigte Zone; eine Einführung; mit 21 Tabellen, Berlin.

Johnson EE (1955) Groundwater and wells. Inc. Saint Paul, Minn., 440 P.

Kruseman GP and de Ridder NA (1994) Analysis and evaluation of pumping test data, International Institute for Land Reclamation and Imporovement,Wageningen,Netherlands.

Kumar C (2013) Numerical modelling of ground water flow using MODFLOW. Indian Journal of Science, 2(4), pp: 86–92.

Mays LW (2005) Water Resource Engineering, John Wiley and Sons, New York, USA.

McDonald MG and Harbaugh AW (1988) A modular three-dimensional finitedifference ground-water flow mode. In Book 6, chap. A1. p. 586.

Peralta RC and Shulstad R (2004) Optimization modeling for groundwater and conjunctive use water policy development. In In Proceedings of FEM-MODFLOW International Conference. Presented by Peralta in Karlovy Vary, Czechoslovakia.

Schaaf SV (2004) Single Well Pumping and Recovery Test to Measure in Situ Acrotelm Transmissivity in Raised Bogs. Journal of Hydrology, 290, pp:152–160.

Seeyan S and Merkel B (2014) Determination of Recharge by Means of Isotopes and Water Chemistry in Shaqlawa-Harrir Basin, Kurdistan Region, Iraq. Hydrology Current Research, 5:179, pp: 1–18. doi: 10.4172/2157-7587.1000179

Seeyan S and Merkel B (2015) Groundwater Recharge Estimation for Shaqlaw-Harrir Basin in Kurdistan Region, Iraq. Journal of Environmental Hydrology, Vol. 23, (Paper 4).

Sohrabi N, Chitsazan M, Amiri V, Nezhad TM (2013) Evaluation of Groundwater Resources in Alluvial Iran. International Journal of Agriculture and Crop Sciences (IJACS), 5-11, pp: 1164–1170.

Todd DK (2005) Groundwater Hydrology. 3rd ed., John Wiley and Sons, New York, USA.

Yaouti F, Mandour A, Khattach D, Kaufmann O (2008) Modelling groundwater flow and advective contaminant transport in the Bou-Areg unconfined aquifer (NE Morocco). Journal of Hydro-environment Research, 2, pp: 192–209.

Comparison between the Two-source Trapezoid Model for Evapotranspiration (TTME) and the Surface Energy Balance Algorithm for Land (SEBAL) in Titas Upazila in Bangladesh

Kanoua, Wael

Institute of Geology, Technische Universität Bergakademie Freiberg, Gustav-Zeuner Str.12, 09599 Freiberg, Germany. Chemical and Petroleum Engineering Faculty, AL Baath University, Homs, Syria.

Email: Wael_kanoua@yahoo.com

Merkel, Broder

Institute of Geology, Technische Universität Bergakademie Freiberg, Gustav-Zeuner Str.12, 09599 Freiberg, Germany.

Email: merkel@geo.tu-freiberg.de

Abstract: Spatial and temporal variation of actual evapotranspiration (ET_a) is of vital importance for different applications, because it is considered a significant water loss from water systems. In this research paper, the Two-Source Trapezoid Model for Evapotranspiration (TTME) and the Surface Energy Balance Algorithm for Land (SEBAL) were used to estimate the spatiotemporal ET_a in the Titas upazila in Bangladesh. The Landsat Thematic Mapper (TM) and Enhanced Thematic Mapper plus (ETM+) satellite images and ground-based meteorological data were used for the calculations. Estimating monthly ET_a in both models was carried out using the evaporative fraction (Λ). Histogram analyses of ET_a, ET_a intercomparison and Class-A-Pan evaporation (E_{pan}) measurements with the normalized difference water index (NDWI) were used to check the performance of the TTME and SEBAL. The river showed the highest ET_a within each satellite image in SEBAL and TTME as it resamples evaporation from the free water surface. ET_a results of TTME and SEBAL over free water surface showed the same trend as the E_{pan}. For TTME results, correlation was significant at 95% confidence level and correlation coefficient $r > 0.836$ using Spearman and Pearson correlation tests on daily-daily, monthly-monthly, and long-term monthly mean-monthly basis. Correlation was also significant for SEBAL with $r > 0.69$ and 95% significance level, with one exception for Pearson test on monthly-monthly basis. Moreover, the daily and monthly results of TTME were used to calculate the daily, monthly, and long-term monthly pan coefficient (k_{pan}) which could be used to convert E_{pan} measurements to actual free water surface evaporation in the study area. The results indicate a promising applicability of TTME with satellite data in the study area.

Keywords: evapotranspiration; remote sensing; SEBAL; Bangladesh, Titas

1 Introduction

In Bangladesh, groundwater represents the main source of freshwater being used for domestic and industrial uses beside irrigation. Agriculture is the most and largest producing sector in Bangladesh. Despite having mightily rivers and heavy precipitation, Bangladesh relies on groundwater to a high extent, and around 4.95 million tube wells are in use (Uddin and Kurosawa 2014). Irrigation, for instance, takes place for half a year from shallow and deep wells (Shahid 2010). Therefore, this high and dense extent of groundwater abstraction might, as already expected, disturb the groundwater flow system and lead to irreversible negative qualitative and quantitative effects on the groundwater. ET_a is an important component of the global water cycle, which is considered the second largest flux term in the terrestrial hydrological cycle (Zhang et al. 2010; Yang and Shang 2013). On basin scale, ET_a is the most important output as it represents the largest water loss from the system under consideration (Long et al. 2014), and 60% of annual precipitation is estimated globally to returns back to the atmosphere through terrestrial evapotranspiration (Oki and Kanae 2006). Therefore, this component (ET_a) is not only a key parameter in determination of crop water requirements in various development stages, but also a vital factor in water resources management and in groundwater modeling. Moreover, ETa patterns can have a significant effect on recharge to groundwater, water table fluctuation, which in turn affects the flow system and contaminants transport (Johnson et al. 2003).Therefore, accurate estimation of ET_a in time and space is of vital importance for the fields of hydrology, hydrogeology, and climate change.

Different stuudies in Bangladesh were devoted to calculate reference evapotranspiration ET_r and potential evapotranspiration ET_p. Mojid et al. (2015) used the United Nations Food and Agriculture Organization (FAO) Penman–Monteith method and the daily weather parameters for a period of 21 years, and found a decreasing trend of ET_o in most of the months, and variability over the months of the year in the climatic parameters causing the observed trend. Masud et al. (2011) compared seven traditional methods of calculating ET_p in Bangladesh, and reported the applicability of the Blaney-Criddle method in such regions. These methods donnot deliver information about ET_a. However, they could be used in water balance to calculate ET_a as a residual, where ET_a is equal to ET_p for water surplus periods and equal to rainfall during the water deficit period. These simplifications, unfortunately, do not enable an accurate estimation of ET_a over areas covering hundreds and sometimes thousands of square kilometers. ET_a point measurements, on the other hand, are other alternatives. Hossen et al. (2012), for instance, used eddy covariance technique to study the surface energy partitioning and evapotranspiration in a double-rice cropping paddy field, and focused on both the rice-growing periods and the inter-cropping periods. They found that most of the radiant energy over irrigated and rain-fed double-cropping paddy field in Bangladesh during crop period and summer fallow period was converted to latent heat, and reported an annual ET_a of 997 mm. These ET_a point measurements, unless dense enough, do not capture the spatial variability in ET_a. Moreover, Bangladesh in general and the study area in particular are lacking such ET_a point measurements.

Remote sensing technology, in this regard, is an effective tool for monitoring spatial and temporal variation of ET_a, especially in areas where this variation is more pronounced. With the increasing imagery resolution, different models have been developed for ET_a esimation with the aid of ground data. These models differ in the way they treat the landscape, either as a mixture of soil and vegetation (one-source scheme) or independent sources of energy turbulent fluxes (two-source scheme) (Long and Singh 2012). Examples of these models are the Surface Energy Balance Algorithm for Land (SEBAL) (Bastiaanssen et al. 1998a; Bastiaanssen et al. 1998b), the Surface Energy Balance Index (SEBI) (Menenti and Choudhury 1993), the Simplified Surface Energy Balance Index (S-SEBI) (Roerink et al. 2000), the Surface Energy Balance System (SEBS) (Su 2002), the Mapping EvapoTranspiration at high Resolution with Internalized Calibration (METRIC) (Allen et al. 2007a; Allen et al. 2007b), the the Moderate Resolution Imaging Spectroradiometer model for terrestrial evapotranspiration MODIS-ET (Mu et al. 2011; Mu et al. 2007), the β approaches (Chehbouni et al. 1997), the Global Land surface Evaporation: the Amsterdam Methodology (GLEAM) (Miralles et al. 2011), the Simplified Two Sources Energy Balance (STSEB) (Sánchez et al. 2008), the Two Sources Energy Balance model (TSEB) (Norman et al. 1995), the ReSET-Raster model (Elhaddad and Garcia 2011), the Two-source Trapezoid Model for Evapotranspiration (TTME) (Long and Singh 2012), and the Hybrid Dual-source

Scheme and Trapezoid Framework-based Evapotranspiration model (HTEM) (Yang and Shang 2013). Remotely sensed gross primary production GPP is another simple approach which is used with ecosystem water use efficiency to invert ET_a (Yang et al. 2013).

Using satellite images with meteorological data, Shopan et al. (2013) calculated ET_a of Boro rice during the growing season using the SEBAL and the FAO recommended Penman-Monteith method for a northwest study area in Bangladesh. They used a time series of MODIS images and found that MODIS underestimates the ground based measurements with a mean absolute error of 0.67 mm/day. In comparison with Landsat (ETM+) it is found that Landsat overestimates ET_a. This study is the the only one conducted in Bangladesh using sattelite data for ET_a. Therefore, it is important to check the performance of a two-source model and compare it with a one-source model.

In this study, the SEBAL and TTME models are used to map spatial and temporal changes of ET_a in the Titas upazila using eight ETM+ and TM satellite images from different years to cover many months throughout the year. Moreover, meteorological ground data in the period 1998–20011 are used for this purpose. The results help in understanding the interannual and seasonal variability of ET in the study area. Section 2 presents an overview of the study area and the used data. The models formulations are presented in Section 3, followed by the results and discussion in Section 4. The conclusions follow in Section 8.

2 Data

2.1 Study area

Titas upazila is located in the eastern part of Bangladesh, south-east of the capital city Dhaka. It is under Comilla district, bounded by Homna Upazila on the north, Daudkandi Upazila on the south, Muradnagar Upazila on the east and Meghna Upazila on the west. Naturally, Titas bordered by Meghna River on the west, Gumti River on the south and east, and Titas River on the south. All of the study area belongs to the Meghna river Basin (Figure 1). The region of interest (ROI) has a humid climate with distinct dry season.

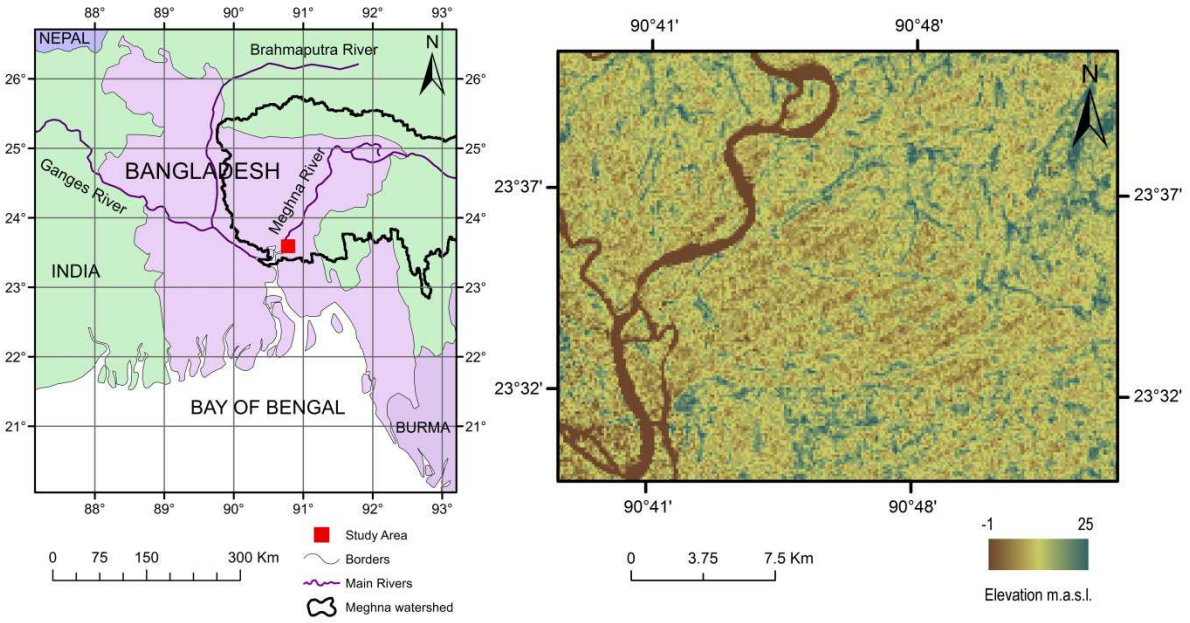

Fig. 1: Location map of the study area. Left: map of Bangladesh and its bordering countries, main rivers and Meghna river basin, Right: SRTM C-band CGIAR-CSI v4.1 digital elevation model DEM (90 m reso-

lution) covering the study area in Titas Upazila showing the elevation range in meter above sea level (m.a.s.l.) and the rivers. Maps datum: World Geodetic System 1984 (WGS 84)

The area is characterized by a flat topography with an elevation varying from 25 m.a.s.l. in the north-east to -1 m.a.s.l in the south-west. The area of interest is approximately 107 km^2 (Figure 1) with the geographic location 90^o 40′ E, 23^o 31′ N for its southwestern corner and 90^o 52′ E, 23^o 52′ N for its northeastern corner. The flat topography is modified to protect people and houses from flooding in the monsoon season. Agriculture is the main activity in the area and constitutes 42% of the occupations. The area is treble crop area, and paddy is the main crop, followed by jute, wheat, potato, mustard seed, and many other vegetables. Irrigation for agriculture in the area takes place in the dry months (Per and Post monsoon), which influences the hydrogeology of the area.

The study area has a subtropical monsoon climate characterized by wide seasonal variations in rainfall, high temperatures and humidity. There are three distinct seasons in Bangladesh: a hot, humid summer from March to June; a cool, rainy monsoon season from June to October; and a cool, dry winter from October to March. In general, maximum summer temperatures range between 27 °C and 29 °C. January is the coldest month, when the average temperature in the study area is about 17 °C. Heavy rainfall is characteristic of Bangladesh, with the exception of the relatively dry western region of Rajshahi. The area receives at least 2197 mm of rainfall per year. Around 87% of annual rainfall happens from May to October, and about 23% of the total annual rainfall occurs in the month of July About 80 percent of Bangladesh's rain falls during the monsoon season. The long-term monthly mean precipitation, temperature and E_{pan} in the study area are shown in Figure 2.

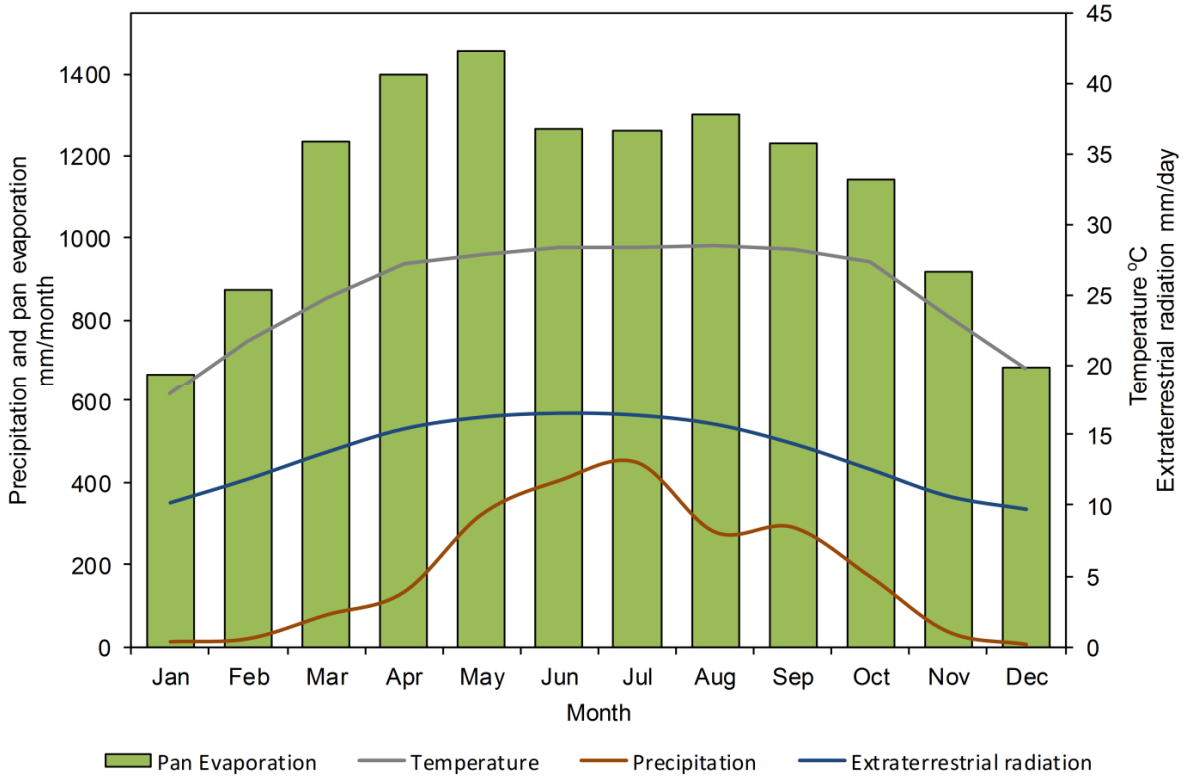

Fig. 2: Monthly distributions of long-term monthly mean E_{pan} mm/month, precipitation mm/month, temperature ^{o}C, and daily extraterrestrial solar radiation mm/day for the period 1998–2007.

2.2 Data preparation

For estimating the ET_a using the two algorithms, ETM+ and TM satellite images (Path 137 Rows 44) which cover different months of the year from different years are used. The basic features and the web source of the three satellite images used in this research are given in Table 1. The images were downloaded free of charge from the URL of the United State Geological Survey (USGS) Global Visualization Viewer (GLOVIS). Unfortunately, it was impossible to get all the satellite images for all months from the same year or at least from two consequent years. This is due to either the availability of dense cloud cover (CC) (100% in some months) or the presence of the small CC exclusively over the study area (Figure 3).

All the bands of the TM and ETM+ images were prepared for the processing steps by clipping them to the extent of the study area. Meteorological data were available on daily basis for the period (1998–2007), and juast Epan were available for longer period (1998-2011). Therefore, required data for processing satellite images aquired after 2007 were used as a long-term daily mean (for the same aquesition day) from the preceding years.

Tab. 1: List of the freely available satellite images used in this study with their acquisition date, spatial resolution, and the full name. GLOVIS: the USGS Global Visualization Viewer

Acquisition date (dd/mm/yyyy)	Image	Full name	Spatial resolution [m]	URL Source
11/01/2009	TM	Landsat Thematic Mapper	30	GLOVIS
15/02/2010	TM	Landsat Thematic Mapper	30	GLOVIS
24/03/2003	ETM+	Enhanced Thematic Mapper plus	30	GLOVIS
03/04/2001	ETM+	Enhanced Thematic Mapper plus	30	GLOVIS
02/05/2000	ETM+	Enhanced Thematic Mapper plus	30	GLOVIS
31/10/2002	TM	Enhanced Thematic Mapper plus	30	GLOVIS
11/11/2009	TM	Landsat Thematic Mapper	30	GLOVIS
05/12/2006	TM	Landsat Thematic Mapper	30	GLOVIS

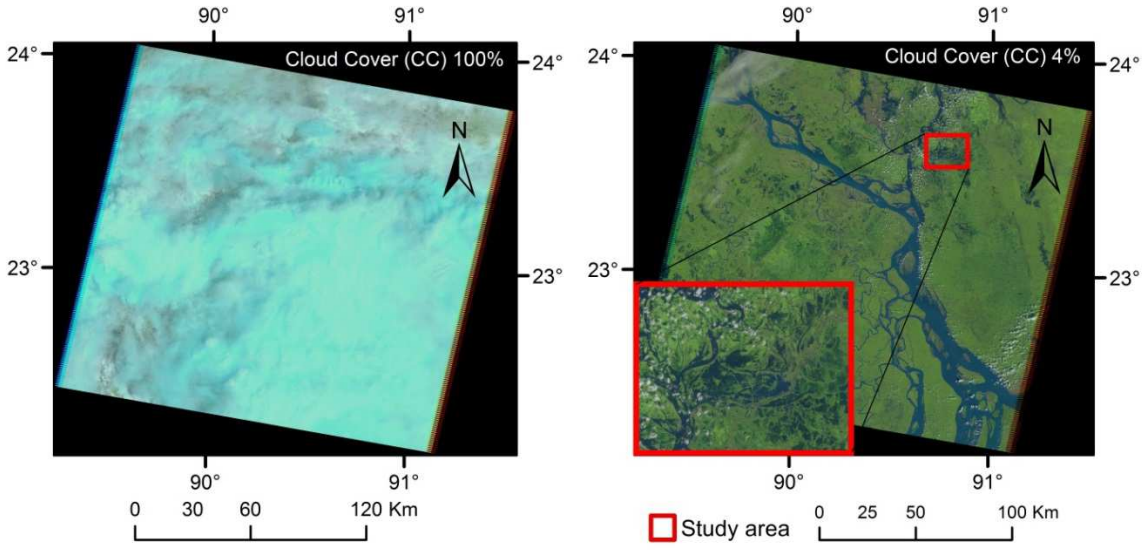

Fig. 3: TM satellite images of the study area showing different CC; left: CC = 100% for image acquired on 08.09.2009, right; CC = 4% for image acquired on 15.10.2005, and Clouds are shown as white dots.

3 Methodology

3.1 Surface Energy Balance Algorithm for Land (SEBAL)

As mentioned before, the study area is flat terrain and the assumptions of constant solar azimuth and solar elevation angles over the area of interest at the satellite overpass time in SEBAL are valid. Therefore, using "SEBAL Mountainous Model" is not required to correct for each pixel depending on the aspect and slope and variation in the incoming solar due to the effect of mountain shadow.

ET_r was estimated using CROPWAT 8 (United Nations Food and Agriculture Organization FAO, Water Resources, Development and Management Service, Rome, Italy) using the available meteorological data. The calculated monthly ET_r was used in SEBAL for the determination of the instantaneous ET_a at the "cold" pixels. The SEBAL model was described in detail by Bastiaanssen et al. (1998), Waters et al. (2002) and in many other following research papers. Briefly, SEBAL computes the latent heat flux (LE) from net surface radiation (R_n), soil heat flux (G_o) and sensible heat flux to the air (H) as following:

$$LE = R_n - (H + G_o) \quad (1)$$

The calculated LE is used to calculate the evaporative fraction (Λ), which is considered constant during daytime hours (Crago 1996; Bastiaanssen 2000; Brutsaert and Sugita 1992), as following:

$$\Lambda = \frac{LE}{R_n - G_o} \quad (2)$$

This (Λ) could be upscaled to one day or longer as following (Bastiaanssen et al. 2002):

$$ET_{24} = \frac{86400 \times 10^3}{\lambda \rho_w} \times \Lambda R_{n24} \text{ mm/day} \quad (3)$$

Satellite images are implemented in the calculations of Rn and G_o, which requires the surface albedo (α), the Normalized Difference Vegetation Index (NDVI), and surface temperature in (T_s °C). All these parameters are calculated from the different bands of the satellite images.

The H is estimated using the difference between aerodynamic surface temperature and the air temperature. SEBAL assumes a linear relationship between the T_s calculated at "hot" and "cold" pixels (extreme pixels) and the air temperature difference (dT). It is assumed that H is equal to zero for the cold pixel and for hot pixels equal to "$R_n - G_o$". The most difficult point here is determining the cold and hot pixels, which is considered the major limitation of the SEBAL model (Wang et al. 2014). Here, the selection of these pixels is done according to the following criteria:

- Cold Pixel Selection

The histogram of the surface temperature is first analysed to remove the outliers caused by artifacts in the image, e.g. clouds, snow cover, and scan line errors (low temperature). The first percentile of the surface temperature is selected. Because the selected pixel should be vegetation and not a settlement or water body, using NDVI will ensure that the selected pixel is vegetation. The pixel with the highest NDVI from the selected surface temperature pixel is designated as wet pixel.

- Hot Pixel Selection

The histogram of the surface temperature is first analysed to remove the outlier high temperature, and then the ninety fifth percentile of the surface temperature is selected. To select the high temperature pixels, NDVI and surface albedo indices are used. Low NDVI ensures the selection of non-vegetated pixel, while low surface albedo ensures that high reflecting surface (e.g. sand dunes, asphalt surface, metal surface, settlements) are not selected. Therefore, pixel with low NDVI and low surface albedo is selected as hot pixel.

3.2 Two-source Trapezoid Model for Evapotranspiration (TTME)

This model was developed by Long and Singh (2012) depending on the trapezoid framework (Figure 4) proposed by Moran et al. (1994) and the soil surface moisture availability isopleths proposed by Carlson (2007). The full formulation of the model is presented in details in (Long and Singh 2012). The main difference between TTME and SEBAL is that TTME enables calculating evaporation and transpiration separately. Moreover, TTME does not depend on the availability of wet and dry pixels throughout the image. However, it depends on determining in iterative manner the shape (upper and low boundaries) of the vegetation cover (f_c)–radiative surface temperature (T_{rad}) space, and the concept of soil surface moisture availability isopleths superimposed on the space (Long and Singh 2012). The theoretical upper boundary condition of TTME is determined by solving for temperatures of the driest bare surface ($T_{s,max}$) and the driest fully vegetated surface ($T_{c,max}$) both implicit in radiation budget and energy balance equations.

After finding the $T_{s,max}$ and $T_{c,max}$, the Λ for the soil and vegetation is calculated according to the following equations:

$$\Lambda_s = \frac{T_{s,max} - T_s}{T_{s,max} - T_a} \cdot \frac{Q_{s,o}}{Q_s} \tag{4}$$

$$\Lambda_c = \frac{T_{c,max} - T_c}{T_{c,max} - T_a} \cdot \frac{Q_{c,o}}{Q_c} \tag{5}$$

For a mixed surface (soil and vegetation), Λ is calculated as following:

$$\Lambda = (f_c)\frac{T_{c,max} - T_c}{T_{c,max} - T_a} \cdot \frac{Q_{c,o}}{Q} + (1 - f_c)\frac{T_{s,max} - T_s}{T_{s,max} - T_a} \cdot \frac{Q_{s,o}}{Q} \tag{6}$$

Where, Λ_s and Λ_c: soil and vegetation evaporative fraction, respectively, $T_{s,max}$ and $T_{c,max}$: temperatures of the driest bare surface and the driest fully vegetated surface, respectively, Q: available energy for each pixel (W m^{-2}), Q_s and Q_c: components (for soil and vegetation) of available energy (W m^{-2}), $Q_{s,0}$ and $Q_{c,0}$: net radiation (W m^{-2}) for the soil and vegetation, respectively, in which their respective temperature is approximated by air temperature (T_a) in outgoing longwave radiation, f_c: fractional vegetation cover which is calculated from the NDVI estimated from the bands of the satellite images.

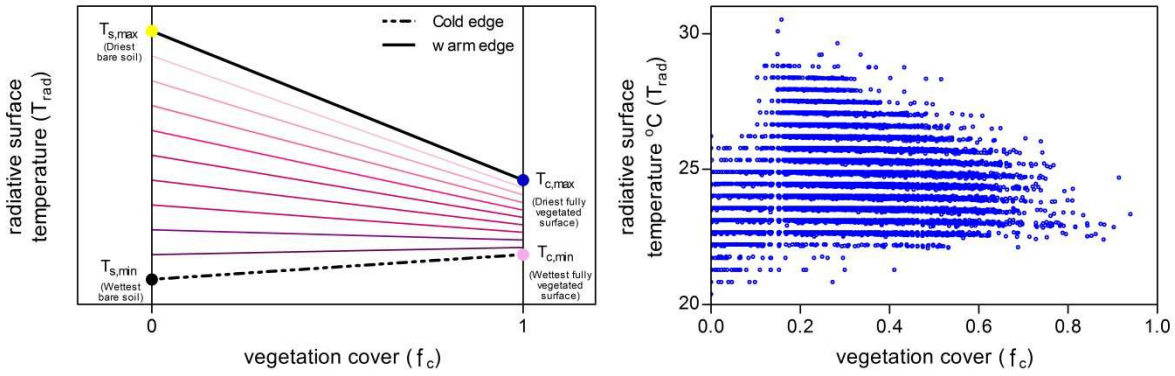

Fig. 4: Left: the f_c–T_{rad} trapezoid space principle in TTME. Colored dots on the four corners of the trapezoid represent the critical points, yellow dot: driest bare surface where f_c=0 and T_{rad}=$T_{s,max}$, black dot: wettest bare surface where f_c=0,T_{rad}=$T_{s,min}$, pink dot: wettest fully vegetated surface where f_c=1, T_{rad}=$T_{c,min}$, and blue dot: driest fully vegetated surface where f_c=1, T_{rad}=$T_{c,max}$. The two bold continuous and dashed lines represent the warm (largest water stress) and cold (without water stress) edges, respectively. Oblique straight lines between the two edges represent superimposed isopleths of soil moisture availability with increasing trend towards the cold edge. All the points on the same isopleth show the same soil surface and vegetation temperatures (T_s and T_c). Right: the f_c–T_{rad} density plot for the satellite image TM acquired on 05.12.2006.

4 Results and Discussion

As mentioned before, eight TM and ETM+ satellite images were used. The images do not belong to the same year due to the CC over the study area which is available almost all over the year and variably from year to year; therefore, it is impossible to find clean satellite images from the same year. The CC is almost 100% during the monsoon season especially from June to September (Figure 3), which means no images are available for processing for these four months. Using another satellite images as MODIS is not useful due to its coarse resolution (500 m) and the small extent of the study area.

Eight-monthly ET_a maps were prepared from the corresponding satellite images, following the procedures of SEBAL and TTME. The calculated Λ for each satellite image was upscaled to monthly ET_a. The resulting ET_a images consist of 334110 pixels (resolution 30 m × 30 m).

4.1 SEBAL and TTME Results

The SEBAL and TTME models present different approachs for estimating ET_a. However, they presented similar spatiotemporal veriation of ET_a as inferred from figures 5 and 6. Figure 5 and Figure 6 represent the monthly ET_a in Titas area calculated with SEBAL and TTME, respectively, within eight months, namely January, February, March, April, May, October, November, and December. All the images within each model are set to the same color scale for easier visual comparison. The higher scale is for May which is 0-805 mm and 0-896 mm for SEBAL and TTME, respectively.

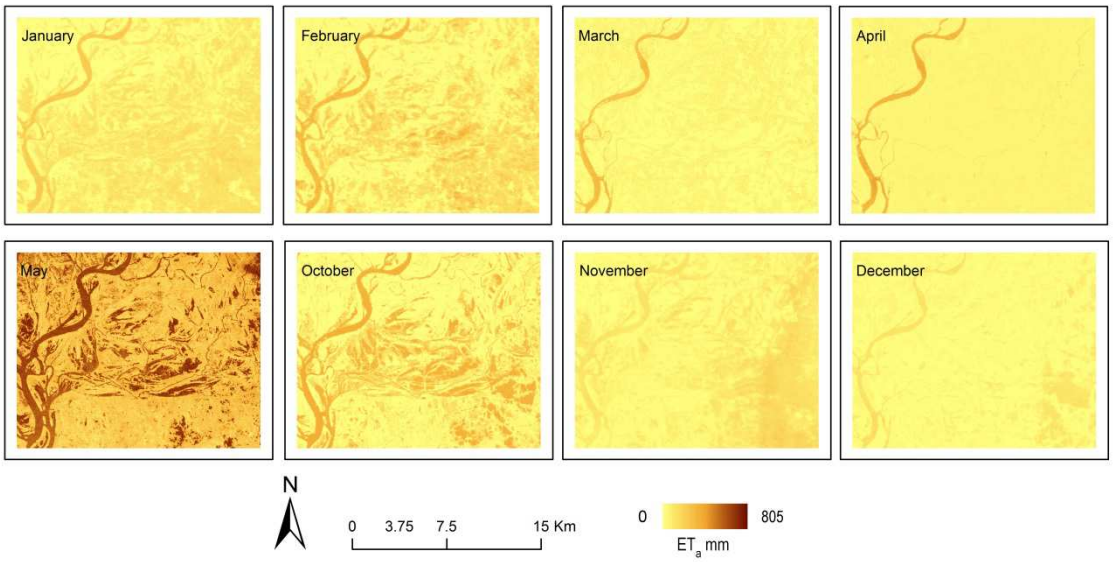

Fig. 5: Monthly ET_a in Titas area calculated with SEBAL within the corresponding months (January, February, March, April, May, October, November, and December) referred to on each map. All the maps are set to the same color scale

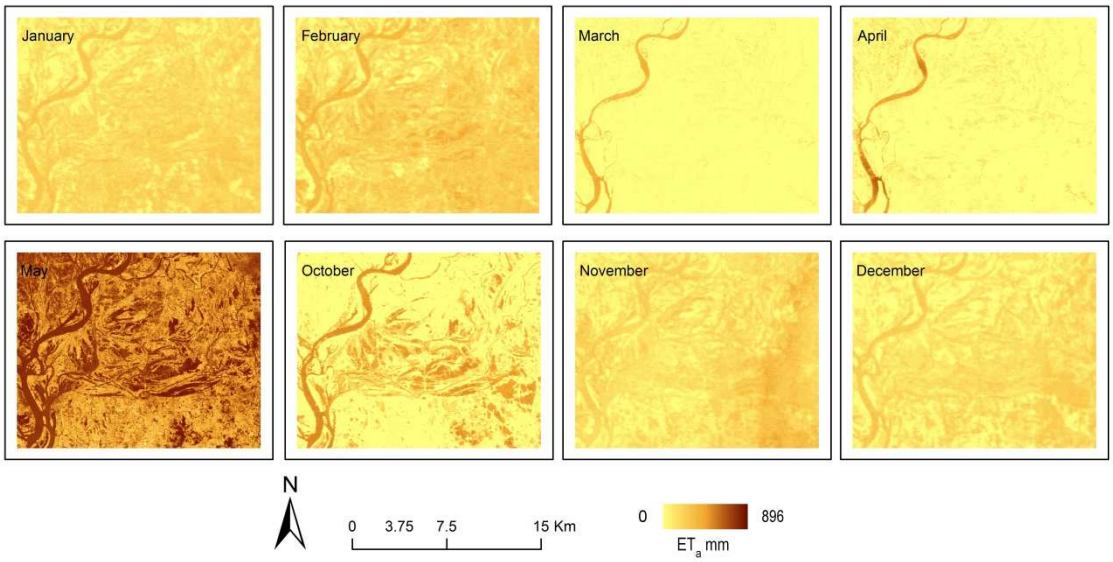

Fig. 6: Monthly ET_a in Titas area calculated with TTME within the corresponding months (January, February, March, April, May, October, November, and December) referred to on each map. All the maps are set to the same color scale

All the maps of the two models, SEBAL and TTME, clearly indicate the spatiotemporal patterns of ET_a for various land use classes that include agricultural crops, native vegetation, dry/barren land and water bodies including the river and streams. The channel of Meghna River is clearly seen in all the maps from January till December. This is logic as it represents the evaporation from a free water surface. Four months (June, July, August, and September) are missing from the calculations due to the aforementioned dense CC. May shows the highest ET_a as it marks the starting of the monsoon season when the temperature is high and heavy rainfall happens with the simultaneous stronger extraterrestrial solar radiation (Figure 2). In the following months, November, December, January, February, March and April; the spatial and temporal variability of ET_a is big due to the active and variable agriculture activities where rice and jute are the main crops, and the different growing stages of the crops.

From the statistical investigation of the different months (Table 2), it is clear that the minimum ET_a for all periods using SEBAL is zero, while it differs in case of TTME. Taking this point into account, TTME results seem more acceptable due to the fact that rainfall happens all over the year. Moreover, the study area represents a completely flat terrain (-1 – 25 m.a.s.l.), which means the magnitude of surface runoff is not so significant. In addition, there is no high infiltration capacity due to the availability of silt and clay, which means that ET_a should take place at least for some months when humidity allows. Therefore, no chance is available for rainfall to rapidly infiltrate or leave the area as surface runoff, and this, in turn, explains the existence of nonzero minimum ET_a (January, May, October, and December) in the case of TTME. Moreover, the range of standard deviation (SD) in the different months shows a high variability in ET_a within and between the months. SD approaches its summit in May for both SEBAL and TTME with 133.8 mm and 119.35 mm, respectively. This high SD reflects a large amount of spatial variation of ET_a in this month, which could be due to the high extent of heterogeneity in the area. In both models, SEBAL and TTME, the successively decreasing SD of ET_a from October to January then increasing from January to May corresponds to the rainfall trend (Figure 2), which represents the soil moisture trend as well. This could be explained by the fact that rainfall leads to an increase in the areas covered with settled water supported by the poorly drained soil and flat terrain, and the rest are the manmade elevated residence areas which show low values of ET_a, leading at the end to a high SD.

Tab. 2: Statistic results of the upscaled results of the SEBAL and TTME ET_a

Month	Count	Maximum (mm)	Minimum (mm)	Mean (mm)	Standard deviation SD (mm)	Sum (mm)
SEBAL						
January	334110	344.9	0	158.1	54.43	52824217
February	334110	447.9	0	173.4	64.8	57944797
March	334110	438.3	0	130.9	45	43736458
April	334110	531.6	0	125.6	56.3	41977134
May	334110	805	0	398	133.8	132975178
October	334110	441.9	0	187.6	57.11	62665974
November	334110	343.4	0	135.3	59.4	45214493
December	334110	265.7	0	100.7	38	33652964
TTME						
January	334110	412	15	202	70.31	67510887
February	334110	550	0	242.88	88	81148860
March	334110	724.27	0	137.84	91.2	46051968
April	334110	800	0	139.8	116.62	46708372
May	334110	896	2	642.1	119.35	214534512
October	334110	649.53	48.55	258.47	146.96	86355488
November	334110	550	0	193.63	87.3	64693200
December	334110	390	9	159.6	74.46	53322831

In Fig. 7 and Fig. 8, the histograms of the spatial patterns of monthly upscaled ET_a generated by each model, show the frequency distribution of values within the modeling domain. There are noteworthy differences between the models, both in terms of magnitude and spatial distribution/pattern. For May, the frequency distribution of SEBAL ET_a shows a bimodal separation of ET_a patterns, which represent evaporation from two different high evaporative surfaces. The pike with lower frequency resamples the evaporation from free water surfaces, and pike with the higher frequency represents the mixed (vegetation cover and settled water). The same month for TTME ET_a also shows a bimodal distribution with the two pikes closer to each other than the case of SEBAL, and with higher frequency for both pikes. Distribution difference is more pronounced between the two models for February and October. The distribution ET_a peaks at different magnitudes and spread over different ranges. This difference in behavior could b due to the fact that SEBAL assumes a full or nearly full range in hydrologic conditions (e.g., H = 0 to H = R_n - G_o) existed within the study area/scene (Choi et al. 2009). This forces an interpolation of H values over this entire range. The TTME scheme, however, does not make any assumption about hydrologic endpoints.

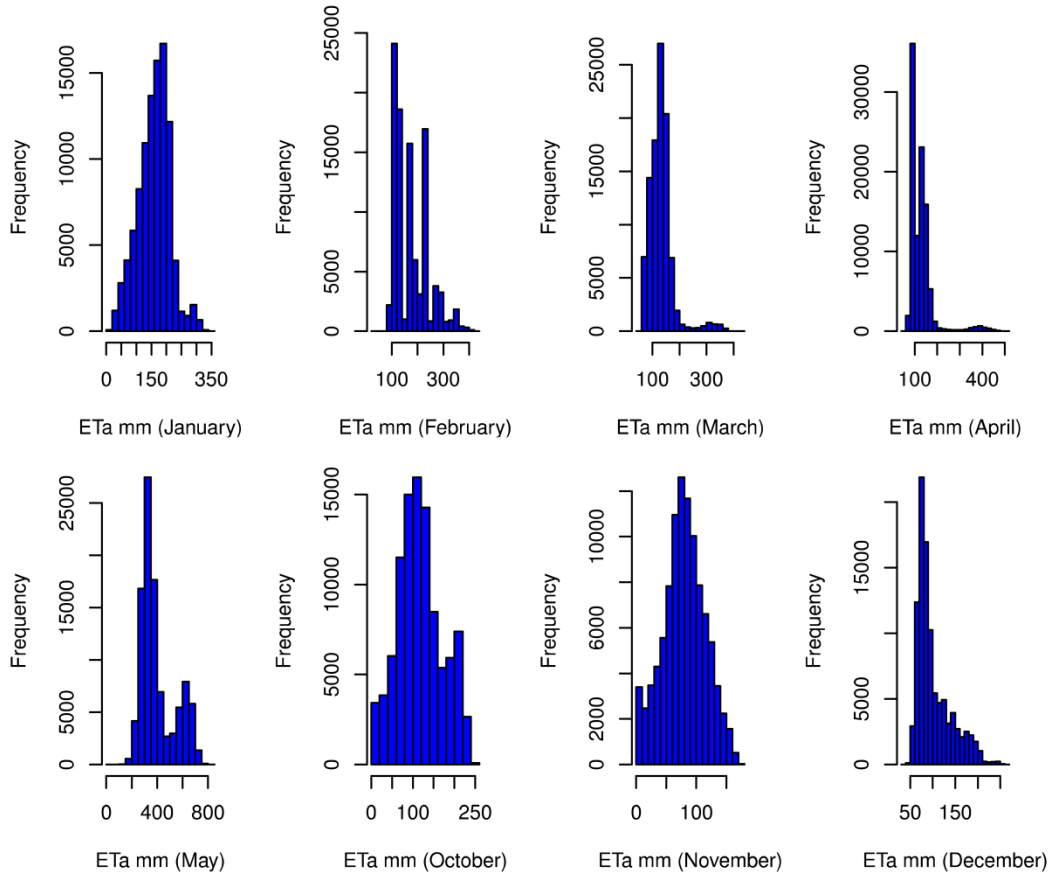

Fig. 7: Frequency distribution of monthly ET_a (mm) from SEBAL using the Landsat TM/ETM+ satellite images on months January, February, March, April, may, June, October, November, and December

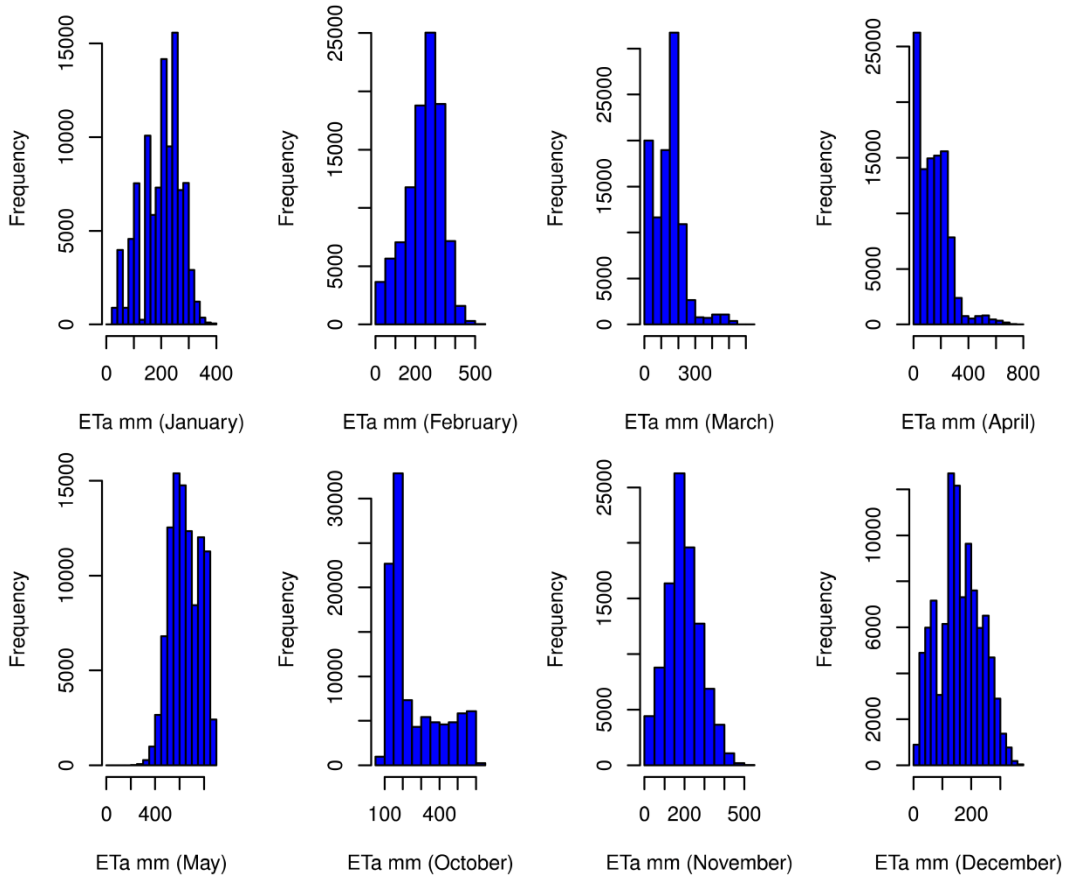

Fig. 8: Frequency distribution of monthly ET_a (mm) from TTME using the Landsat TM/ETM+ satellite images on months January, February, March, April, may, June, October, November, and December.

Figure 9 presents the inert comparison between the monthly ET_a values obtained by SEBAL and TTME algorithms. It is possible to observe the correlation behavior between the ET_a estimated by SEBAL and TTME to different satellite images. In general, the correlations between them present values greater than 0.84, evidencing a stronger agreement between these two algorithms. It is possible, however, to identify that TTME delivers ET_a values higher than SEBAL ET_a as almost all the points are locating above the line of ratio 1:1. It is difficult to judge whether SEBAL is underestimating or TTME is overestimating the ET_a. SEBAL, however, is reported in different studies to underestimate the LE and accordingly the ET_a (French et al. 2005a; French et al. 2005b; Timmermans et al. 2007). This behavior of minimum ET_a by SEBAL might be the result of the accuracy of selecting the extreme pixels (wet and cold pixels) in this algorithm, which is regarded as one of the main drawbacks in SEBAL algorithm (Li et al. 2009). Investigating the difference between SEBAL and TTME ET_a showed the sum of absolute difference and the Mean Absolute Difference (MAD) are less than 78.5 and 0.000235 mm/month, respectively, for January, February, March, April, October, November, and December. May is an exception with the sum of absolute difference and the MAD are 243.8 and 0.00073 mm/month, respectively. The high values in May could be the result of ET_a upscaling, as the applicability of temporal extension of TTME daily results to monthly has not been proved yet (Long and Singh 2012). Moreover, May marks the beginning of monsoon season and the area receives heavy rainfall during this season and gets flooded; therefore, the scene is primarily comprised of flooded fields and ponds alongside with vegetated rain fed crops with no obvious minimum and maximum surface temperature endpoints.

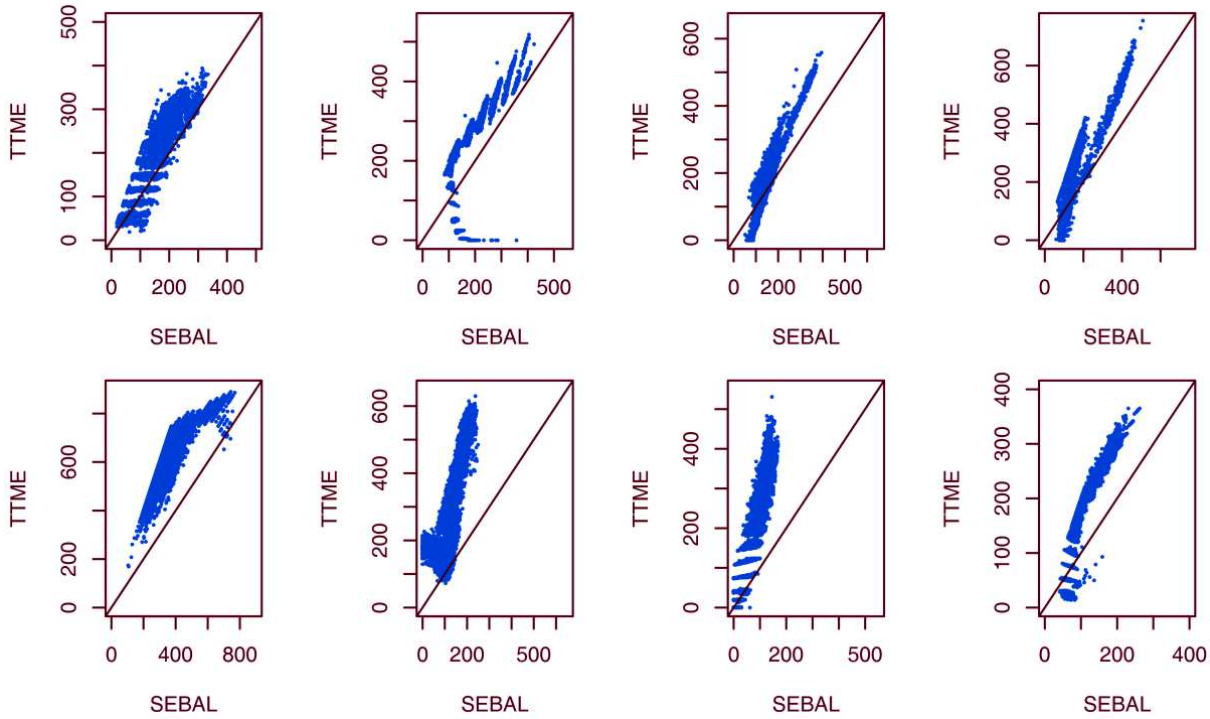

Fig. 9: Correlation between the monthly ET_a (mm/month) values to January, February, March, April, May, October, November, and December obtained by SEBAL and TTME algorithms. Black continuous line represents the ratio 1:1.

4.2 Class-A-Pan evaporation

Measurements of E_{pan} are used for comparison with the calculated ET_a from SEBAL and TTME. By definition, E_{pan} is the amount of water lost by evaporation from standard set leveled on the ground in a grassy location not close to obstacles (Eagleman 1967). E_{pan} is estimated not to be equal to evaporation from natural free water surfaces, even if the pan and the free water surface are under the same conditions. E_{pan} normally exceeds the evaporation from the water body (Kanoua and Merkel 2014; McMahon et al. 2013; Tanny et al. 2008). This difference cold be explained by the different thermal conditions of reservoir water and pan water. While the water reservoir has significant energy storage capacity and can gain or lose energy, pan cannot store energy. Moreover, pan enhances advective heat fluxes through its sides and bottom. Therefore, estimating of free water surface evaporation (E) is often obtained by multiplying E_{pan} by k_{pan} (Martínez et al. 2006; Fekih et al. 2013; Ertek et al. 2006):

$$E = K_{pan} \times E_{pan} \quad (7)$$

The comparison was done here between the trend of E_{pan} and the trend of ET_a from SEBAL and TTME over water areas recognized on the satellite images. E_{pan} measurements were available on daily basis for the study area. The comparison was done on daily, monthly, and long-term monthly mean basis, but just monthly-monthly comparison is presented her graphically (Figure 10). For monthly and long-term monthly mean comparison, daily E_{pan} measurements were accumulated to get the monthly E_{pan} and thereafter the long-term monthly means were estimated. To get SEBAL and TTME ET_a over free water surface, ET_a over the river and the parcels of free surface water in each month. These parcels of free surface water were delineated by applying the NDWI which enables delineating open water features and enhance their presence in remotely-sensed digital imagery (McFEETERS 1996; Gao 1996). The NDWI was calculated for each satellite image and water areas were delineated and the values of ET_a over the river and these areas were averaged for each image. The averaged ET_a value is considered unique and representative to the whole area during the corresponding month, because the area is small scale and entirly flat.

Figure 10 shows the monthly-monthly comparison between monthly E_{pan} and the monthly SEBAL and TTME ET_a for the free water surface. Evaporation from free water surface for SEBAL and TTME are in all months with no exception less than the E_{pan}. It is clear that TTME results follow almost the trend of E_{pan}, with the maximum value in May (776 mm/month) and ET_a increases from January till May (maximum ET_a), then decreases from October on. The minimum ET_a (332 mm/month) is reached in December. On the other hand, SEBAL results shows the same trend with an increase in ETa from January till its maximum value (697.8 mm/month) in May then decreases from October on, and also reaches its minimum value (226.5) in December. One exception in SEBAL is in March, when ETa shows a slight decrease (399.5 mm/month) in comparison with February (425.5 mm/month). This sudden decrease in monthly ET_a in March in comparison with February is not normal, taking into consideration the meteorological data which shows steady increase in temperature and rainfall from January till May (Figure 2). The reason might be that the procedures used in this research failed to capture the right edge (hot and cold) pixels in some months. This problem is also encountered when working in some areas, e.g, England no dry area, Sahara no wet pixels (Courault et al. 2003).

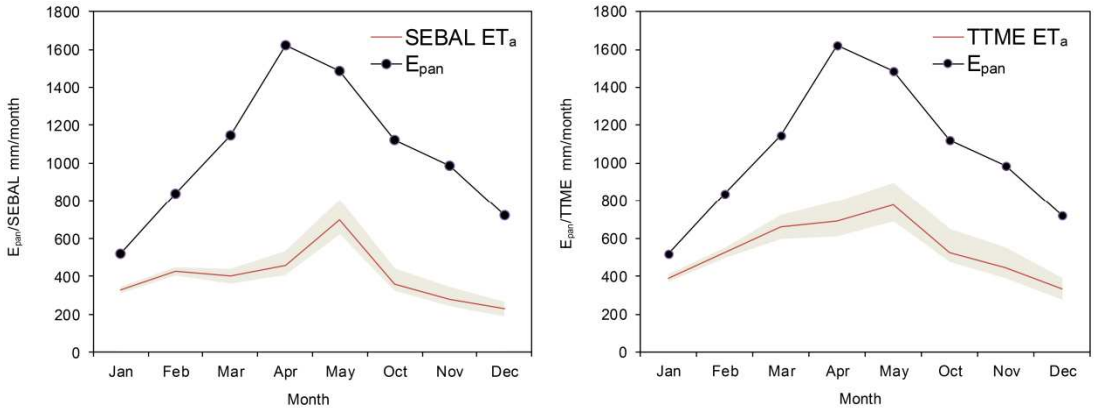

Fig. 10: Comparison between monthly E_{pan} and monthly ET_a calculated with the two models SEBAL (left) and TTME (right) for the eight months (January, February, March, April, May, October, November, December) in Titas area. Backgrounds indicate max-min in each in the series

The results from regression analyses between the three datasets (E_{pan}, SEBAL, and TTME) are shown in Figure 11. Regression analyses is carried out here on daily-daily, monthly-monthly, and long-term monthly mean-monthly basis for eight months (January, February, March, April, May, October, November, and December). In general, there is a reasonable fit between E_{pan} and TTME and SEBAL ET_a for daily-daily, monthly-monthly, and long-term monthly mean-monthly correlations. Correlation tests are also conducted to estimate the strength of the relationship between the E_{pan} from one side and ET_a of SEBAL and TTME from another side. Due to the small number of points in the datasets, it is better to check the correlation using Spearman and Pearson tests, because in such cases the difference between Spearman and Pearson can be dramatic. Using Spearman test, there is a positive correlation between daily TTME and daily E_{pan} (correlation coefficient, $r = 0.898$; sample size, $n = 8$; significance level, $p < 0.05$) and the correlation is also significant in the case of daily SEBAL and daily E_{pan} ($r = 0.743$, $n = 8$, $p < 0.05$). Pearson test also showed the same results of significant correlation ($r = 0.848$, $n = 8$, $p < 0.05$) between daily TTME and daily E_{pan} and significant correlation ($r = 0.746$, $n = 8$, $p > 0.05$) between daily SEBAL and daily E_{pan}. The results of all correlation tests are summarized in Table 3. Correlation tests between the results of SEBAL and TTME and E_{pan} are significant in almost all cases at 95% significance level. One exception is the correlation between SEBAL ET_a and E_{pan} on monthly-monthly basis using Pearson test. Despite the difference in correlation coefficients between the Spearman and Pearson tests, both tests give credit to the TTME in comparison to SEBAL results. The difference in the correlation coefficient between the two correlation tests is due to the fact that each test benchmarks a different relationship; Pearson benchmarks linear relationship, while Spearman benchmarks monotonic relationship.

Tab. 3 Results of Spearman and Pearson correlation tests (two–tailed) between E_{pan} data and ET_a of SEBAL and TTME models on daily-daily, monthly-monthly, and long-term monthly mean-monthly basis

Correlation Basis	Datasets	Correlation Method	correlation coefficient (r)	P–value (significance level)
[Daily]-[Daily]	[E_{pan}]-[TTME]	Spearman	0.898	< 0.05
		Pearson	0.848	< 0.05
	[E_{pan}]-[SEBAL]	Spearman	0.743	< 0.05
		Pearson	0.746	< 0.05
[Monthly]-[Monthly]	[E_{pan}]-[TTME]	Spearman	0.88	< 0.05
		Pearson	0.836	< 0.05
	[E_{pan}]-[SEBAL]	Spearman	0.738	< 0.05
		Pearson	0.69	> 0.05
[Long-term monthly mean]-[Monthly]	[E_{pan}]-[TTME]	Spearman	0.905	< 0.05
		Pearson	0.926	< 0.05
	[E_{pan}]-[SEBAL]	Spearman	0.762	< 0.05
		Pearson	0.777	<0.05

As mentioned before, E_{pan} is frequently converted to free water surface evaporation by multiplying E_{pan} by K_{pan}. Different conversion coefficients between E_{pan} and natural water surface evaporation can be found in literature; however, these conversion coefficients are not just site specific, but also pan type (Class-A evaporation pan, ISI evaporation pan, Colorado Sunken evaporation pan, and USGS Floating evaporation pan) specific (Rahman et al. 2014; Fekih and Saighi 2012). Therefore, caution should be taken when using K_{pan} estimated for special area to use in another area. Assuming the accuracy of TTME results of this study, at least over water bodies, K_{pan} can be calculated hereby using equation 7 for each month in the study area. Table 4 represents the K_{pan} based on TTME ET_a results on daily-daily, monthly-monthly, and long-term monthly mean-monthly basis.

The mean K_{pan} is 0.51 ± 0.11, 0.48 ± 0.12, and 0.47 ± 0.06 for daily, monthly, and long-term monthly mean estimations, respectively. The minimum K_{pan} is in December for the three cases. The maximum K_{pan} is in March for daily and long-term monthly mean basis, and in January for monthly one. It is clear from the results of daily and monthly K_{pan} that there is an inverse relationship between E_{pan} and K_{pan} (Figure 12). This inverse relationship was reported different studies (Linacre 2002; Sumner and Jacobs 2005). Taking K_{pan} as constant vale for the whole year is not an accurate approach; however, its value is variable and a variety of environmental variables are considered as explanatory factors for K_{pan} variation. Linacre (2002) noted that K_{pan} generally decreases with increasing E_{pan} as a result of disproportionally enhanced radiative and convective transfer of energy from the surrounding areas to the pan during periods of high E_{pan}.

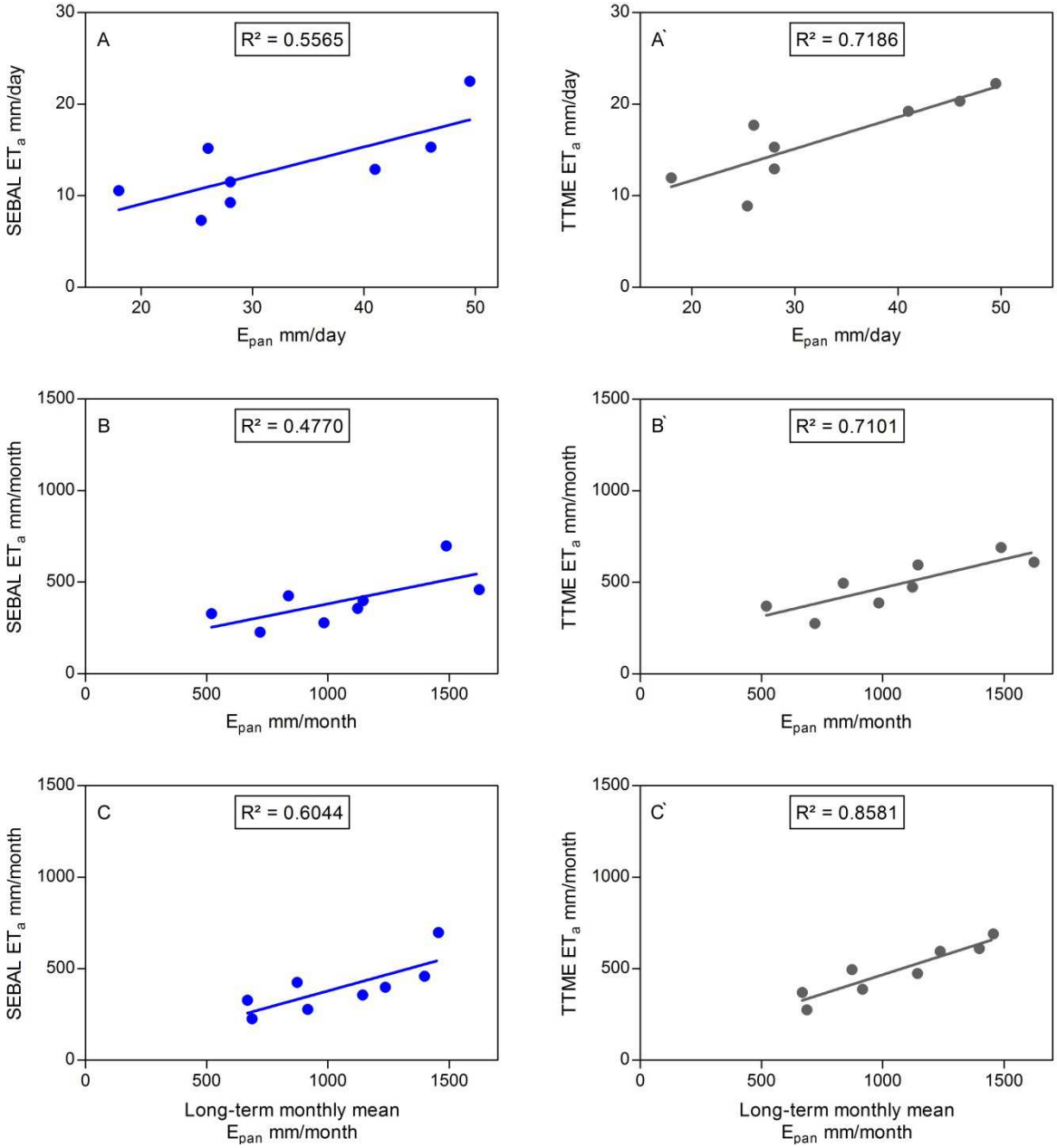

Fig. 11: Regression analyses between E_{pan} and ET_a of the two models SEBAL (blue) and TTME (grey) for eight months (January, February, March, April, may, October, November, and December) on daily - daily(A, A`), monthly-monthly (B, B`), and long-term monthly mean-monthly (C, C`) basis in Titas area

Tab. 4: TTME ET_a, E_{pan} and the calculated K_{pan} on daily-daily, monthly-monthly, and long-term monthly mean-monthly basis.

		Jan	Feb	Mar	Apr	May	Oct	Nov	Dec
TTME ET_a	Daily (mm/day)	11.96	17.7	19.2	20.3	22.3	15.31	12.95	8.9
	Monthly (mm/month)	370.8	495.9	596	610	690	474.5	388.5	275.5
E_{pan}	Daily (mm/day)	18	26	41	46	49.5	28	28	25.4
	Monthly (mm/month)	520	837	1144.8	1624	1488	1122	984	720.6
	long-term monthly mean (mm/month)	668	873	1237	1398	1456	1143	916	687
K_{pan}	Daily-Daily	0.66	0.68	0.47	0.44	0.45	0.55	0.46	0.35
	Monthly-Monthly (mm/month)	0.71	0.59	0.52	0.38	0.46	0.42	0.4	0.38
	long-term monthly mean-monthly (mm/month)	0.56	0.57	0.48	0.44	0.47	0.42	0.42	0.40

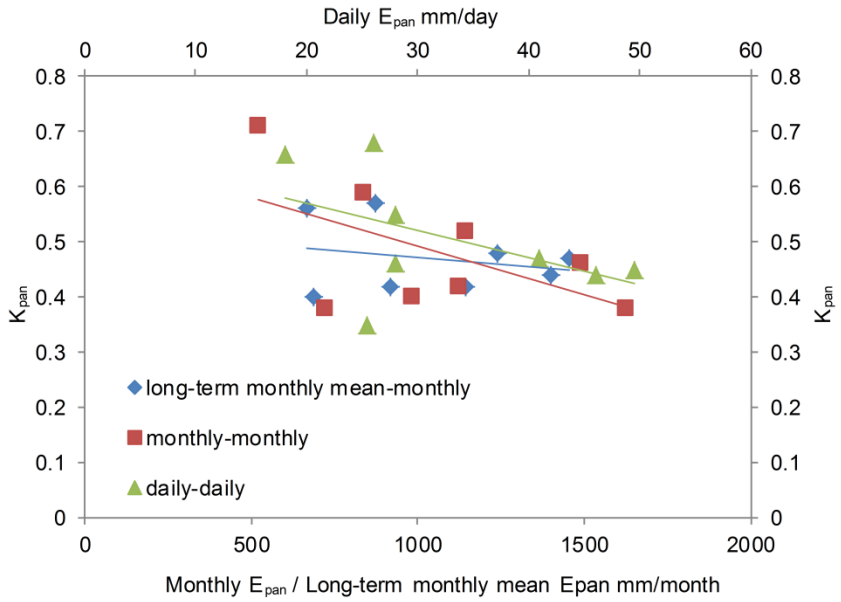

Fig. 12: Linear regression between E_{pan} and K_{pan} on daily-daily, monthly-monthly and long-term monthly mean-monthly basis. Continous stratight lines represent the tred within each dataset.

5 Conclusions

This study compared the performance of the Surface Energy Balance Algorithm for Land (SEBAL) and the Two-Source Trapezoid Model for Evapotranspiration (TTME) for the study area in Titas in Bangladesh. The inputs of these models were eight TM/ETM+ satellite images with E_{pan} and meteorological data. The two models were compared from different aspects, and the results were compared with E_{pan} measurements on different basis (daily, monthly, and long-term monthly mean).

SEBAL and TTME produced the spatial and temporal variation of ET_a in Titas area. Both models resulted in the highest ET_a in May when precipitation increases dramatically in comparison with the previous months. Satellite images are not available for June, July, August, and September due to the CC; ET_a in these months, however, could be considered not far from its magnitude in May, and this decision depends on the fact that temperature stays almost constant 28.3 ± 0.23 ^{o}C during these months, intensive precipitation 348.8 ± 74 mm/month and almost constant extraterrestrial radiation 15.8 ± 0.8 mm/day.

SEBAL depends on the existence of hot and cold pixels in each satellite image. These pixels may not be identified correctly for some scenes by using NDVI, albedo, and surface temperature for each image. Accordingly, this is considered the main drawback of SEBAL.

TTME could deliver better results at least over the free water surface. Correlation between E_{pan} measurements and TTME ET_a was significant at 95% confidence level using Pearson and Spearman correlation tests. The correlation coefficients were > 0.836 by conducting the correlations on daily-daily, monthly-monthly, and long-term monthly mean-monthly basis.

The results of TTME in this study gave an idea about the temporal and spatial ET_a, which could be used in different applications, e.g, monitoring of irrigation water needs, hydrological and hydrological modeling studies, and water budget as essential part of water management.

Simple accuracy check of TTME ET_a results was done by comparison with E_{pan}. However, the accuracy of TTME performance is recommended to be carried out using meteorological-flux tower measurements (LE, sensible heat flux, and incoming and outgoing shortwave and longwave radiation), which are, unfortunately, not available in this study.

6 Acknowledgements

This research was financially supported by the Syrian ministry of higher education. Satellite images are courtesy of the online data pool of USGS/EROS Center for Earth Resources Observation & Science (http://eros.usgs.gov/). The authors are grateful to Dr. Shamsudduha and the Bangladesh Water Development Board (BWDB) for providing the meteorological data.

7 List of references

Allen R, Ralf W, Bastiaanssen W.G.M (2002) Surface Energy Balance Algorithms for Land (SEBAL) Advanced Training and Users Manual. Raytheon company, Idaho-USA, 1–98.

Allen RG, Tasumi M, Morse A, Trezza R, Wright JL, Bastiaanssen WGM, Kramber W, Lorite I, Robison CW (2007) Satellite-Based Energy Balance for Mapping Evapotranspiration with Internalized Calibration (METRIC)—Applications. Journal of Irrigation and Drainage Engineering 133(4):395–406.

Allen RG, Tasumi M, Trezza R (2007) Satellite-Based Energy Balance for Mapping Evapotranspiration with Internalized Calibration (METRIC)—Model. Journal of Irrigation and Drainage Engineering 133(4):380–94.

Bastiaanssen WGM (2000) SEBAL-Based Sensible and Latent Heat Fluxes in the Irrigated Gediz Basin, Turkey. Journal of Hydrology 229(1–2):87–100. doi:http://dx.doi.org/10.1016/S0022-1694(99)00202-4.

Bastiaanssen WGM, Menenti M, Feddes RA, Holtslag AAM (1998) A Remote Sensing Surface Energy Balance Algorithm for Land (SEBAL). 1. Formulation. Journal of Hydrology 212–213 (0):198–212. doi:http://dx.doi.org/10.1016/S0022-1694(98)00253-4.

Bastiaanssen WGM, Pelgrum H, Wang J, Ma Y, Moreno JF, Roerink GJ, van der Wal T (1998) A Remote Sensing Surface Energy Balance Algorithm for Land (SEBAL). Part 2: Validation. Journal of Hydrology 212–213(0):213–29. doi:http://dx.doi.org/10.1016/S0022-1694(98)00254-6.

Bastiaanssen WGM, Ahmad M, Chemin Y (2002) Satellite Surveillance of Evaporative Depletion across the Indus Basin. Water Resources Research 38(12):9. doi:10.1029/2001WR000386.

Brutsaert W, Sugita M (1992) Application of Self-Preservation in the Diurnal Evolution of the Surface Energy Budget to Determine Daily Evaporation. Journal of Geophysical Research: Atmospheres 97(D17):18377–82. doi:10.1029/92JD00255.

Carlson T (2007) An Overview of the 'Triangle Method' for Estimating Surface Evapotranspiration and Soil Moisture from Satellite Imagery. Sensors 7(8):1612–29. doi:10.3390/s7081612.

Chehbouni A, Seen DL, Njoku EG, Lhomme JP, Monteny B, Kerr YH (1997) Estimation of Sensible Heat Flux over Sparsely Vegetated Surfaces. Journal of Hydrology 188–189(0): 855–68. doi:http://dx.doi.org/10.1016/S0022-1694(96)03174-5.

Choi M, Kustas WP, Anderson MC, Allen RG, Li F, Kjaersgaard JH (2009) An Intercomparison of Three Remote Sensing-Based Surface Energy Balance Algorithms over a Corn and Soybean Production Region (Iowa, U.S.) during {SMACEX}. Agricultural and Forest Meteorology 149(12):2082–97. doi:http://dx.doi.org/10.1016/j.agrformet.2009.07.002.

Courault D, Seguin B, Olioso A (2003) Review to Estimate Evapotranspiration from Remote Sensing Data: Some Examples from the Simplified Relationship to the Use of Mesoscale Atmospheric Models. In ICID Workshop on Remote Sensing of ET for Large Regions, 18.

Crago RD (1996) Conservation and Variability of the Evaporative Fraction during the Daytime. Journal of Hydrology 180(1–4):173–94. doi:http://dx.doi.org/10.1016/0022-1694(95)02903-6.

Eagleman JR (1967) Pan Evaporation, Potential and Actual Evapotranspiration. Journal of Applied Meteorology and Climatology 6(3):482–88.

Elhaddad A, Garcia LA (2011) ReSET-Raster: Surface Energy Balance Model for Calculating Evapotranspiration Using a Raster Approach. Journal of Irrigation and Drainage Engineering 137(4):203–10.

Ertek A, Şensoy S, Küçükyumuk C, Gedik I (2006) Determination of Plant-Pan Coefficients for Field-Grown Eggplant (Solanum Melongena L.) Using Class A Pan Evaporation Values. Agricultural Water Management 85(1–2):58–66. doi:http://dx.doi.org/10.1016/j.agwat.2006.03.013.

Fekih M, Bourabaa A, Mohamed S (2013) Evaluation of Two Methods for Estimation of Evaporation from Dams Water in Arid and Semi Arid Areas in Algeria. International Journal of Application or Innovation in Engineering & Management (IJAIEM) 2(1):376–81.

Fekih M, Saighi M (2012) Measurement and Estimation of Evaporation from Water Surfaces: Application to Dams in Arid and Semi Arid Areas in Algeria. International Journal of Mathematical, Computational, Natural and Physical Engineering 6(8):23–26.

French AN, Jacob F, Anderson MC, Kustas WP, Timmermans W, Gieske A, Su Z (2005a) Corrigendum to 'Surface Energy Fluxes with the Advanced Spaceborne Thermal Emission and Reflection Radiometer (ASTER) at the Iowa 2002 {SMACEX} Site (USA)' [Remote Sensing of Environment 2005 99/1–2;55–65]. Remote Sensing of Environment 99(4):471. doi:http://dx.doi.org/10.1016/j.rse.2005.10.001.

French AN, Jacob F, Anderson MC, Kustas WP, Timmermans W, Gieske A, Su Z, Su H, McCabe MF, Li F, Prueger J, Brunsell N (2005b) Surface Energy Fluxes with the Advanced Spaceborne Thermal Emission and Reflection Radiometer (ASTER) at the Iowa 2002 {SMACEX} Site (USA). Remote Sensing of Environment 99(1–2):55–65. doi:http://dx.doi.org/10.1016/j.rse.2005.05.015.

Gao B (1996) NDWI—A Normalized Difference Water Index for Remote Sensing of Vegetation Liquid Water from Space. Remote Sensing of Environment 58(3):257–66. doi:http://dx.doi.org/10.1016/S0034-4257(96)00067-3.

Hossen S, Mano M, Miyata A, Baten A, Hiyama T (2012) Surface Energy Partitioning and Evapotranspiration over a Double-Cropping Paddy Field in Bangladesh. Hydrological Processes 26(9):1311–20. doi:10.1002/hyp.8232.

Johnson RL, Thoms RB, Zogorski JS (2003) Effects of Daily Precipitation and Evapotranspiration Patterns on Flow and VOC Transport to Groundwater along a Watershed Flow Path. Environmental Science & Technology 37(21):4944–54. doi:10.1021/es026252c.

Kanoua W, Merkel BJ (2014) Groundwater Recharge in Titas Upazila in Bangladesh. Arabian Journal of Geosciences 8(3):1361–71. doi:10.1007/s12517-014-1305-2.

Li ZL, Tang R, Wan Z, Bi Y, Zhou C, Tang B, Yan G, Zhang X (2009) A Review of Current Methodologies for Regional Evapotranspiration Estimation from Remotely Sensed Data. Sensors 9(5):3801–53. doi:10.3390/s90503801.

Linacre ET (2002) Ratio of Lake to Pan Evaporation Rates. http://www-das.uwyo.edu/~geerts/cwx/notes/chap04/eoep.html [cited April 2015].

Long D, Longuevergne L, Scanlon BR (2014) Uncertainty in Evapotranspiration from Land Surface Modeling, Remote Sensing, and GRACE Satellites. Water Resources Research 50(2):1131–51. doi:10.1002/2013WR014581.

Long D, Singh VP (2012) A Two-Source Trapezoid Model for Evapotranspiration (TTME) from Satellite Imagery. Remote Sensing of Environment 121(0):370–88. doi:http://dx.doi.org/10.1016/j.rse.2012.02.015.

Martínez JMM, Alvarez VM, González-Real MM, Baille A (2006) A Simulation Model for Predicting Hourly Pan Evaporation from Meteorological Data. Journal of Hydrology 318(1–4):250–61. doi:http://dx.doi.org/10.1016/j.jhydrol.2005.06.016.

Masud MB, Ferdous J, Ahmed M, Ghosh AK (2011) Water Deficit Period for Irrigation Agriculture Based on Evapotranspiration and Dependable Rainfall. Bangladesh Research Publication Journal 5(4):321–28.

McFeeters SK (1996) The Use of the Normalized Difference Water Index (NDWI) in the Delineation of Open Water Features. International Journal of Remote Sensing 17(7):1425–32. doi:10.1080/01431169608948714.

McMahon TA, Peel MC, Lowe L, Srikanthan R, McVicar TR (2013) Estimating Actual, Potential, Reference Crop and Pan Evaporation Using Standard Meteorological Data: A Pragmatic Synthesis. Hydrology and Earth System Sciences 17(4):1331–63. doi:10.5194/hess-17-1331-2013.

Menenti M, Choudhury BJ (1993) Parameterization of Land Surface Evaporation by Means of Location Dependent Potential Evaporation and Surface Temperature Range. In Proceedings of IAHS Conference on Land Surface Processes, 561–68. on Land Surface Processes. IAHS Publ.

Miralles DG, Holmes TRH, De Jeu RAM, Gash JH, Meesters AGCA, Dolman AJ (2011) Global Land-Surface Evaporation Estimated from Satellite-Based Observations. Hydrology and Earth System Sciences 15(2):453–69. doi:10.5194/hess-15-453-2011.

Mojid MA, Rannu RP, Karim NN (2015) Climate Change Impacts on Reference Crop Evapotranspiration in North-West Hydrological Region of Bangladesh. International Journal of Climatology 1097-0088. doi:10.1002/joc.4260.

Moran MS, Clarke TR, Inoue Y, Vidal A (1994) Estimating Crop Water Deficit Using the Relation between Surface-Air Temperature and Spectral Vegetation Index. Remote Sensing of Environment 49(3):246–63. doi:http://dx.doi.org/10.1016/0034-4257(94)90020-5.

Mu Q, Heinsch FA, Zhao M, Running SW (2007) Development of a Global Evapotranspiration Algorithm Based on {MODIS} and Global Meteorology Data. Remote Sensing of Environment 111(4):519–36. doi:http://dx.doi.org/10.1016/j.rse.2007.04.015.

Mu Q, Zhao M, Running SW (2011) Improvements to a {MODIS} Global Terrestrial Evapotranspiration Algorithm. Remote Sensing of Environment 115(8):1781–1800. doi:http://dx.doi.org/10.1016/j.rse.2011.02.019.

Norman JM, Kustas WP, Humes KS (1995) Source Approach for Estimating Soil and Vegetation Energy Fluxes in Observations of Directional Radiometric Surface Temperature. Agricultural and Forest Meteorology 77(3–4): 263–93. doi:http://dx.doi.org/10.1016/0168-1923(95)02265-Y.

Oki T, Kanae S (2006) Global Hydrological Cycles and World Water Resources. Science 313(5790):1068–72. doi:10.1126/science.1128845.

Rahman A, Rahman M, Lair NAM, Chu CM (2014) Pond Evaporation Systems for Harvesting Algae. In International Conference on Mechanical, Industrial and Energy Engineering, 6. Khulna Bangladesh.

Roerink GJ, Su Z, Menenti M (2000) S-SEBI: A Simple Remote Sensing Algorithm to Estimate the Surface Energy Balance. Physics and Chemistry of the Earth, Part B: Hydrology, Oceans and Atmosphere 25(2):147–57. doi:http://dx.doi.org/10.1016/S1464-1909(99)00128-8.

Sánchez JM, Kustas WP, Caselles V, Anderson MC (2008) Modelling Surface Energy Fluxes over Maize Using a Two-Source Patch Model and Radiometric Soil and Canopy Temperature Observations. Remote Sensing of Environment 112(3):1130–43. doi:http://dx.doi.org/10.1016/j.rse.2007.07.018.

Shahid S (2010) Spatio-Temporal Variation of Aridity and Dry Period in Term of Irrigation Demand in Bangladesh. American-Eurasian Journal of Agricultural & Environmental Sciences 7(4):386–96.

Shopan AA, Saiful Islam AKM, Dey NC, Bala SK (2013) Estimation of Evapotranspiration of Boro Rice in the Northwest Region of Bangladesh. In 4th International Conference on Water & Flood Management, 325–36.

Su Z (2002) The Surface Energy Balance System (SEBS) for Estimation of Turbulent Heat Fluxes. Hydrology and Earth System Sciences 6(1):85–100. doi:10.5194/hess-6-85-2002.

Sumner DM, Jacobs JM (2005) Utility of Penman–Monteith, Priestley–Taylor, Reference Evapotranspiration, and Pan Evaporation Methods to Estimate Pasture Evapotranspiration. Journal of Hydrology 308(1–4):81–104. doi:http://dx.doi.org/10.1016/j.jhydrol.2004.10.023.

Tanny J, Cohen S, Assouline S, Lange F, Grava A, Berger D, Teltch B, Parlange MB (2008) Evaporation from a Small Water Reservoir: Direct Measurements and Estimates. Journal of Hydrology 351(1–2):218–29. doi:http://dx.doi.org/10.1016/j.jhydrol.2007.12.012.

Timmermans WJ, Kustas WP, Anderson MC, French AN (2007) An Intercomparison of the Surface Energy Balance Algorithm for Land (SEBAL) and the Two-Source Energy Balance (TSEB) Modeling Schemes. Remote Sensing of Environment 108(4):369–84. doi:http://dx.doi.org/10.1016/j.rse.2006.11.028.

Shamim Uddin Md, Kurosawa K (2014) Effects of Peat and Water Quality Parameters on Groundwater Arsenic Contamination in Bangladesh. Water and Environment Journal 28(2):165–72. doi:10.1111/wej.12017.

Wang XG, Wang W, Huang D, Yong B, Chen X (2014) Modifying SEBAL Model Based on the Trapezoidal Relationship between Land Surface Temperature and Vegetation Index for Actual Evapotranspiration Estimation. Remote Sensing 6(7):5909–37. doi:10.3390/rs60x000x.

Yang Y, Long D, Shang S (2013) Remote Estimation of Terrestrial Evapotranspiration without Using Meteorological Data. Geophysical Research Letters 40(12):3026–30. doi:10.1002/grl.50450.

Yang Y, Shang S (2013) A Hybrid Dual-Source Scheme and Trapezoid Framework–based Evapotranspiration Model (HTEM) Using Satellite Images: Algorithm and Model Test. Journal of Geophysical Research: Atmospheres 118(5):2284–2300. doi:10.1002/jgrd.50259.

Zhang K, Kimball JS, Nemani RR, Running SW (2010) A Continuous Satellite-Derived Global Record of Land Surface Evapotranspiration from 1983 to 2006. Water Resources Research 46(9). doi:10.1029/2009WR008800.

Secchi disc visibility and its relationship with water quality parameters in the photosynthesis zone of Mosul Dam Lake, Northern Iraq

Khattab, Mohammed F. O. — Institute of Geology, Technische Universität Bergakademie Freiberg, Gustav-Zeuner Str.12, 09599 Freiberg, Germany.

Remote Sensing Center, Mosul University, Mosul, Iraq.

Email: mohummedz2004@yahoo.com

Merkel, Broder — Institute of Geology, Technische Universität Bergakademie Freiberg, Gustav-Zeuner Str.12, 09599 Freiberg, Germany.

Email: merkel@geo.tu-freiberg.de

Abstract: Generally, the top layer of a lake is playing an important role in determination the trophic level for aquatic system. The current study include discover and drive algorithms for retrieval of water quality parameters of the first 6 meter of Mosul Lake in Northern Iraq from the light penetration. Secchi disc visibility was read during July 2011 in a range between 0.9 and 6.1 m. Simultaneously, 25 samples were collected from the surface to a 6 m depth at the same sites. Water quality parameters included temperature, turbidity, chlorophyll-a, phosphorus, total inorganic carbon, dissolved organic carbon, total dissolved solids, electrical conductivity and pH. The result shows that the vertical distribution pattern T and pH with Secchi disc were decreased towards the lower secchi disk readings with depth. While, phosphorus, electrical conductivity, total dissolved solids and total inorganic carbon were increased towards the lower secchi disk readings with depth. The regression analysis gave us significant empirical algorithms to calculate both the turbidity and pH depending on secchi disc values at the different depths ($R2 > 0.9$, $P < 0.001$ and $SEE < 1.0$), ($R2 > 0.8$, $P < 0.05$ and $SEE < 0.01$), respectively. Also, the signal regression analysis displayed significant correlation between the TDS, temperature, TIC, DOC, EC and phosphorus concentration with secchi disc visibility at most of the depths ($R2 > 0.7$). Furthermore, multiple linear regression analysis was significant for calculating the turbidity, phosphorus concentration, and total inorganic carbon depending on simple routine field parameters ($R2 > 0.5$ and $p < 0.05$).

Keywords: photosynthesis, Mosul Lake, water quality, Secchi disc

1 Introduction

Photosynthesis is a process by which organisms use the energy of light to convert carbon dioxide and water into chemical energy. Photosynthesis is one of the most important biological processes on earth where it forms the basis of almost all other growth in an ecosystem(Cunningham and Saigo 1999). In the ecosystem of most lakes, photosynthetic organisms are usually the base of the food chain which in turn impacts on the trophic level (Bridgham et al., 1988). Commonly in aquatic environments, photosynthesis is limited by three factors which include light, nutrients and temperature. These factors vary seasonally, and are generally low through winter and high during summer (Davies et al., 2004). Usually the top layer of water accounts for more than 80% of photosynthesis biomass (Ambasht & Ram, 1976). Thus, the light intensity in lakes provides an index for ecology and the activities of photosynthetic organisms as well as controlling nutrients (Balali et al., 2012). One of the very simplest methods for the evaluation of light penetration in water is the secchi disk; in many cases secchi disk measurements have been used successfully for computing the trophic state. This is due to the relation between secchi disk values and the free floating algae concentration or the primary biological productivity of a lake (Fuller et al., 2004; Fuller & Minnerick, 2007; Lucas & Southgate, 2012).

The aims of this study were firstly to discover the changes with vertical distribution for water quality parameters which included temperature, turbidity, chlorophyll-a, phosphorus, total inorganic carbon (TIC), dissolved organic carbon (DOC), total dissolved solids (TDS), electrical conductivity (EC) and pH in conjunction with water clarity for the first 6 m of the Mosul Dam Lake. Secondly, to explore empirical algorithms for the retrieval of water quality parameters from secchi disk (SD) measurements at different depths. Thirdly the study aimed to estimate the measurement of the trophic factors along the first 6 m of the Mosul Lake depending on routinely measured environmental parameters.

2 Description of the study area

Mosul Dam Lake is one of the biggest artificial reservoirs in Iraq. Constructed in 1985, it is located on the Tigris River about 60 km north of Mosul city and 80 km from the borders of Syria and Turkey (Fig. 1). The length of the lake is about 45 km, its width ranges between 2 and 14 km with a surface area of about 385 km^2 at the maximum operation level (330 m above sea level), and it has a total storage volume of 11.11 billion m^3. The maximum water depth of the reservoir is 80 m and its drainage basin reaches to 4200 km^2 inside Iraq (Al-Taiee & Sulaiman, 1990; Kelley et al., 2007). The majority of the water entering the lake comes from Turkey. Mean annual discharge of the Tigris River is in the range of 270 to 1371 m^3/sec for the period 1931-1997 (Saleh, 2010). The average annual outflow of the lake was 555 m^3/sec for the period 1986-2011(Al-Ansari et al., 2013). The study area is located in a semi-arid region, where the average rainfall between 1980 and 2005 was 370.4 mm/year and the average mean maximum temperatures during July and January between 1985 and 2008 were 43.1°C and 6.3 °C, respectively. The lake does not freeze and can be classified as monomictic with a single turnover usually in November. The surface temperature of the lake drops to about 12 °C during winter, and reaches 10 °C at the lake bottom; the surface and bottom temperature are on average 31 °C and 14 °C during summer. Hence, thermal stratification is permanent overall for most of the year (Al-Hamadani & Khattab, 2005; Al-Kawaz, 1996; Khattab & Merkel, 2012).

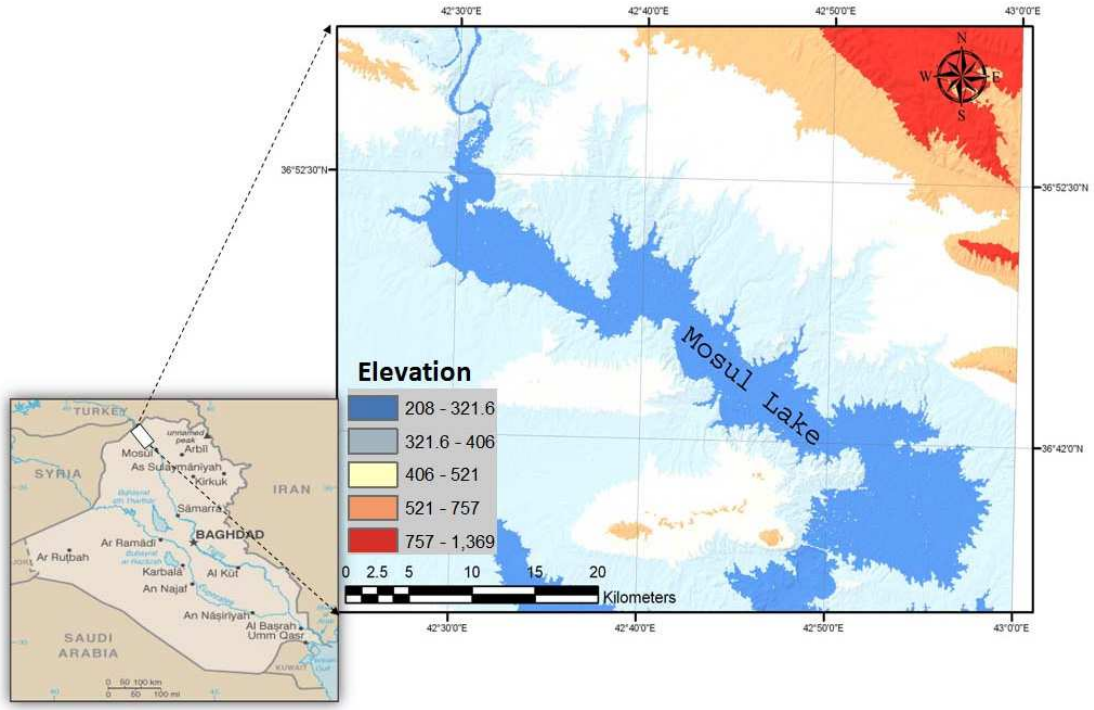

Fig. 1: Location map of study area

3 Materials and methods

In the current study, water quality samples and secchi disk measurements were used to discover the photic characteristics of Mosul Dam Lake, and to derive simple and accurate algorithms for the retrieval of water quality parameters along the photic zone, depending on routinely measured parameters. The exact locations of the measurements and sampling were determined using a GPS device.

3.1 Collection of water quality samples

Fig. 2: Locations of water quality samples

Twenty-five samples from five locations were collected in July 2011 (Fig. 2). Sampling was conducted at different depths using a Van Dorn Water Sampler and sterile 100 ml glass bottles. Bottled samples were stored inside a cool box for up to six hours before reaching the laboratory. Chlorophyll samples were transferred to the College of Science Department of Biology at Mosul University in Iraq. Samples for TIC, DOC, and phosphorus were transferred to the geological department of TU Bergakademie Freiberg, Germany.

3.2 Water quality parameters

A Multi Water Quality Checker (Model U-52) was used to measure temperature, pH, TDS, turbidity and EC. Chlorophyll-a (Chl-a) was analyzed according to the standard methods for the examination of water and wastewater (Eaton et al. 2005). TIC and DOC were measured by liquiTOC (Elementar Analysensysteme GmbH). DOC was measured after filtering the water through 0.45 micrometer filters. The phosphorus was measured using an ICP-MS (inductively coupled plasma mass spectrometry, Thermo Scientific Element 2). Water transparency (m) was recorded using a Secchi disk at each sampling site.

4 Result and discussion

4.1 Water quality attributes

Water clarity is an essential variable in the study of lakes and rivers where it reflects the primary regulator and ecological behavior of an aquatic environment (Hakanson 2006). Secchi depth is a classic measurement of water clarity in lakes; usually this consists of a 20 c (8 inch) diameter, metal or weighted plastic disk, typically black and white (Hakanson 2006; Lotspeich 2007). The results of water clarity depending on Secchi disk readings highly fluctuated in Mosul Dam Lake; the Secchi disk measurements ranged between 6.1 and 0.9 m. The highest Secchi disk values were read close to the dam, while the lower values were found at the inflow of the Dohuk River (Tab. 1). The increased light penetration at the southern part of the lake is due to the effect of waves. Furthermore, the energy of the water that reaches this part is not great enough to carry a large amount of nutrients, which explains the limited bottom sediments in the mud (Al-Ansari et al. 2013). Furthermore, the decrease in water clarity at the northern part of the lake is a result of the entry of the Tigris River and the influence of waves on this area. Also, the presence of the lowest values of water clarity at the tributary of the Dohuk River is a reflection of the quantity of nutrients that are transported by this river. Overall, according to the water clarity, Mosul Dam Lake is within the mesotrophic level, except for the Dohuk river influx, which is at the eutrophic level.

Tab. 1: Secchi disk values of study area.

Site Location	*Secchi disk (m)*
1	6.1
2	5.3
3	0.9
4	2.5
5	4.25

4.2 Vertical distribution

Generally, the characteristics of the photic zone of natural water are governed by incident solar radiation and vertical light attenuation (Overmann and Tilzer 1989). The comparisons between the vertical distribution of physical and chemical parameters with regards to the Secchi disk values of the first 6 m for the five sites are shown in Figure 3. Almost uniformly, the vertical distribution of temperature shows an increase with the temperature at the surface toward lower Secchi disk readings. While at a 6 m depth, the opposite happens and the difference in temperature was 0.77 ◦C (Fig. 3). Where there is a presence of suspended particles in the water, light rays are scattered and absorbed, which in turn increases the surface water temperature and decreases the temperature of the depths through reducing the depth of sunlight penetration (Dzurik 2003). The vertical distribution of water quality data for Mosul Dam Lake indicated that EC and TDS increase with increasing water clarity at the surface which is consistent with the results of Oliver et al (2010). This is not unpredictable considering that the concentration of divalent ions is very significant in coagulating colloidal particles (Oliver et al. 1999).
Also, the vertical distribution of EC and TDS shows an inverse correlation between the salinity and clarity of water at the 6 m depth. Here, the light transmission is reduced by the absorbance and scattering of suspended particulate matter as well as decreasing chlorophyll and organic matter compared to other nutrients, leading to increasing salinity at this depth (Khattab and Merkel 2013; Smayda and Borkman 2008). The vertical distribution of turbidity displays a clear positive relationship between the turbidity and Secchi disk values. At the surface of the lake the turbidity reading ranged between 0.8 and 14.4 NTU. Turbidity is one of the most important factors playing a significant role in changing water clarity values (Koenings and Edmundson 1991). Figure 3 also shows a high increase of turbidity below the depth of 4 m at sample site 3. This change in turbidity could be the result of interflow turbidity currents that exist at the outlet of the Dohuk River. The differences in temperature and the content of dissolved and suspended solids are partly responsible for forming these currents (Chen and Wu 2006). When the temperature of the lake decreases quickly with depth during summer, this leads to clearly isolated parts of variance in temperature and density (Lavelli et al. 2002). The differences between the density of incoming river flow, surface, and deep waters of the lake determine the level of incoming river water to the lake (Fig. 4) (Lavelli et al. 2002). Figure 3 shows the turbidity current of the Dohuk River entering the lake that at 4 m of depth. Also, this distribution explains the increase of both EC and TDS and the decrease of temperature at this depth. The pH at the surface of the water ranged between 8.8 and 8.4 for the five sites (Fig. 3).

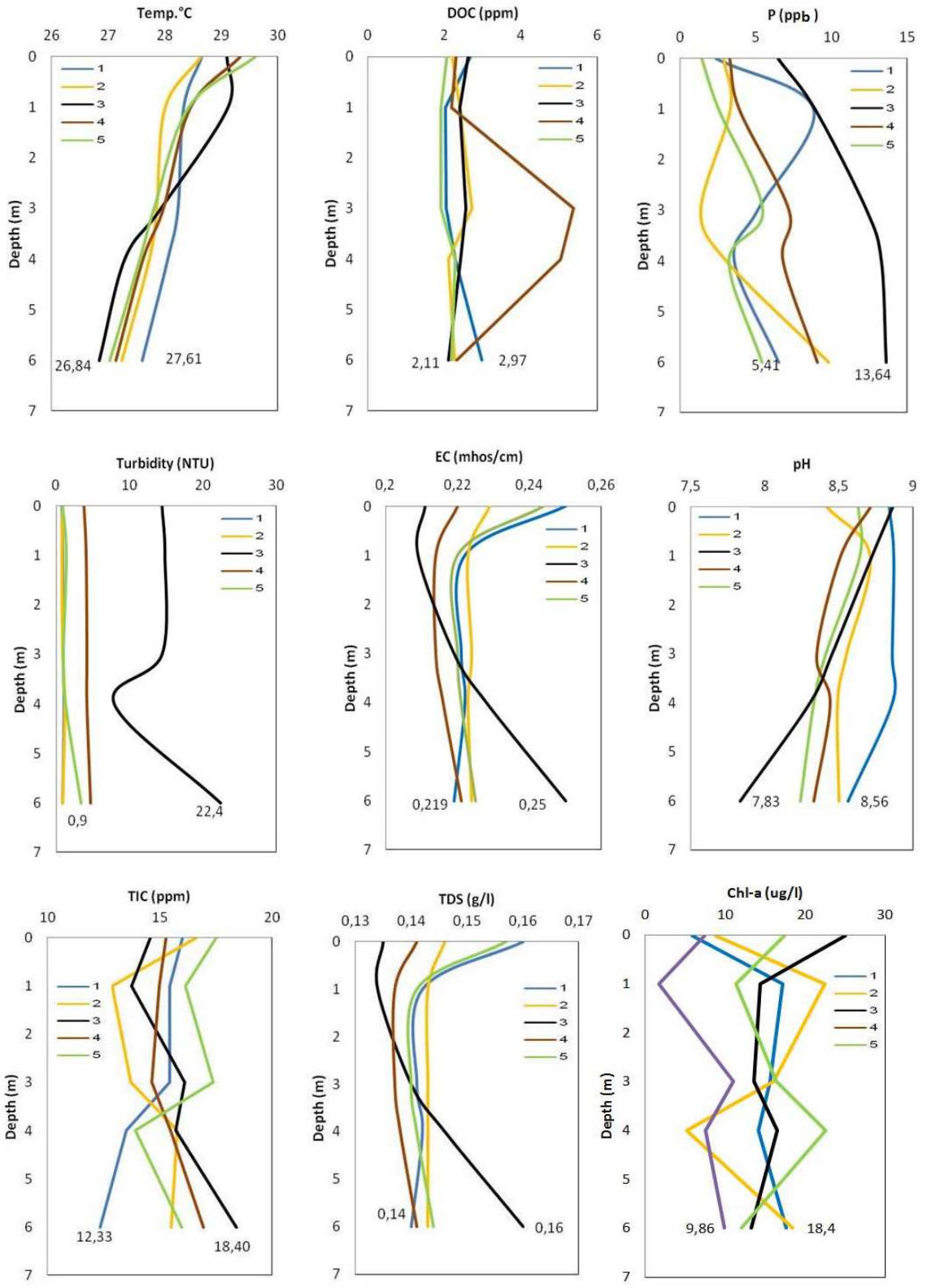

Fig. 3: Vertical distribution of water quality parameters with regard to the first 6 m of depth in Mosul Lake. Secchi disk site values: 6.1m (—), 5.3m (—), 4.2m (—), 2.5m (—), 0.9m (—).

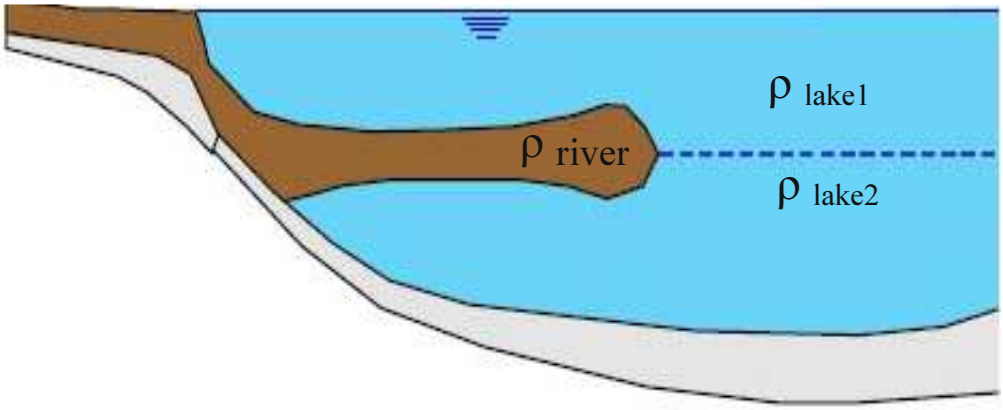

Fig. 4: Interflow density current in stratified lake, ρ is density(De Cesare, 1998;Lavelli et al., 2002)

The differences in the pH are 8.6–7.8 at the depth of 6 m for the sites studied. Through the process of photosynthesis the concentration of hydrogen ions decreases and thereby increases the pH. Usually, during the daytime photosynthesis uses up carbon dioxide and releases dissolved oxygen and therefore the pH increases (Ji, 2008; Zamfirescu et al. 2012). At 6 m depth, the lowest values of water clarity and a significant decrease in pH value were found compared with other sites which had high values of clarity (Fig. 3). Also, the vertical distribution for pH displayed variation in the degree of inclination at the 4 m depth for all sites, which could be a result of lake stratification.

Phosphorus is one of the most important vital nutrients in the environment through its conversion of the energy of sunlight to a chemical energy form that can be used to maintain cellular, production and growth (Glasbergen and Blowers 2003). Generally, the concentration of phosphorus shows an increase with decreasing water clarity (Fig. 3). A high concentration of phosphorus existed at the depths of 1 m and 4 m for the higher and lower Secchi disk sites, respectively. This variation is due to the influence of limiting factors on phosphorus concentration such as temperature, pH , oxygen, light, waves, wind, and other biological factors (Yang et al. 2008). DOC, TIC, and chlorophyll did not show a clear variation between the sites, however, the TIC displayed a significant difference between the sites at a 6 m depth. The highest concentration was 18.4 ppm at the 0.9 m Secchi disk site and 12.33ppm at 6.1 m. With decreasing water temperature alkalinity leads to an increase in the concentration of TIC in aquatic environments (Katano et al. 2009).

4.3 Regression analysis

4.3.1 Simple curve fitting regression

Linear or nonlinear regression analysis is a very commonly considered analysis method for quantitatively examining the relationship between two variables (Seltman 2013). Regarding water quality, the application of a simple fitting model requires two parameters to describe realistic water situations (Heydari et al. 2013). In this study simple empirical models for regression analyses were created to examine the relationship between the water clarity and water quality parameters of Mosul Dam Lake in Northern Iraq. The water quality parameters employed in this analysis were temperature, turbidity, pH, EC, Chl-a, P, TIC, DOC, and TDS. SPSS software was used to establish empirical regression models for the Secchi disk depth values and water quality parameters at the surface, 1 m, 3 m, 4 m, and 6 m. Tables 2 to 6 show the obtained regression models between water clarity and water quality parameters for the surface, 1, 3, 4, and 6 m, respectively, of depth in Mosul Dam Lake.

The performance of these equations was checked depending on the determination coefficient (R^2), the standard error of the estimate, a measure of the accuracy of predictions, (SEE), and significance test (P value). Generally, the regression analysis for Secchi disk and quality parameters showed a clear rela-

tionship between water clarity and water quality parameters, with $R^2 > 0.7$ (Tables 2, 3, 4, 5, and 6). The turbidity was strongly significant and inversely correlated with Secchi disk values at the depths studied ($R^2 > 0.9$, $P < 0.001$, and SEE < 1.0); the inverse models gave the best fit to simulate this relation except at the depth of 4 m, where the logarithmic model was a better fit.

Tab. 2: Regression models between Secchi disk depth and water quality parameters at the surface of Mosul Dam Lake.

Water quality parameter	*Model*	R^2	*SEE*	*P value*
EC	$= 0.20615\ e^{0.029122SD}$	0.76	0.039	0.05
Turbidity	= -2.025568+14.7344/SD	0.99	0.404	0.0001
DOC	= 2.042+0.524/SD	0.91	0.084	0.04
TIC	$= 15.326-1.6385SD+0.947SD^2 -0.108SD^3$	0.92	0.617	0.3
Chl. a	$= 52.91- 41.65SD+12.45SD^2 -1.13SD^3$	0.86	5.9	0.4
Temperature	$= 28.648+0.557SD-0.094SD^2$	0.70	0.322	0.2
pH	= 8.95-0.091 SD	0.93	0.058	0.03
TDS	$= 0.132e^{0.0288SD}$	0.72	0.0432	0.06
P	= 1.379+4.552/SD	0.89	0.702	0.01

Tab. 3: Regression models between Secchi disk depth and water quality parameters at 1 m depth of Mosul Dam Lake.

Water quality parameter	*Model*	R^2	*SEE*	*P value*
EC	$= 0.209081*SD^{0.034562}$	0.95	0.006	0.004
Turbidity	= -1.90252+15.013014/SD	0.99	0.249	0.0001
DOC	= 2.051529+0.302026/SD	0.30	0.215	0.34
TIC	$= e^{2.782211-0.147013/SD}$	0.86	0.030	0.07
Chl. a	=16.30617+8.55415/SD	0.35	5.246	0.2
Temperature	= 28.072061+.947918/SD	0.86	0.169	0.02
pH	$= 8.267e^{0.0107SD}$	0.94	0.005	0.03
TDS	$= 0.134022SD^{0.034051}$	0.94	0.007	0.006
P	$= 15.003304-7.20661SD+0.9817SD^2$	0.84	1.848	0.15

Tab. 4: Regression models between Secchi disk depth and water quality parameters at 3 m depth of Mosul Dam Lake.

Water quality parameter	*Model*	R^2	*SEE*	*P value*
EC	= 0.23278-0.020919SD+0.006847SD^2-0.000611SD^3	0.97	0.001	0.18
Turbidity	= -1.833995+14.611577/SD	0.99	0.444	0.0001
DOC	= -0.4409+13.976458/SD	0.84	0.784	0.08
TIC	= 17.476-2.33608SD+0.78287SD^2-0.0775SD^3	0.105	2.648	0.9
Chl. a	=25.899-19.66962SD+7.32196SD^2-0. 75159SD^3	0.98	0.84	0.14
Temperature	= 27.518817+.666952SD-0.261596SD^2+0.028092SD^3	0.98	0.040	0.15
pH	= 8.655237-0.251122SD+0.045649SD^2	0.96	0.056	0.03
TDS	= 0.148184-0.012313SD+0.003969SD^2-0.00035SD^3	0.94	0.001	0.3
P	= 2.466643+9.129568/SD	0.82	1.942	0.03

Tab. 5: Regression models between Secchi disk depth and water quality parameters at 4 m depth of Mosul Dam Lake.

Water quality parameter	*Model*	R^2	*SEE*	*P value*
EC	= 0.247783-0.028802SD+0.008147SD^2-0.000676SD^3	0.99	0.000	0.08
Turbidity	= 7.460169-3.767253lnSD	0.97	0.498	0.001
DOC	= 2.274419-0.089839SD+0.03568SD^2-0.00274419SD^3	1.00	0.000	0
TIC	= 14.685824-0.183584SD	0.91	0.154	0.04
Chl. a	=39.95-18.20613SD-6.26119SD^{2+} 0.60116SD^3	0.13	12.94	0.97
Temperature	= 26.683029+.910305SD-0.286442SD^2+0.028582SD^3	0.99	0.019	0.04
pH	= 7.864137+0.688491SD-0.250974SD^2+0.027032SD^3	0.99	0.003	0.009
TDS	= 0.159399-0.019456SD+0.00549SD^2-0.000454SD^3	0.99	0.001	0.01
P	= 18.349904-6.142957SD+0.611351SD^2	0.99	0.773	0.001

Tab. 6: Regression models between Secchi disk depth and water quality parameters at 6 m depth of Mosul Dam Lake

Water quality parameter	*Model*	R^2	*SEE*	*P value*
EC	= 0.215079+0.030303/SD	0.90	0.004	0.01
Turbidity	= -3.067996-22.696308/SD	0.99	1.034	0.0001
DOC	= 1.328514+1229462SD-0.448197SD^2-0.047561SD^3	0.97	0.106	0.1
TIC	= 19.553056-0.97399SD	0.83	1.053	0.02
Chl. a	=21.72278-12.2455SD+3.59176SD^2 - 0.27505SD^3	0.89	2.37	0.4
Temperature	= 26.232706+.927085SD-0.305557SD^2+0.031291SD^3	0.99	0.041	0.09
pH	= 7.893898$SD^{0.042475}$	0.87	0.014	0.01
TDS	= 0.13737+0.019604/SD	0.90	0.002	0.01
P	= 6.022096+6.839406/SD	0.71	1.970	0.07

Where turbidity is the optical parameter, in turn, these particles scatter and absorb the light (Ritter 2010). Also, pH values were significantly positively correlated with Secchi disk values at the depths studied ($R^2 > 0.8$, $P < 0.05$, and SEE < 0.01). The linear model shows the best fit for this relationship at the surface of the lake ($R^2 > 0.9$ and $P < 0.05$) (Table 2). At the depth of 3 and 4 m, the quadratic model was more suitable for simulating the correlation between pH and water clarity (Tables 4 and 5). The exponential and power models display a good pattern to this relationship at the depths of 1 and 6 m, respectively, (Tables 3 and 6). Regarding the relationship between pH and water clarity, in natural lake water the pH value usually reflects chemical and biological operations. A low pH value indicates an increase in the dissolved organic matter in the water while a high pH indicates an increase of salts in the water (Lotspeich 2007; Wetzel 2001). Both TDS and EC show a similar regression model with water clarity values through the depths studied (Tables 2, 3, 4, 5, and 6). The exponential model was the best for expressing this relationship at the surface of the lake ($R^2 > 0.7$ and $P < 0.06$). At the 1 m depth, the power model gave a better fit and significance ($R^2 > 0.9$ and $P < 0.01$), while at the depths of 3 and 4 m, the quadratic model was better suited for simulating the relation between EC and TDS with the Secchi disk values ($R^2 > 0.9$). Table 6 shows that the inverse model is clearly significant for evaluating the correlation between EC and TDS and the Secchi disk values ($R^2 > 0.9$ and $P < 0.05$). A decline in light penetration at this depth causes a decrease in chlorophyll and organic matter compared to other nutrients, leading to an increase in the salinity (Khattab and Merkel 2013; Smayda and Borkman 2008). In the current study, the predicated inverse relationship between phosphorus and water clarity values has been proved. An increase in phosphorus concentration leads to an increase in turbidity and a decrease of water clarity (Bachmann et al. 2002). Tables 2, 3, and 5 show that the inverse and quadratic models were more significant to simulate the relationship between turbidity and water clarity at the surface, 3, and 4 m of the lake depth ($R^2 > 0.8$ and $P < 0.05$). Also, the inverse and quadratic models were suitable for presenting this relationship at the depths of 1 and 6 m ($R^2 > 0.7$). DOC showed a significant correlation with the Secchi disk at the surface and a 4 m depth of the lake ($R^2 > 0.9$ and $P < 0.05$). DOC and the Secchi disk values at the depth of 3 and 6 m depth of the lake were not significantly correlated ($R^2 > 0.8$ and $P < 0.1$), and at the 1 m depth, R^2 was only 0.3 (Table 1). The DOC relationship with water clarity supported the use of DOC as an indicator of the productivity of the lake (Dunalska 2011; Read and Rose 2013). Furthermore, DOC is an essential parameter for several chemical, physical, and biological features of the aquatic environment, thereby influencing the transparency of water (Read and Rose 2013). The weak relationship at the 1 m depth between DOC and water clarity could be a result of the activity of the photochemical degradation of dissolved organic matter which dominated at this depth (Chen and Wangersky 1996; Gonsior et al. 2013;

Grubisic et al. 2012). Generally, the TIC was strongly correlated with the Secchi disk ($R^2 > 0.8$), (Tables 2, 3, 5, and 6). TIC and Secchi disk values at the depths of 4 and 6 m are significant and inversely correlated ($R^2 > 0.8$ and $P < 0.05$). TIC has been used to describe the net productivity of aquatic systems (Szyper and Ebeling 1993). The significant increase of TIC at these depths could be a result of the depletion of dissolved oxygen during the summer, indicating photosynthesis reduction (Zhang 2013). The positive correlation between TIC and water clarity has been observed at the surface and the 1 m depth ($R^2 > 0.8$). This is due to aeration and photosynthesis operations. Where the aeration process is increasing the rate of CO_2 eradication, CO_2 is also reduced by photosynthesis, which together work to raise the pH value at these depths (Fig. 3) (Zhang, 2013). Consequently, the high TIC concentration refers to the high value of water clarity at the surface and 1 m depth of Mosul Dam Lake. Generally, the temperature shows a good relationship with water clarity at most of the depths studied (Tables 2, 3, 4, 5, and 6). The significant inverse and quadratic models simulated this relation at depths of 1 and 4 m, respectively ($R^2 > 0.8$ and $P < 0.05$) (Tables 3 and 5).

Low water transparency works to block most sunshine at the surface of the water body (Mwaura 2003). Thus, temperature has a negative correlation with the first depths of water and a positive correlation with the depths of more than 4 m of Mosul Dam Lake (Fig. 3). The regression analysis between chlorophyll-a and the water clarity of Mosul Dam Lake shows that there is a certain relationship between them but this relationship is not significant ($R^2 > 0.8$ and $P > 0.05$). Chlorophyll-a is one of the sources causing turbidity in Secchi disk clarity (Jamu et al. 1999). The insignificant correlation between Chl-a and the Secchi disk may indicate the significant contribution of the other causes of water clarity.

4.3.2 Multiple linear regression analysis

The multiple linear model is an extension of simple linear regression and can be used to measure the magnitude of a variable depending on several quantitative variables (Seltman 2013). These types of models can be helpful in complicated cases where the concerned variable is affected by the behavior of other multiple variables (The Cadmus Group 2010). In the current study the multi-linear regression models were performed in order to estimate the trophic factors of Mosul Dam Lake depending on routine field parameters. For further validation, the root mean square error (RMSE) was computed to demonstrate the certainty of trophic factor models, and they are calculated as follows (Liu et al. 2013):

$$\text{RMSE} = \sqrt{\frac{1}{n}\sum_{i=1}^{n}(y_i - \acute{y}_i)^2} \qquad \text{----------} \quad (1)$$

The results of multiple linear models provided acceptable equations to evaluate the turbidity, TIC, and total phosphorus depending on simple measurements through the first 6 m of Mosul Dam Lake ($R^2 > 0.5$ and $P < 0.01$) (Table 7). This demonstrated that each parameter of temperature, pH, EC, TDS, and water clarity somehow impacts on the variation of turbidity, P, and TIC along the photic zone of the lake. Moreover, the results of multiple linear models show that there are no significant linear correlations between DOC and Chl. a and the simple field measurements (temperature, pH, EC, TDS, and water clarity).

Tab. 7: Multiple linear models between Turbidity, P and TIC and routine field parameters for Mosul Dam Lake

Water quality parameter	*Multiple linear model*	R^2	*SEE*	*P value*
Turbidity	= -31.088 - 3.065SD + 6.869pH + 839. 02EC - 1038.04TDS - 1.8Temp.	0.75	3.26	0.001
TIC	= -3.812 - 0.097SD - 2.874pH + 907.56EC - 1296.58TDS + 0.944Temp.	0.5	1.19	0.01
P	= 32.678 - 1.694SD + 7.913pH + 862.938 EC - 1207.84TDS - 3.848Temp.	0.66	2.36	0.001

In general, multiple linear regression models present significant correlation between the predicated and observed turbidity, P, and TIC with R > 0.7 and RMSE between 2.7 and 1.03 (Fig. 5). The best forecast results exist for TIC with RMSE = 1.03. Although there are errors in estimating values of the trophic predictive factors, still these values are acceptable for considering monitoring of the nutrients of aquatic environments.

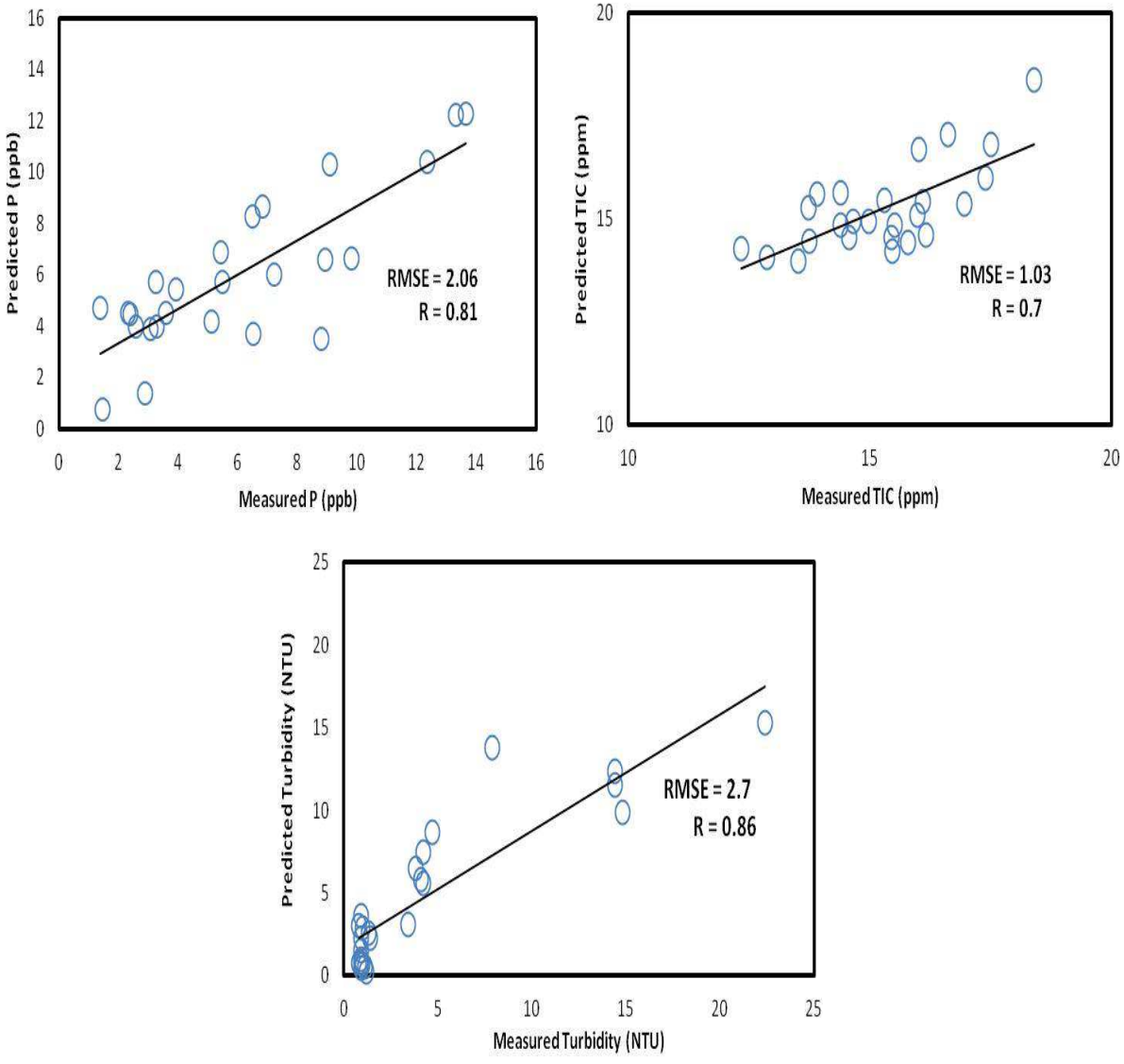

Fig. 5: Scatter plots of measured and predicted Turbidity, P and TIC for Mosul Dam Lake.

5 Acknowledgements

This work was supported by the German Academic Exchange Service. The authors would like to express their sincere appreciation to Dr. Adil Al- Hamadani, Dr. Basheer Al-Ni'ma, and Hazim Al-Naemi for assisting in the achievement of the field work.

6 References

Al-Ansari N, Issa IE, Sherwani G, Knutsson S (2013) Sedimentaion in the Mosul Reservoir of Northern Iraq. Journal of Environmental Hydrology 21:1–10.

Al-Hamadani B, Khattab O (2005) Variation of characteristic quality with depth of water of Mosul Dam Lake. Rafidain Journal of Science, 16, 104–114.

Al-Kawaz HA (1996) Geochemistry and mineralogy of recent sediments and Miocene rocks and the nature of their interaction with the Southern part of Saddam Lake waters. Dessertation, University of Mosul.

Al-Taiee TM, Sulaiman YI (1990) Preliminary water balance of Saddam Dam Lake. In: The Second Scientific Conference of S*DRC*. 121–134.

Ambasht RS, Ram K (1976) Stratified primary productive structure of certain macrophytic weeds in a large Indian Lake. In: Varshney CK, Aquatic Weeds in South East Asia, Proceeding of a Regional Seminar on Noxious Aquatic vegetation, pp 147-155.

Bachmann RW, Horsburgh CA, Hoyer MV., Mataraza LK, Canfield JE(2002) Relations between trophic state indicators and plant biomass in Florida lakes. Hydrobiologia*,* 470:219–34.

Balali S, Hoseini SA, Ghorbani R, Balali B (2012) Correlation of Chlorophyll-A with Secchi disk depth and water turbidity in the International Alma Gol Wetland, Iran. World Journal of Fish and Marine Sciences 4:504–8.

Bridgham SD, McNaught DC, Meadows C (1988) Effects of complex effluents on photosynthesis in Lake Erie and Lake Huron. In: Jr CJ, Praat JR (eds.) American Society for Testing and Materials, Philadelphia, Penslyvannia, pp 74-85.

Chen W, Wangersky PJ (1996) Rates of microbial degradation of dissolved organic carbon from phytoplankton cultures. Journal of Ptanktoo Research, 18, 1521–1533.

Chen Y-JC, Wu S-C (2006) Behavior of storm-induced suspension interflow in subtropical Feitsui Reservoir, Taiwan. Limnol. Oceanogr, 51, 1125–1133.

Cunningham WP, Saigo BW (1999) Environmental science: a global concern 5th ed., Boston MA, McGraw-Hill.

Davies J-M., Nowlin WH, Mazumder A (2004) Variation in temporal [14C]plankton photosynthesis among warm monomictic lakes of coastal British Columbia. Journal of Plankton Research, 26, 763–778.

De Cesare G. (1998) Alluvionnement des retenues par courants de turbidité. Lausanne. Dessertation, University of Lausanne.

Dunalska JA (2011) Total organic carbon as a new index for monitoring trophic states in lakes. *Oceanological and Hydrobiological Studies*, 40(2), 112–115.

Dzurik AA (2003) Water Resources Planning 3rd ed., Rowman & Littlefield, Oxford.

Eaton AD et al. (2005) Standard Methods for the Examination of Water and Wastewater 21st ed. American Water Works Association, Water Pollution Control Federation, Washington, D.C.

Fuller LM, Aichele SS, Minnerick, RJ (2004) *P*redicting Water quality by Relating Secchi-Disk Transparency and Chlorophyll a Measurments to Stallite Imagery for Michigan Inland Lakes, August 2002., Available at: http://pubs.usgs.gov/sir/2004/5086/.

Fuller LM, Minnerick RJ (2007) Predicting water quality by relating Secchi-Disk transparency and chlorophyll a measurements to landsat satellite imagery for Michigan Inland Lakes, 2001–2006, Available from: http://pubs.usgs.gov/fs/2007/3022/pdf/FS2007-3022.pdf.

Glasbergen P, Blowers A (2003) Environmental Policy in an International Context. Perspectives, Open University of Netherlands.

Gonsior M, Schmitt-Kopplin P, Bastviken D (2013) Depth-dependent molecular composition and photoreactivity of dissolved organic matter in a Boreal Lake under winter and summer conditions. Biogeosciences Discuss, 10, 8949–8975.

Grubisic LM, Brutemark, A et al (2012) Effects of stratification depth and dissolved organic matter on brackish bacterioplankton communities. Marine Ecology Progress Series, 453, 37–48.

Hakanson L (2006) The relationship between salinity, suspended particulate matter and water clarity in aquatic systems. Ecological Research, 21, 75–90.

Heydari, MM, Abasi A. et al (2013) Correlation study and regression analysis of drinking water quality in Kashan City, Iran. Middle-East Journal of Scientific Research, 13, 1238–1244.

Jamu DM., Lu Z, Piedrahita RH (1999) Relationship between Secchi disk visibility and chlorophyll a in aquaculture ponds. Aquaculture, 170, 205–214.

Ji Z-G (2008) Hydrodynamics and Water Quality, Modelling Rivers, Lakes, and Estuaries, New Jersey, John Wiley and Sons.

Katano T, Lee J et al. (2009) Effect of temperature on inorganic carbon. Journal of Freshwater Ecology, 24(2), 255–260.

Kelley JR, Wakeley LD et al (2007) Geological setting of Mosul Dam and its engineering implications. http el.erdc.usace.army.mil/elpubs/pdf/tr07-10.pdf. Accessed February 7, 2013.

Khattab, MFO, Merkel BJ (2012) Distribution of Hetrotrophic Bacteria and Water Quality Parameters of Mosul Dam Lake, Northern Iraq. In: Brebbia, C.A. (ed.) Water Pollution XI. Southampton: WIT Press, 195–207.

Khattab MFO, Merkel BJ (2013) Application of Landsat 5 and Landsat 7 images data for water quality mapping in Mosul Dam Lake, Northern Iraq. Arabian Journal of Geosciences, 7, 3557-3573.

Koenings JP, Edmundson JA (1991) Secchi disk and photometer estimates of light regimes in Alaskan lakes: Effects of yellow color and turbidity. Limnolg. Oceanogr. 36, 91–105.

Lavelli A, Boillat1 J-L, De Cesare G (2002) Numerical 3D modelling of the vertical mass exchange induced by turbidity currents in Lake Lugano (Switzerland). In: 5th International Conference on Hydro-Science and -Engineering (ICHE-2002). (Reference: LCH-CONF-2002-012 Note: [355]).

Liu J, Sun D et al (2013) Pre-classification improves relationships between water clarity, light attenuation, and suspended particulates in turbid inland waters. Hydrobiologia, 711, 71–86.

Lotspeich RR (2007) The Quality of Water and Bottom Material in Lunge Reservoir, Virginia, September 2004 Through August 2005, U.S. Geological Survey Open-File Report 2007–1053, 52 p.

Lucas JS, Southgate PC (2012) Aquaculture, Farming Aquatic Animals and Plants 2nd ed., Oxford, Wiley-Blackwell.

Mwaura F (2003) The spatio-temporal characteristics of water transparency and temperature in shallow reservoirs in Kenya. Lakes & Reservoirs: Research and Management, 8, 259–268.

Oliver RL, Hart BT et al (1999) The Darling River Algal Growth and the Cycling and Sources of Nutrients. Murray-Darling Basin Commission Project M386.

Oliver RL, Mitrovic SM, Rees C (2010) Influence of salinity on light conditions and phytoplankton growth in a turbid river. River Research and Applications, 26, 894–903.

Overmann J, Tilze MM (1989) Control of primary productivity and the significance of photosynthetic bacteria in a meromictic kettle lake. Mittlerer Buchensee, West-Germany. Aquatic Sciences, 51, 161–278.

Read JS, Rose KC (2013) Physical responses of small temperate lakes to variation in dissolved organic carbon concentrations. Limnol. Oceanogr: Association for the Sciences of Limnology and Oceanography, Inc., 58, 921–931.

Ritter J (2010). Water quality (Principles and practices of water supply operations) 4th ed., United State of America: American Water Works Assn.

Saleh DK (2010) Stream gage descriptions and streamflow statistics for sites in the Tigris River and Euphrates River basins, Iraq, U.S. Geological Survey, Reston, Virginia: 2010.

Seltman HJ (2013) Experimental design and analysis. Retrieved from: http://www.stat.cmu.edu/hseltman/309/Book/Book.pdf.

Smayda TJ, Borkman DG (2008) Nutrient and plankton dynamics in Narragansett Bay. In: Desbonnent A, Costa-Pierce BA (eds.), New York, Springer, pp 431-484.

Szyper JP, Ebeling, JM (1993) Photosynthesis and community respiration at three depths during a period of stable phytoplankton stock in a eutrophic brackish water culture pond. Marine Ecology Progress Series, 94, 229–238.

The Cadmus Group, I. (2010) Pleasant Bay Alliance Water Quality Monitoring Program: Statistical Analysis of Multi-year Water Quality Monitoring Data, Watertown. Available from: pleasantbay.org/wp-content/.../PBA-Water-Quality-Analysis-Final.pdf.

Wetzel RG (2001) Limenology lake and river ecosystems 3rd ed., San Diego: Elsevier Acadamic Press.

Yang X, Wu X et al (2008) Mechanisms and assessment of water eutrophication. Journal of Zhejian University science B, 9, 197–209.

Zamfirescu C, Dincer I, Naterer GF (2012) Molecular charge transfer and quantum efficiency analyses of a photochemical reactor for hydrogen production. International Journal of Hydrogen Energy, 37(12), 9537–9549.

Zhang X (2013) Restoration of a small, shallow, eutrophic lake by submerged aeration and comparison with a similar lake. Dessertation, University of Colorado State.

Precipitation characteristics and trends in the Palestinian territories during the period 1951–2010

Hänsel, Stephanie — Interdisciplinary Environmental Research Center, Technische Universität Bergakademie Freiberg, Brennhausgasse 5, 09599 Freiberg, Phone: +49 (0)3731 393533, Fax: +49 (0)3731 394060, Email: Stephanie.haensel@ioez.tu-freiberg.de

Zurba, Kamal — Interdisciplinary Environmental Research Center, Technische Universität Bergakademie Freiberg, Brennhausgasse 5, 09599 Freiberg, Phone: +49 (0)3731 393533, Fax: +49 (0)3731 394060, Email: zurba@ioez.tu-freiberg.de

Abstract: Precipitation is an important part of the hydrological cycle impacting many natural and human systems. The study area, covering the Palestinian territories and surrounding areas, is located in the subtropical dryland zone that is characterized by a wet season (October to May) and a dry season (June to September). Analyzing changes in precipitation totals and their timing within the year is of immense importance for the Palestine economy and particularly the agricultural management, as Palestine faces a chronic water shortage. The regional rainfall characteristics and their changes within the period 1951–2010 are studied using two gridded data sets, VASClimO and E-OBS. The annual precipitation totals in the study area range for individual grid cells from below 50 mm in the arid South to more than 650 mm in semi-arid North. The magnitude of the values depends on the chosen data set, but the general characterization of the moisture status of the months and years, respectively, is well comparable in most years. The timing of drought and wet events is compared and the spatial structure of rainfall is analyzed using the modified Rainfall Anomaly Index. Annual precipitation trends are mainly small and non-significant – except for the southern parts of the study area, where distinct precipitation decreases emerge in the E-OBS data set. Intra-annual precipitation changes are more pronounced with increasing precipitation in January and October (using E-OBS also in September) and decreases in April and December (using E-OBS also in March, May and November).

Keywords: VASClimO, E-OBS, regional climate change, climate variability, modified rainfall anomaly index (mRAI), drought

1 Introduction

Precipitation is an important part of the hydrological cycle with impacts on many natural and human systems. Affected socio-economic sectors are for instance water management, agriculture, forestry, industrial sector, and human health. Some of the effects of rainfall on these sectors are direct ones, like the shortage or excess of water for some activity, while others are more indirect, e. g., by impacts of precipitation on the land fertility (Rice, 1886).

The study area covering the Palestinian territories and surrounding areas is located in the subtropical dryland zone (Kafle and Bruins, 2009) with strong seasonal variations of temperature, precipitation and evapotranspiration (Salim and Wildi, 2005). It is characterized by a wet season (October to May) and a dry season (June to September; WRAP, 2013). Aridity and uncertainty are major characteristics of the hydrologic cycle of the area, due to its location in a transition zone (Bakour and Kolars, 1994). Thus, the climate shows large regional differences, although the study area only covers a comparatively small area. These differences are particularly pronounced between the Gaza strip and the hilly areas of the West bank (e.g., Nablus, Ramallah, Jerusalem and Hebron). The climate of the Gaza strip is characterized by coastal climate conditions with mild winters and humid, hot summers. West bank on the other hand has cold winters and mild summers. Average temperatures range between 13–25°C in Gaza strip and 8–23°C in West bank, respectively (Ibrik, 2009). Evapotranspiration rates are generally high (Rofe and Raffety, 1965), due to high temperatures and solar radiation. Thus, most precipitation is lost by evapotranspiration (67–68 %), less stored in the subsurface through infiltration (29–30 %), and only 2–3% are lost by run-off (Rofe and Raffety, 1965). Therefore it is no surprise that the Middle East region is suffering of water shortage. The coolest years within the study area were 1982/1983 and 1991/1992, while the year 1998/1999 was the warmest and at the same time the most severe drought year. Kafle and Bruins (2009) pointed out that 1998 also occurred the strongest El Nino event in the 20th century. An analysis by Price et al. (1998) found a significant correlation between El Nino events and above average winter precipitation in the northern regions of Palestine.

Changes in the water cycle are expected to occur within a warming climate. In the study area the earth surface temperature significantly increased in the second half of the 20th century (Ben-Gai et al., 1999; Kafle and Bruins, 2009; Gurevich et al., 2011) and further increases are projected for the 21st century (Evans, 2009; IPCC, 2013). Kafle and Bruins (2009) found a negative correlation between temperature and precipitation trends over the region; an increase of 1°K in annual temperature is connected with a decline of 13–40 mm in the annual precipitation in the northern Negev, 147 mm in the coastal plain and 120–126 mm in the inland eastward.

Several studies on the precipitation trends over Israel and Palestine have been conducted. Most of them find no statistically significant changes in annual precipitation totals, e.g. Kafle and Bruins (2009) for 1970–2002, Ziv et al. (2014) for 1975–2010, Yosef et al. (2009) for 1950-2003 and Givati and Rosenfeld (2013) for 1950–2010. Yet, most trend analyses show slight increases of rainfall for the comparatively wet part of the study area, and slight decreases for the Eastern inlands and the Northern Negev desert with the strongest precipitation decreases in the super-arid areas (Kafle and Bruins, 2009; Ziv et al., 2014; Givati and Rosenfeld, 2013). Older analyses for the period 1961–1990 showed increases in the Southern regions and decreases in the northern parts of Palestine (Steinberger and Gazit-Yaari, 1996). Ben-Gai et al. (1994) described increases of up to 30% in the annual average rainfall in the semi-arid Naqab desert for the same period. Seasonally, more pronounced precipitation changes have been observed than for the annual time scale. Ziv et al. (2014) detected a statistically significant decrease in spring rainfalls of more than 15 % per decade. Climate model studies project

decreasing annual precipitation totals in the Eastern Mediterranean for the end of the 21st century (e.g., Evans, 2009; Chenoweth et al., 2011; Smiatek et al. 2011). This would further aggravate the water scarcity problems in the region.

Studies on the causes of the described changes in precipitation as well as in other climate elements discuss the influence of land use and albedo pattern changes (Ben-Gai et al., 1993; Ben-Gai et al., 1998a). For instance, the installation of National Water Carrier in the early 1960's by the Israeli government is discussed to have a major influence on the regional climate (Ben-Gai et al., 1993). Via this pipeline a lot of water was transported from the north to the south, enabling intensive and extensive agriculture in the southern regions. The transformation of this area from a desert to agriculturally used areas increased the evapotranspiration rates. This lead to modifications in the surface radiation balance, the surface heat fluxes and the stability conditions of the Planetary Boundary Layer (Ben-Gai et al., 1993).

The regional water demand and supply is furthermore affected by socioeconomic changes as well as ecological changes (Salim and Wildi, 2005). The most important water resource in the study area of Palestine is groundwater. In 2008, 73.1 % (225.7 million m^3) of the water came from wells and 8.2 % (25.2 million m^3) from natural springs, another 18.7 % of the water needed to be imported; 57.8 million m^3 were purchased from the Israeli Water Company Mekorot (PCBS, 2009b). This water also mainly (70 %) comes from groundwater and natural springs (MEKOROT, 2012). As groundwater recharge strongly depends on rainfall, precipitation is the major factor in determining the regional water availability.

According to the land use statistics in 2010/2011, about 25 % of the land in the West bank and Gaza are cultivated (1,034.9 km²), whereby a high percentage of the cultivated lands are rain-fed agriculture strongly depending on precipitation. Out of them, 63.8 % are cropped with horticulture trees (89.9% are rain-fed), 23.7 % with field crops (94.1% are rain-fed) and 12.5 % with vegetables (13.6% are rain-fed) (PCBS, 2012). This high percentage of rain-fed agriculture is also related to the political situation in the region, which shaped and affected the landscape and its use. The land and water resources are controlled by Israel and the Palestinians are imposed severe restrictions to access their land and water resources (Temper, 2009). Thus, rainfall plays not only an important role in agricultural production in the region, but the agricultural output almost completely depends on the climatic parameters; mainly precipitation. On one hand Palestine has a chronic water shortage (Al-Rimmawi et al., 2010) and on the other hand agriculture is an important economic sector, contributing to about 6 % of the GDP and about 12 % of the total employment (The World Bank, 2013). Therefore the analysis of changes in the precipitation totals and their timing within the year is of immense importance for the Palestine economy and particularly the agricultural management.

Data of rain gauge stations of the Israel Meteorological Service are not always available for Palestinians, but global or European gridded datasets are. Here, we are going to explore the rainfalls characteristics and trends in the Palestinian territories and surroundings using two gridded precipitation datasets, the global dataset VASClimo (Beck *et al.*, 2004) and the European dataset E-OBS (Haylock et al., 2008).

2 Materials and methods

2.1 Study area

The geographical scope of this study includes the Palestinian territories and Israel. The study area lies between 34°20′–35°30′ E and 31°10′–32°30′ N (Ibrik, 2009) along the southeastern Mediterranean coast (Goldreich, 1995) and covers approximately 27,000 km^2. The area is divided into four physiographic regions: the Mediterranean coastal plain, the Central hills, the Jordan Rift Valley and the al-Naqab desert (MFA, 2015). These physiographic regions are represented by the applied grid data only to a limited extent. Despite its small size, Palestine is characterized by a great variation in topography with altitudes ranging from 350 m below sea level near the Dead sea to more than 1000 m above sea level in parts of the west bank. These variations in topography are directly reflected by the regional climate variability. Both aspects also strongly influence the distribution and diversification of agricultural patterns in the region (Isaac et al., 2011).

Palestine is impacted by different climatic systems, due to its location at the intersection of three continents; Europe, Asia and Africa (Samuels et al., 2011). Therefore it is classified as a transition zone between hyper-arid and relatively humid regions (Alpert and Jin, 2009; Bakour and Kolars, 1994). Generally, the area has a Mediterranean climate with long, hot, rainless summers, and cool, wet and relatively short winters. The average annual temperatures for the Palestinian territories range from 15.4 to 22.7°C (PCBS, 2009a) and annual precipitation totals for Israel including West Bank are between less than 200 mm in the south and east, and 300-900 mm in the north and west (Bar-Or and Matzne, 2010). Ziv et al. (2014) even reported annual precipitation totals of more than 1000 mm for the northern mountains.

The official rainfall year lasts from the first of August to the end of July (Goldreich, 1995). We are using this allocation in our analyses. Regarding the timing of the rain or wet season different dates are given in the literature. The rain seasons starts in October (Samuels et al., 2011; Ben-Gai et al., 1998b; Yosef et al., 2009) or November (Rice, 1886; Carmi et al., 2004) and extends till April (Samuels et al., 2011; Rice, 1886; Carmi et al., 2004) or May (Ben-Gai et al., 1998b; Yosef et al., 2009).

2.2 Data

Two data sources were used in this study. The first one is the global gridded data set VASClimO version 1.1 (Variability Analyses of Surface Climate Observations; Beck et al., 2004), covering the period 1951–2000. The second one is the European gridded data set E-OBS (Haylock et al., 2008), where monthly data (aggregated from daily data) are considered for the period 1951–2010.

2.2.1 VASClimO

The VASClimO dataset of monthly precipitation totals over land areas is interpolated from station data by using a variant of kriging. In comparison to other global precipitation datasets like the UEA CRU (University of East Anglia Climate Research Unit's) TS 2.1 data set (Mitchell and Jones, 2005) and the

GPCC (Global Precipitation Climatology Centre's) Full Data Reanalysis version 5 (Rudolf et al., 2010) data set, VASClimO is optimized with respect to temporal homogeneity. This means that only stations with complete records or such that could be reasonably completed were used for building the gridded dataset. These records were submitted to quality control in order to detect outliers and temporal inhomogeneities. Furthermore, as few different data sources as possible were considered and it was assured that the used data sources correspond well to each other. These data sources include the Food and Agriculture Organization of the UN (FAO), the Climate Research Unit (CRU), the Global Historical Climatology Network (GHCN), national meteorological and hydrological services and regional research projects. Altogether, 9343 station data series with at least 90 % data availability within 1951–2000 were used to build the grid – with the highest data density over Germany and France and sparse data over the Sahara Desert, central Africa, the Arabian Peninsula or central Australia. A global comparison of the three gridded datasets with regard to the spatial variability of annual precipitation totals by Sokol Jurković and Pasarić (2013) showed strong similarities.

VASClimO is available at three gridded resolutions; 0.5°×0.5°, 1.0°×1.0°, and 2.5°×2.5° latitude/longitude. The resolution of 0.5 degrees was selected to study the regional precipitation characteristics and changes, to represent the geographical differences within the comparatively small study area. The study area is covered by 23 grid cells that may be classified into four regions with similar precipitation characteristics (Figure 1). It has to be noticed that the resolution of the grid cells is still too coarse to resolve the precipitation characteristics arising from the variable relief in the study area.

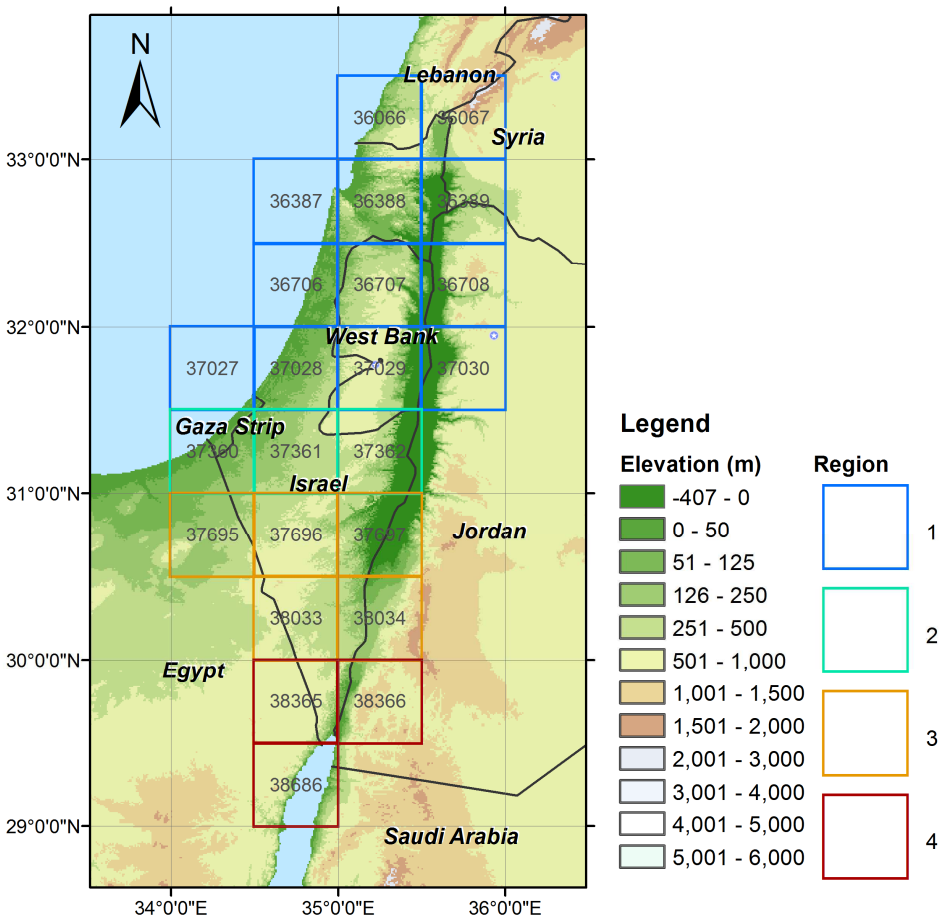

Figure 1: Selected grid cells with grid-cell numbers and region classification according to the VASClimO dataset. The grid-cells of E-OBS cover the same area, but no data are available for grid cells covered mainly by water (36387, 36706 and 37027).

2.2.2 E-OBS

The second gridded dataset used in this study is the E-OBS dataset (a European daily high-resolution gridded dataset of surface temperature and precipitation), which was developed within the EU Framework program 6 project ENSEMBLES (Haylock et al., 2008). It is a land-only data set that covers the area 25°–75°N, 40°W–75°E. The E-OBS dataset is based on more than 2.000 stations that are available by the European Climate Assessment and Data set (ECA&D; http://eca.knmi.nl/; Klok and Klein Tank, 2009). The number of stations used for the interpolations varies over time, which may lead to inhomogeneities and limitations in the use of this dataset for climate change studies.

Aims in developing this dataset were its use for the validation of Regional Climate Models (RCMs) and for climate change studies (Haylock et al., 2008). For these purposes different versions are available: a regular lat-lon grid (0.25 and 0.5 degree resolution) that is the same as the monthly CRU data grid (available from the Climatic Research Unit, http://www.cru.uea.ac.uk/) and a rotated pole grid (0.22 and 0.44 degree resolution, the north pole at 39.25N, 162W) to foster the comparability to the regional climate models produced within the ENSEMBLES project. We use the E-OBS dataset version 5 in the same spatial resolution of 0.5 degree like VASClimO to ensure the comparability of the two datasets and their respective trends.

For building the grid a three-step process of interpolation was used (Haylock et al., 2008). First, the monthly precipitation totals were interpolated using three-dimensional thin-plate splines. Second, the daily anomalies were interpolated using indicator and universal kriging. In the last step the monthly and daily estimates were combined. Additionally, the dataset provides an estimate of interpolation uncertainty by providing daily standard errors for every grid square (Haylock et al., 2008). Within the ENSEMBLES project efforts were made to select the most appropriate methodology for interpolating the point observations to a regular grid. The current best-of-class methods were compared in detail and according results are presented by Hofstra et al. (2009). Hofstra et al. (2009) also evaluated the homogeneity of the E-OBS dataset and its comparability to existing data. They found high overall correlations to other datasets, but large relative differences in precipitation, whereby E-OBS usually delivers lower values than other datasets. Applying the Wijngaard et al. (2003) homogeneity tests revealed many potential inhomogeneities in the gridded dataset. These are often related to inhomogeneities in the station data contributing to the value of the grid. Other inhomogeneities are probably introduced by variations in the station network (Hofstra et al., 2009).

2.3 Precipitation anomalies

Wet and dry precipitation anomalies are studied using the modified Rainfall Anomaly Index mRAI (Hänsel et al., 2015), that delivers comparable results to the well-known Standardized Precipitation Index (SPI; McKee et al. 1993), at least in moderate climate zones. The mRAI has been calculated on the timescales of 1, 12 and 24 months for every grid cell using the following equation (Hänsel et al., 2015):

$$mRAI = \pm SF * (P - \overline{P}) / (\overline{E} - \overline{P}) \qquad [1],$$

where P = precipitation sum of the respective timescale
$\overline{P}$ = median precipitation of the validation period 1951–2000 for the respective timescale
$\overline{E}$ = arithmetic average of the 10% most extreme precipitation sums (10% percentile for positive anomalies, 90% percentile for negative anomalies) of the validation period 1951–2000
$\pm SF$ = scaling factor (positive for $P > \overline{P}$, and negative for $P < \overline{P}$)

We use the same scaling factor of SF = 1.7 like Hänsel et al. (2015), as the analysis of the resulting frequency distributions shows a good agreement to the expected normal distribution. The mRAI calculations on a monthly time-scale (mRAI-1) were only done for the grid cells and months, where $\overline{E}$ of the 10 % (five events within 1951–2000) driest events was larger than zero. A calculation of precipitation anomalies is not reasonable for hyper-arid climate conditions, where zero precipitation is frequently observed. Thus the mRAI-1 has been only analysed for the wet season, whereas the mRAI on the timescales of 12 and 24 months can be calculated continuously.

The use of an anomaly index that evaluates the current precipitation totals against the normal conditions enables the comparison of grid cells with different climate characteristics and the identification of drought and wet events on different time scales. The dimensionless mRAI values are evaluated according to a classification scheme (Table 1) that is comparable to the one suggested for the SPI (McKee et al., 1993). There are nine classes ranging from extremely wet to normal to extremely dry.

Table 1 Moisture condition classes of the mRAI

Class	mRAI-value	Description
1	≥ 2.00	Extremely wet
2	1.50 to 1.99	Very wet
3	1.00 to 1.49	Moderately wet
4	0.50 to 0.99	Slightly wet
5	-0.49 to 0.49	Near normal
6	-0.99 to -0.50	Slightly dry
7	-1.49 to -1.00	Moderately dry
8	-1.99 to -1.50	Very dry
9	≤ -2.00	Extremely dry

2.4 Trend analysis approach

Different approaches of calculating trends are used within this study. The simplest approach is the calculation of the **difference of means** of two time series segments:

$$\Delta\overline{y} = \overline{y}_2 - \overline{y}_1 = \frac{2}{N}\left(\sum_{t=\frac{N}{2}+1}^{N} y_t - \sum_{t=1}^{\frac{N}{2}} y_t\right), \text{ with } N = \text{number of time series values.}$$

Following the recommendations of Rapp (2000) time series segments of equal length were used to include all time series values with the same weight. Furthermore, those two segments should not overlap and cover the whole analysis period. Therefore, we are comparing the periods 1951–1975 with 1976–2000 for VASClimO and 1951–1980 with 1981–2010 for E-OBS. This approach was used for the comparison of the frequency distribution of the moisture anomaly classes of the mRAI.

Linear trends were calculated using simple **linear regression** for the precipitation and mRAI time series. It determines an explicit functional relationship that is described in a relation equation. A straight line is drawn through the time series y_t of length N (Schönwiese 2006):

$$\hat{y}_n = \alpha + \beta \cdot t_n ,$$

with the ordinate values of the regression line $\hat{y}_n$ at the times t_n and the regression coefficients α and β. The regression equation is calculated using the "least square method" that minimises the quadratic deviations of the original data from the regression line (Schönwiese 2006; Rapp 2000):

$$\sum_{n=1}^{N} \left(y_n - \hat{y}_n\right)^2 = Min .$$

There are different ways to indicate the trend T (Rapp 2000):

(1) mere information about trend direction: $T = \mathrm{sgn}\beta$,

(2) absolute trend calculating the difference of the first and last ordinate value of the regression line for the studied timeframe: $T = \Delta\hat{y} = \hat{y}_N - \hat{y}_1 = \beta(N-1)$, with the number of time series values N ($t_n = 1,...,N$),

(3) relative trend: $T = \frac{\Delta\hat{y}}{\bar{y}}$ or $T = \frac{\Delta\hat{y}}{\hat{y}_1}$, respectively.

The advantage of relative tends is that they allow comparison of data series with spatially varying averages. While absolute trends reflect small-scale geographical dependencies, relative trends better illustrate larger-scale climatological structures (Rapp 2000).

Linear regression assumes normal distributed data and linear trends – an assumption that climatological as well as hydrological time series typically do not satisfy (e.g., Helsel and Hirsch, 1992). Therefore, a non-parametric trend test is performed in addition; the **Mann-Kendall trend test** (Schönwiese 2006), developed by Mann (1945) and modified by Kendall (1970). The advantages of this trend test are that it does not assume a normal distribution, it can also be applied for non-linear trends and it is less susceptible to outliers than linear regression analysis. One shortcoming of this test is that the quality of the results is still susceptible to autocorrelation in the time series (von Storch, 1995).

The test value Q_s is calculated counting the algebraic signs of all differences of time series values (y) and relating the sum S to the number of all possible combinations of time series values for $i < j$:

$$Q_s = \frac{\sum_{i=1}^{N-1} \sum_{j=i+1}^{N} \mathrm{sgn}(y_j - y_i)}{\frac{1}{2}N(N-1)} = \frac{S}{\frac{1}{2}N(N-1)}$$

For a number of time series values $N > 10$, the test value Q_s follows approximately a normal distribution with the mean $\mu = 0$ and the variance $\sigma^2 = \frac{2(2N+5)}{9N(N-1)}$.

The trend Q is calculated by standardizing the test value Q_s:

$$Q = \frac{Q_s - \mu}{\sigma} = \frac{S}{\sqrt{\frac{1}{18}N(N-1)(2N+5)}}$$

For identical time series values, KENDALL (1970) modified the test:

$$Q = \frac{S}{\sqrt{\frac{1}{18}\left[N(N-1)(2N+5) - \sum_l b_l(b_l-1)(2b_l+5)\right]}},$$

with b_l as the number of identical time series values of ordinate value y_l (Rapp 2000).

The non-parametric Mann-Kendall trend test is used for assessing the **significance** of trends. For the test values Q the confidence limits V and probability values α of normal distribution listed in **Table 2** are valid. Information on the significance of trends is completed by evaluating the spatial and temporal representativeness of trends.

Table 2: Significance of Mann-Kendall trend test value Q for specified confidence limits C and probability values α for a standard normal distributed test statistics (Rapp 2000)

Q	C	α
> 1,282	> 80%	< 0,2
> 1,645	> 90%	< 0,1
> 1,960	> 95%	< 0,05
> 2,576	> 99%	< 0,01
> 3,290	> 99,9%	< 0,001

As climate is highly variable in time and space, climate changes cannot be confirmed using single data series. Significant developments have to be temporarily stable and to occur area-wide (Rapp 2000). This is studied by assessing, besides the significance of trends, their spatial and temporal representativeness. Thereby, **temporal representativeness** refers to variations in the trend values, when the study period is being shifted gradually (Rapp 2000). It may be studied by calculating and comparing the trends of many time-series subintervals. Generally, the significance of a trend increases with decreasing variations superposing the trend. Thus relatively high or low values at the beginning or end of a time series have particularly high influence, primarily on linear trends and may distort them (Schönwiese and Janoschitz 2005). This source of error may be countered by successively shifting the analysis period. In this study, such kind of temporal-shifting analysis was used for 30-year-trends to assess the temporal representativeness of trends. Schönwiese and Janoschitz (2005) showed that trends tend to become unstable for time series shorter than 30 years. They concluded that trend calculation should be done for time series with a length of at least 30 years, 50- to 100-year trends are considered as relatively reliable.

In our analysis we are calculating the m-RAI values as well as the precipitation and mRAI trends for every single grid cell separately. In the regional analysis of precipitation characteristics the individual grid cell mRAI-values are averaged (arithmetic average) and the standard deviation is given additionally for regions comprising at least three grid cells.

3 Results and discussion

3.1 Precipitation characteristics

3.1.1 Annual precipitation

The annual precipitation totals in the study area range from below 30 mm in the arid South of the study area to more than 500 mm in semi-arid North (Figure 2). The magnitude of the values for individual grid cells may vary considerably in dependence of the chosen gridded data set. Generally, the annual precipitation totals for the period 1951–2000 are higher in the VASClimO than in the E-OBS dataset (Figure 2). Just for two cells (36708 and 37030) in the Northeast and four cells in the arid south (38034, 38365, 38366, 38686; mainly region 4) the E-OBS dataset delivers higher annual precipitation totals. The local variations in precipitation totals are even considerably higher as the values of the grid cells only represent spatially strongly smoothed signals. Analyses based on station data describe annual precipitation totals of more than 1000 mm for the northern mountains (e.g., Ziv et al. 2014). The West Bank – mainly represented by the VASClimO grid cells 36707 and 37029 – belongs to region 1 with comparatively high annual precipitation totals. The very south of the West Bank as well as the Gaza Strip belong to region 2 with annual precipitation totals mainly below 400 mm.

Time series of precipitation anomalies – using the modified Rainfall Anomaly Index mRAI (Hänsel et al. 2015) – are shown in Figure 3 and 4 for the entire study area as well as the four sub-regions and the West Bank area. In Figure 3 the results are displayed for the hydrological years (August to July) to cover the entire wet season and in Figure 4 for the precipitation anomalies on a time scale of 24 months to illustrate long-term wet and dry anomalies relevant for water management.

The identification of wet and dry anomalies by the two gridded datasets is in many cases well comparable, although the ranking of the most severe drought and wet years may vary with the considered dataset. Polynomial trends are displayed in addition to the yearly mRAI values in Figure 3 in order to illustrate the oscillation between periods with predominantly dry and wet anomalies, respectively. These show a drying trend in the first third of the time series, followed by a wetting trend that reverses again to a drying trend till the end of the study period. Between 1957/58 and 1963/64 almost all hydrological years were drier than normal with 1959/60 and 1962/63 being particularly dry in most regions. Wet anomalies have been slightly more abundant than dry anomalies between 1964 and 1992, with the hydrological years 1964/65, 1973/74, 1979/80, 1984/85, and 1991/92 being particularly wet. The last six years of the 20th century were mainly dry, whereby 1998/99 has been one of the most severe drought years. Also in the first ten years of the 21st century dry anomalies were more abundant than wet anomalies. The described oscillation is particularly visible in the regions 3 and 4 and less in regions 1 and 2.

Longer records would be very valuable in order to verify the observed oscillation between phases of abundant dry and wet conditions, respectively, that potentially mimics precipitation trends depending on the studied period. The comparison of the four sub-regions shows that the trend toward drier than normal conditions at the end of the 20th and beginning of the 21st century is particularly pronounced in the southern part of the study area (regions 3 and 4; Figure 3 and 4) that is already very dry (Figure 2).

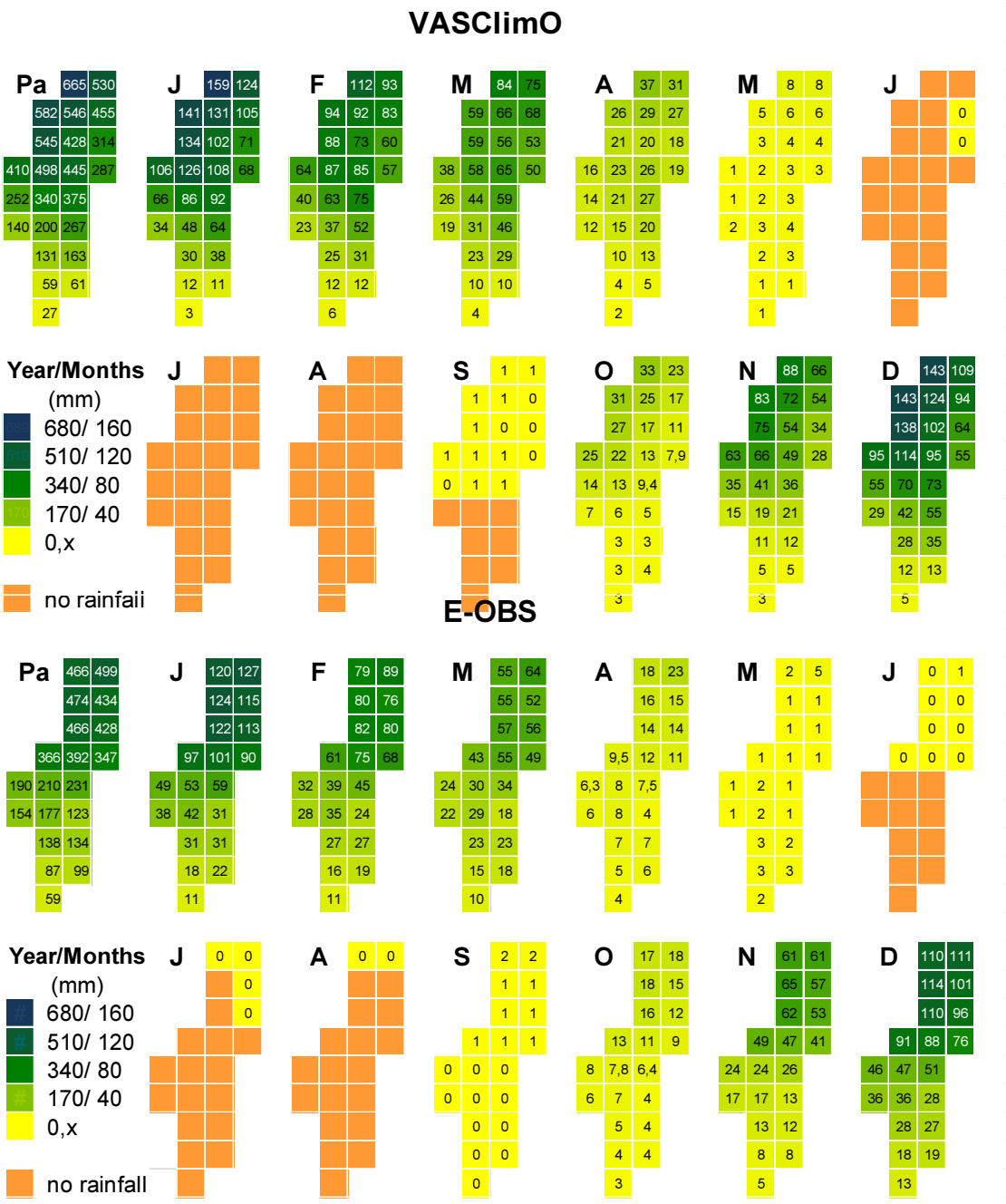

Figure 2: Maps of yearly and monthly precipitation totals for period 1951–2000 for the VASClimO and the E-OBS datasets. A continuous color scheme is used to illustrate the magnitude of yearly/ monthly (first/ second value in the legend) precipitation totals (exception: no rainfall within the study period is printed in orange).

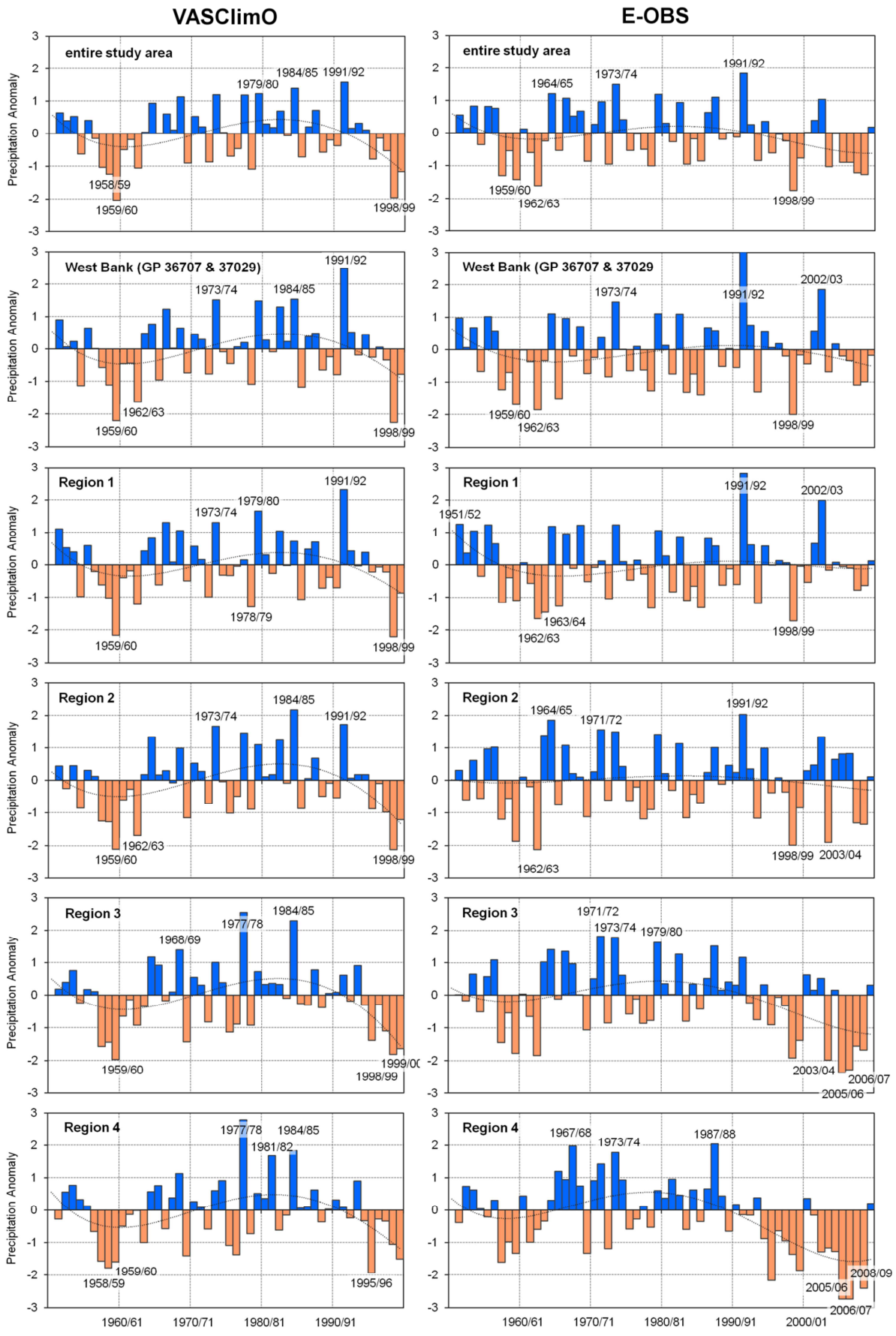

Figure 3: Precipitation anomalies (mRAI-values, see section 2.3) of the hydrological years (August to July) for the entire study area and selected sub-collectives with the three wettest and driest years and polynomial trends using the VASClimO (left) and the E-OBS (right) dataset.

The oscillation between long-term phases of dry and wet conditions is also visible in the time series of the mRAI on a timescale of 24 months (Figure 4). The period between 1957 and 1964 has been drier than normal in all sub-regions with the two peaks 1959/60 and 1962/63 already visible in the hydrological year data. Another period of long-term drought conditions over all sub-regions started in the mid 1990s and lasted till the beginning of the 21st century. In the northern regions 1 and 2 this drought event was interrupted by one to two wet phases being 2002–2005 in region 1 and 2002/03 and 2006/07 in region 2. In the two southern regions 3 and 4 wet anomalies of mRAI-24 occurred between 1995 and 2010 only for short periods (around 2002) and the magnitude of these positive anomalies was considerably smaller than in the regions 1 and 2. Between 2006 and 2009 the mRAI-24 indicated severely to extremely dry conditions in region 3 and 4, which is an exceptional long time of extreme drought conditions.

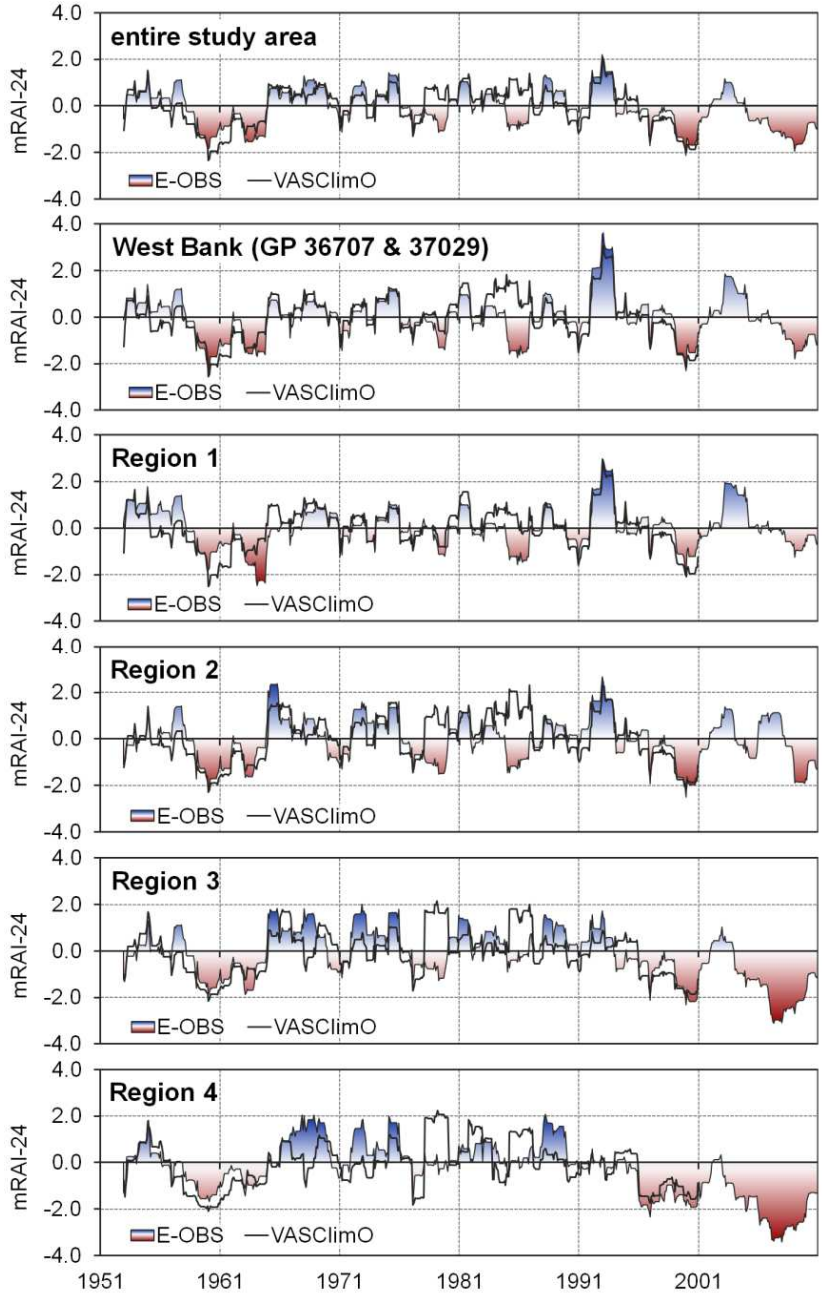

Figure 4: 24-month precipitation anomalies (mRAI-24) for the entire study area and selected sub-collectives comparing the VASClimO and the E-OBS datasets.

Additionally, Figure 4 also allows for a comparison of the two datasets with regard to the identified long-term wet and dry anomalies that are very important for water management issues. Although, both datasets correlate well (linear product moment correlation coefficients of grid cells and regional averages generally above 0.6, except for region 3 with correlations around 0.5) there are periods, where there is considerable disagreement between the two datasets. This applies, e.g., for 1978/79 and 1985/86 where VASClimO indicates wet anomalies, whereas E-OBS indicates dry conditions. These differences disappear in some regions, while being particularly pronounced in others. For instance, both dataset are well comparable in 1978/79 in the West Bank area and region 1, while the differences are very pronounced in the other regions. This suggests that the differences in the station data used for building the grid led to omissions and inclusions of individual regional rainfall events, respectively, and thus inaccuracies in the gridded datasets.

3.1.2 Frequency distribution

The frequency distributions of the precipitation anomalies of the hydrological year using the mRAI are compared between the two gridded datasets in Figure 5 for the entire study area and sub-regions. The distributions resemble the expected normal distribution, particularly averaged over the entire study area – demonstrating that the mRAI delivers good results for the study area – at least at a 12-month scale. It is remarkable that using the VASClimO dataset delivers about 10 % more events in the class "near normal" than the E-OBS dataset, while underestimating the wet classes. The frequency distribution of precipitation anomalies is also more symmetric for the E-OBS than for the VASClimO dataset.

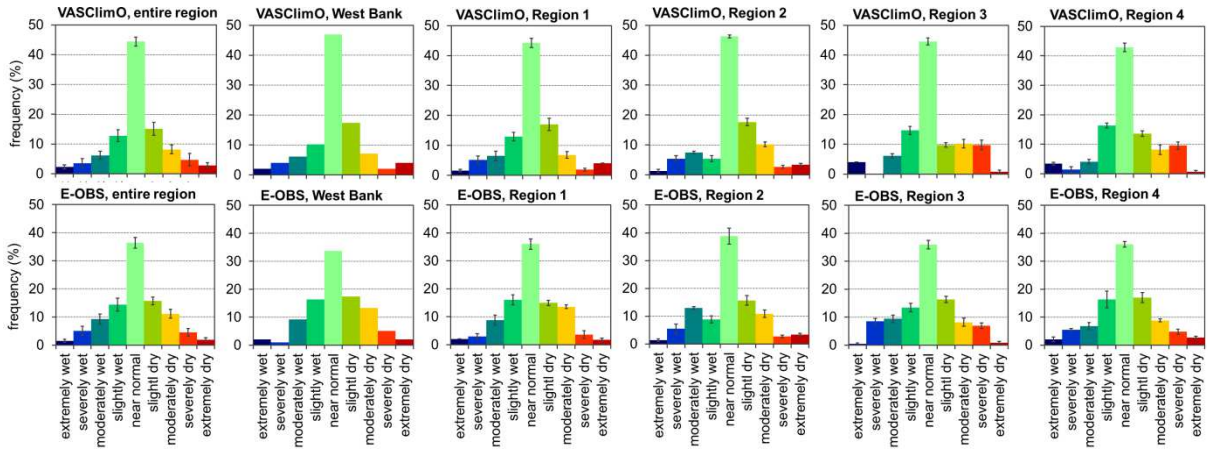

Figure 5: Frequency distributions of the hydrological year (August to July) precipitation anomalies using the mRAI for classifying the moisture conditions; period 1951–2000; the error bars indicate the spatial standard deviations (only for regions comprising at least three grid cells)

The spatial variability of the annual precipitation anomalies is displayed in Figure 6 using the nine moisture classes of mRAI (Table 1). In dry years negative precipitation anomalies are often present over the entire study area and the differences between individual grid cells are comparatively low, whereas wet years often show strong regional gradients in the moisture anomalies. Comparing the two datasets reveals that the spatial variability of moisture anomaly classes is slightly higher in the E-OBS than in the VASClimO dataset.

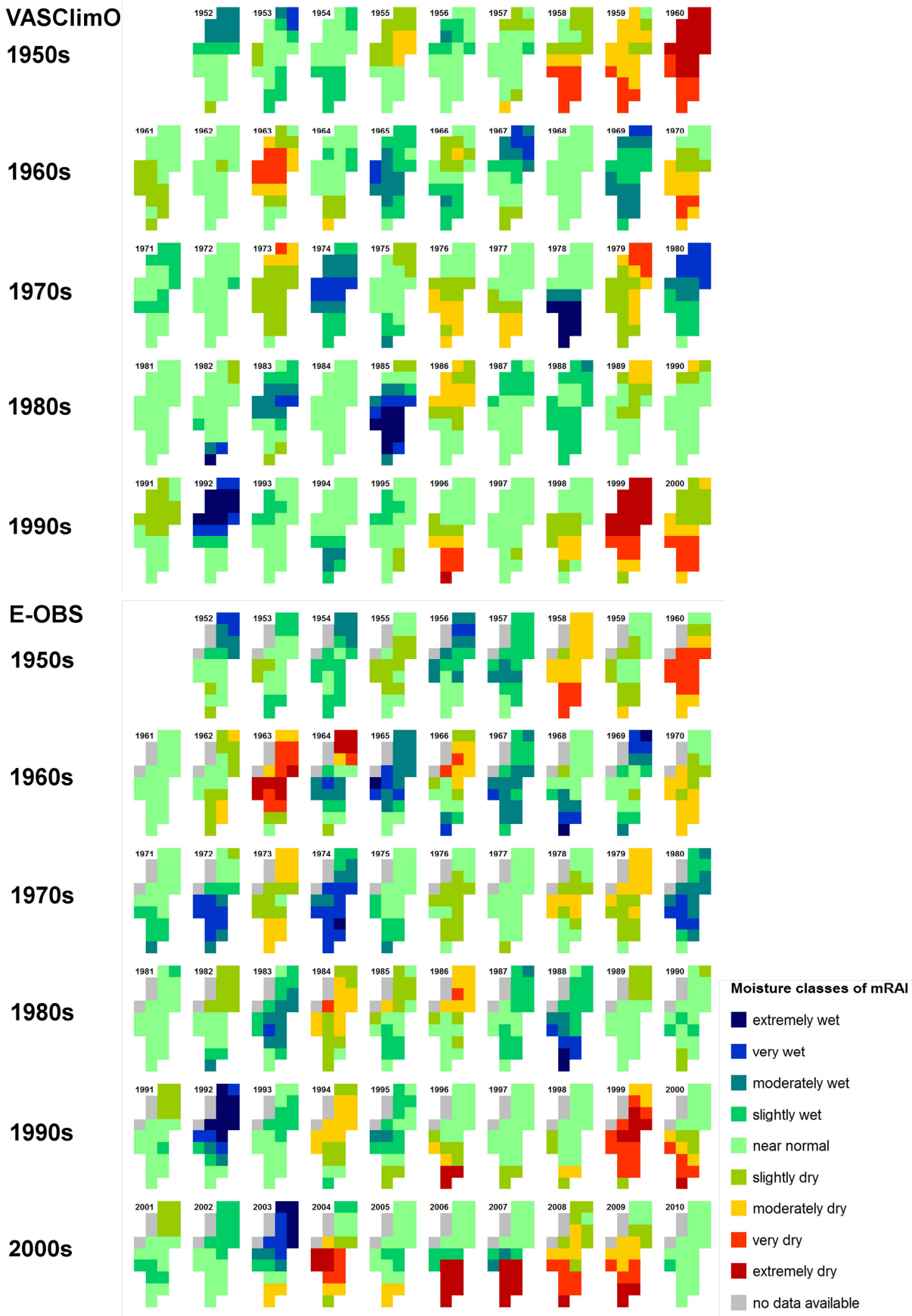

Figure 6: Spatial variability of annual (hydrological year; August to July) precipitation anomalies (using the mRAI; for moisture classification see table 1 and for colors the figure's legend; grey colors indicate missing data) for the hydrological years 1951/52 till 1999/2000 and 2009/10, respectively, according to the VASClimO and the E-OBS dataset

The general identification of wet and dry anomalies is comparable between the datasets in most years, but there are also some distinct differences, as already described for the mRAI time series of Figure 3 and 4. For instance, there are severe to extreme wet anomalies in the VASClimO dataset in the hydrological years 1977/78 and 1984/85 in the southern part of the study area (region 3 and 4). The E-OBS dataset delivers almost normal conditions during these years. These dissimilarities are probably due to differences in the station database used for creating the grids and potentially influence the computed precipitation trends.

3.1.3 Seasonal cycle

The seasonal precipitation cycle is very similar in the entire study area, as the low standard deviation values in Figure 7 illustrate. Generally, the study area is characterized by a wet season starting in October and lasting till May. The highest precipitation totals are normally recorded in December and January (together about 45 % of the annual precipitation). Generally, no precipitation is registered from June to August. Some precipitation is possible in September in the middle and northern part (region 1 and 2) of the study area and in May the precipitation totals are very low over the entire region.

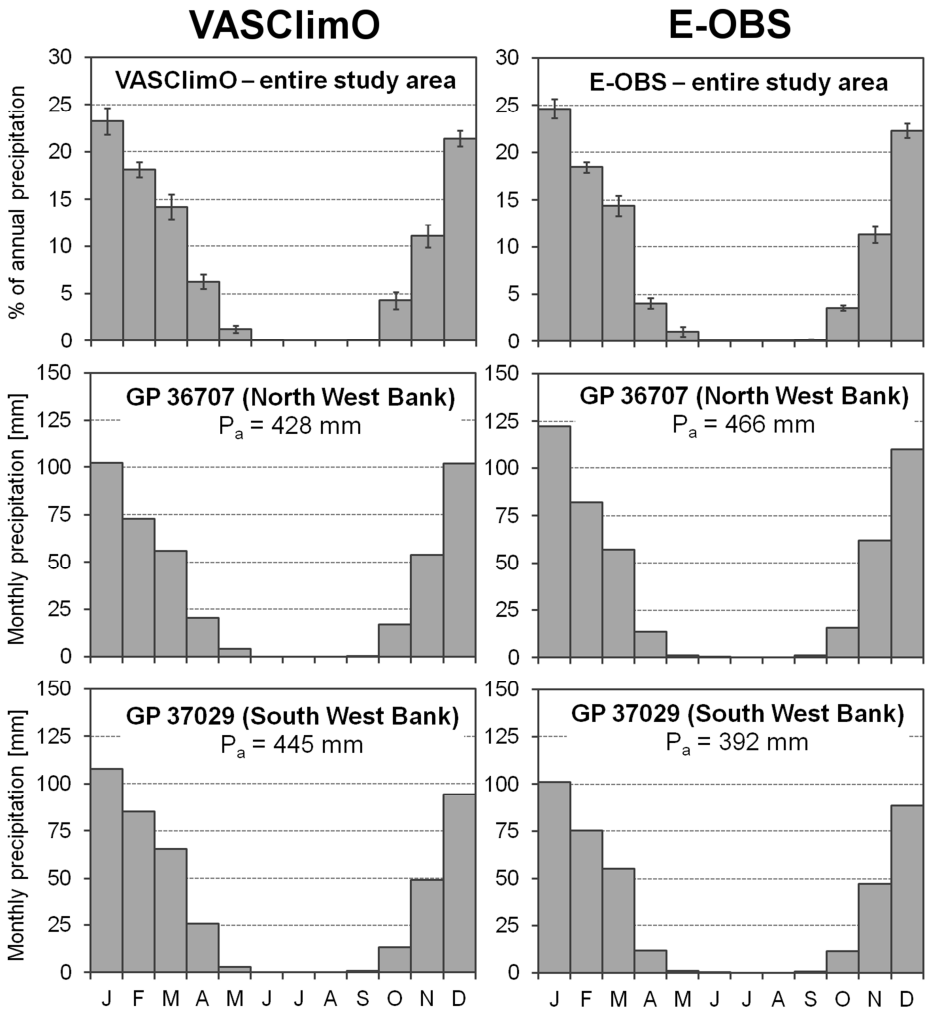

Figure 7: Seasonal precipitation cycle averaged over the entire study area (in % of the annual precipitation total) and for two selected grid cells representing the West Bank area (in mm) in the VASClimO (left) and the E-OBS (right) dataset

The North-South gradient of precipitation with the highest values in the North and decreasing precipitation totals to the South is represented by both datasets, although the gradient is a bit more pronounced in the VASClimO dataset (Figure 8). But this dataset does not represent the precipitation gradient in the West Bank territory. The two grid cells with the major coverage of the West Bank area deliver almost the same average annual precipitation total (Figure 2 and Figure 7). Within the E-OBS dataset the grid cell representing the Northern part of West Bank has higher annual precipitation totals than the grid cell representing the Southern part. This reflects in lower monthly precipitation totals during all months.

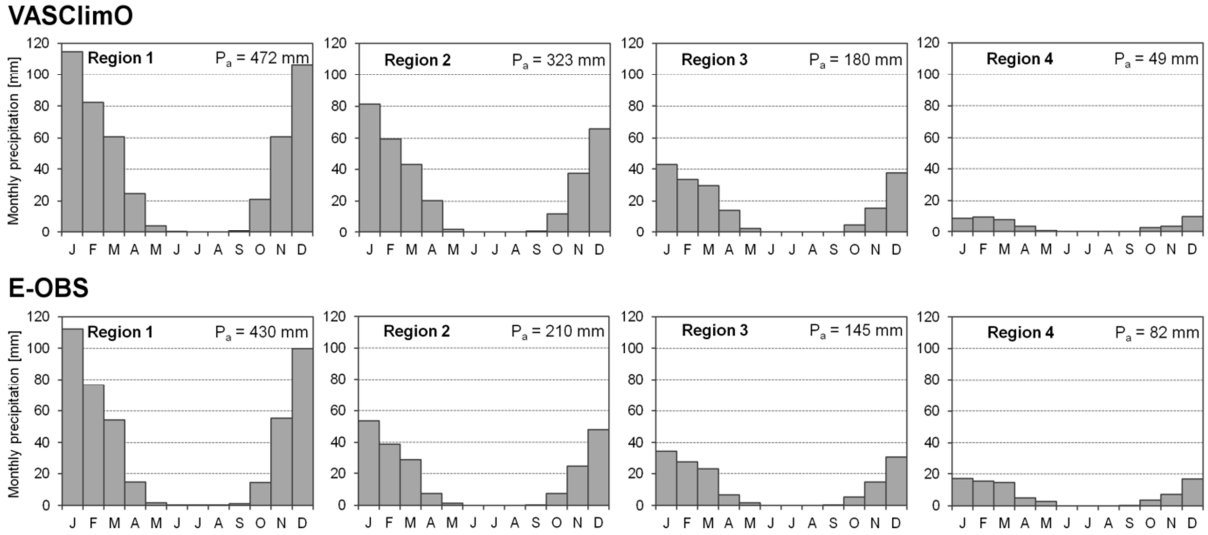

Figure 8: Comparison of the seasonal precipitation cycle of the four sub-regions between the two datasets

The seasonal variability of precipitation anomalies within the three most extreme dry and wet hydrological years, respectively, is displayed in the maps of Figure 9. Thereby, the monthly anomalies of five wet and four dry years are displayed, as the two datasets show slight differences in the identification of the most extreme drought and wet events. The precipitation totals of April within the E-OBS dataset are often zero, so that no mRAI has been computed for the majority of grid cells. There are distinct differences in the anomaly classification between the two datasets in selected months (Figure 9), like already described for the hydrological year anomalies. This applies, e.g., for February 1959 that is classified as moderately to extremely wet by the E-OBS dataset, but as near normal to moderately wet by the VASClimO dataset. The already described wet anomalies in the hydrological year 1984/85 in the southern part of the study area as indicated by the VASClimO dataset are due to wet anomalies in December 1984 and March 1985 that are not reflected by the E-OBS data.

3.2 Precipitation trends

3.2.1 Changes in annual precipitation totals

As shown in Figure 3 there is a large temporal variability in the annual precipitation totals and there seems to be a long-term oscillation between phases of drier and wetter than normal conditions, respectively. Nonetheless, linear regression analysis has been done and the relative linear trends are displayed in the maps of Figure 10.

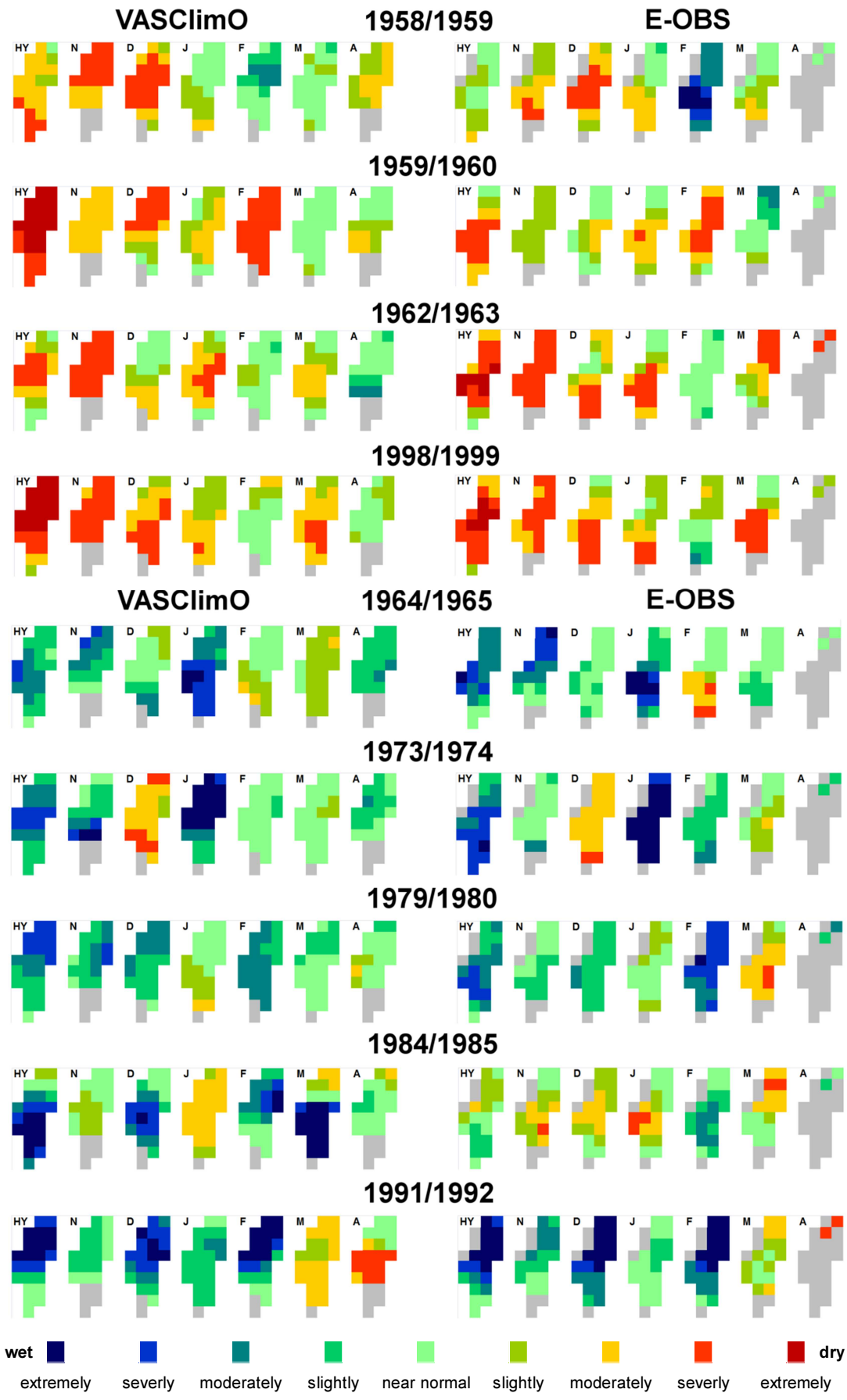

Figure 9: Spatial variability of monthly mRAI moisture classes (grey, i.e. precipitation averages are too low for the mRAI computation) for the three most extreme dry (upper maps) and wet (lower maps) hydrological years (HY) within the two datasets VASClimO (left) and E-OBS (right)

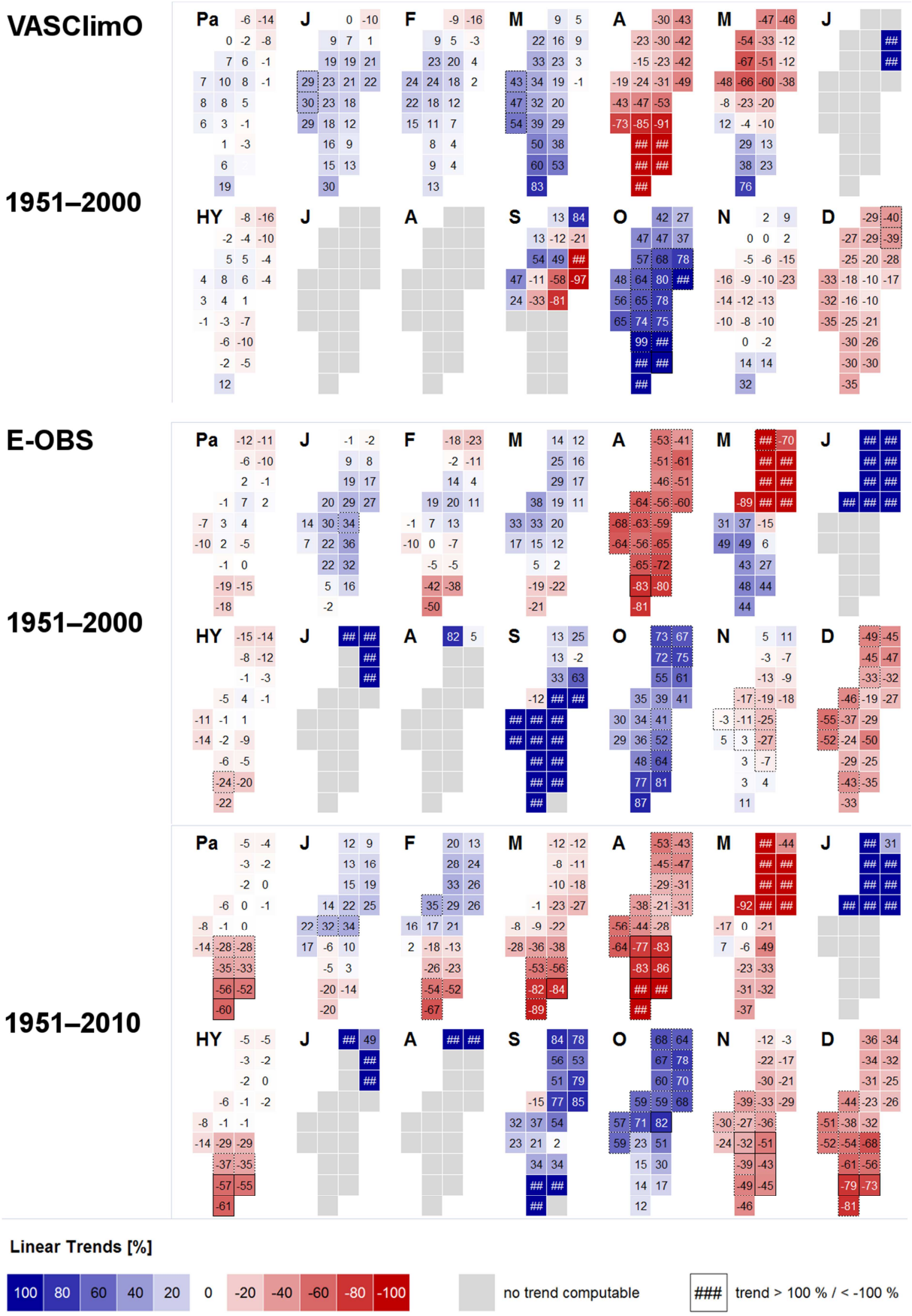

Figure 10: Maps of relative linear trends (in %) of the VASClimO and the E-OBS datasets for the year (Pa), the hydrological year (HY) and the months (from January [J] to December [D]). The statistical significance of the grid cell trends according to the Mann-Kendall trend test (not for the months June to August) is indicated by dotted ($p < 0.2$) and solid ($p < 0.05$) black grid lines.

There are no significant changes in the annual precipitation totals for period 1951–2000, independent if the calendar or the hydrological year is considered. In both datasets most of the annual linear trends for this period are between ±15 % (Figure 10) and the Mann-Kendall trend test (Mann, 1945; Kendall, 1970) delivers non-significant values for all grid cells. The trends get considerably larger in the southern part of the study area for the ten years longer period 1951–2010 with a decrease in by on average -27 % (-6.6 mm/decade) in region 3 and -56 % (-7.5 mm/decade) in region 4. The changes of all grid cells in region 4 are significant with a p-value of < 0.01 and the trends of the southern grid cells of region 3 have a p-value of < 0.1 according to the Mann-Kendall trend test (Figure 10).

3.2.2 Changes in the seasonal precipitation cycle

A redistribution of precipitation within the year may take place, even if annual changes are small and insignificant. Figure 10 shows that precipitation increased mainly in January, March and October – using the E-OBS dataset additionally also in September. Precipitation decreases were observed for April, November and December and in the northern part of the study area also for May. Most of these trends are insignificant for the period 1951–2000. Only for October (VASClimO) and April (E-OBS) several grid cells show trends with a low statistical significance. More cells with significant trends and higher significance levels, respectively, exist in April, October, November and December, if period 1951–2010 is considered. Thereby, the precipitation increases in October are weakly significant in the northern part (region 1 and 2) of the study area, while the precipitation decreases in November and December are mainly significant in the south (region 3 and 4). Significant precipitation decreases for almost all grid cells were observed for April with the highest significance in regions 3 and 4.

3.2.3 Changes in the frequency distribution

Besides changes in the average precipitation characteristics changes in the frequency distribution have been studied by comparing the time slices 1976–2000 vs. 1951–1975 for the VASClimO dataset and 1981–2010 vs. 1951–1980 for E-OBS. The mRAI was used for studying the dry and wet events, whereby dry events are such months, seasons and years, respectively, with mRAI values below -1 and wet events are defined by an mRAI value above 1.

Changes in the nine mRAI classes (Table 1) are calculated for every grid cell and the average and the standard deviation over the (sub-)region are displayed in Figure 11. The changes in dry and wet events often, but not always, agree with the trends in total precipitation. Generally, the disagreement between the change signals of the two grid datasets is larger for the moderately to extreme dry and wet conditions, respectively than for the precipitation averages. Thereby, the disagreement between the two datasets is particularly high for the wet events. Thus, no general statements about the development of wet events are possible. The frequency of dry events increased most markedly in November, although precipitation totals decreases were most pronounced in December. The strongest decrease in dry event frequency was observed for February, although average precipitation changes in February were spatially inconsistent and thus comparatively small if averaged over the entire area.

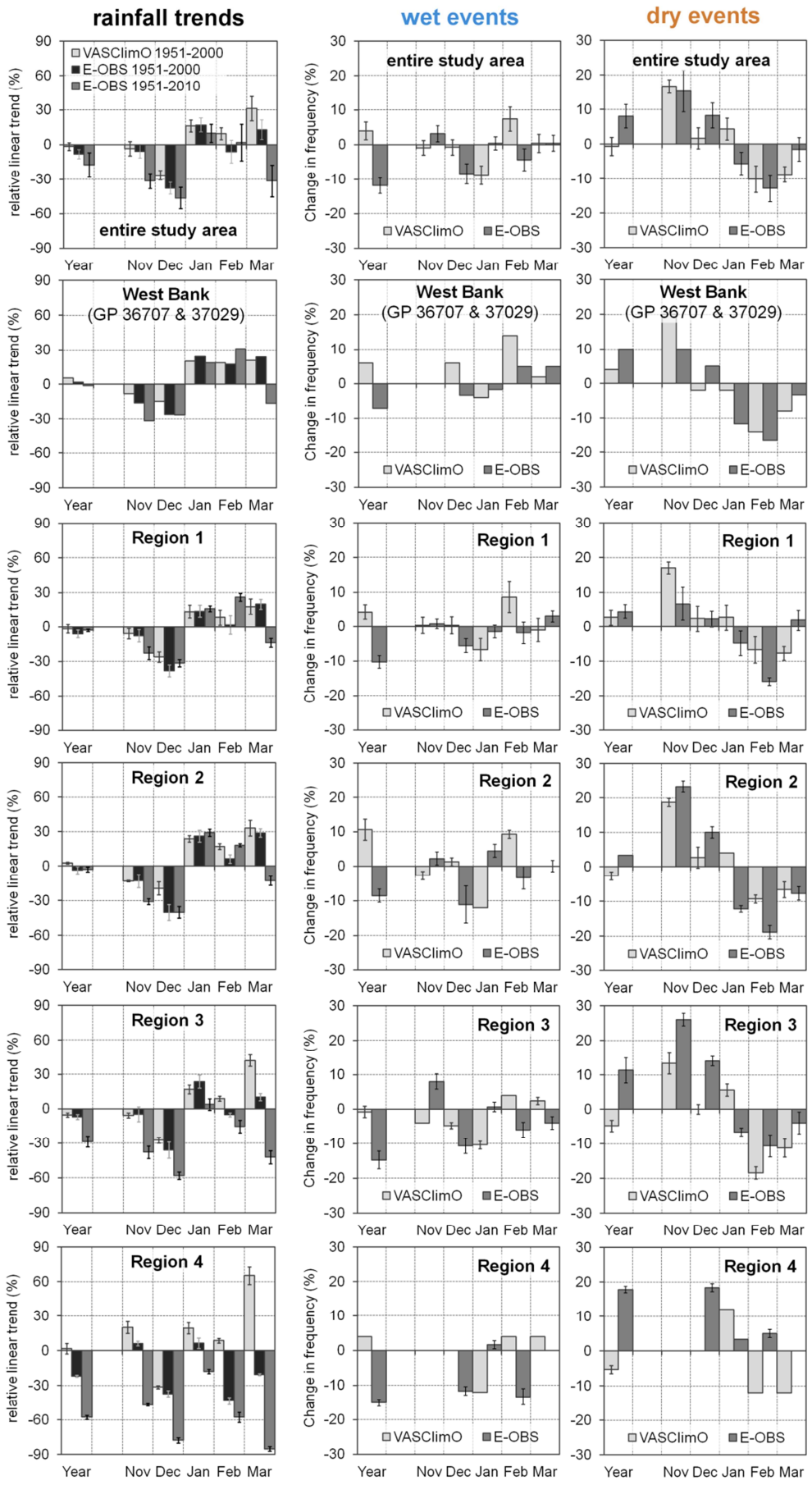

Figure 11: Changes in the frequency of wet years (mRAI > 1) and dry years (mRAI < -1) between 1976–2000/1981–2010 and 1951–1975/1951–1980 for the VASClimO /E-OBS dataset

3.2.4 Temporal trend stability

Due to the large temporal variability of precipitation the temporal stability of the observed trends is rather low, at least if 30 to 50 year trends are considered. In Figure 12 the 30-year trends, obtained via linear regression analysis, are displayed starting with the trend value for 1951–1981 and ending with the one for 1980–2010.

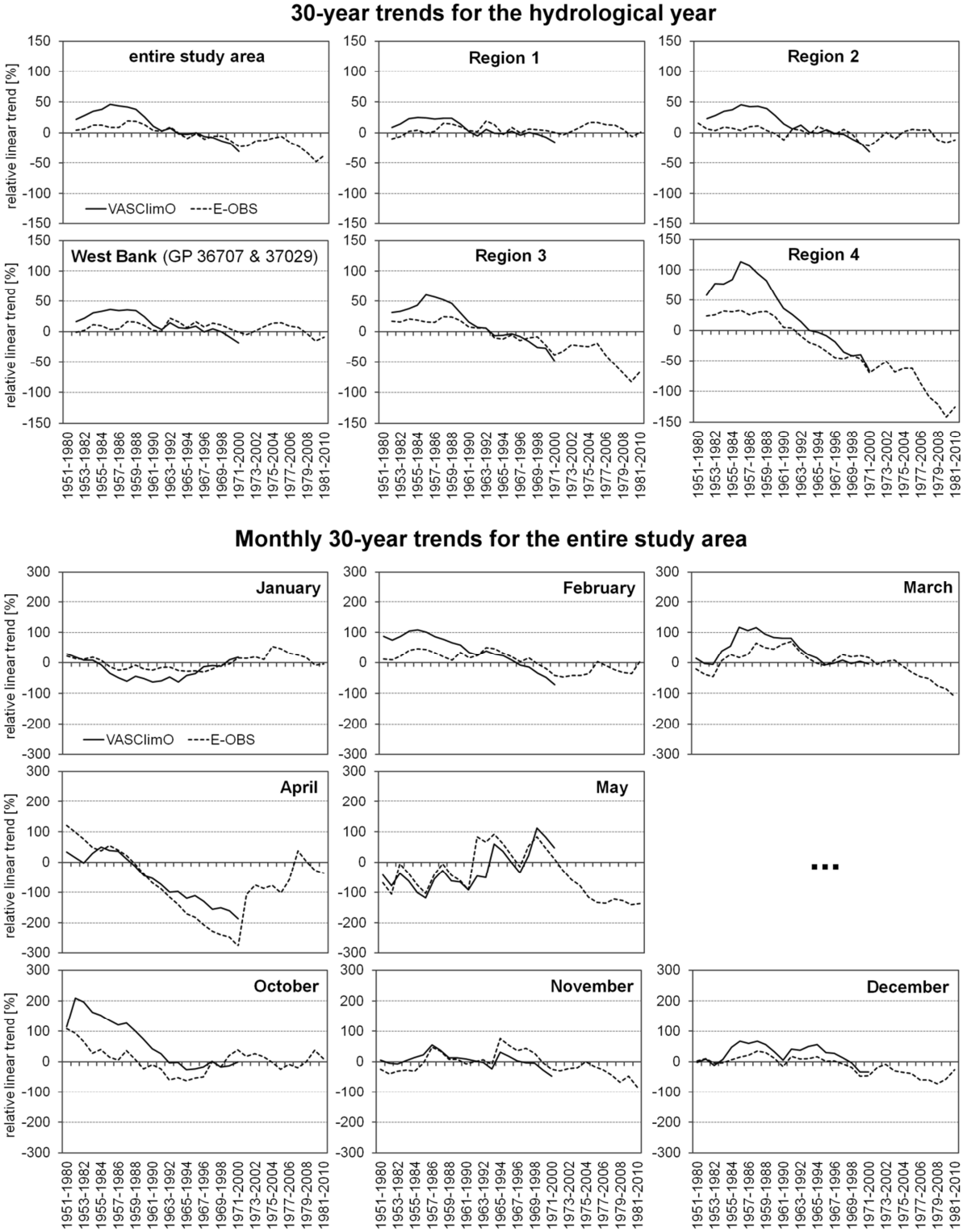

Figure 12: 30-Year trend values (relative linear trends in %) of annual (hydrological year; upper panels) and monthly (lower panels) precipitation totals for the two datasets from 1951–1980 to 1981–2010

The trends for the hydrological year for the entire study area are slightly positive for the first calculation periods and get negative for 30-year trends starting in the mid 1960's (Figure 12). This is true for both datasets although the VASClimO dataset tends to deliver higher trend values than E-OBS. Regionally, there a strong differences in the trend behavior. In region 1 and 2 as well as the West Bank area the trend values more or less fluctuate around zero, whereas both datasets show a shift from positive hydrological year trends (until about 1961–1990) to strongly negative trend values (particularly since 1971–2000) in the regions 3 and 4.

The 30-year trend values are considerably larger for individual months than for the entire hydrological year (attention: change in scale in Figure 12), due to opposite seasonal precipitation trends. Generally, the trend direction indicated by the two datasets is well comparable. The change from positive to negative trend values visible in the hydrological year trends occurs in February, March, November and December. January, April and October trends change from positive to negative and back to positive trend values. Thereby, the April trend values are very large (< -100 % between 1963–1992 and 1972–2001 for E-OBS), which is due to the low average precipitation totals of April that easily lead to high relative changes. May has even lower average precipitation totals, but the 30-year trends are smaller than for April. Besides, May is the only month where the trend values are negative for the first ten of the 30-year study periods, then change to positive values and back to negative ones for the last ten periods. The generally large variability in the short term trends (over 30 years) of precipitation averages reflects the strong temporal rainfall variability in the study area that strongly restricts robust conclusions about statistically significant changes.

4 Conclusions

Rainfall characteristics and trends within 1951–2010 have been studied for the Palestinian territories and adjacent areas on the basis of two gridded datasets – VASClimO and E-OBS. Both datasets have their individual pros and cons, with VASClimO being specifically designed for trend analysis purposes (Beck et al., 2004), but only available for 50 years and E-OBS with its longer time series in daily resolution, but problems with temporal homogeneity due to homogeneity problems in the station data and changes in the station collective (Hofstra et al., 2009). Additionally, both gridded datasets have the same limitations in comparison to station data, with regard to interpolation errors and the underestimation of extremes. Yet, due to the political situation high quality and long-term station data as collected by the Israel Meteorological Service are only available for Palestinians to a limited extent.

Generally, VASClimO delivers higher precipitation totals than E-OBS, but in the Southern part of the study area rainfall is higher in the E-OBS data. Although, there is a reasonable correlation between the VASClimO and E-OBS time series we observed considerable differences between the two datasets with respect to the identification of wet and dry rainfall anomalies for some years and seasons, particularly in the arid and data sparse South of the study area. These differences are probably due to differences in the station collective forming the basis of the grids and they potentially have a considerable impact on the identified rainfall trends. For instance, the March trends in the Southern regions 3 and 4 are strongly positive for 1951–2000 in the VASClimO dataset, whereas they range from slightly positive to negative in E-OBS. This is due to high precipitation totals in 1985 in VASClimO, not reflected in E-OBS and high rainfall totals in 1953 in E-OBS.

The datasets agree in identifying 1991/92 as the most extreme wet year in the study area, particularly the Northern part, as already described by Kafle and Bruins (2009) and Salim and Wildi (2005). This

year has been at the same time one of the coldest years (Kafle and Bruins, 2009). One of the driest years in the record has been 1998/99 that also was one of the warmest years and characterized by the strongest El-Nino event in the 20th century (Kafle and Bruins, 2009).

No significant annual rainfall trends have been observed in both datasets for 1951–2000, but there are more negative trends in the E-OBS than in the VASClimO dataset. The extension of the study period until 2010 (in E-OBS) leads to more and stronger negative precipitation trends in the Southern region, where most of the first ten years of the 21st century have been drier than normal. These precipitation decreases are statistically significant according to the non-parametric Mann-Kendall trend test. Further decreases of precipitation totals are projected for the 21st century by several climate modeling studies for the Eastern Mediterranean area and Israel (e.g., Evans, 2009; Chenoweth et al., 2011; Smiatek et al. 2011), potentially aggravating water stress in the region.

Seasonally, more significant trends emerge than for the annual data, particularly for 1951–2010. Increasing precipitation totals (low statistical significance) were mainly observed for October and significant decreases for April – in the Southern regions precipitation also decreased significantly in March, November and December. The temporal stability and thus representativeness of these trends is low for most months with 30-year trends changing from positive to negative values between 1951–1980 and 1981–2010.

Relations of the temporal and spatial rainfall patterns and trends in the region to atmospheric circulation are a further interesting field of study that we are going to explore in a follow-up study. Several studies already addressed the relation between precipitation and the Arctic Oscillation (AO; Thompson and Wallace, 1998) as well as the North Atlantic Oscillation (NAO; Hurrell, 1995) that can be viewed as the regional expression of the AO in the Atlantic sector. The NAO is a measure of pressure difference between the Icelandic Low and the Azores High and is associated with changes in the surface westerlies across the North Atlantic into Europe (Rogers 1985). Givati and Rosenfeld (2013) described negative correlations between the Arctic Oscillation (AO) and surface humidity in the northern part of the study area. Under positive AO conditions the subtropical Jet stream is weaker, the relatively humidity is lower and the CAPE is smaller than during negative AO conditions. Precipitation anomaly maps for Europe by Hoy et al. (2014) show that above normal precipitation in the Palestinian territories (and Israel) are connected to low pressure areas moving from west- or north-west towards the study area. The South-eastern tip of the Mediterranean appears as the only Mediterranean region, which receives more (less) precipitation during the positive (negative) phase of the NAO – explainable by the faded impact of the Azores Anticyclone in this area (maps in Hoy et al., 2014).

The E-OBS dataset with its daily resolution also offers the possibility of analyzing rainfall extremes like changes in the magnitude and frequency of heavy precipitation events or changes in the duration of dry and wet spells. We intend to carry out these analyses, using the E-OBS dataset in the higher resolution of 0.25 degree in order to better “catch” heavy precipitation events that often occur at small spatial scales. These trends of precipitation extremes would probably be even more unstable in time and space than the studied average changes on monthly and annual time scales. Ziv et al. (2014), for instance, described for Israel a decrease in rain days for 1975–2010 with a decrease in the wet season period of three days per decade. Our analyses indicate that precipitation trends for such short study periods are highly unreliable – at least for the considered region – and further studies of longer time series are needed.

5 Acknowledgements

We acknowledge the E-OBS dataset from the EU-FP6 project ENSEMBLES (http://ensembles-eu.metoffice.com) and the data providers in the ECA&D project (http://www.ecad.eu). We thank Andreas Hoy and an anonymous reviewer for their critical remarks und comments on an earlier version of this manuscript that helped to clarify and improve the paper.

6 References

Alpert, P., and Jin, F. (2009) Future predictions of moisture budget over the eastern Mediterranean based on a super-high-resolution global model, Proceeding of the Dahlia Greidinger International Symposium, Crop Production in the 21st Century: Global Climate Change, Environmental Risks and Water Scarcity: Haif.

Al-Rimmawi, H., Ghanem, M., and Shalash, I. (2010) Rainfall Trends in the District of Ramallah and Al-Bireh, Palestine: Water Resource and Protection, v. 2, p. 345-352.

Bakour, Y., and Kolars, J. (1994) The Arab Mashrek: Hydrologic history, problems and perspectives, In Water in the Arab world: Perspectives and prognoses (Rogers, P., Lydon, P., Eds.), pp 121–146, Harvard University Press, Cambridge, MA, USA.

Bar-Or, Y., and Matzne, O. (2010) State of the Environment in Israel Indicators, Data and Trends, Ministry of Environmental Protection.

Beck, C., Grieser, J., and Rudolf, B. (2004) A New Monthly Precipitation Climatology for the Global Land Areas for the Period 1951 to 2000, *Klimastatusbericht*, 181-190.

Ben-Gai, T., Bitan, A., Manes, A., and Alpert, P. (1993) Long-term change in October rainfall patterns in southern Israel: Theoretical and Applied Climatology, v. 46, p. 209-217.

Ben-Gai, T., Bitan, A., Manes, A., and Alpert, P. (1994) Long-Term Changes in Annual Rainfall Patterns in Southern Israel: Theor. Appl. Climatol. v. 49, p. 59-67.

Ben-Gai, T., Bitan, A., Manes, A., Alpert, P., and Israeli, A. (1998a) Aircraft measurements of surface albedo in relation to climate changes in southern Israel: Theor. Appl. Climatol., v. 61, p. 207-215.

Ben-Gai, T., Bitan, A., Manes, A., Alpert, P., and Rubin, S. (1998b) Spatial and Temporal Changes in Rainfall Frequency Distribution Patterns in Israel: Theoretical and Applied Climatology, v. 61, p. 177-190.

Ben-Gai, T., Bitan, A., Manes, A., Alpert, P., and Rubin, S. (1999) Temporal and Spatial Trends of Temperature Patterns in Israel, Theor Appl Climatol 64, 163-177.

Carmi, N., Bashir, B., and Rabi, A. (2004) Drought Analysis And The Effect Of Climate Change In The West Bank/Palestine, In BALWOIS, Ohrid, FY Republic of Macedonia.

Chenoweth, J.P., Hadjinicolaou, A. Bruggeman, Lelieveld, J., Levin, Z., Lange, M.A., Xoplaki, E., Hadjikakou, M. (2011) Impact of climate change on water resources of the eastern Mediterranean and Middle East region: modeled 21st century changes and implications. Water Resour. Res. 47. http://dx.doi.org/10.1029/2010WRR010269.

Evans, J. (2009) 21st century climate change in the Middle East, Climatic Change 92, 417-432.

Givati, A., and Rosenfeld, D. (2013) The Arctic Oscillation, climate change and the effects on precipitation in Israel. Atmospheric Research 132–133(0): 114-124.

Goldreich, Y. (1995) Temporal Variations of Rainfall in Israel: Climate Research, v. 5, p. 167-179.

Gurevich, G., Hadad, Y., Ofir, A., and Ohayon, B. (2011) Statistical analysis of temperature changes in Israel: An application of change point detection and estimation techniques, Global Nest Journal 13, 215-228

Hänsel, S., Schucknecht, A., and Matschullat, J. (2015) The Modified Rainfall Anomaly Index (mRAI)—is this an alternative to the Standardised Precipitation Index (SPI) in evaluating future extreme precipitation characteristics?, Theor Appl Climatol, 1-18. 10.1007/s00704-015-1389-y

Haylock, M. R., Hofstra, N., Klein Tank, A. M. G., Klok, E. J., Jones, P. D., and New, M. (2008) A European daily high-resolution gridded data set of surface temperature and precipitation for 1950–2006, Journal of Geophysical Research: Atmospheres 113, D20119, doi:10.1029/2008JD10201

Helsel, D.R., Hirsch, R.M. (1992) Statistical Methods in Water Resources. Elsevier, Amsterdam, 552 pp.

Hofstra, N., Haylock, M., New, M., and Jones, P. D. (2009) Testing E-OBS European high-resolution gridded data set of daily precipitation and surface temperature, Journal of Geophysical Research: Atmospheres 114, D21101, doi:10.1029/2009JD011799.

Hoy, A., Schucknecht A., Sepp M, Matschullat J. (2014) Large-Scale Synoptic Types and Their Impact on European Precipitation. Theoretical and Applied Climatology 116, Nr. 1-2, 19–35. doi:10.1007/s00704-013-0897-x.

Hurrell, J.W. (1995) Decadal trends in the North Atlantic Oscillation: regional temperatures and precipitation. Science 269, 676-679.

Ibrik, I. (2009) Energy Profile and the Potential of Renewable Energy Sources in Palestine. Renewable Energy in the Middle East. M. Mason and A. Mor, Springer Netherlands: 71-89.

IPCC, (2013) Climate Change 2013: The Physical Science Basis. Contribution of Working Group I to the Fifth Assessment Report of the Intergovernmental Panel on Climate Change [Stocker, T.F., D. Qin, G.-K. Plattner, M. Tignor, S.K. Allen, J. Boschung, A. Nauels, Y. Xia, V. Bex and P.M. Midgley (eds.)]. Cambridge University Press, Cambridge, United Kingdom and New York, NY, USA, 1535 pp

Isaac, J., Khair, A., and Hilal, J. (2011) Status of the Environment in the occupied palesinian territory - A Human Based Approach, Applied Research Institute - Jerusalem (ARIJ).

Kafle, H. and Bruins, H. (2009). Climatic trends in Israel 1970–2002: warmer and increasing aridity inland. Climatic Change 96(1-2): 63-77.

Kendall, Maurice. Rank Correlation Methods. 4th Edition. London: Griffin, 1970.

Klok, E. J., and Klein Tank, A. M. G. (2009) Updated and extended European dataset of daily climate observations, International Journal of Climatology 29, 1182-1191, doi:10.1002/joc.1779.

Mann, Henry B. „Nonparametric Tests Against Trend“. Econometrica 13 (3), 245-59. doi:10.2307/1907187.

McKee, T. B., Doesken, N. J., and Kleist, J. (1993) The relationship of drought frequency and duration to time scales, In Eighth Conference on Applied Climatology, Anaheim, California.

Mekorot (2012) Retrieved 15.05.2012, from http://www.mekorot.co.il/eng/newsite/Pages/default.aspx.

MFA (2015) "THE LAND: Geography and Climate." Retrieved 30.04.2015, from http://www.mfa.gov.il/MFA/Pages/default.aspx.

Mitchell, T. D., and Jones, P. D. (2005) An improved method of constructing a database of monthly climate observations and associated high-resolution grids, International Journal of Climatology 25, 693-712, doi:10.1002/joc.1181.

PCBS (2009a) Palestinian Environment in the Figures: Palestinian Central Bureau of Statistics, Ramallah-Palestine.

PCBS (2009b) Water Statistics in the Palestinian Territory Annual Report 2008: Palestinian Central Bureau of Statistics, Ramallah-Palestine.

PCBS (2012) Agriculture Statistics Survey, 2010/2011, Main Results: Palestinian Central Bureau of Statistics, Ramallah, Palestine.

Price, C., Stone, L., Huppert, A., Rajagopalan, B., and Alpert, P. (1998) A possible link between El Nino and precipitation in Israel: Geophysical Research Letters, v. 25, p. 3963-3966.

Rapp J (2000): Konzeption, Problematik und Ergebnisse klimatologischer Trendanalysen für Europa und Deutschland. Berichte des DWD 212, German Weather Service: Offenbach/Main, Germany. 145 pp.

Rice, E.W. (1886) Rainfall in Palestine: Journal of the Society of Biblical Literature and Exegesis, v. 6, p. 69-72.

Rofe and Raffety (1965) Nablus District Water Resources Survey, Geological and Hydrological Report for Hashemite Kingdom of Jordan, Central Water Authority, Westminster, London.

Rogers, J.C. (1985) Atmospheric circulation changes associated with the warming over the North Atlantic in the 1920s. Journal of Climate and Applied Meteorology 24, 1303-10.

Rudolf, B., Becker, A., Schneider, U., Meyer-Christoffer, A., and Ziese, M. (2010) The new “GPCC Full Data Reanalysis Version 5” providing high-quality gridded monthly precipitation data for the global land-surface is public available since December 2010. GPCC Status Report December 2010. Available at http://gpcc.dwd.de.

Salim, N., and Wildi, W. (2005) Impact of global climate change on water resources in the Israeli, Jordanian and Palestinian region, Terre et Environnement 50, 125–140.

Samuels, R., Smiatek, G., Krichak, S., Kunstmann, H., and Alpert, P. (2011) Extreme value indicators in highly resolved climate change simulations for the Jordan River area: journal of geophysical research, v. 116.

Schönwiese, C.-D. (2006): Praktische Statistik für Meteorologen und Geowissenschaftler, eth Edition, Gebrüder Borntraeger, Berlin, 302 pp.

Schönwiese, C.-D., Janoschitz, R. (2005) Klima-Trendatlas Deutschland 1901-2000. report No. 4, Institute Atmosphere Environment, University Frankfurt/Main, Germany. Available at: https://www.uni-frankfurt.de/45447808/Inst_Ber_4_21.pdf

Smiatek, G., Kunsmann, H., Heckl, A. (2011) High resolution climate change simulations for the Jordan River area. J. Geophys. Res. 116, D16111. http://dx.doi.org/10.1029/2010JD015313.

Sokol Jurković, R., and Pasarić, Z. (2013) Spatial variability of annual precipitation using globally gridded data sets from 1951 to 2000, International Journal of Climatology 33, 690-698.

Steinberger, E.H., and Gazit-Yaari, N. (1996) Recent Changes in the Spatial Distribution of Annual Precipitation in Israel: Journal of Climate, v. 9, p. 3328–3336.

Thompson, D.W.J., Wallace, J.M. (1998) The arctic oscillation signature in the wintertime geopotential height and temperature fields. Geophys. Res. Lett. 25, 1297-1300.

Von Storch, V.H. (1995) Misuses of statistical analysis in climate research. In: Storch, V.H. and Navarra, A. (Eds.) Analysis of Climate Variability: Applications of Statistical Techniques, Springer, Berlin. Applied Statistics, 11-26.

Temper, L. (2009) Creating facts on the ground: Agriculture in Israel and Palestine (1882-2000). Historia Agraria (48):75-110+7.

The World Bank (2013) Fiscal Challenges and Long Term Economic Costs: Economic Monitoring Report to the Ad Hoc Liaison Committee.

Wijngaard, J. B., Klein Tank, A. M. G., and Können, G. P. (2003) Homogeneity of 20th century European daily temperature and precipitation series, International Journal of Climatology 23, 679-692, doi:10.1002/joc.906.

WRAP (2013) A Comparative Study of Water Data Across Israel, West Bank, and Jordan.

Yosef, Y., Saaroni, H., and Alpert, P. (2009) Trends in Daily Rainfall Intensity Over Israel 1950/1-2003/4: The Open Atmospheric Science Journal, v. 3, p. 196-203.

Ziv, B., Saaroni, H., Pargament, R., Harpaz, T., and Alpert, P. (2014) Trends in rainfall regime over Israel, 1975–2010, and their relationship to large-scale variability, Reg Environ Change 14, 1751-1764, doi:10.1007/s10113-013-0414-x.